

Imperial College London  
Department of Electrical and Electronic Engineering

**Acoustic sensing as a novel approach  
for cardiovascular monitoring  
at the wrist**

Piyush Sharma

February 2020

Supervised by Prof. Esther Rodriguez-Villegas

Submitted in part fulfilment of the requirements for the degree of  
Doctor of Philosophy in Electrical and Electronic Engineering of Imperial College  
London and the Diploma of Imperial College London

# Abstract

**Objective:** Cardiovascular diseases are the number one cause of deaths globally. An increased cardiovascular risk can be detected by a regular monitoring of the vital signs including the heart rate, the heart rate variability (HRV) and the blood pressure. For a user to undergo continuous vital sign monitoring, wearable systems prove to be very useful as the device can be integrated into the user's lifestyle without affecting the daily activities. However, the main challenge associated with the monitoring of these cardiovascular parameters is the requirement of different sensing mechanisms at different measurement sites. There is not a single wearable device that can provide sufficient physiological information to track the vital signs from a single site on the body. This thesis proposes a novel concept of using acoustic sensing over the radial artery to extract cardiac parameters for vital sign monitoring. A wearable system consisting of a microphone is designed to allow the detection of the heart sounds together with the pulse wave, an attribute not possible with existing wrist-based sensing methods.

**Methods:** The acoustic signals recorded from the radial artery are a continuous reflection of the instantaneous cardiac activity. These signals are studied and characterised using different algorithms to extract cardiovascular parameters. The validity of the proposed principle is firstly demonstrated using a novel algorithm to extract the heart rate from these signals. The algorithm utilises the power spectral analysis of the acoustic pulse signal to detect the S1 sounds and additionally, the K-means method to remove motion artifacts for an accurate heartbeat detection. The HRV in the short-term acoustic recordings is found by extracting the S1 events using the relative information between the short- and long-term energies of the signal. The S1 events are localised using three different characteristic points and the best representation is found by comparing the instantaneous heart rate profiles. The possibility of measuring the blood pressure using the

wearable device is shown by recording the acoustic signal under the influence of external pressure applied on the arterial branch. The temporal and spectral characteristics of the acoustic signal are utilised to extract the feature signals and obtain a relationship with the systolic blood pressure (SBP) and diastolic blood pressure (DBP) respectively.

**Results:** This thesis proposes three different algorithms to find the heart rate, the HRV and the SBP/ DBP readings from the acoustic signals recorded at the wrist. The results obtained by each algorithm are as follows:

- The heart rate algorithm is validated on a dataset consisting of 12 subjects with a data length of 6 hours. The results demonstrate an accuracy of 98.78%, mean absolute error of 0.28 bpm, limits of agreement between -1.68 and 1.69 bpm, and a correlation coefficient of 0.998 with reference to a state-of-the-art PPG-based commercial device. A high statistical agreement between the heart rate obtained from the acoustic signal and the photoplethysmography (PPG) signal is observed.
- The HRV algorithm is validated on the short-term acoustic signals of 5-minutes duration recorded from each of the 12 subjects. A comparison is established with the simultaneously recorded electrocardiography (ECG) and PPG signals respectively. The instantaneous heart rate for all the subjects combined together achieves an accuracy of 98.50% and 98.96% with respect to the ECG and PPG signals respectively. The results for the time-domain and frequency-domain HRV parameters also demonstrate high statistical agreement with the ECG and PPG signals respectively.
- The algorithm proposed for the SBP/ DBP determination is validated on 104 acoustic signals recorded from 40 adult subjects. The experimental outputs when compared with the reference arm- and wrist-based monitors produce a mean error of less than 2 mmHg and a standard deviation of error around 6 mmHg.

Based on these results, this thesis shows the potential of this new sensing modality to be used as an alternative, or to complement existing methods, for the continuous monitoring of heart rate and HRV, and spot measurement of the blood pressure at the wrist.

# Contents

<b>Abstract</b>	<b>2</b>
<b>List of Figures</b>	<b>8</b>
<b>List of Tables</b>	<b>16</b>
<b>List of Publications</b>	<b>18</b>
<b>Acknowledgements</b>	<b>19</b>
<b>Declaration of Originality</b>	<b>20</b>
<b>Copyright Declaration</b>	<b>21</b>
<b>Terms and Abbreviations</b>	<b>22</b>
<b>Units</b>	<b>24</b>
<b>Thesis Structure</b>	<b>25</b>
<b>1 An introduction to non-invasive cardiovascular monitoring techniques and systems</b>	<b>28</b>
1.1 Introduction . . . . .	28
1.2 Heart rate and its variability: definitions and monitoring techniques . . .	31
1.2.1 Contact-based HR/ HRV monitoring techniques . . . . .	33
1.2.1.1 Sensing the electrical activity . . . . .	33
1.2.1.2 Sensing the optical activity . . . . .	35
1.2.1.3 Sensing the acoustic activity . . . . .	36
1.2.2 Non contact-based HR/ HRV monitoring techniques . . . . .	37
1.2.2.1 Sensing the mechanical activity . . . . .	37
1.2.2.2 Radar-based heartbeat detection . . . . .	38
1.2.2.3 Resonator-based heartbeat detection . . . . .	39
1.2.3 Commercially available HR/ HRV monitors . . . . .	39
1.2.4 Summary . . . . .	48



1.3	Blood pressure: What is it? How is it measured? . . . . .	49
1.3.1	Non-invasive blood pressure monitoring techniques . . . . .	50
1.3.1.1	The auscultatory method . . . . .	50
1.3.1.2	The oscillometric method . . . . .	51
1.3.1.3	Ultrasound method . . . . .	53
1.3.1.4	The finger-cuff method . . . . .	53
1.3.1.5	Pulse transit time method . . . . .	54
1.3.2	Factors affecting the blood pressure measurement . . . . .	55
1.3.3	Commercially available BP monitors . . . . .	56
1.3.4	Summary . . . . .	64
	References . . . . .	65
<b>2</b>	<b>Wearable sensing of the pulse sounds at the wrist</b>	<b>76</b>
2.1	Introduction . . . . .	76
2.1.1	The circulatory system . . . . .	76
2.1.2	The pulse . . . . .	77
2.1.2.1	Pressure wave . . . . .	77
2.1.2.2	Flow wave . . . . .	79
2.1.3	Arteries . . . . .	80
2.2	Literature review of sensing the radial pulse . . . . .	82
2.2.1	Monitoring techniques and their applications . . . . .	82
2.2.2	Summary . . . . .	89
2.3	Wearable sensing of the pulse sounds . . . . .	90
2.3.1	Types of acoustic sensors . . . . .	92
2.3.1.1	Contact microphone . . . . .	93
2.3.1.2	Capacitor microphone . . . . .	93
2.3.1.3	MEMS microphone . . . . .	95
2.3.1.4	Summary . . . . .	98
2.3.2	Power supply . . . . .	99
2.3.2.1	Battery size . . . . .	100
2.3.2.2	Supply voltage . . . . .	101
2.3.2.3	Supply current . . . . .	102
2.3.2.4	Battery capacity and life . . . . .	102
2.3.2.5	Battery choice . . . . .	103
2.3.3	Data acquisition hardware . . . . .	104
2.4	Designing the wearable acoustic sensor . . . . .	106
	References . . . . .	109
<b>3</b>	<b>Characterising the pulse sounds for continuous heart rate monitoring</b>	<b>116</b>
3.1	Introduction . . . . .	116

3.2	Characteristics of pulse sounds . . . . .	116
3.2.1	Temporal characteristics . . . . .	117
3.2.2	Spectral characteristics . . . . .	118
3.3	Optimal sensor site . . . . .	121
3.4	Noise artefacts . . . . .	122
3.4.1	Noise internal to the wrist . . . . .	123
3.4.2	Noise due to the motion artefacts . . . . .	124
3.4.3	Environmental noise . . . . .	127
3.4.4	Summary . . . . .	128
3.5	An algorithm to extract heart rate from pulse sounds . . . . .	129
3.5.1	Algorithmic blocks . . . . .	129
3.5.2	Acoustic data pre-processing . . . . .	130
3.5.3	S1 sound extraction . . . . .	131
3.5.4	Peak detection . . . . .	134
3.5.4.1	Constructing energy envelope of the extracted S1 sounds	134
3.5.4.2	Artefact identification and elimination . . . . .	134
3.5.5	Subjects and experimental protocol . . . . .	137
3.5.6	Results . . . . .	138
3.6	Discussion . . . . .	143
	References . . . . .	146
<b>4</b>	<b>An algorithm to determine heart rate variability in short-term acoustic recordings</b>	<b>147</b>
4.1	Introduction . . . . .	147
4.2	Existing methods . . . . .	149
4.3	Data acquisition protocol . . . . .	161
4.4	S1 waveform extraction method . . . . .	162
4.5	Peak detection algorithm . . . . .	164
4.6	Results and discussion . . . . .	169
4.6.1	Optimal choice of parameters . . . . .	169
4.6.2	Time-domain HRV analysis . . . . .	170
4.6.3	Frequency-domain HRV analysis . . . . .	177
4.7	Conclusion . . . . .	180
	References . . . . .	181
<b>5</b>	<b>Blood pressure measurement by sensing Korotkoff sounds at the wrist</b>	<b>188</b>
5.1	Introduction . . . . .	188
5.2	Hardware development for step-wise pressure inflation . . . . .	189
5.3	Studying the variation of the acoustic signal with the inflating pressure levels . . . . .	191

5.4	Algorithm for determining the diastolic blood pressure . . . . .	195
5.4.1	Pre-processing the acoustic signal . . . . .	195
5.4.2	Artifact removal and missed peaks detection . . . . .	196
5.4.3	Feature signals to find the diastolic blood pressure . . . . .	198
5.4.3.1	Amplitude envelope . . . . .	198
5.4.3.2	Energy envelope . . . . .	198
5.4.3.3	Diastolic band analysis of the S1 sounds . . . . .	200
5.4.4	Utilising the feature signals to identify the S1 sound corresponding to the diastolic blood pressure . . . . .	202
5.5	Algorithm for determining the systolic blood pressure . . . . .	205
5.5.1	Feature signals to find the systolic blood pressure . . . . .	206
5.5.1.1	Amplitude envelope . . . . .	206
5.5.1.2	Systolic band analysis of the S1 sounds . . . . .	206
5.5.1.3	Template matching coefficient envelope . . . . .	210
5.5.2	Utilising the feature signals to identify the S1 sound corresponding to the systolic blood pressure . . . . .	212
5.6	Experimental procedure . . . . .	215
5.7	Results and discussion . . . . .	217
5.8	Conclusion . . . . .	221
	References . . . . .	222
<b>6</b>	<b>Conclusions</b>	<b>224</b>
6.1	Contributions . . . . .	224
6.2	Further Work . . . . .	226
	<b>Appendices</b>	<b>227</b>
<b>A</b>	<b>Permission for the third party copyrighted works used in this thesis</b>	<b>228</b>

# List of Figures

1.1	An example of IBI tachogram representing the time-interval between each subsequent beat ( $\sim 1600$ beats).	32
1.2	An example of a ECG signal consisting of P wave, QRS complex and T wave. All the R-peaks are marked.	34
1.3	An example of a PPG signal. All the systolic peaks are marked.	35
1.4	An example of a PCG signal consisting of S1 and S2 sounds.	37
1.5	An example of a typical arterial blood pressure waveform [103].	50
1.6	Oscillometric method for blood pressure measurement. (a) Pressure oscillations superimposed on the deflating pressure curve. (b) Oscillometric waveform envelope corresponding to the detrended pressure oscillations. The fixed ratios are used to estimate the SBP, DBP from the maximum oscillation peak [111]	52
2.1	Cardiac cycle events with variation in atrial, ventricular and aortic pressure [6].	78
2.2	Normal arterial pressure waveform corresponding to systolic and diastolic phase of the cardiac cycle [8].	79
2.3	(a) Origin of the radial artery from bifurcation of the brachial artery at the cubital fossa of the forearm [11]. (b) Anatomy of the radial artery and the deep flexor muscles of the left forearm [12].	80
2.4	Distal, middle and proximal locations on the radial artery to sense the pulse.	81
2.5	Design approach for a wireless wearable device to sense pulse sounds at the wrist.	91
2.6	Frequency response of a contact microphone when facing its rubber sensing pad to piston-like displacement of a structure [96].	92
2.7	(a) Cross-sectional view of a condenser microphone with an air gap between the moveable diaphragm and the backplate [98]. (b) Condenser microphone connected to an external bias voltage source, parasitic capacitance and a preamplifier [98].	95
2.8	Frequency response curve of an ECM (CMC-5044PF, CUI Inc.) with sensitivity at a baseline of -44 dB [101].	96

2.9	(a) MEMS microphone with transducer, ASIC and wire bonding. Top package has sound port on top (in lid) and bottom package has sound port on bottom (in PCB substrate) [103]. (b) Cross-sectional schematic view of a MEMS microphone with the sound port in the PCB substrate [104].	97
2.10	Frequency response of a capacitive MEMS microphone (INMP411, InvenSense Inc.) [105]. . . . .	98
2.11	Analogue front end designs for data acquisition from the microphone. (a) The first design includes a high pass filter followed by an inverting amplifier and first-order passive RC low pass filter. (b) The second design includes a high pass filter followed by a non-inverting amplifier and a second-order active low pass filter. . . . .	105
2.12	Hardware design flow (consisting of the microphone, an analogue front end and nRF52 platform) for the acoustic wearable device to sense pulse sounds at the wrist. . . . .	107
2.13	Wearable device used to acquire acoustic signals. The device consists of a MEMS microphone sensor integrated with Bluetooth low energy transmission. . . . .	108
3.1	Temporal characteristics of the acoustic signal with respect to the PPG signal. . . . .	117
3.2	Characterisation of the acoustic signal: (I) Pulse waveform recorded by placing the miniaturised device on the middle position of the radial artery at wrist. (II) Comparison of acoustic and PPG waveforms to synchronise both the signals by matching the nearest systolic peaks. PPG data was recorded using SOMNOscreen pulse oximeter [1]. (III) Joint time-frequency analysis of the acoustic signal obtained using STFT. The colour intensity of the grids demonstrates their relative power. (IV) Frequency response (FFT) of the acoustic signal. . . . .	119
3.3	Spectral characteristics of the acoustic signals with different morphology and recorded from different subjects. . . . .	121
3.4	PSDs of the acoustic signal obtained with the microphone placed on distal, middle and proximal site. For illustration, the PSD of the noise obtained from the signal recorded by completely blocking the microphone port is also plotted. . . . .	123
3.5	PSD of the acoustic signal obtained with the microphone placed on the opposite side of the wrist. The noise PSD corresponds to the sealed microphone port. . . . .	124
3.6	Different types of hand movements that can introduce significant noise in the recording setup. . . . .	125
3.7	Frequency response of artefacts introduced due to different finger movements.	126

3.8	Frequency response of artefacts introduced due to wrist, elbow, shoulder and arbitrary movements. . . . .	127
3.9	PSDs of the acoustic signal recorded in the presence of vocal speech (normal and loud volume) and loud music. . . . .	128
3.10	Block diagram of the proposed algorithm to determine HR from the acoustic signal by extracting S1 sounds using the STFT analysis. . . . .	129
3.11	Pre-processing of the acoustic signal sensed by the system: (a) Original signal. (b) Low-pass filtered and downsampled signal to remove higher frequency components and redundant information respectively. (c) Clustering using the K-means method to identify signal segments corrupted with motion artefacts. Symbol + and $\square$ represents the features and cluster centroids respectively. (d) Signal segment corrupted with motion artefact (due to wrist/ finger movement) removed from the downsampled signal. .	132
3.12	S1 sounds extraction from a different pre-processed signal with no corrupted segment: (a) Acoustic signal after initial low-pass filtering, down-sampling and K-means application. (b) PSD of the signal obtained using STFT to extract S1 sounds. (c) Rectangular windows representing the regions of interest. (d) S1 sounds extracted by adding a tolerance of 150 milliseconds on both sides of the rectangular windows. . . . .	133
3.13	Peak detection in a clean signal: (a) Squared energy of the S1 sound waveform in Fig. 3.12(d). (b) Energy peaks obtained using the moving average filter. * represent the time indexes corresponding to the S1 sounds.	135
3.14	Peak detection in a corrupted signal: (a) Input acoustic signal corrupted with motion artefacts (introduced by wrist/ finger movements). (b) Squared energy of the signal obtained after PSD analysis. The redundant peaks due to the motion artefacts in systolic and diastolic phases of the cardiac cycle can be observed. (c) Energy envelope obtained using the moving average filter. (d) Thresholding of energy peaks to remove envelopes corresponding to the motion artefacts. (e) Time indexes of energy peaks corresponding to S1 sound waveforms in the signal. This shows how the algorithm successfully distinguishes between motion artefacts and S1 waveforms. . . .	136
3.15	Results obtained for one of the subjects: (a) HR comparison between the estimated output (HR-APS) and reference output (HR-PPG) with upper and lower HR bounds of $\pm 5\%$ respectively. (b) Bland-Altman analysis with more than 95% of HR differences lying within LOAs, defined by $(\mu \pm 2 \times \sigma)$ . (c) Line of best fit between the estimated and ground truth HR values. The $R^2$ and RMSE value, a measure of fitness of line to the data, were 0.992 and 0.397 respectively. The Pearson correlation was 0.996.	139

3.16	Results obtained for the complete dataset: (a) Bland-Altman analysis of the HR comparisons for all the subjects. (b) Line of best fit between the estimated and ground truth HR values for all the subjects. The $R^2$ and RMSE value are 0.997 and 0.861 respectively. The Pearson correlation is 0.998. . . . .	140
3.17	Variation of HR in individual subjects. HR-STD: standard deviation of the range; HR-MIN: minimum value of the range; HR-MEAN: mean value of the range; HR-MAX: maximum value of the range; HR-RMS: root-mean-square value of the range. . . . .	141
4.1	Generic block diagram for R-peak extraction from the ECG signal. . . . .	149
4.2	Relative energy algorithm implemented on the acoustic pulse signal. (a) Original input acoustic signal consisting of different S1 waveforms. (b) Normalised short- and long-term energies of the input signal depicting numerator and denominator in Eq. 4.1. (c) The coefficient signal, $c(n)$ . (d) The output signal, $y_{re}(n)$ . . . . .	164
4.3	Morphological variations in the pulse waveform. (a) Acoustic pulse transitioning from a positive peak to zero crossing to a negative peak. (b) Acoustic pulse transitioning from a negative peak to zero crossing to a positive peak. Symbol $\times$ , $\circ$ and $\diamond$ denotes the positive peak ( $APS_p$ ), zero crossing ( $APS_z$ ) and negative peak ( $APS_n$ ) respectively. Symbol $*$ represents the nearest zero crossings on either sides of $APS_z$ . . . . .	165
4.4	Localisation of characteristic points in the signal. (a) Clipped positive and negative waveforms of the original input signal. (b) Squared energy of the relative energy signal with its corresponding maximum. (c) Symbol $\times$ , $\circ$ and $\diamond$ denote the time-localisation of the positive peak ( $APS_p$ ), the zero crossing ( $APS_z$ ) and the negative peak ( $APS_n$ ) respectively in the relative energy signal. Symbol $*$ represents the nearest zero crossings on either sides of $APS_z$ . . . . .	166
4.5	Localisation of the characteristic points in the acoustic signal corrupted with artifacts. (a) Clipped positive and negative waveforms of the original input signal. (b) Squared energy of the relative energy signal with its corresponding maximum. (c) Symbol $\times$ , $\circ$ and $\diamond$ denoting the time-localisation of positive peak ( $APS_p$ ), zero crossing ( $APS_z$ ) and negative peak ( $APS_n$ ) respectively on the relative energy signal. Symbol $*$ represents the nearest zero crossings on either sides of $APS_z$ . (d) Time-domain features plotted for waveforms extracted in Fig. 4.4(c). (e) Time-domain features plotted for waveforms extracted in Fig. 4.5(c). . . . .	167

4.6	Effect of short- and long-term sliding windows on performance metrics of the proposed algorithm. (a) Contour plot for depicting variation in sensitivity ( $S_e$ ). (b) Contour plot for depicting variation in positive predictive value (PPV). (c) Contour plot for depicting variation in detection error rate (DER). . . . .	170
4.7	IHR comparisons for subject 8. (a) Full IHR time series, correlation analysis and Bland-Altman plot between APS- and PPG-derived HR. (b) Full IHR time series, correlation analysis and Bland-Altman plot between APS- and ECG-derived HR. . . . .	173
4.8	IBI comparisons for subject 8. (a) Full IBI time series, correlation analysis and Bland-Altman plot between APS- and PPG-derived IBI. (b) Full IBI time series, correlation analysis and Bland-Altman plot between APS- and ECG-derived IBI. . . . .	174
4.9	IHR and IBI comparisons for the complete dataset. (a) Correlation analysis and Bland-Altman plot between APS- and PPG-derived HR. (b) Correlation analysis and Bland-Altman plot between APS- and PPG-derived IBI. (c) Correlation analysis and Bland-Altman plot between APS- and ECG-derived HR. (d) Correlation analysis and Bland-Altman plot between APS- and ECG-derived IBI. . . . .	175
4.10	HRV spectra for acoustic signal recorded from subject 10. (a) NN interval tachogram with its corresponding mean and variance. (b) VLF, LF and HF central frequency and power in absolute value, calculated by a FFT based non-parametric algorithm. The LF component is indicated by dark shaded areas and the HF component by light shaded areas. (c) VLF, LF and HF central frequency, power in absolute value and power in normalised units (n.u.), calculated by parametric autoregressive modelling. In (a) and (b), the peak frequency and the power were calculated by integrating the PSD in the defined frequency bands. . . . .	178
5.1	Pressure control system to apply varying pressure levels on the site under test. . . . .	190
5.2	Variation in the acoustic signal with respect to the inflating pressure inside the air cuff. (a) Pressure applied on the arm increases between zero and a value above the systolic blood pressure. (b) Acoustic signal recorded from the radial artery in synchronisation with the pressure signal. n.u. denote the normalised units. (c) STFT analysis of the varying time-frequency characteristics of the acoustic signal. . . . .	192



5.3	Frequency spectrum of the S1 sounds in the acoustic signal. (a) Pressure inside the air cuff increases between zero and a value above the systolic blood pressure. (b) Time-domain acoustic signal with numbered S1 sounds of interest. (c)-(r) FFT of the sixteen S1 sounds marked in the acoustic signal. The FFT coefficients are plotted in absolute units. . . . .	194
5.4	Pre-processing the acoustic signal to reduce the noise content. (a) Original acoustic signal with significant interference from the motor noise. (b) Reduction of the external interference using low pass filtering, downsampling, wavelet denoising and median filtering. . . . .	196
5.5	Identification of the erroneous peaks and missed S1 peaks in the acoustic signal. (a) S1 peaks detected by the relative energy algorithm. The peaks in the blue and magenta circles are the erroneous and missed peaks respectively. (b) S1 peaks detected by the relative energy algorithm in acoustic signal low-pass filtered with 25 Hz. (c) The peaks in (b) are utilised to remove the erroneous peaks and trace back the missed S1 peaks in the acoustic signal. . . . .	197
5.6	Energy and amplitude envelopes of the Korotkoff sounds with peaks marked in the negative side of the acoustic signal. (a) Pressure applied on the arm increases between zero and a value above the SBP. (b) Pre-processed acoustic signal with all the S1 peaks identified. (c) Energy envelope of the Korotkoff sounds falling after the 40 mmHg pressure level. The experimentally determined Korotkoff sound location for DBP determination is also plotted along with the reference wrist and reference arm DBP location. An error of 5 and 1 mmHg was obtained with respect to the wrist and arm DBP references respectively. (d) Amplitude envelope of the negative amplitudes (lower envelope) of the S1 peaks falling after the 40 mmHg pressure level. The bounds used in the proposed algorithm are also plotted. (e) Amplitude envelope of the positive amplitudes (upper envelope) of the S1 peaks falling after the 40 mmHg pressure level. . . . .	199
5.7	Wide-band analysis of the normalised energy envelope in different frequency bands for the DBP determination. Normalised energy of seven S1 sounds centred at the reference DBP are plotted. . . . .	201

5.8	Energy and amplitude envelopes of the Korotkoff sounds with peaks marked in the positive side of the acoustic signal. (a) Pressure applied on the arm increases between zero and a value above the SBP. (b) Pre-processed acoustic signal with all the S1 peaks identified. (c) Energy envelope of the Korotkoff sounds falling after the 40 mmHg pressure level. The experimentally determined Korotkoff sound location for DBP determination is also plotted along with the reference wrist and reference arm DBP location. An error of 3 mmHg was obtained with respect to the wrist and arm reference DBP. (d) Amplitude envelope of the positive amplitudes (upper envelope) of the S1 peaks falling after the 40 mmHg pressure level. The bounds used in the proposed algorithm are also plotted. (e) Amplitude envelope of the negative amplitudes (lower envelope) of the S1 peaks falling after the 40 mmHg pressure level. . . . .	204
5.9	Energy and amplitude envelopes of the Korotkoff sounds with peaks marked in the negative side of the acoustic signal. (a) Pressure applied on the arm increases between zero and a value above the SBP. (b) Pre-processed acoustic signal with all the S1 peaks identified. (c) Energy envelope of the Korotkoff sounds falling after the 40 mmHg pressure level. The experimentally determined Korotkoff sound location for SBP determination is also plotted along with the reference wrist and reference arm SBP location. An error of 2 and 4 mmHg was obtained with respect to the wrist and arm SBP references respectively. (d) Amplitude envelope of the negative amplitudes (lower envelope) of the S1 peaks falling after the 40 mmHg pressure level. The bounds used in the proposed algorithm are also plotted. (e) Template matching coefficients envelope of the S1 peaks falling after the 40 mmHg pressure level. The bounds used in the proposed algorithm are also plotted.	207
5.10	Wide-band analysis of the normalised energy envelope in different frequency bands for the SBP determination. Normalised energy of seven S1 sounds centred at the reference SBP are plotted. . . . .	208
5.11	S1 waveforms in the acoustic signal recorded from a subject (a) before cuff inflation, (b) around the DBP, (c) before reaching the SBP. The zero crossings of these peaks are also marked. . . . .	210

5.12	Energy and amplitude envelopes of the Korotkoff sounds with peaks marked in the positive side of the acoustic signal. (a) Pressure applied on the arm increases between zero and a value above the systolic blood pressure. (b) Pre-processed acoustic signal with all the S1 peaks identified. (c) Energy envelope of the Korotkoff sounds falling after the 40 mmHg pressure level. The experimentally determined Korotkoff sound location for SBP determination is also plotted along with the reference wrist and reference arm SBP location. An error of 0 and 6 mmHg was obtained with respect to the wrist and arm SBP references respectively. (d) Amplitude envelope of the positive amplitudes (upper envelope) of the S1 peaks falling after the 40 mmHg pressure level. The bounds used in the proposed algorithm are also plotted. (e) Template matching coefficients envelope of the S1 peaks falling after the 40 mmHg pressure level. The bounds used in the proposed algorithm are also plotted. . . . .	213
5.13	Results obtained for the DBP determination from the acoustic signal. (a) Bland-Altman analysis for the DBP comparisons with the wrist DBP reference. (b) Correlation analysis for the DBP comparisons with the wrist DBP reference. (c) Bland-Altman analysis for the DBP comparisons with the arm DBP reference. (d) Correlation analysis for the DBP comparisons with the arm DBP reference. . . . .	218
5.14	Results obtained for the SBP determination from the acoustic signal. (a) Bland-Altman analysis for the SBP comparisons with the wrist SBP reference. (b) Correlation analysis for the SBP comparisons with the wrist SBP reference. (c) Bland-Altman analysis for the SBP comparisons with the arm SBP reference. (d) Correlation analysis for the SBP comparisons with the arm SBP reference. . . . .	219

## List of Tables

1.1	Comparison of features and functions of different wearable devices capable of monitoring HR and/or HRV. . . . .	42
1.2	BHS grading criteria [134]. . . . .	58
1.3	ESH-IP 2010 grading criteria [135]. . . . .	59
1.4	Comparison of features and functions of different blood pressure monitors. . . . .	60
2.1	Specifications for commonly used non-rechargeable (primary) and rechargeable (secondary) batteries with varying physical sizes that can be used in different wearable applications [106], [107]. . . . .	101
2.2	Current consumption of different components of the hardware platform. . . . .	108
3.1	Pseudo-code algorithm for estimating HR from acoustic pulse signal. The symbol notations are referenced in the main text. . . . .	130
3.2	Performance metrics of the proposed method obtained by comparing the estimated and ground truth HR. . . . .	141
3.3	Performance metrics of the proposed method for acoustic signals recorded in a noisy environment. . . . .	142
3.4	Performance comparison of the proposed method with results obtained from different PPG-based wrist devices used in the commercial market. The table only compares the results of the data collected at the rest position and provides an illustrative comparison because the experimental conditions varied between different works. The data length is for all the subjects combined together. SD was calculated from the results of 95% equivalence testing given in this paper. The results provided in the paper were obtained by averaging the data to 5 seconds epochs. . . . .	143
4.1	R-peak extraction algorithms with different operating principles and feature signals. . . . .	150
4.2	HRV extraction from pulse waveforms recorded at different sensing locations. Studies are grouped according to the pulse sensing method. . . . .	154
4.2	HRV extraction from pulse waveforms recorded at different sensing locations. Studies are grouped according to the pulse sensing method. . . . .	155

4.2	HRV extraction from pulse waveforms recorded at different sensing locations. Studies are grouped according to the pulse sensing method. . . . .	156
4.2	HRV extraction from pulse waveforms recorded at different sensing locations. Studies are grouped according to the pulse sensing method. . . . .	157
4.3	Performance metrics of the IHR determination for different characteristic points of APS with respect to PPG and ECG signals for a total of 12 subjects. . . . .	172
4.4	Time-domain HRV parameters for IBI estimated from APS, PPG and ECG signals. . . . .	176
4.5	Frequency-domain HRV parameters for IBI estimated from APS using FFT based non-parametric algorithm. . . . .	179
5.1	Rank ordering the frequency bands as the best spectral feature band for determining the DBP. The bands are compared for a total of 35 files and ranked according to the closeness of the maximum energy ratio with the DBP location obtained from the commercial arm and wrist monitor. . . .	202
5.2	Rank ordering the frequency bands as the best spectral feature band for determining the SBP. The bands are compared for a total of 35 files and ranked according to the closeness of the maximum energy ratio with the SBP location obtained from the commercial arm and wrist monitor. . . .	209
5.3	Statistical information about the participants in the data acquisition. . . .	215
5.4	Comparison results from the Bland-Altman analysis. . . . .	220
5.5	Percentage SBP/ DBP samples below the absolute differences of 5mmHg, 10 mmHg and 15 mmHg respectively. . . . .	220
A.1	Summary of the permissions taken for the third party copyrighted works used in this thesis. . . . .	229

# List of Publications

The following papers have been published as part of the research carried out during the PhD.

## Journal papers

- Sharma, Piyush, Syed Anas Imtiaz, and Esther Rodriguez-Villegas. “Acoustic Sensing as a novel Wearable Approach for cardiac Monitoring at the Wrist.” *Scientific Reports* 9, no. 1 (2019): 1-13.
- Sharma, Piyush, Syed Anas Imtiaz, and Esther Rodriguez-Villegas. “An algorithm for heart rate extraction from acoustic recordings at the neck.” *IEEE Transactions on Biomedical Engineering* 66, no. 1 (2018): 246-256.

## Peer reviewed conference papers

- Sharma, Piyush, and Esther Rodriguez-Villegas. “A Novel Algorithm for HRV Estimation from Short-Term Acoustic Recordings at Neck.” In *2019 41st Annual International Conference of the IEEE Engineering in Medicine and Biology Society (EMBC)*, pp. 6343-6346. IEEE, 2019.

# Acknowledgements

First of all, I would like to thank God for always showing me the right path and blessing me in many ways. This journey had an equal contribution from my wife, Surbhi, who helped me immensely in creating a perfect environment for me to focus on my research. She travelled with me hand-in-hand both in good and tough times and always supported me throughout my PhD. I would like to thank my parents for believing in my potential and always motivating me to learn, grow and accomplish more in life. I cannot even think of the sacrifices they have made for me to reach these levels of accomplishment.

I sincerely thank my supervisor Prof. Esther Rodriguez-Villegas for mentoring me over the last few years and encouraging me to become a good researcher. I appreciate her time and effort in arranging my scholarship and helping me with ideas, directions and invaluable feedback during my PhD. I am thankful to her for giving me the freedom to pursue different ideas, commit mistakes, learn from them and grow as a researcher.

I must thank Dr. Syed Anas Imtiaz for his continuous support in both academic and non-academic aspects of my PhD. He was not only my co-supervisor but a good friend who motivated me and helped me to grow my skills in a number of areas. A special thanks to my dear friend Amit who stuffed me with tasty Indian food all the time. I would also cherish my friendship with some great people including Saam, Zhou, Stuart, Irene, Renard, Xuen, Majd, Aamir, Jakub, Ruchir and Mohammad. Thank you for making the environment lively and fun throughout the course of this journey. I have definitely lived some unforgettable moments with you all and learnt a lot from your diversity. My deepest gratitude to Dr. Zohaib for being my first contact point and helping me innumerable times during all the difficulties. He is truly a go-giver in his personality. A big heartfelt thank you to Wiesia for loving me and taking care of me like my mother during my time at Imperial. I appreciate all your help with the administrative work.

## Declaration of Originality

I hereby confirm that the work presented in this thesis is my own, and all the materials which are not my work has been properly acknowledged and referenced.

Piyush Sharma

February, 2020.



## Copyright Declaration

The copyright of this thesis rests with the author and its contents are licensed under a Creative Commons Attribution-Non Commercial-No Derivatives 4.0 International Licence (CC BY-NC-ND). Under this licence, the researchers may copy and redistribute the material in any medium or format on the condition that they credit the author, do not use it for commercial purposes and do not distribute modified versions of the work. When reusing or sharing this work, the researchers must ensure that they make the licence terms clear to others by naming the licence and linking to the licence text. The researchers are asked to seek permission from the copyright holder for uses of this work that are not included in this licence or permitted under UK Copyright Law.

# Terms and Abbreviations

<b>Term</b>	<b>Meaning</b>
CVD	Cardiovascular disease
CHD	Coronary heart disease
SA	Sinoatrial
AV	Atrioventricular
SL	Semilunar
AR	Autoregressive
ULF	Ultra low frequency
VLF	Very low frequency
LF	Low frequency
HF	High frequency
ANS	Autonomic nervous system
ECG	Electrocardiography
PPG	Photoplethysmography
PCG	Phonocardiography
BCG	Ballistocardiography
SCG	Seismocardiography
SPI	Serial peripheral interface
USB	Universal serial bus
GUI	Graphical user interface
SVM	Support vector machine
RMSE	Root mean square error
PTT	Pulse transmit time
PAT	Pulse arrival time
PWV	Pulse wave velocity
BP	Blood pressure
PP	Pulse pressure
MAP	Mean arterial pressure
SBP	Systolic blood pressure
DBP	Diastolic blood pressure
OMWE	Oscillometric waveform envelope
IR	Infrared

<b>Term</b>	<b>Meaning</b>
LED	Light-emitting diode
HRV	Heart rate variability
PRV	Pulse rate variability
IHR	Instantaneous heart rate
IBI	Inter-beat interval
RF	Radio frequency
MEMS	Micro-electro-mechanical systems
ECM	Electret condenser microphone
ASIC	Application specific integrated circuit
ADC	Analogue to digital converter
SOC	System-on-chip
SAR	Successive approximation register
FFT	Fast-Fourier transform
STFT	Short-time Fourier transform
PSD	Power spectral density
APS	Acoustic pulse signal
MAE	Mean absolute error
MAEP	Mean absolute error percentage
PCC	Pearson correlation coefficient
ME	Mean error
SD	Standard deviation
LOA	Limits of agreement
SE	Standard error
PPV	Positive predictive value
DER	Detection error rate
SNR	Signal-to-noise ratio

# Units

Units	Full form
mmHg	millimetres of mercury
s/sec	seconds
h/hr	hours
ms	milliseconds
bpm	beats per minute
V	volts
mA	milliamperes
MAH	milliampere hour
g	grams
mm	millimetres
cm	centimetres
$\Omega$	ohms
dB	decibels

# Thesis Structure

This thesis is organised into five main chapters and the details of each chapter are summarised below.

## **Chapter 1: An introduction to non-invasive cardiovascular monitoring techniques and systems**

An introduction to the cardiovascular diseases and their important types is presented. Their impact on the world and specifically on the U.K. population is discussed to understand the importance of creating novel solutions in reducing the cardiovascular mortalities and morbidities. It is found that a regular monitoring of the heart rate, the heart rate variability and the blood pressure can provide critical information about these diseases and contribute in their early diagnosis. These physiological markers are subsequently discussed in detail with an emphasis on existing monitoring techniques. The advantages and disadvantages of every technique are also explained to understand the feasibility of a technique in different applications. Further, a comparison of the features and functions of the commercial monitors currently available in the market is done. The validation of these monitors in the literature is also discussed to grade their respective accuracies. Finally, the limitations of the existing systems are summarised and a novel approach for the cardiovascular monitoring at the wrist is proposed.

## **Chapter 2: Wearable sensing of the pulse sounds at the wrist**

In this chapter, the formation of the pulse is discussed in relation to the propagation of blood through the circulatory system. The pulse components, namely the pressure wave and the flow wave are explained to justify the choice of radial artery as an ideal site for pulse assessment. Further, a comprehensive literature review of different techniques and applications of measuring the radial pulse is provided. The conclusions drawn from the literature review are used to explain the need of wearable acoustic sensing as an alternative new physiological signal to extract cardiac information from the radial artery. For sensing the pulse sounds using a wearable device, different types of acoustic sensors, batteries and data acquisition hardware are explored. A detailed comparison of these choices is provided to find the electronic components matching the required specifications of the device. Finally, the blueprint of the proposed wearable device is discussed.

### **Chapter 3: Characterising the pulse sounds for continuous heart rate monitoring**

The proposed wearable device is used to record the acoustic pulse signal from the radial artery. To establish a correlation of these signals with the cardiac activity, the temporal and spectral characteristics of the pulse sounds are studied. Since the signal quality depends highly on the measurement site, the optimal sensor location on the wrist is found. Just like other devices, the proposed sensor is also prone to some motion artefacts. This chapter identifies the common noise sources and characterises them to incorporate their removal from the acoustic signal. These characteristics of the recorded signals are used to present a novel algorithm for average heart rate estimation. The heart rate profiles obtained from the proposed algorithm are compared with the synchronously recorded photoplethysmography signals. The results demonstrate the feasibility of heart rate monitoring at the wrist using the acoustic sensing of the radial pulse. Finally, the performance of the proposed algorithm over various parameters is compared with some of the monitors available commercially.

### **Chapter 4: An algorithm to determine heart rate variability in short-term acoustic recordings**

In this chapter, a novel algorithm to extract the heart rate variability from the short-term acoustic recordings at the wrist is proposed. Firstly, a comprehensive literature review of the existing algorithms based on different monitoring techniques (including the contact and non-contact approaches) is provided. Further, the data acquisition involving the synchronous recordings of the acoustic signal, electrocardiography signal and photoplethysmography signal is explained. The relative energy concept to detect the S1 sounds in the acoustic signal along with the other stages of the proposed algorithm are also discussed. The S1 sounds represented by three different characteristic points are localised and the instantaneous heart rate is calculated to find the most suitable characteristic point. The peak detection at a beat-to-beat resolution is then utilised to extract the time-domain and frequency-domain heart rate variability parameters. The comparison with the reference signals proves the performance of the proposed algorithm in accurately extracting the heart rate variability from the acoustic signals recorded at the wrist.

### **Chapter 5: Blood pressure measurement by sensing Korotkoff sounds at the wrist**

This chapter explores the possibility of recording the Korotkoff sounds from the radial artery to measure the systolic and diastolic blood pressure at the wrist. The hardware required to inflate the air cuff and apply varying levels of external pressure on the upper arm is described. The roles and specifications of different components in the hardware development are also provided for reference. Further, the hypothesis of measuring the

blood pressure at the wrist is tested by recording the acoustic signal in synchronisation with inflating pressure levels. The temporal and spectral characteristics of the acoustic signal under the influence of external pressure on the arterial branch are studied and analysed. These characteristics are utilised to propose separate algorithms for the diastolic and systolic blood pressure determination. The interference from the artefacts and their removal is also considered to extract reliable feature signals from the acoustic signal, and use them in different stages of the algorithm. The adopted experimental procedure in accordance with the international guidelines is described. Finally, the blood pressure estimations from the proposed algorithms are compared with two reference monitors (wrist and arm) and the conclusions about the feasibility of measuring the blood pressure at the wrist using the acoustic sensing of the pulse are drawn.

# 1 An introduction to non-invasive cardiovascular monitoring techniques and systems

## 1.1 Introduction

The human cardiovascular system is a closed tubular system in which the heart takes the central position and propels the blood to every part of the body through a network of blood vessels. The network consists of arteries, capillaries and veins as its main components [1]. The arteries carry blood away from the heart and branches further into smaller arterioles. These arterioles branches into a wide distribution network of microscopically small capillaries. While the arteries carry the blood from one location to another, it is the capillaries that interact with every cell in the body to carry out an exchange of oxygen, nutrients and metabolic waste. The capillaries rejoin to form their counterparts called venules, which further unite to form the veins. The veins take the blood burdened with the metabolic waste back to the heart. Since the cardiovascular system is essentially a network of the heart and the blood vessels, any condition that affects a normal functioning of this network is known as a cardiovascular disease (CVD). While there are different types of CVDs [2], four of the main diseases are described below:

1. *Coronary heart disease*: It is a disease that causes a blockage or interruption in the transportation of the oxygen-rich blood to the heart muscle due to a build-up of fatty substances in the coronary arteries. These fatty deposits, also known as atheroma, can clog the arterial walls to cause atherosclerosis.
2. *Stroke*: Any disruption of the blood supply (rich with oxygen and nutrients) to the brain can cause its cells to die possibly leading to a brain injury, disability and death. The interruption can be caused either from the blockage (ischaemic stroke) or the rupture of a blood vessel (haemorrhagic stroke).
3. *Peripheral arterial disease*: It is a disease related to the build-up of fatty deposits in the arteries responsible for supplying blood to the arms and legs. These fatty deposits are generally made up of cholesterol and other wastes, and causes the arterial walls to constrict. The narrowing of the arteries restricts the blood flow to the limbs causing moderate to severe pain.



4. *Aortic disease*: Aorta is the largest blood vessel in the body and is responsible for carrying blood away from the heart to the rest of the body. Any bulging or swelling in the aorta, also known as aortic aneurysm, can create a possibility of aortic rupture which can lead to life-threatening bleeding conditions.

Some of the risk factors associated with these different types of CVDs include high blood pressure, physical inactivity, high cholesterol, use of tobacco, excessive alcohol consumption, unhealthy diet, diabetes, ageing and high body mass index [3].

CVDs are the number one cause of deaths globally [4]. In 2016, an estimated 17.9 million people died from CVDs, amounting for 31% of all the global deaths. This number is expected to rise to 22.2 million in 2030 owing to the ageing and increasing population. According to a report from World Health Organisation in 2014 [5], the CVDs are responsible for 37% of all the non-communicable deaths in premature ( $< 70$  years) population. While majority of the CVD deaths occur in developing countries, in the UK alone, around 170,000 deaths including 45,000 premature deaths happen due to the heart and circulatory diseases each year [6]. These deaths amount to 28% of all the UK deaths and accounts for an average of 460 deaths each day or one death every three minutes. Currently in the UK, around 7.4 million people are suffering from the heart and circulatory diseases. The healthcare costs related to the CVDs raises another alarm as a large proportion of the UK economy as high as £9 billion are spent on the treatment of these diseases each year. This cost is estimated to £19 billion each year if the informal costs and costs related to the premature deaths and disability are also included. Although the number of CVD deaths in the UK have significantly reduced from around 320,000 deaths in 1961, the CVD statistics still project an alarming and distressing picture. While the quality of the medical care has significantly improved over the last few decades, it is important to understand the causes of the CVDs so that preventive measures can be taken at early stages.

The Global Status Report on Noncommunicable Diseases in 2014 by World Health Organization recognised nine main targets for the countries to act upon to reduce the mortality and morbidity rates [5]. Some of these targets relate to the risk factors associated with the CVDs and demand a reduction in the harmful use of alcohol, insufficient physical activity, use of tobacco, obesity and diabetes. While these factors recommend a pathway to a healthy lifestyle, it is their interplay with the physiological behaviour of the body that yield the insights into the prevention, etiology, course, and treatment of the CVDs. The most important physiological signs related to the CVDs include the heart rate, the heart rate variability and the blood pressure. The Framingham study [7] followed a cohort of 5209 subjects for 30 years and recorded the resting heart rate using ECG in the supine position. A total of 5070 subjects were free from any type of CVDs when they entered into the study. The study found that in both the sexes and at all the ages, the cardiovascular and coronary mortality rates increased progressively in relation

to the antecedent heart rates. Woodward *et al.* also studied the association between the resting heart rate, cardiovascular disease and mortality in 112,680 men and women from the Asia-Pacific region [8]. A continuous and increasing association between the resting heart rate above 65 beats/min and the cardiovascular mortality was found with no evidence of associations below this threshold. The study suggested similar changes in the lifestyle as stated above to reduce the resting heart rate. Several other studies have also emphasised the importance and simplicity of recording the resting heart rate as a prognostic factor and potential therapeutic target in reducing the mortality rates related to the CVDs [9]–[13].

Heart rate variability (HRV) is another important risk factor associated with the CVDs. HRV mainly occurs because of the adaptive changes in the heart rate caused by the sympathetic and parasympathetic nervous system [14]. Therefore, any autonomic imbalance can be assessed using HRV that have been associated with a wide range of conditions including CVD [15]. A substantial amount of evidence in the literature proves that a decreased HRV is associated with high cardiovascular risk [16]–[19]. The autonomic imbalance have been associated with increased morbidity and mortality, and it has been found that the lowering of the cardiovascular risk profiles require an elevation in the HRV [15]. While the association of HRV in individuals with a known CVD has been already established, the study in [20] analysed the association between HRV and cardiovascular events in populations without known CVD. The study found that a low HRV is associated with a 32-45% increased risk of a first cardiovascular event in populations without known CVD. Therefore, a regular HRV monitoring can prove to be very useful in diagnosing the risk of developing a first cardiovascular event.

Blood pressure has been repeatedly shown to be an independent and a significant risk factor associated with CVDs including CHD and stroke [21]–[23]. Several studies suggest that a higher blood pressure (hypertension) is a stronger predictor than a lower blood pressure in middle-aged and older populations [24]–[26]. The Global Burden of Disease Study organised by the World Health Organization has also pointed towards hypertension as the most important global risk factor for morbidity and mortality [27]. Even in the UK, high blood pressure is the leading medical risk factor for heart and circulatory diseases. In the UK alone, an estimated 27% (14 million) of the adult population suffer from high blood pressure and possibly 6-8 million people are living with an undiagnosed or uncontrolled high blood pressure [6]. Around 50% of the heart attacks and strokes in the UK are associated with high blood pressure. Therefore, the awareness about the early detection, prevention and control of high blood pressure must be spread across the population starting from the age of young adulthood.

The association of heart rate, heart rate variability and blood pressure with an increased cardiovascular risk demand a regular monitoring of these vital signs as a preventive and diagnostic measure. The following sections provide a more detailed discussion

on monitoring these physiological signals using different techniques and also lists the commercially available monitors to record and monitor these parameters.

## 1.2 Heart rate and its variability: definitions and monitoring techniques

Heart rate is one of the most basic physiological markers and is defined as the the number of times a person's heart beats per minute. A normal range of the heart rate at rest is between 60 and 100 beats per minute (bpm), however, it varies from person to person, and depends on the time of measurement and the activities performed before the measurement [28]. A heart rate lower than 60 bpm is medically known as bradycardia whereas a heart rate higher than 100 bpm is classified as tachycardia. Even when the resting heart rate is stable, the time difference between the consecutive heartbeats can vary substantially [29]. These variations in the inter-beat intervals, known as HRV, represent one of the most promising markers and have various applications in studying the cardiac events. Primarily, the HRV is used to understand the status of the autonomic nervous system (ANS). The ANS consists of the sympathetic and parasympathetic components. While the sympathetic branch responds to an external stimuli (e.g., stress, exercise) by increasing the heart rate (cardio-acceleration), the parasympathetic activity decreases the heart rate (cardio-deceleration) depending on the internal stimulus generated from the functionality of the organs, allergic reactions, irritants, etc. [30]. This way the interplay between both the ANS components regulate the physiological autonomic function of the body. These components introduce separate rhythmic contributions in modulating the heart rate at different frequencies. The sympathetic activity is associated with the low frequency range (0.04-0.15 Hz) and the parasympathetic activity is associated with the high frequency range (0.15-0.4 Hz). Therefore, the spectral analysis of the HRV can allow to study these components separately and intervene at an early stage in case of any autonomic imbalance.

HRV records the amount of heart rate fluctuations around the mean heart rate by examining the beat-to-beat variations in a time-series profile. These inter-beat intervals (IBIs), also known as normal-to-normal (NN) intervals, can be plotted against time to generate an IBI tachogram as shown in Fig. 1.1. The simplest HRV analysis is performed by extracting the time-domain measures from the IBI tachogram. While the HRV parameters are conventionally obtained from 24-hour long-term recordings, the short-term 5-minute recordings have also been accepted as an appropriate option for the HRV analysis [31]. The time-domain HRV measures are mainly divided into two types: ones that are directly obtained from the NN intervals and others that are obtained from the differences between the NN intervals. These parameters carry different statistical meanings [29], [31], [32] as discussed below:

- The *standard deviation of the NN intervals (SDNN)* reflects the short- and long-term NN variations in the recording.
- The *standard deviation of the average NN interval (SDANN)* is usually calculated over short periods of 5 minutes, and therefore it provides an estimate of the changes in the heart rate over cycles longer than 5 minutes.
- The *SDNN index* calculates the mean of standard deviation of NN intervals in short windows (usually 5 minutes) for the whole recording to measure the variability across the short windows.
- The *square root of the mean squared differences (RMSSD)* reflects the beat-to-beat variance in the heart rate and is used to estimate the cardiac vagal control in mediating the HRV changes.
- The *NN50 parameter* counts the number of adjacent NN intervals that differ from each other by more than 50 milliseconds. The percentage of such NN intervals is known as *pNN50*. The pNN50 is closely correlated with the high frequency power or the parasympathetic activity of the HRV.

The HRV can also be studied in the frequency-domain by calculating the power spectral density (PSD) using non-parametric or parametric methods [31], [32]. Although both the methods provide comparable results, the non-parametric method is simple to implement (using Fast Fourier Transform) and provides high processing speed. On the contrary, the parametric method generates smoother spectral components using the autoregressive (AR) modelling allowing an easy post-processing of the frequency bands. The HRV in the frequency domain is analysed in four different bands: ultra low frequency (ULF) band ( $\leq 0.003$  Hz), very low frequency (VLF) band (0.003-0.04 Hz), low frequency (LF) band (0.04-0.15 Hz) and high frequency (HF) band (0.15-0.40 Hz). Since the ULF band

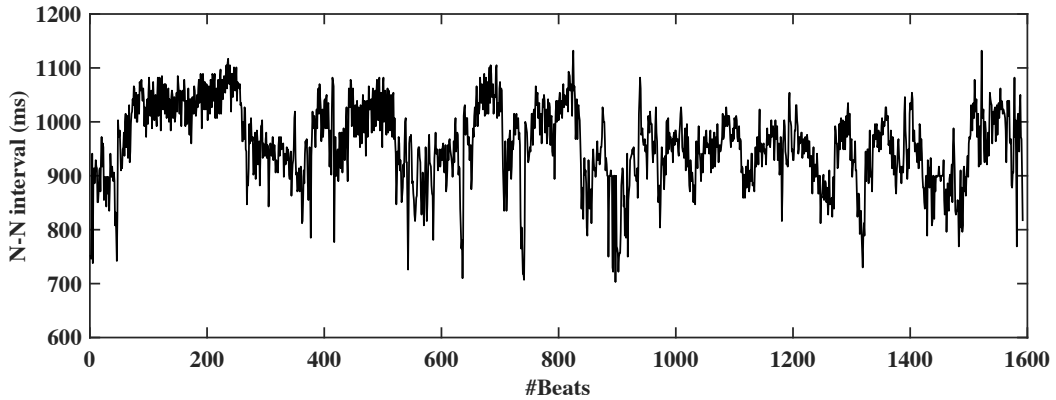


**Figure 1.1:** An example of IBI tachogram representing the time-interval between each subsequent beat ( $\sim 1600$  beats).

correlates with the biological processes that act very slow, it is generally calculated from 24-hour recordings. It is believed that the circadian rhythms are the primary driver of the ULF band [33]. A low power in the VLF band is associated strongly with all-cause mortality and is considered as more fundamental to health [34]. While the power in LF and HF bands may be produced by both the sympathetic and parasympathetic nervous system, it has been shown that the sympathetic activity is a major contributor to the LF band [35]. Similarly, the HF band reflects more of the parasympathetic activity [32]. The power measurements in VLF, LF and HF bands are generally made in absolute values of power ( $\text{ms}^2$ ), however, LF and HF bands can also be measured in normalised units (n.u.). Apart from the absolute and normalised power in different spectral bands, the frequency-domain HRV parameters also include LF norm, HF norm and LF/HF ratio as other measures. These parameters are defined as follows:

$$\begin{aligned}\text{LF norm (n.u.)} &= \frac{\text{LF}}{\text{Total Power-VLF}} \times 100 \\ \text{HF norm (n.u.)} &= \frac{\text{HF}}{\text{Total Power-VLF}} \times 100 \\ \text{LF/HF} &= \frac{\text{LF} [\text{ms}^2]}{\text{HF} [\text{ms}^2]}\end{aligned}\tag{1.1}$$

The extraction of the time-domain and frequency-domain HRV parameters require a continuous measurement of the heart rate (or IBIs) on a beat-to-beat resolution. While a spot measurement of the heart rate can simply be obtained by checking the pulse, its continuous measurement requires the usage of automatic heart rate monitors. These monitors operate using different measurement principles with the sensing mechanisms either requiring a contact with the site under test or recording the signals without any body contact. Some of the commonly used measurement techniques that employ portable/wearable sensing systems are discussed in detail below.

### 1.2.1 Contact-based HR/ HRV monitoring techniques

#### 1.2.1.1 Sensing the electrical activity

The cardiac output of the heart, also described as the volume of blood being pumped by the heart, is vital to sustain blood flow throughout the body. In addition to regulating the blood volume, the heart must sustain continuous cycles of contraction and relaxation to fulfil the needs of the body. These cycles take place within four chambers of the heart: left and right atrium, left and right ventricle, in an orderly sequence. During the systolic period, the contraction of the atria is followed by the contraction of the ventricles after which all the four chambers relax during the diastolic phase of the cardiac cycle. The regularity of the cardiac cycles is established by a series of complex electrophysiological

events within the cardiac tissues. The triggering of these events originate in a specialised cardiac conduction system and subsequently spreads to all the parts of the myocardium. The main components of this conduction system in the heart are the sinoatrial node (SA node), the inter nodal atrial pathways, the atrioventricular node (AV node), the bundle of His and its branches, and the Purkinje system [36]. In a normal cardiac cycle, the SA node discharges rapidly with the electrical depolarisation spreading through the right atrium and across the interatrial septum into the left atrium. It is the rate of discharge of the SA node that determines the heart rate in normal conditions. The further transmission of electrical depolarisation from atria to the ventricles happens through the atrial pathways to the AV node. The AV node allows the depolarisation to spread into the left and right ventricles via the route of interventricular septum branching into the left and right bundle branches respectively. The two ventricles in normal conditions contract simultaneously to achieve maximum cardiac efficiency. The complete depolarisation of the heart is immediately followed by the repolarisation of the myocardium to begin a new cardiac cycle with next cycle of depolarisation. The discharge pattern in every cell of the heart during the depolarisation cycle is quite unique, and the sum of these discharge patterns is what generates an electrocardiograph [37]. The electrocardiography (ECG), therefore, is the process of measuring the electrical activity of the heart by placing several electrodes on the patient's skin. An illustration of a normal ECG signal consisting of several heartbeats is shown in Fig. 1.2. An ECG waveform constitutes of a P wave, a QRS complex and a T wave. These components correlate with the depolarisation of the atria, depolarisation of the ventricles and repolarisation of the myocardium respectively.

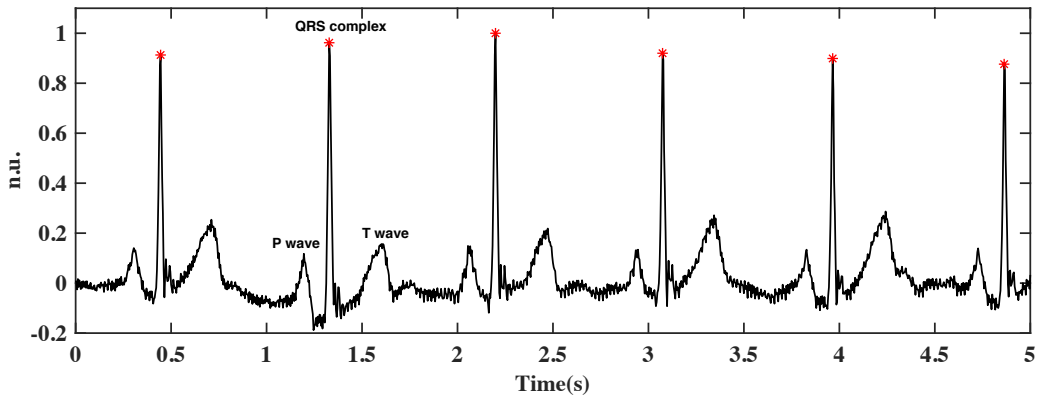


**Figure 1.2:** *An example of a ECG signal consisting of P wave, QRS complex and T wave. All the R-peaks are marked.*

ECG is the gold standard approach to measure the heart rate and the HRV. It is traditionally recorded using a Holter monitor, a battery-operated portable device that consists of a central unit connected with several wires and extending to small-sized electrodes that attach to the patient's skin on the chest. The Holter monitor is generally used for ambulatory recordings of the ECG over continuous periods of 24 hours or longer.

While the monitor provides an accurate and reliable representation of the heart's electrical activity to diagnose any cardiac disorders, the cumbersome setup involving the wires and the skin preparation required to attach the electrode patches makes it quite uncomfortable for the subject to undergo a long-term cardiac monitoring. The cardiac monitoring generally require the detection of R-peaks in the ECG signal to derive the inter-beat intervals, however, several algorithms based on identifying the instantaneous heart rate frequency in the spectral domain have also been proposed in the literature. These algorithms will be reviewed in the later chapters of this thesis.

### 1.2.1.2 Sensing the optical activity

The contraction and relaxation of the heart during the systolic and diastolic phases of the cardiac cycle produces a corresponding effect in the circulatory system. During the systolic period, the heart pumps blood through aorta to reach the peripheral sites of the body. A reverse phenomenon occurs during the diastolic period where blood is carried back to the heart. These periodic blood volume changes in the microvascular bed of tissue can be detected using an optical technique called photoplethysmography (PPG). A PPG waveform is essentially a pulsatile ('AC') physiological waveform superimposed on a slowly varying ('DC') baseline. While the AC waveform is formed by periodic changes in the blood volume with each cardiac cycle, the DC baseline is mainly attributed to respiration, sympathetic nervous system activity and thermoregulation [38]. The PPG components provide valuable information about the cardiovascular system, and can be recorded using a few optoelectronic components including an active light source to illuminate the tissue and a photodetector to measure the small variations in light intensity corresponding to the varying absorption by the blood volume [39]. PPG conventionally uses an infra-red light of wavelength around 940nm for the light source to measure the peripheral pulse at one of the different sites (including finger, wrist, neck, ear, forehead, etc.) in a non-invasive manner. An illustration of a PPG signal recorded from the index

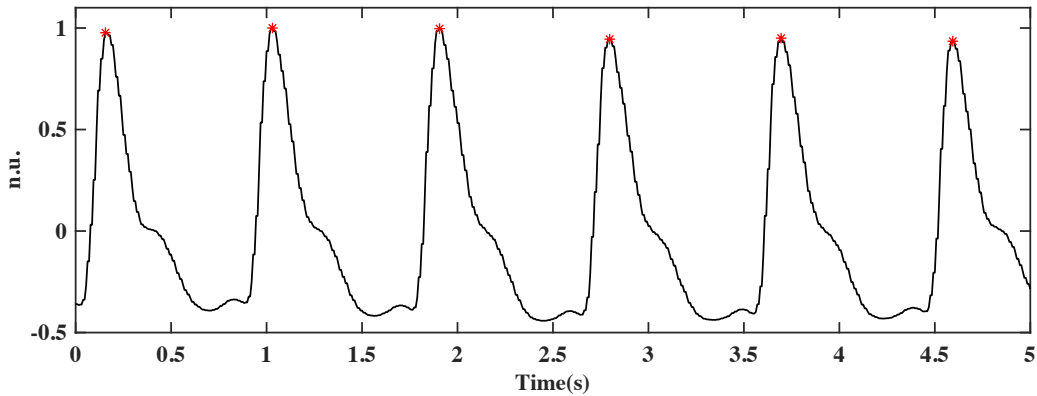


**Figure 1.3:** An example of a PPG signal. All the systolic peaks are marked.

finger is shown in Fig. 1.3 where the maximum (systolic) peaks are also marked. The inter-beat intervals are generally extracted by determining the systolic peaks, however, the onset of pulse and the maximum slope point in the PPG waveform are also considered as other fiducial points for the heart rate measurement. While the PPG technology provides a simple, low-cost and easy to set up sensing mechanism, some of the key challenges associated with the PPG sensors include the requirement of a stable contact force between the sensor and the measurement site, cancelling the effects of ambient light, accommodating different skin conditions and colors, and dealing with motion artifacts [40]. In addition, the requirements of an active input signal limit either the size of the system and/or the battery lifetime.

### 1.2.1.3 Sensing the acoustic activity

Cardiac auscultation using a stethoscope provides an easy, quick and an inexpensive way of diagnosing the cardiac disorders by listening to the heart sounds. The genesis of the heart sounds relate to the blood flow within the four chambers of the heart which are separated by the AV and the semilunar (SL) valves. These valves act as the only passage of blood from one chamber to the other in normal conditions. A complete cardiac cycle consists of filling the blood inside the atria, transferring the blood from atria to ventricles through the AV valves, and subsequently ejecting the blood away from the ventricles through the SL valves. Depending on the blood volume in respective chambers of the heart, a pressure difference between the atria and ventricles is created. The pressure difference controls the opening and closure of the heart valves to allow the passage of blood in a particular direction in different phases of the cardiac cycle. It is the opening and closing of the heart valves along with the acceleration and deceleration of the blood flow that produces the heart sounds [41], [42]. While the heart sounds are commonly heard using a basic stethoscope, they can also be captured automatically by placing an acoustic sensor on the chest wall [43]. The process of recording and representing the heart sounds graphically is known as phonocardiography (PCG). A major advantage of recording the cardiac activity acoustically is its passive sensing mechanism using a miniaturised, low power microphone. Unlike the PPG signal, the cardiac auscultation does not require a power consuming input signal, therefore, allowing a longer battery life.

The fundamental heart sounds, also known as the S1 and S2 sounds are primary to the cardiac auscultation. The S1 sound is heard at the onset of the systolic phase and results from the sequential closure of the AV valves. On the contrary, the S2 sound is heard at the onset of the diastolic phase and results from the closure of the SL valves. Other sounds such as S3 and S4 sounds, and murmurs can also be heard during the cardiac auscultation to reflect different pathological conditions related to the heart [44]. A PCG signal consisting of the fundamental heart sounds is illustrated in Fig. 1.4. Traditionally, the PCG signal is recorded from the chest, however, recent studies in the literature have



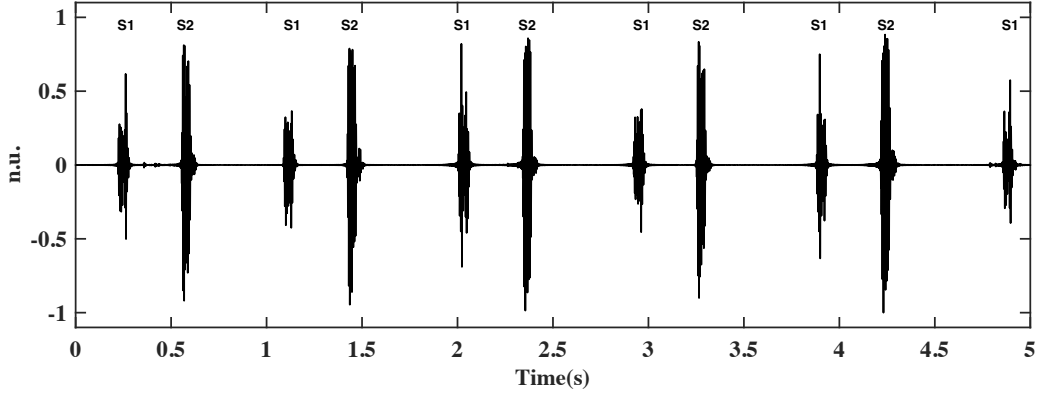


**Figure 1.4:** *An example of a PCG signal consisting of S1 and S2 sounds.*

also shown the possibility of recording the heart sounds from the suprasternal notch at the neck [45]. While the systolic phase corresponds to the S1-S2 interval, the diastolic phase is formed by the time interval between the adjacent S2 and S1 sounds. Therefore, a complete cardiac cycle is represented by the S1-S2-S1 cycle. The detection of such cardiac cycles in the PCG signal to determine the heart rate generally requires the segmentation and classification of the heart sounds using different methods.

### 1.2.2 Non contact-based HR/ HRV monitoring techniques

The contact-based methods of heart rate monitoring required a sensor contact with the patient's skin. A continuous and intensive monitoring using such sensors is only feasible in the clinical settings, for example, a touch-based wiring of the patient using the gold standard approach of ECG. However, to improve the early detection and prevention of cardiac disorders, more comfortable ways to enable vital sign monitoring in home settings is required. Some of the methods that enable such convenience by sensing cardiac parameters through fully clothed persons or through blankets and mattresses for patients lying in beds, and feasible in every day conditions are discussed below.

#### 1.2.2.1 Sensing the mechanical activity

The body movements occurring in relation to the heartbeat is an old concept, and the effort of recording such movements have been made for past several decades [46]. The recent advancements in the development of electromechanical sensors have made it possible to record the mechanical activity of the heart by using mechanocardiography techniques. One such technique is known as ballistocardiography (BCG) which measures the recoil forces of the body in reaction to the ejection of blood at each cardiac cycle. The recoil forces are primarily generated to maintain the overall body momentum in response to the change in center of mass caused by the blood travelling along the vascular tree [47]. These micro-motions can be sensed as a displacement, velocity, or acceleration signal by

integrating different types of sensors (pressure sensor, multiple strain gauges, electromechanical film sensor, etc.) in bed, table, chair, pillow, mattress, or weighing scale-based BCG systems.

Another approach to measure the local mechanical vibrations of the chest wall in response to the heartbeat is known as seismocardiography (SCG). These vibrations are produced by the ventricular contraction of the heart and ejection of the blood into the vascular tree [47]. While the BCG systems employ a non-contact sensing approach, SCG is usually detected by placing a low-noise accelerometer on the chest. Both the BCG and the SCG waveforms are characterised by several fiducial points corresponding to different events of the heartbeat. The heart rate from the BCG signal is generally extracted by identifying the J-peak (the point of highest amplitude in the BCG waveform) and measuring the J-J inter-beat intervals between the consecutive peaks. Although the BCG systems provide an unobtrusive manner of monitoring the cardiac activity and does not require the sensor attachment with the patient's skin, their applicability for long-term cardiac monitoring is restricted to bed-ridden subjects and standardised conditions. The sensitivity of these systems towards the body movements is also very high causing the signal-to-noise ratio of the recorded signals to be significantly lower than the ECG and PPG signals [48]. Therefore, the detection of heart rate from these signals require advanced signal processing methods which put further constraints on the system design.

#### **1.2.2.2 Radar-based heartbeat detection**

A better way of monitoring the micro-motions of the human body than the BCG is based on the radar technology. The radar-based sensing mechanism allows a touch-free measurement of the cardiac vibrations by sensing the changes in the distance or displacement caused by the contraction of the heart muscles. These systems offer a convenient and comfortable approach for the heartbeat detection since the transmitted electromagnetic waves can easily penetrate the clothing and bedding in an experimental setup [49]. The fundamental mechanism of a continuous-wave Doppler radar is based on transmitting an unmodulated signal with a specific carrier frequency and phase towards a human body at a distance up to a few tens of metres. The transmitted electromagnetic wave is reflected by the physiological movements of the chest wall as a phase modulated signal which can be detected using a radar receiver. The received signal is digitised using an analogue-to-digital converter (ADC) to process and extract the cardiac information from the reflected waves. Several front-end architectures for the Doppler radar including the homodyne, heterodyne, double-sideband architecture, direct IF sampling and self-injection locking have been recently proposed in the literature [50]. These architectures address some of the key issues concerning the radar-based systems. Since the strength of the reflected waves are quite low, an efficient and reliable detection requires multiple building blocks such as a low-noise amplifier, down-conversion mixer, baseband amplifier,

and filters in the system design. In addition to a proper choice of the carrier frequency, these systems must also avoid the mixing of the phase noise of the oscillator with the received echo signal [50]. In conclusion, the radar-based sensors can be easily integrated within the environment of the patient undergoing cardiac monitoring, however, they are still in very early development stages and their deployment in commercial systems require addressing some critical issues inherent to the sensing mechanism.

### **1.2.2.3 Resonator-based heartbeat detection**

The continuous-wave Doppler radar generally operates at high frequencies (GHz) to maintain a narrow transmitted beam over larger distances. It allows to monitor the heart rate at a distance of few metres away from the chest. However, the reflected waves in such scenario are significantly affected by the motion artefacts and the noise introduced by the random body movements [51]. A very similar approach to radar-based sensing resolves this issue by measuring the cardiac activity at very short distances (few centimetres) away from the chest. The near-field detection using the radio frequency (RF) resonators allow the integration of these sensors into clothing, watch straps or blankets. The fundamental theory behind the RF resonators is similar to the radar-based sensing in terms of detecting the physiological movements of a subject by measuring the electromagnetic near-field variation for vital sign monitoring. Several resonator-based systems have been proposed in the literature to measure the pulse at the wrist [51], [52]. These systems, similar to the radar sensors, are also in the research stages and have not been commercialised yet.

### **1.2.3 Commercially available HR/ HRV monitors**

The cardiac monitoring techniques discussed above measure different types of cardiac signals using semi- or fully-automated sensing systems to monitor the heart rate (HR). However, the heart rate monitoring for several centuries, before the development of the electronics industry, was performed by placing an ear on the patient’s chest and listening to the heart sounds. An accurate cardiac auscultation was only made possible with the invention of the stethoscope by René Laennec in 1816. While the heart sounds provided vital information about the functionality of the heart, the electrocardiograph invented by Willem Einthoven in 1895 created an accurate picture of the heart’s electrical activity and allowed a better diagnosis of the cardiac disorders. The development of the Holter monitor made it possible to record the ambulatory ECG continuously for 24 hours, however, the cumbersome setup involving a central unit connected with several wires made it uncomfortable for the patients to undergo a long-term cardiac monitoring. Only when the wireless functionality, consisting of a transmitter at the chest and a receiver at the wrist, was added to the ECG recording setup in 1977 by Polar Electro, the concept of heart rate monitoring became feasible for a larger population [53]. Over the last few decades, the advancements in the electronics industry have led to a miniaturisation of

the sensors allowing the development of battery-operated, small-sized systems that can be worn by the subjects for vital sign monitoring. Several companies in the industry have commercialised such wearable monitors to track HR/ HRV in non-clinical settings. While these monitors aim to perform the same task of monitoring the heart rate using different measurement principles, there are factors and functions that set one apart from the other. Some of the important features that are helpful in differentiating the wearable heart rate monitors are discussed below.

1. *Measurement technique:* The previous section discussed different contact and non-contact sensing principles to record the heartbeats on a continuous basis. However, the wearable monitors available in the market are mainly based on sensing either the optical (PPG) or the electrical (ECG) activity of the heart.
2. *Sensing location:* The monitors track the cardiac activity from different locations including the chest, wrist, finger, ear, neck, etc. However, an abundance of monitors based on the wrist-sensing are available in the market mainly because of an easy and comfortable integration of such sensors into the patient's lifestyle without requiring any significant change. The wrist-based monitors also have a higher social acceptance in comparison to other sensing locations.
3. *Power source and operating lifetime:* The ECG recording machines in the clinical wards are generally powered by the mains, however, the wearable monitors utilise a small-sized battery as the power source. An important constraint of the wearable heart rate monitors is the battery lifetime as a frequent charging of the device from the user's perspective is highly undesirable. Depending on the size/ capacity of the battery, the number of in-built sensors, and the sampling frequency for the wireless transmission, a single battery charge can last from a few hours to a few days.
4. *Size and weight:* The heart rate monitors must be small and light-weighted to be used in either the clinical or home settings. Since these monitors are designed to be worn for longer durations, their size and weight are important factors in determining their usage period. The size and shape of the device should also take into account the varying morphology of the site under test in different subjects.
5. *Tracking functions:* While the primary function of these monitors is to track the heart rate, the integration of different sensors in the same device allows the monitoring of different features such as sleep monitoring, number of steps, distance travelled, calories burned, speed, and modes of walking, running, cycling, swimming, training, etc. The embedded functionality of tracking such features is what attracts a large user base. Therefore, one of the competitive features for the heart rate monitors is the availability of multiple tracking functions.

6. *Sensors*: The heart rate monitoring in the commercially available monitors is performed using an optical sensor or the ECG electrodes connected with a chest strap. However, the tracking of other activities require the integration of other sensors. Some of these sensors include an accelerometer, gyroscope, barometer, compass, GPS, etc. Although a higher number of sensors provide more functionality to the end user, the battery life in such cases is generally compromised.
7. *Water resistance*: Some of these commercial monitors also put up water resistance as an attractive feature to allow the usage of such devices during shower, swimming, rain, etc. While majority of the devices can sustain a pressure of up to 5 atmosphere (atm) under water, they are not designed for heart rate monitoring during the deep diving.
8. *Validation in literature*: There is an abundance of heart rate monitors in the market. The validation of these monitors to assess their accuracy in monitoring the heart rate and other activities is a very important criteria for choosing a specific device. The validation is generally performed by comparing the heart rate profiles obtained from the concerned monitor and the synchronously recorded ECG signals (gold standard) from the chest. An agreement between both the methods is observed by running different types of comparative analysis to conclude about the reliability of a particular device.

The factors discussed above serve as an important criteria in differentiating the usability of different wearable heart rate monitors available commercially. Table 1.1 compares the features and functions of some commonly available heart rate monitors from different companies and also provide references to the associated validation literature. The listed devices are chosen on the following basis:

- Only the monitors that provide heart rate as an output are shortlisted.
- Only the monitors that have been validated in the last 5 years (2014 - 2019) are shortlisted.
- Since the basic sensing technology behind different models from the same company remain the same, only the latest model available to buy on the company's website is shortlisted.
- If the same company manufactures heart rate monitors based on different sensing locations, then the latest devices from each of those categories are included.

Only details that are available from the manufacturer are listed in the table. These devices generally use lithium-ion (Li-Ion) or lithium-polymer (Li-Po) batteries, however, the battery type for several devices are unknown.

**Table 1.1:** *Comparison of features and functions of different wearable devices capable of monitoring HR and/or HRV.*

Monitor (Sensing Location)	Company Details	Battery Specifications	Tracking Functions	Sensors	Additional General Details	Associated Validation Literature
Apple Watch Series 5 (Wrist)	Apple Inc., Cupertino, California, USA, <a href="http://www.apple.com/uk/apple-watch-series-5/">www.apple.com/uk/ apple-watch-series-5/</a>	Non-removable Li-Ion battery, wireless charging, stand-by time of up to 18 hours	Heart rate, atrial fibrillation, cycling, yoga, swimming, running, high-intensity interval training, noise levels, fall detection, menstrual cycle, calories	Accelerometer, gyroscope, electrical heart rate sensor (ECG), optical heart sensor (PPG), barometer, compass, ambient light sensor, NFC, GPS, speaker, microphone	44×38×10.7 mm, 47.8 g, 50m water resistant, ECG certified, OLED capacitive touchscreen	[54]–[73]
Fitbit Charge 3 (Wrist)	Fitbit Inc., San Francisco, California, USA, <a href="http://www.fitbit.com/uk/shop/charge3">www.fitbit.com/ uk/shop/charge3</a>	Li-Po battery, 2-hours charging time, battery life of up to 7 days	Heart rate, steps, distance, calories, floors, running, biking, swimming, yoga, sleep tracking, SpO2	Accelerometer, altimeter, vibration motor, optical heart rate sensor, NFC, GPS	38×18.3×11.8 mm, 29 g, 50m water resistant, greyscale OLED touchscreen	[54]–[56], [59]–[65], [67]–[72], [74]–[83]
Garmin Forerunner 235 (Wrist)	Garmin Ltd., Lenexa, Kansas, USA, <a href="https://buy.garmin.com/en-GB/GB/p/529988">https://buy.garmin. com/en-GB/GB/p/529988</a>	Up to 9 days in watch mode; up to 11 hours in GPS mode with HRM	Heart rate, steps, sleep monitoring, calories burned, distance travelled, intensity minutes, GPS-based speed and distance, interval training, VO2 max	GPS, Glonass, Garmin elevate optical wrist heart rate monitor, accelerometer	45×45×11.7 mm, 42 g, water resistant up to 5 atm pressure, sunlight-visible and transflective memory-in-pixel colour display	[54], [55], [61], [65], [67], [69], [72], [84]
Samsung Galaxy Watch (Wrist)	Samsung Electronics Co., Ltd., Suwon-si, South Korea, <a href="http://www.samsung.com/uk/wearables/galaxy-watch/">www.samsung.com/uk/ wearables/ galaxy-watch/</a>	Non-removable 472 mAh battery, up to 7 days battery life, wireless charging	Heart rate, sleep monitoring, calories, running, yoga, walking, cycling	Accelerometer, barometer, gyroscope, optical heart rate sensor, light sensor, NFC, GPS, Glonass	49×46×13 mm, 63 g, 50m water resistant, super AMOLED display	[56], [61], [62], [64], [68], [70], [72]
MioPOD (Upper arm)	Mio Labs Inc., Santa Clara, California, <a href="https://mio-labs.com/products/miopod">https://mio-labs.com/ products/miopod</a>	24-hour battery life	Resting heart rate, burned calories, running, training insights	Optical heart rate sensor, NFC	Swim proof, stores up to 30 hours of workout data	[68], [70], [71], [79], [82], [85]–[87]

**Table 1.1:** *Comparison of features and functions of different wearable devices capable of monitoring HR and/or HRV.*

Monitor (Sensing Location)	Company Details	Battery Specifications	Tracking Functions	Sensors	Additional General Details	Associated Validation Literature
Polar H10 (Chest)	Polar Electro Oy, Kempele, Finland, <a href="http://www.polar.com/uk-en/products/accessories/polar_h10_heart_rate_sensor">www.polar.com/uk-en/products/accessories/polar_h10_heart_rate_sensor</a>	CR 2025 battery, 400 hours of battery lifetime	Heart rate, all training and workout related parameters	ECG (connected with a chest strap)	34×65×10 mm, 60 g, water resistant up to 30 m	[57], [61], [65]–[67], [80], [82], [88]–[90]
Polar Vantage V Titan (Wrist)	Polar Electro Oy, Kempele, Finland, <a href="http://www.polar.com/uk-en/vantage/v-titan">www.polar.com/uk-en/vantage/v-titan</a>	320 mAh Li-Po battery, battery life up to 40 hours in training mode (GPS and wrist-based heart rate) or up to 7 days in watch mode with continuous heart rate tracking	Continuous heart rate, sleep tracking, steps, distance, cardio and muscle load, running, calories, swimming, altitude ascent and descent	Integrated GPS and GLONASS, Galileo, QZSS, optical heart rate sensor, barometer	46×46×13 mm, 59 g, always-on colour touch display, laminated Gorilla Glass lens with anti-fingerprint coating	[57], [61], [65]–[67], [80], [82], [88]–[90]
Zephyr HxM BT (Chest)	Medtronic PLC, Dublin, Ireland, <a href="http://www.zephyranywhere.com/system/hxm">www.zephyranywhere.com/system/hxm</a>	Rechargeable Li-Po battery, 3 hours charging time, 24 hours charge duration, 500 charge cycles	Heart rate, heart rate variability, breathing rate, posture, activity, peak acceleration, impact, peak force, jump height and flight time, estimated core body temperature, caloric burn, training intensity, speed, distance	ECG module connected with a chest strap, GPS	65×32×11.5 mm (excluding strap), 47 g	[76], [91], [92]
Misfit Vapor X (Wrist)	Misfit, San Francisco, California, USA, <a href="http://www.misfit.com/smartwatches/misfit-vapor-x/">www.misfit.com/smartwatches/misfit-vapor-x/</a>	24+ hour battery life, 300/ 330 mAh battery power, charges to 80% in 50 minutes	Heart rate tracking, activity tracking	Accelerometer, altimeter, ambient light, gyroscope, microphone, optical heart rate sensor, NFC, untethered GPS	42×20×12 mm, 43 g, water resistant up to 30 m, 1.2 full round AMOLED display, 328 pixels per inch	[61], [64], [72], [81]

**Table 1.1:** *Comparison of features and functions of different wearable devices capable of monitoring HR and/or HRV.*

Monitor (Sensing Location)	Company Details	Battery Specifications	Tracking Functions	Sensors	Additional General Details	Associated Validation Literature
Huawei Band 4 (Wrist)	Huawei Technologies Co., Ltd., Shenzhen, China, <a href="https://consumer.huawei.com/uk/wearables/band4/">https://consumer.huawei.com/uk/wearables/band4/</a>	91 mAh battery capacity; charging time of about 1.5 hours, battery life up to 9 days	Heart rate, sleep tracking, running, walking, cycling, steps, distance, speed, calories	3-axis acceleration sensor, infrared wear sensor, optical heart rate sensor	56×18.5×12.5 mm, 24 g, water resistant up to 5 atm, TFT colour screen with 80 x 160 pixels resolution	[62], [64]
Xiaomi Mi Smart Band 4 (Wrist)	Xiaomi Corporation, Beijing, China, <a href="https://www.mi.com/global/mi-smart-band-4">https://www.mi.com/global/mi-smart-band-4</a>	Li-Po battery of 135 mAh capacity, charging time ≤ 2 hours, standby time up to 20 days	Count steps, distance, calories burned, outdoor running, cycling, walking, pool swimming, sleep and heart rate monitoring	3-axis accelerometer, 3-axis gyroscope, PPG heart rate sensor, capacitive proximity sensor	0.95 inches screen size, 22.1 g, on-cell capacitive touchscreen, AMOLED display	[62]
Scosche Rhythm+ Armband (Upper arm)	Scosche Industries Inc., Oxnard, California, USA, <a href="http://www.scosche.com/rhythm-plus-orange">www.scosche.com/rhythm-plus-orange</a>	Internal rechargeable battery, 8 hour battery life	Running, cycling, swimming, heart rate, heart rate variability	Green/ yellow optical sensor array	10×5×10 mm, 115 g, sweat-proof and water-proof, submersible up to 1 meter	[69], [82], [87]
Suunto 9 Baro (Wrist)	Suunto Oy, Vantaa, Finland, <a href="https://www.suunto.com/en-gb/Products/sports-watches/suunto-9-baro/suunto-9-baro-line/">https://www.suunto.com/en-gb/Products/sports-watches/suunto-9-baro/suunto-9-baro-line/</a>	Rechargeable Li-Ion battery, 7 days of battery life	Step counter, calories burned, heart rate tracking, sleep tracking, speed, distance, swimming, running, cycling	GPS, altimeter, barometer, compass, optical heart rate sensor	50×24×16.8 mm, 72 g, water resistant up to 100 m, LED back-light	[90]
Hexoskin smart shirt (Chest)	Carré Technologies Inc., Montréal, Canada, <a href="http://www.hexoskin.com/">www.hexoskin.com/</a>	12-30+ hours of battery life, 600+ hours of standalone recording	Heart rate, heart rate variability, breathing rate, breathing volume (minute ventilation), activity intensity, peak acceleration, steps, cadence, calories, positions, sleep tracking, VO2 max	ECG, dual-channel breathing sensors, 3D accelerometer	Device size: 13×42×72 mm, 40 g, shirts available in different sizes	[93]



**Table 1.1:** *Comparison of features and functions of different wearable devices capable of monitoring HR and/or HRV.*

Monitor (Sensing Location)	Company Details	Battery Specifications	Tracking Functions	Sensors	Additional General Details	Associated Validation Literature
PulseOn OHR Tracker (Wrist)	PulseOn Oy, Espoo, Finland, <a href="https://pulseon.com/ohr/ohr-tracker">https://pulseon.com/ohr/ohr-tracker</a>	Battery life up to 5 days, 30 hours minimum in continuous measurement mode	Heart rate, heart rate variability, steps, calories, running, walking	Accelerometer, optical heart rate sensor	Mono color OLED display	[68], [94], [95]
Motorola Moto 360 (Wrist)	Motorola Inc., Chicago, Illinois, United States, <a href="https://moto360.com/">https://moto360.com/</a>	Non-removable Li-Ion 355 mAh battery, battery life up to 48 hours, 0-100% charging in 60 minutes	Heart rate, steps, calories burned, speed, distance	Accelerometer, gyroscope, barometer, ambient light sensor, optical heart rate sensor, GPS, GLONASS, Galileo	42.8×42.8×11.68 mm, 52 g, full color AMOLED display, water resistant up to 3 atm	[72]
Sony SmartBand 2 (Wrist)	Sony Mobile Communications Inc., Tokyo, Japan, <a href="http://www.sonymobile.com/gb/products/smart-products/smartband-2/">www.sonymobile.com/gb/products/smart-products/smartband-2/</a>	Li-Ion battery, charging time of 1 hour and 15 minutes, battery life up to 2 days and 5 days with HR measuring turned off	Heart rate, steps, running, walking, sleeping	Optical heart rate sensor, accelerometer, NFC	40.7×15.3×9.5 mm, 25 g, water resistant up to 3 m	[72]
Catapult Vector (Back of neck)	Catapult, Melbourne, Australia, <a href="https://www.catapultsports.com/products/vector">https://www.catapultsports.com/products/vector</a>	Battery life up to 6 hours	ECG-derived heart rate, athletic features (designed for different sports)	Accelerometer, gyroscope, magnetometer, ECG, GPS, GLONASS	81×43×16 mm, 53 g, monitor woven into the vest	[90]
Jabra Elite Sport Earbuds (Ear)	Jabra, Copenhagen, Denmark, <a href="http://www.jabra.co.uk/sports-headphones/jabra-elite-sport">www.jabra.co.uk/sports-headphones/jabra-elite-sport</a>	Battery life up to 4.5 hours, charging time of 2 hours	Heart rate, step count, rep count, VO2 measurement, race time predictor	Earbuds with in-ear optical heart rate sensor, 4×digital MEMS microphones	27×30×22.5 mm, earbuds weight: 6.5 g × 2, water and dust proof	[85]

**Table 1.1:** *Comparison of features and functions of different wearable devices capable of monitoring HR and/or HRV.*

Monitor (Sensing Location)	Company Details	Battery Specifications	Tracking Functions	Sensors	Additional General Details	Associated Validation Literature
Actxa Tempo 3C (Wrist)	Actxa, Singapore, <a href="https://actxa.com/sg/tempo3c/">https://actxa.com/sg/tempo3c/</a>	110mAh battery capacity, battery life of approx. 5 days, charging time of up to 2 hours, magnetic charging	Heart rate, steps, calories burned, active time and distance travelled	3-axis accelerometer, optical heart rate sensor	Strap length and width: 275×20 mm, 30 g, TFT color screen 80×160, water resistant up to 1 m	[57]
Cosinuss One (Ear)	Cosinuss GmbH, Munich, Germany, <a href="https://www.cosinuss.com/products/one/">https://www.cosinuss.com/products/one/</a>	50 mAh Li-Ion battery, battery life up to 7 hours, charging time of approx. 1 hour	Heart rate, heart rate variability, body temperature	In-ear optical heart rate sensor (LED and photo-diode), resistance temperature sensor, 3D-axis accelerometer	45×38×18 mm, 6.5 g, splash-water proof	[96]
BioStam- pRC System (Chest)	MC10 Inc., Cambridge, Massachusetts, United States, <a href="https://www.mc10inc.com/">https://www.mc10inc.com/</a>	Li-Po rechargeable battery (15mAh), less than 120 minutes recharge time	Heart rate, heart rate variability, respiration rate, sleep assessment, posture quantification, step count and cadence	Accelerometer, gyroscope, ECG electrodes	66×34×4.5 mm, 7 g	[97]
Moov HR Burn (Chest)	Moov Inc., California, USA, <a href="https://welcome.moov.cc/moovhr">https://welcome.moov.cc/moovhr</a>	CR2032 3V battery, battery life up to 10 months, replaceable battery	Heart rate, running, walking, cycling, swimming, calorie count	Optical heart rate sensor (Pulsevision technology)	71.1×12.7×38.1 mm, 22 g, monitor attached to the chest strap	[61]
Moov HR Sweat (Forehead)	Moov Inc., California, USA, <a href="https://welcome.moov.cc/moovhr">https://welcome.moov.cc/moovhr</a>	Li-Po battery, battery life up to 4 hours, rechargeable core	Heart rate, running, walking, cycling, swimming, calorie count	Optical heart rate sensor (Pulsevision technology)	25.4×7.6×25.4 mm, 13 g, monitor attached to the headband (temple), water resistant up to 10 m	[61]

**Table 1.1:** *Comparison of features and functions of different wearable devices capable of monitoring HR and/or HRV.*

Monitor (Sensing Location)	Company Details	Battery Specifications	Tracking Functions	Sensors	Additional General Details	Associated Validation Literature
Equival EQO2 (Chest)	Equival Inc., New York, USA, <a href="https://www.equival.com">https://www.equival.com</a>	Li-Po battery, battery life up to 48 hours, 1 hour recharge time	Heart rate, inter-beat interval, breathing rate, respiratory effort, skin temperature, activity, body position, motion, fall detection	3-axis accelerometer, ECG, GPS, thermistor	78×55×11 mm, 38 g, monitor attached to a belt and also integrates with external compatible sensors	[98]
Dash Pro (Ear)	Bragi, Munich, Germany, <a href="https://bragi.com/">https://bragi.com/</a>	Rechargeable 100mAh Li-Ion polymer battery, up to 5 hour battery life with continuous playback	Heart rate, steps, cadence, speed, duration, breaths, swimming lengths, distance and calories	Two high-resolution optical touch sensors, dual pulse oximeter sensors, accelerometer, gyroscope, magnetometer	Sensors integrated into earbuds, multicolor LED, 13 g, waterproof up to 1m	[96]
Withings Pulse HR (Wrist)	Withings, Issy-les-Moulineaux, France, <a href="https://www.withings.com/uk/en/pulse-hr">https://www.withings.com/uk/en/pulse-hr</a>	Battery life of up to 20 days, charging time up to 2 hours, magnetic charging	Steps, distance, calories, running, swimming, heart rate, sleep quality, multi-sport tracking	3-axis MEMS accelerometer, optical light sensor	Diameter: 18.16 mm, thickness: 10.45 mm, height: 252.5 mm (inc. wristband), 45 g, OLED screen, water resistance up to 50 m	[61]
Bose Sound- Sport Pulse (Ear)	Bose Corporation, Massachusetts, USA, <a href="https://www.bose.com/content/consumer_electronics/b2c/north_america/websites/en_us/product/soundsport_pulse_wireless.html">https://www.bose.com/content/consumer_electronics/b2c/north_america/websites/en_us/product/soundsport_pulse_wireless.html</a>	Rechargeable Li-Ion battery, run-time up to 5 hours	Heart rate	In-ear built-in optical heart rate sensor	1.1×0.9×1.2 in, 23 g	[67]

#### 1.2.4 Summary

It can be observed that majority of the heart rate monitors (HRMs) listed in Table 1.1 are based on optical sensing of the cardiac activity at the wrist. Several studies have validated the PPG-based HRMs specifically designed by Apple, Fitbit, Garmin, Samsung and Mio Labs respectively. While all these monitors demonstrated a strong agreement with the ECG-based heart rate measurement at rest, many studies found a decline in the accuracy corresponding to the PPG signals recorded during a medium to high intensity exercise [61], [99]. Other PPG-based HRMs also showed similar results when compared with the ECG. However, the ECG-based monitors such as Polar H10, Zephyr HxM BT, BioStamp RC sensors exhibited a high level of agreement with the reference ECG signal during rest as well as high intensity exercises [66], [91]. These monitors are commonly used by the athletes to measure a number of physiological and biomechanical measurements including the HRV. They have a central unit integrated with the ECG electrodes and are connected to the chest using a strap. The integration of optical sensors in the earphones/ headphones have also been adopted to allow the monitoring of heart rate while listening to the music during athletic activities. Although these monitors showed promising results, the validation studies found a deviation from the ground truth heart rate values under the influence of motion artefacts [96].

As a summary, the commercially available ECG-based wearable HRMs are the most accurate and reliable way of monitoring the heart rate on a continuous basis. These devices also provide an added functionality of HRV monitoring along with the other activity tracking features. However, the signal acquisition using ECG-based HRMs generally require the use of electrode gel to establish an electrode contact with the patient's skin. This process can sometimes be uncomfortable specially for men with a hairy chest in which case a small amount of hair may be shaved to make sure the electrodes stick to the skin [100]. From a usability point of view, a better way of monitoring the heart rate is made possible with the PPG-based HRMs. These monitors are generally designed to be worn on the wrist and tracks multiple activities by integrating different sensors within the same wearable system. The accuracy and reliability of these devices, however, is vulnerable to a number of factors including the motion artifacts, brightness of the environment, or having a stable contact force between the sensor and the measurement site. These monitors also suffer from a short battery life of 1-2 days because of high power demands from the infrared LEDs. Therefore, there is a strict need of alternative sensing mechanisms that can simultaneously provide the user-friendliness of the PPG-based HRMs as well as a longer operational lifetime without compromising on the accuracy of the heart rate monitoring. As with the sounds on the chest, this thesis explores the possibility of recording the cardiac rhythms from the radial artery at the wrist using a very small, low power microphone, without requiring any additional power consuming input signal. This could potentially be used either as an alternative new physiological signal to extract

cardiac information from a wearable device, or as an additional physiological channel to complement existing systems, without posing an overhead in terms of size.

The next section discusses the blood pressure measurement (BPM) using different monitoring techniques as another important parameter to CVDs. Some commonly available blood pressure monitors in the market are also compared and the factors affecting the BPM using these monitors are discussed in detail.

### 1.3 Blood pressure: What is it? How is it measured?

During a cardiac cycle, the heart pumps blood with a certain force throughout the body. Blood pressure is a measure of this force and reflects the variable pressure exerted by the blood flow on the arterial walls. Systolic blood pressure (SBP) and diastolic blood pressure (DBP) are the two main components that are reported during the clinical BPM because of their direct association with increased CVD risk factors. The SBP is the maximum pressure of the blood ejected by the heart during the ventricular contraction in the systolic phase of the cardiac cycle. On the contrary, the DBP is the minimum arterial pressure obtained while the heart is relaxing in the diastolic phase of the cardiac cycle. Both the higher SBP and the higher DBP are linked to increased CVD mortalities [22], [24], [101]. Several other measures can also be determined from SBP/ DBP measurements. The pulse pressure (PP), defined as the difference of SBP and DBP, serves as an important marker for arterial stiffness and provides a measure of pulsatile hemodynamic stress. The mean arterial pressure (MAP) defined in Eq. 1.2 provides an estimate of the overall arterial pressure during a complete cardiac cycle. It represents the area under one cycle of the arterial pressure waveform.

$$\begin{aligned} \text{PP} &= \text{SBP} - \text{DBP} \\ \text{MAP} &= \text{DBP} + \alpha (\text{SBP} - \text{DBP}), \quad \alpha \in [0.2, 0.4] \end{aligned} \tag{1.2}$$

The arterial pressure waveform as shown in Fig. 1.5 is measured continuously through the insertion of a catheter into a suitable artery. It is generally classified into three distinct components [102] as follows:

- The systolic phase is characterised by a rapid increase of the pressure due to the opening of the aortic valve by the ventricular contractions. The systolic peak corresponds to the maximum pressure in the central arteries, also known as the SBP. The rising slope during this phase is followed by a rapid decline because of an end to the ventricular contractions.
- The dicrotic notch is the point at which the aortic valves are closed. The sharpness of this notch depends on the arterial measurement site. It is most sharp at the aortic valve and almost disappears at the peripheral sites.

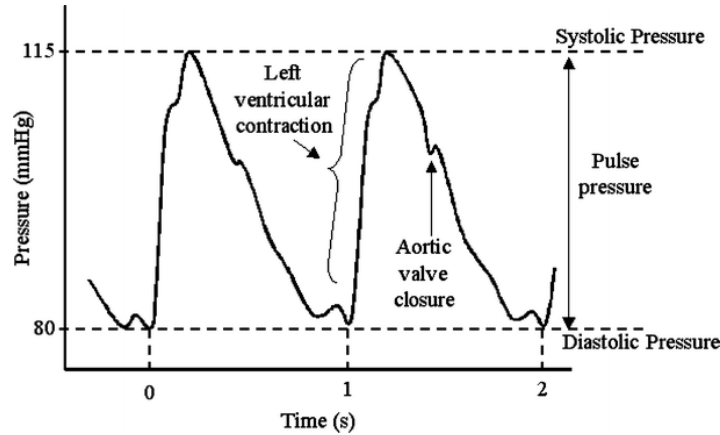


**Figure 1.5:** *An example of a typical arterial blood pressure waveform [103].*

- The pressure drops gradually during the diastolic run-off to attain a minimum arterial pressure, also known as the DBP. This end-diastolic pressure is the pressure exerted by the vascular tree back upon the aortic valve.

Further details about the arterial pressure waveform from the perspective of waves propagating from the heart to the circulatory system are discussed in the next chapter. Although the invasive monitoring of the arterial pressure using catheterization can provide a detailed representation of the blood pressure waveform, the non-invasive techniques can mostly determine the SBP/ DBP readings by sensing different physiological signals. Some of the commonly used non-invasive methods are discussed in the next section.

### 1.3.1 Non-invasive blood pressure monitoring techniques

#### 1.3.1.1 The auscultatory method

The gold standard approach to measure the blood pressure is based on the auscultation of the brachial artery at the upper arm using a stethoscope. The auscultatory method employs a mercury sphygmomanometer to display the pressure variations in a mercury column corresponding to the inflation/ deflation of an air cuff. In 1905, Korotkoff found that when an external pressure applied on an arterial branch through a Riva-Rocci cuff is gradually reduced from above the systolic pressure to the zero pressure, a series of different sounds can be heard using a stethoscope [104]. He concluded that the appearance of the first sound during the deflation indicated the SBP whereas the point of disappearance of the last sound identified the DBP. These sounds are now commonly known as the Korotkoff sounds. Goodman and Howell [105] recognised five different phases of the Korotkoff sounds and explained them using the following characteristics:

1. Phase I: “a loud clear-cut snapping tone.”
2. Phase II: “a succession of murmurs.”

3. Phase III: “the disappearance of the murmurs and the appearance of a tone resembling to a degree the first phase but less well marked.”
4. Phase IV: [the tone] “becomes less clear in quality or dull.”
5. Phase V: “the disappearance of all sounds.”

The spectral energy of the Korotkoff sounds recorded from the brachial artery are generally above the threshold of hearing allowing their auscultation using a stethoscope [106]. However, the environmental noise must be kept to a minimum as it can often cause difficulties in listening to these sounds.

Although the auscultatory method is regarded as the gold standard approach for the BPM, the widespread ban on the use of mercury sphygmomanometers continues to diminish its usage [107]. The replacement of mercury sphygmomanometers with the aneroid manometers did not provide satisfying results because of less accuracy and frequent need of calibration. However, the introduction of electronic pressure monitors resolved the issue to an extent by combining electronic features with the traditional auscultation method [108]. Another concern related to the auscultatory method is the unresolved consensus about choosing either the fourth ( $K_4$ ) or the fifth ( $K_5$ ) Korotkoff sound as the actual location of the DBP. Several studies on large cohorts of population have been performed to address this ambiguity. While in some subjects, a minimal difference between  $K_4$  and  $K_5$  have been observed, the other group of subjects showed a significant difference of around 10 mmHg between these sounds [102]. The studies suggested to log the pressure at both these phases to improve the communication about the blood pressure readings.

#### 1.3.1.2 The oscillometric method

The auscultation of the Korotkoff sounds is usually performed by a trained clinician using a stethoscope. Due to the human involvement in manually recording the blood pressure readings, the observer error and the observer bias are common sources of error in the auscultation method. The differences in the auditory acuity among different observers may also lead to significant errors in identifying the appearance and disappearance of the Korotkoff sounds. The digit preference by the observers is another common instance where majority of the readings are rounded off to end in 0 or 5 [109]. The oscillometric method removes these sources of error by providing an automated way of measuring the blood pressure. The method works on the principle that when the pressure inside a sphygmomanometer cuff is gradually reduced from the full occlusion of the brachial artery, a series of small pressure oscillations are superimposed on the deflating pressure curve as shown in Fig. 1.6(a). These oscillations start to appear before the SBP and continue after the DBP, and can be isolated by removing the baseline pressure. Unlike the auscultatory method, the SBP/ DBP readings cannot be estimated directly and requires empirically

derived algorithms to obtain the BPM. However, it has been proved that the maximum amplitude of the oscillation envelope, also known as the oscillometric waveform envelope (OMWE), corresponds to the MAP [110]. Since there is no universal oscillometric algorithm, different brands use their own proprietary algorithms to estimate the SBP/DBP from the oscillometric waveforms, the details of which are not available publicly. These monitors are generally validated with the manual auscultatory measurements to find an agreement between both the techniques. In the literature, different algorithms have been proposed to utilise the amplitude and slope characteristics of the OMWE and find a correlation with the SBP/DBP readings. Some of the commonly used methods include the heuristically derived ratios based on the maximum OMWE amplitude [112], [113] (e.g., fixed-ratio method employed in Fig. 1.6(b) to find SBP/DBP location using the MAP location), ratios based on the slope of OMWE envelope [114], [115], neural networks [116], [117], and deep learning [118]. Although the ratio based methods are simple to implement, the assumption of a fixed ratio or a range of ratios does not account

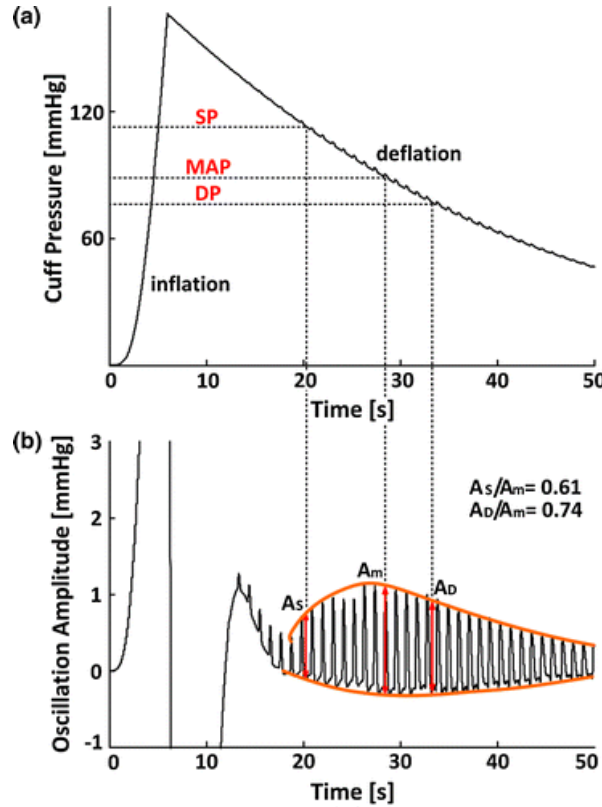


**Figure 1.6:** *Oscillometric method for blood pressure measurement. (a) Pressure oscillations superimposed on the deflating pressure curve. (b) Oscillometric waveform envelope corresponding to the detrended pressure oscillations. The fixed ratios are used to estimate the SBP, DBP from the maximum oscillation peak [111]*



for the variation of different physiological factors over time. These ratios are generally determined by minimising the error relative to the manual auscultatory measurements, therefore, fitting the ratios only to the database under consideration [118]. The neural network and deep learning based algorithms are more robust in determining the blood pressure, however, they are computationally expensive and may need larger database to train the network.

From the hardware perspective, the oscillometry-based monitors only need the pressure sensor as a transducer to be placed over the brachial artery. Therefore, these monitors have a better resistance to the external noise and interference than the stethoscope in the auscultatory method. A major disadvantage of the oscillometric technique is its high susceptibility to the motion artefacts and mechanical vibrations [108]. These artefacts can interfere with the OMWE envelope and produce significant errors in the blood pressure estimation. However, the ease of monitoring and the automation provided by the oscillometry-based monitors have allowed their wide deployment for self BPMs in the home and clinical settings. Although the monitors based on the wrist and the upper-arm are available in the market, the wrist monitors have been found to overestimate the blood pressure at the upper arm [119], [120].

#### **1.3.1.3 Ultrasound method**

The ultrasound technique consists of a transmitter and a receiver to be placed on the brachial artery under a sphygmomanometer cuff. The fundamental principle is the observation of the changes in the Doppler echo signal when a high frequency sound wave (higher than the upper threshold of human hearing) is projected on the site under test. During the cuff deflation from above the systolic pressure, the ultrasound receiver observes a Doppler phase shift just below the SBP due to a sudden rush of the blood flow. The Doppler phase shift varies with different levels of arterial occlusion and attains a minimum value at the DBP where a laminar or non-turbulent flow of blood takes place. The ultrasound method is of a particular value in subjects with very faint Korotkoff sounds and oscillometric pulsations [108]. This method is also useful for determining the blood pressure in infants and children [121]. While the ultrasound technique can provide an accurate measurement of the SBP/ DBP readings, the recording setup is generally bulky, expensive and power-hungry.

#### **1.3.1.4 The finger-cuff method**

The methods discussed above only provide a snapshot of the BPM. Therefore, the patients requiring a regular monitoring usually take multiple readings over the day to generate a blood pressure profile either manually or using a smartphone/ web application. For the critically ill patients, this approach of understanding the blood pressure variations is not feasible because the hemodynamics of the body changes on a regular basis [122].

The continuous monitoring of blood pressure in such patients becomes quite important. The finger cuff method is a non-invasive approach to measure the arterial blood pressure continuously, and is based on the measurement of arterial pulsations using a PPG sensor placed under an inflatable cuff. The goal is to keep the pulsating finger artery in a constant partially opened state by using the PPG output as a feedback to drive the servo-motor system in order to apply a suitable counter pressure through the finger cuff. The constant blood volume in the artery causes the intra-arterial pressure to become equal to the cuff pressure which can be measured through an external pressure gauge. Due to this reason, the finger-cuff method is also known as the “vascular unloading” technique. The resulting arterial pressure waveform obtained from the finger is used to estimate the brachial waveform, and therefore obtain the beat-to-beat BPMs [122]. This method was first introduced by Penaz and later improved by Wesseling who developed an instrument named Finapres (finger arterial pressure) that allowed the ambulatory blood pressure monitoring of a subject [123]. Successors of the Finapres included the Finometer, the Portapres and the Nexfin, however, all the commercially available monitors based on the finger-cuff method are generally bulky, cumbersome, and are recommended to be used in the clinical settings.

#### **1.3.1.5 Pulse transit time method**

Although the oscillometric and finger-cuff methods provide automated BPMs, these techniques incorporate the use of an air cuff in the recording setup. The size of the cuff, as discussed in the next section, plays an important role in an accurate measurement since a small-sized cuff can significantly overestimate the blood pressure [124]. The pulse transit time (PTT) method provides a cuff-less technique to estimate the blood pressure by utilising the time taken by a cardiac pulse to travel from the heart to a peripheral site or between the two peripheral sites [125], [126]. While there are different variations to this method including the correlation of PTT with the blood pressure and cuff pressure respectively, the fundamental theory behind the technique remains the same. The pulse wave velocity (PWV) can be expressed in terms of the blood density, the arterial dimensions and the elastic modulus of the vessel wall. The parameter PWV is inversely proportional to PTT in cases where the effect of arterial elongation can be ignored. Since the velocity of the blood flow is governed by the aortic pressure, the time interval between the pulse onset times at two different sites can be correlated indirectly with the blood pressure [127]. The correlation is generally found using a mathematical model which involves the computation of several parameters to reduce the inter-patient variability. Due to an unavailability of a universal model, different studies use different parameters (e.g. heart rate, patient’s height, etc.) to estimate the blood pressure from the PTT. These parameters usually require frequent calibration for every user by taking a reference blood pressure with one of the standard approaches [128]. The use of two different sensors at

distant arterial sites probably using a wired connection also makes it uncomfortable for a subject undergoing ambulatory blood pressure monitoring.

### 1.3.2 Factors affecting the blood pressure measurement

Several factors external to the measurement principle of both the cuff-based and cuff-less techniques can affect the BPM significantly. Some of the important factors discussed below must be addressed during the data acquisition protocol to reduce the potential sources of error in the BPM.

- **Body posture:** Although the blood pressure is commonly recorded while the subject is seated, it can also be measured in the supine or standing body postures. The seated position is also accepted as the recommended posture by some of the international guidelines [107]. Generally, there is no significant difference between the readings taken from any of these positions, however, high discrepancies can be observed in some subjects [129]. In such cases, the body posture must be reported along with the blood pressure readings.
- **Body position:** The BPMs are influenced by the relative position of the arm/ wrist with respect to the heart [130]. Any difference in the vertical height of the two sites can introduce hydrostatic pressure in the blood pressure readings. To minimise the effect of hydrostatic pressure, the arm/ wrist must be kept at the level of heart, with the whole forearm supported on a plane surface. It should also be ensured that the subject is seated comfortably, with the arm slightly flexed and the back supported during the measurements. Otherwise, the DBP may be overestimated significantly if a subject sits in the bolt upright position [108].
- **Cuff size and placement:** An inappropriate size of cuff is another source of error in the BPM. A common mistake of using a small-sized cuff can significantly overestimate the blood pressure [124]. This error can be minimised by using a large-sized cuff on subjects with medium to large arm/ wrist circumferences. Generally, the bladder length and the width of the cuff should be around 80% and 40% of the arm circumference respectively. The American Heart Association recommends different cuff sizes for a newborn (<6 cm), infant (6-15 cm), child (16-21 cm), small adult (22-26 cm), adult (27-34 cm), large adult (35-44 cm) and adult thigh (45-52 cm) [108]. The placement of cuff is also critical to the BPM. Ideally, the mid-line of the cuff bladder should be positioned over the brachial site at which the arterial pulsations can be easily palpated. For the auscultatory method, a gap of 2-3 cm between the lower end of the cuff and the antecubital fossa should be kept to allow a proper placement of the stethoscope. The cuff placement is not critical for the oscillometric measurements.

- **Cuff inflation/deflation rate:** The new monitors available in the market are capable of measuring the blood pressure during the inflation of the air cuff. However, the cuff-based techniques were originally based on sensing the signals during the deflation cycles. The inflation/ deflation rate has an important effect on the SBP/ DBP readings [102]. For different subjects, the heart rate and inflation/ deflation rate decides the count of the events of interest recorded over the whole length of the pressure variation. Since the performance of the algorithm depends on these events, a suitable inflation/ deflation rate must be chosen for the BPM. As per the recommendations from the international guidelines, the cuff should be inflated to at least 20-30 mmHg above the full occlusion of the radial artery. Depending on the operating mode of a particular monitor, an inflation/ deflation rate of 2-3 mmHg per second can be chosen [131]. Any higher rates can cause the SBP to appear lower and the DBP to appear higher.
- **Cuff inflation hypertension:** In majority of the subjects, the cuff inflation itself does not change the actual blood pressure. However, a significant increment in the blood pressure readings coinciding with the process of cuff inflation has been observed in some subjects [132]. The cuff inflation hypertension is different from the white coat hypertension, which refers to the cohort of subjects with higher blood pressure readings observed only during the clinical visits. The blood pressure for these subjects fall within the normal range when they are outside the clinical settings. This condition is generally treated as low-risk in comparison to the sustained hypertensive state and can be diagnosed reliably by measuring the blood pressure in the home settings [108].

### 1.3.3 Commercially available BP monitors

The monitoring techniques revealed the association of different types of signals including the Korotkoff sounds, pressure oscillations, pulse arrival time, etc. with the blood pressure. These signals are recorded using semi- or fully-automated blood pressure monitors. Among the different sensing mechanisms, the automatic blood pressure monitors available in the market are mainly based on the oscillometric technique. This is because the auscultation of the Korotkoff sounds using a stethoscope require intensive training and is usually operated in the clinical settings. The cumbersome setup involved in the ultrasound and PTT-based methods also limit their usage in the clinical environment. However, the user-friendliness of the oscillometry-based monitors offers the self measurement of blood pressure at home using small portable devices. Both the wrist- and arm-based monitors are available in the market and different features and functions set one apart from the other. Some of the important features that are helpful in differentiating these monitors are discussed below.

1. *Measurement technique:* Although the market is dominated by the oscillometry-based monitors, few of the monitors also use automated auscultation of the Korotkoff sounds on the upper-arm to measure the blood pressure.
2. *Sensing location:* Apart from the upper arm and wrist as commonly used locations, the research has also explored the possibility of measuring the blood pressure at other locations including the calf, ankle, ear, etc. [133]. However, the commercial monitors are mainly based on sensing the pressure oscillations either at the upper arm or the wrist.
3. *Power source:* The power source in the monitors is critical to the number of blood pressure readings a user can take without changing the batteries. Since these monitors are mainly based on inflation/ deflation of the air cuff through a motor, a high current drive is demanded from the batteries. Due to a trade-off between the operational lifetime and the size/ weight of the monitor, usually two to four AA/ AAA alkaline batteries are required for the operation. Majority of the monitors can also operate by connecting an AC adapter to the mains.
4. *Size and weight:* The spot measurement of the blood pressure does not require a subject to wear the monitor at all times. Also, majority of the blood pressure monitors have a control unit connected to the air cuff through the tubing. Although the size and weight of the control unit does not affect the BPMs, the portability of these monitors is compromised if the dimensions and weight are significantly larger. This is specially true for the monitors which integrate the control unit with the cuff and are placed on the upper arm/ wrist.
5. *Additional tracking functions:* While the primary function of these monitors is to measure the SBP/ DBP, the integration of different sensors within the same monitor also allows to track other parameters such as body movement, irregular heart beat detection, etc. The inbuilt position sensor in the wrist-based monitors significantly increases the accuracy of BPM by minimising the effect of hydrostatic pressure. The errors raised in case of an incorrectly wrapped cuff also avoids the under- or over-estimation of the blood pressure.
6. *Validation in literature:* All the international guidelines recommend taking the BPMs at home using automated blood pressure monitors. Due to the abundance of such monitors in the market, their validation in the literature to assess the accuracy of BPM prove to be an important criteria in choosing a specific monitor. The validation for non-invasive automatic blood pressure monitors is generally performed using one of the three international guidelines, the details of which are summarised below.

- i. *British Hypertension Society (BHS) Protocol [134]*: The BHS protocol requires 85 participants such that 8 subjects have a SBP:  $< 90$  mmHg and DBP:  $< 60$  mmHg; 20 subjects have a SBP: 90-129 mmHg and DBP: 60-79 mmHg; 20 subjects have a SBP: 130-160 mmHg and DBP: 80-100 mmHg; 20 subjects have a SBP: 161-180 mmHg and DBP: 101-110 mmHg; 8 subjects have a SBP:  $> 180$  mmHg and DBP:  $> 110$  mmHg respectively. Sequential same arm measurements are carried out for three times in the following order: two different observers measure the blood pressure using the mercury sphygmomanometer followed by a measurement using the test instrument. Depending on the percentage of differences between the test device and the reference measurements falling within the certain limits, a BHS grade is awarded as follows:

**Table 1.2:** *BHS grading criteria [134].*

Grade	Absolute difference between standard and test device		
	$\leq 5$ mmHg	$\leq 10$ mmHg	$\leq 15$ mmHg
Cumulative percentage of readings			
A	60	85	95
B	50	75	90
C	40	65	85
D	Worse than C		

- ii. *European Society of Hypertension International Protocol (ESH-IP) revision 2010 [135]*: The ESH-IP requires 33 participants all above 25 years of age with at least 10 males and 10 females. A minimum of 10-12 subjects in each of the low, medium and high blood pressure ranges are required during the recruitment process. The low range is divided into two subgroups of  $< 90$  mmHg and 90-129 mmHg for the SBP, and  $< 40$  mmHg and 40-79 mmHg for the DBP. The medium range for the SBP and DBP are 130-160 mmHg and 80-100 mmHg respectively. The high range is also divided into two subgroups of 161-180 mmHg and  $> 180$  mmHg for the SBP, and 101-130 mmHg and  $> 130$  mmHg for the DBP. Similar to the BHS protocol, the sequential same arm measurements are carried out for three times in the following order: two different observers in presence of a supervisor measure the blood pressure using the mercury sphygmomanometer followed by a measurement using the test instrument. The absolute blood pressure differences between the experimental readings and the reference measurements for 33 subjects are determined. These differences are graded according to the ESH-IP criteria shown in Table 1.3. The criteria consists of two parts where the first part checks the cumula-

**Table 1.3:** *ESH-IP 2010 grading criteria [135].*

<b>Part 1</b>		$\leq 5 \text{ mmHg}$	$\leq 10 \text{ mmHg}$	$\leq 15 \text{ mmHg}$
Pass requirement	Two of	73%	87%	96%
	All of	65%	81%	93%
<b>Part 2</b>		$2/3 \leq 5 \text{ mmHg}$	$0/3 \leq 5 \text{ mmHg}$	
Pass requirement		$\geq 24$	$\leq 3$	

tive percentage of differences falling within 5 mmHg, 10 mmHg and 15 mmHg respectively. The second part checks the number of subjects with difference of at least two readings less than 5 mmHg, and the number of subjects with zero readings below 5 mmHg. A test instrument is passed only when both the parts of the grading criteria are satisfied.

- iii. *American National Standards Institute/ Association for the Advancement of Medical Instrumentation/ International Organization for Standardization (ANSI/AAMI/ISO) Protocol [136]:* This protocol requires 85 participants with at least 30% males and 30% females respectively. The age of every subject must be greater than 12 years. The reference blood pressure should meet the following distribution: at least 5%  $\text{SBP} \leq 100 \text{ mmHg}$ , at least 5%  $\text{SBP} \geq 160 \text{ mmHg}$ , at least 20%  $\text{SBP} \geq 140 \text{ mmHg}$ , at least 5%  $\text{DBP} \leq 60 \text{ mmHg}$ , at least 5%  $\text{DBP} \geq 100 \text{ mmHg}$ , at least 20%  $\text{DBP} \geq 85 \text{ mmHg}$ . Three measurements including the two reference readings and one experimental reading are recorded from the same arm of every subject. For the validation, the mean and standard deviation of the blood pressure differences corresponding to 255 blood pressure pairs ( $85 \times 3$ ) are calculated. A test instrument is passed if it obtains a mean of less than 5 mmHg and a standard deviation of less than 8 mmHg respectively. The second criterion of the protocol compares the standard deviation of the SBP/DBP with a predefined table of maximum permissible standard deviations as a function of the mean value of the blood pressure differences [136].

The factors discussed above serve as an important criteria in differentiating the usability of different blood pressure monitors available commercially. Table 1.4 compares the features and functions of some commonly available blood pressure monitors from different companies and also provide references to the associated validation literature. The listed devices are chosen using the same criteria as described for the heart rate monitors in Section 1.2.3.

**Table 1.4:** *Comparison of features and functions of different blood pressure monitors.*

Monitor	Company Details	Monitor Type	Battery Specifications	General Details	Remarks	Associated Validation Literature
Microlife BP B6 Connect	Microlife Corporation, Taipei, Taiwan, <a href="https://www.microlife.com/consumer-products/blood-pressure/upper-arm-automatic/bp-b6-connect">https://www.microlife.com/consumer-products/blood-pressure/upper-arm-automatic/bp-b6-connect</a>	Upper-arm oscillometric BP monitor	4×1.5 V alkaline batteries; size AA or mains adapter DC 6V, 600 mA (optional)	157.5×105×61.5 mm, 415 g (including batteries), measuring range: 20-280 mmHg (blood pressure); 40-200 bpm (pulse)	Validated for pregnant women, diabetics, patients in end-stage renal disease or obese people and children from the age of 12 years, stroke risk detection (atrial fibrillation), accuracy of $\pm 3$ mmHg and $\pm 5\%$	[137], [138]
Microlife BP W100	Microlife Corporation, Taipei, Taiwan, <a href="https://www.microlife.com/consumer-products/blood-pressure/upper-arm-automatic/bp-b6-connect">https://www.microlife.com/consumer-products/blood-pressure/upper-arm-automatic/bp-b6-connect</a>	Wrist oscillometric BP monitor	2×1.5 V alkaline batteries; size AAA	80×70×70 mm, 130 g (including batteries), measuring range: 20-280 mmHg (blood pressure); 40-200 bpm (pulse)	Detects possible heart arrhythmia, clinically tested for measurement accuracy (BIHS, grade A/A), accuracy of $\pm 3$ mmHg and $\pm 5\%$	—
Omron M7 Intelli IT	Omron Corporation, Kyoto, Japan, <a href="https://www.omron-healthcare.co.uk/blood-pressure-monitors/M7_Intelli_IT.html">https://www.omron-healthcare.co.uk/blood-pressure-monitors/M7_Intelli_IT.html</a>	Upper-arm oscillometric BP monitor	4×1.5 V alkaline batteries; size AA or optional AC adapter	124×90×161 mm, 390 g (including batteries), measurement range: 0 to 299 mmHg, 40-180 bpm (pulse), 360° accuracy from the upper arm cuff	Accuracy of $\pm 3$ mmHg and $\pm 5\%$ , clinically validated for diabetics and pregnant women	[139], [140]
Omron R7 Intelli IT	Omron Corporation, Kyoto, Japan, <a href="https://www.omron-healthcare.co.uk/blood-pressure-monitors/R7_Intelli_IT_2.html">https://www.omron-healthcare.co.uk/blood-pressure-monitors/R7_Intelli_IT_2.html</a>	Wrist oscillometric BP monitor	Two LR03 alkaline batteries (AAA)	78×65.5×37.2 mm, 150 g (including batteries), measurement range: 0 to 299 mmHg, 40-180 bpm (pulse)	Accuracy of $\pm 3$ mmHg and $\pm 5\%$ , clinically validated for obese subjects, in-built positioning sensor, irregular heartbeat detection for stroke prevention, body movement detection	[141], [142]



**Table 1.4:** *Comparison of features and functions of different blood pressure monitors.*

Monitor	Company Details	Monitor Type	Battery Specifications	General Details	Remarks	Associated Validation Literature
iHealth Clear	iHealth Lab Inc., Mountain View, California, United States, <a href="https://ihealthlabs.com/blood-pressure-monitors/clear">https://ihealthlabs.com/blood-pressure-monitors/clear</a>	Upper-arm oscillometric BP monitor	1×3.7 V Li-ion, 2200 mAh battery or optional 5 V DC power	119×118×51 mm, 350 g (excluding cuff), measurement range: 0-300 mmHg, 40-180 bpm (pulse)	Accuracy of $\pm 3$ mmHg and $\pm 5\%$ , wireless functionality	[139], [143]
Andon KD-5965	Andon Health Co. Ltd., Tianjin, China, <a href="https://medaval.ie/device/andon-kd-5965/">https://medaval.ie/device/andon-kd-5965/</a>	Upper-arm oscillometric BP monitor	4 × AA alkaline batteries	100×145×61 mm, 362 g, measurement range: 0-295 mmHg, 40-199 bpm (pulse)	Accuracy of $\pm 3$ mmHg and $\pm 5\%$ , irregular heartbeat detection, talking function	[144]
Avita BPM65 series	AVITA Corporation, Taiwan, China, <a href="http://www.avita.com.tw/BPM65en.html">http://www.avita.com.tw/BPM65en.html</a>	Upper-arm oscillometric BP monitor	4 × AA alkaline batteries, optional AC adapter	143×93×56 mm, 280 g (excluding batteries), measuring range: 30-280 mmHg, 40-199 bpm (pulse)	Accuracy of $\pm 3$ mmHg and $\pm 4\%$ , ambient temperature sensor	[145]
Avita BPM18 series	AVITA Corporation, Taiwan, China, <a href="http://www.avita.com.tw/BPM18en.html">http://www.avita.com.tw/BPM18en.html</a>	Wrist oscillometric BP monitor	2 × AAA alkaline batteries	58×88.5×28.3 mm, 106 g (excluding batteries), measuring range: 30-280 mmHg, 40-199 bpm (pulse)	Accuracy of $\pm 3$ mmHg and $\pm 4\%$	[146], [147]
Bpump BF-1112	Shenzhen Pump Medical System Co. Ltd., Shenzhen, China, <a href="https://medaval.ie/device/bpump-bf-1112/">https://medaval.ie/device/bpump-bf-1112/</a>	Upper-arm oscillometric BP monitor	4 × AA alkaline batteries, optional AC adapter	140×110×70 mm, 294 g (excluding batteries), measurement range: 0-280 mmHg, 40-180 bpm (pulse)	Accuracy of $\pm 3$ mmHg and $\pm 5\%$	[148]
G.Lab MD2222	Aceso Healthcare Products, Inc., California, USA, <a href="https://glab-usa.com/">https://glab-usa.com/</a>	Wrist oscillometric BP monitor	2 × 1.5 V AAA alkaline batteries	70×80×32 mm, measurement range - SBP: 50-250 mmHg, DBP: 30-200 mmHg, 40-180 bpm (pulse)	Accuracy of $\pm 3$ mmHg and $\pm 5\%$	[149], [150]

**Table 1.4:** *Comparison of features and functions of different blood pressure monitors.*

Monitor	Company Details	Monitor Type	Battery Specifications	General Details	Remarks	Associated Validation Literature
Hingmed WBP-02A	Hingmed Medical Instrument Co. Ltd., Shenzhen, China, <a href="http://en.hingmed.com/products_detail/productId=35.html">http://en.hingmed.com/products_detail/productId=35.html</a>	Upper-arm oscillometric BP monitor	3.7 V, 1000 mAh Lithium battery	119×52×21 mm, 105 g (including batteries), measurement range - SBP: 40-260 mmHg, DBP: 20-210 mmHg, 40-200 bpm (pulse)	Accuracy of $\pm 3$ mmHg, records the body position	[151]
Health and Life HL868ED	Health and Life Co. Ltd., Taiwan, <a href="https://www.healthandlife.com.tw/index.php?action=products_data&amp;id=161&amp;width=1440">https://www.healthandlife.com.tw/index.php?action=products_data&amp;id=161&amp;width=1440</a>	Upper-arm oscillometric BP monitor	4 × AAA LR03 (1.5V) alkaline battery, optional 6V 1A AC/DC adapter	140×110×52.5 mm, 229 g (including batteries), measurement range: 0-300 mmHg, 40-199 bpm (pulse)	Accuracy of $\pm 3$ mmHg and $\pm 5\%$	[152]
Pangao PG-800A36	Pangao Electronic Co. Ltd., Guangdong, China, <a href="http://en.pan-go.com/products_detail/productId=234.html">http://en.pan-go.com/products_detail/productId=234.html</a>	Wrist oscillometric BP monitor	Rechargeable lithium battery	72×67×30 mm, 130 g (excluding batteries), measurement range: 30-280 mmHg, 40-199 bpm (pulse)	Accuracy of $\pm 3$ mmHg and $\pm 5\%$	[153]
Pangao PG-800B11	Pangao Electronic Co. Ltd., Guangdong, China, <a href="http://en.pan-go.com/products_detail/productId=208.html">http://en.pan-go.com/products_detail/productId=208.html</a>	Upper-arm oscillometric BP monitor	AC adapter or 4 × 1.5 V (LR6 or AA)	140×100×50 mm, 450 g (excluding batteries), measurement range: 30-280 mmHg, 40-199 bpm (pulse)	Accuracy of $\pm 3$ mmHg and $\pm 5\%$ , irregular heart rate detection	[154], [155]
Rossmax CF175	Rossmax International Ltd., Taiwan, China, <a href="https://www.rossmax.com/1v/produkti/monitoring/blood-pressure-monitors.html">https://www.rossmax.com/1v/produkti/monitoring/blood-pressure-monitors.html</a>	Upper-arm oscillometric BP monitor	6 V DC power, 4 × AAA batteries	124×85×68.6 mm, 355 g (excluding batteries), measurement range: 30-260 mmHg, 40-199 bpm (pulse)	Accuracy of $\pm 3$ mmHg and $\pm 5\%$ , movement detection, irregular heart rate detection	[156]
Sejoy BP-1307	Sejoy Electronics and Instruments Co. Ltd., Hangzhou, China, <a href="http://www.sejoy.com/products_show.php?cid=35&amp;id=16">http://www.sejoy.com/products_show.php?cid=35&amp;id=16</a>	Upper-arm oscillometric BP monitor	4 × AA batteries, optional AC adapter	166×114×72 mm, 468 g, pressure range: 0-300 mmHg, pulse: 30-180 bpm	Accuracy of $\pm 3$ mmHg, irregular heart rate detection	[157]

**Table 1.4:** *Comparison of features and functions of different blood pressure monitors.*

Monitor	Company Details	Monitor Type	Battery Specifications	General Details	Remarks	Associated Validation Literature
InBody BPBIO320	InBody Co. Ltd., Seoul, Korea, <a href="https://inbody.com/global/product/BPBIO320.aspx">https://inbody.com/global/product/BPBIO320.aspx</a>	Upper-arm oscillometric BP monitor	AC 100-120/200-240V, 50/60Hz power source	489×409×284 mm, 9000 g, measurement range: 0-300 mmHg, pulse: 30-240 bpm	Accuracy of $\pm 3$ mmHg and $\pm 2\%$ , body type analysis, results sheet print-out	[158]
Welch Allyn ProBP 2000	Welch Allyn Inc., USA, <a href="https://www.welchallyn.com/content/welchallyn/emeai/en/products/categories/blood-pressure-measurement.html">https://www.welchallyn.com/content/welchallyn/emeai/en/products/categories/blood-pressure-measurement.html</a>	Upper-arm oscillometric BP monitor	4 × AA alkaline batteries, 6 V DC, optional AC power supply	142×94×66 mm, 283 g (excluding batteries), measurement range: 0-299 mmHg, SBP: 50-260 mmHg, DBP: 25-220 mmHg, pulse: 40-199 bpm	Accuracy of $\pm 3$ mmHg and $\pm 4\%$ , readings in around 20 seconds during inflation, 97% completion rate in the presence of motion	[159]
YuWell YE690A	Jiangsu Yuyue Medical Equipment and Supply Co. Ltd. (Yuwell), Jiangsu, China, <a href="https://medaval.ie/device/yuwell-ye-690a/">https://medaval.ie/device/yuwell-ye-690a/</a>	Upper-arm oscillometric BP monitor	4 × AAA batteries or 6 V DC power	133×100×83 mm, measuring range - SBP: 60-230 mmHg, DBP: 40-130 mmHg, pulse: 40-200 bpm	Accuracy of $\pm 3$ mmHg and $\pm 5\%$ , irregular heart rate detection	[160], [161]
A&D UA 1200BLE	A&D Company, Tokyo, Japan, <a href="https://www.aandd.jp/products/medical/consumer/ble_series_2.html">https://www.aandd.jp/products/medical/consumer/ble_series_2.html</a>	Upper-arm oscillometric BP monitor	3.7 V Li-ion 325 mAh battery	126×44×26 mm, 220 g (including batteries), measurement range: 0-299 mmHg, SBP: 60-279 mmHg, DBP: 40-200 mmHg, pulse: 40-180 bpm	Accuracy of $\pm 3$ mmHg and $\pm 5\%$ , atrial fibrillation indicator, lightest tubeless and wireless monitor	[162]
Tango M2 Stress Test Monitor	SunTech Medical Inc., Eynsham, U.K., <a href="https://www.suntechmed.com/bp-products">https://www.suntechmed.com/bp-products</a>	Upper-arm auscultatory BP monitor	100-240 VAC @ 1.5 A, 50-60 Hz	240×174×115 mm, 1680 g, measurement range - SBP: 40-270 mmHg, DBP: 20-160 mmHg, pulse: 40-200 bpm	Accuracy equivalent to a trained observer using a cuff/stethoscope auscultation method per ANSI/AAMI/ISO 81060-2 protocol, monitor uses Korotkoff sound analysis on the brachial artery	—

### 1.3.4 Summary

All the monitors listed in Table 1.4 are based on the oscillometric technique except the “Tango M2 stress test monitor” from SunTech Medical which also provide an added functionality of recording the Korotkoff sounds by placing a wired microphone under a specially designed cuff. However, this monitor has not been validated in the literature for the BPM using the auscultation method. Although both the auscultatory and the oscillometric methods are cuff-based techniques, the oscillometry-based monitors are more prevalent because of their user-friendliness and automatic measurement of the blood pressure. The automation allows the self BPM at home, a feature that also minimises the effect of white coat hypertension. While all the companies manufacturing these monitors claim an accuracy of  $\pm 3$  mmHg to  $\pm 5$  mmHg with respect to the gold standard, the accuracy of oscillometry-based monitors suffer from several challenges. This technique is solely based on analysing the pressure oscillations during the cuff inflation/ deflation. These oscillations can be irregular and weak in strength for the obese subjects and the subjects suffering from atrial fibrillation and atherosclerosis [163]. A major drawback of this technique when compared with the auscultatory method is an absence of direct correlation of the pressure oscillations with the SBP/ DBP readings. The blood pressure estimation is usually based on deriving empirical coefficients from a specific cohort of subjects. While these coefficients can provide accurate BPMs for the study undertaken, it may be unreliable in diverse patient populations and measurement scenarios [164].

The gold standard approach of measuring the blood pressure is based on sensing the Korotkoff sounds at the upper-arm. Although the auscultation of these sounds using a stethoscope requires intensive training and adequate auditory acuity, the direct relationship between the appearance/ disappearance of the Korotkoff sounds with the SBP/ DBP still makes this method as the most accurate and reliable for the BPM. As with the Korotkoff sounds on the upper-arm, this thesis explores the possibility of recording these sounds from the radial artery at the wrist for the first time in the literature. The requirement of any training or human involvement is completely avoided by automating the process of listening to the Korotkoff sounds using a small, battery-powered wearable device. The measurement at the wrist using the auscultatory method also proves to be beneficial for the obese subjects as the wrist circumference does not vary as much as the arm circumference.

In conclusion, this thesis proposes a wearable device to be worn on the wrist that can continuously measure the heart rate and the heart rate variability, and can also record the Korotkoff sounds for the spot measurement of the blood pressure. The measurement of all three important physiological markers associated with the CVDs using the same wearable device are based on the acoustic sensing of the cardiac activity at the wrist. The relevant algorithms to extract the heart rate, heart rate variability, SBP/ DBP from the acoustic signals recorded at the wrist are also proposed in this thesis.

## References

- [1] “Human cardiovascular system,” 2019. [Online]. Available: <https://www.britannica.com/science/human-cardiovascular-system>
- [2] E. M. Antman and E. Braunwald, “Heart disease: A textbook of cardiovascular medicine,” *Heart disease: A textbook of cardiovascular medicine*, 1997.
- [3] *Prevention of cardiovascular disease*. World Health Organization, 2007.
- [4] “Cardiovascular Diseases,” 2017. [Online]. Available: [https://www.who.int/en/news-room/fact-sheets/detail/cardiovascular-diseases-\(cvds\)](https://www.who.int/en/news-room/fact-sheets/detail/cardiovascular-diseases-(cvds))
- [5] “Global status report on noncommunicable diseases 2014,” World Health Organization, Tech. Rep., 2014.
- [6] “Heart and Circulatory Disease Statistics 2019.” [Online]. Available: <https://www.bhf.org.uk/what-we-do/our-research/heart-statistics/heart-statistics-publications/cardiovascular-disease-statistics-2019>
- [7] W. B. Kannel, C. Kannel, R. S. Paffenbarger Jr, and L. A. Cupples, “Heart rate and cardiovascular mortality: the Framingham Study,” *American heart journal*, vol. 113, no. 6, pp. 1489–1494, 1987.
- [8] M. Woodward, R. Webster, Y. Murakami, F. Barzi, T.-H. Lam, X. Fang, I. Suh, G. D. Batty, R. Huxley, and A. Rodgers, “The association between resting heart rate, cardiovascular disease and mortality: evidence from 112,680 men and women in 12 cohorts,” *European journal of preventive cardiology*, vol. 21, no. 6, pp. 719–726, 2014.
- [9] K. Fox, J. S. Borer, A. J. Camm, N. Danchin, R. Ferrari, J. L. L. Sendon, P. G. Steg, J.-C. Tardif, L. Tavazzi, M. Tendera *et al.*, “Resting heart rate in cardiovascular disease,” *Journal of the American College of Cardiology*, vol. 50, no. 9, pp. 823–830, 2007.
- [10] P. Palatini and S. Julius, “Elevated heart rate: a major risk factor for cardiovascular disease,” *Clinical and experimental hypertension*, vol. 26, no. 7-8, pp. 637–644, 2004.
- [11] C. Perret-Guillaume, L. Joly, and A. Benetos, “Heart rate as a risk factor for cardiovascular disease,” *Progress in cardiovascular diseases*, vol. 52, no. 1, pp. 6–10, 2009.
- [12] M. T. Cooney, E. Vartiainen, T. Laakitainen, A. Juolevi, A. Dudina, and I. M. Graham, “Elevated resting heart rate is an independent risk factor for cardiovascular disease in healthy men and women,” *American heart journal*, vol. 159, no. 4, pp. 612–619, 2010.
- [13] M. Böhm, J.-C. Reil, P. Deedwania, J. B. Kim, and J. S. Borer, “Resting heart rate: risk indicator and emerging risk factor in cardiovascular disease,” *The American journal of medicine*, vol. 128, no. 3, pp. 219–228, 2015.
- [14] S. Akselrod, D. Gordon, J. B. Madwed, N. C. Snidman, D. C. Shannon, and R. J. Cohen, “Hemodynamic regulation: investigation by spectral analysis,” *American Journal of Physiology-Heart and Circulatory Physiology*, vol. 249, no. 4, pp. H867–H875, 1985.
- [15] J. F. Thayer, S. S. Yamamoto, and J. F. Brosschot, “The relationship of autonomic imbalance, heart rate variability and cardiovascular disease risk factors,” *International journal of cardiology*, vol. 141, no. 2, pp. 122–131, 2010.
- [16] A. Haensel, P. J. Mills, R. A. Nelesen, M. G. Ziegler, and J. E. Dimsdale, “The relationship between heart rate variability and inflammatory markers in cardiovascular diseases,” *Psychoneuroendocrinology*, vol. 33, no. 10, pp. 1305–1312, 2008.
- [17] M. Wolf, G. Varigos, D. Hunt, and J. Sloman, “Sinus arrhythmia in acute myocardial infarction,” *Medical Journal of Australia*, vol. 2, no. 2, pp. 52–53, 1978.

- [18] M. T. La Rovere, J. T. Bigger Jr, F. I. Marcus, A. Mortara, P. J. Schwartz, A. A. Tone, R. A. M. I. Investigators *et al.*, “Baroreflex sensitivity and heart-rate variability in prediction of total cardiac mortality after myocardial infarction,” *The Lancet*, vol. 351, no. 9101, pp. 478–484, 1998.
- [19] J. T. Bigger Jr, J. L. Fleiss, R. C. Steinman, L. M. Rolnitzky, R. E. Kleiger, and J. N. Rottman, “Frequency domain measures of heart period variability and mortality after myocardial infarction,” *Circulation*, vol. 85, no. 1, pp. 164–171, 1992.
- [20] S. Hillebrand, K. B. Gast, R. de Mutsert, C. A. Swenne, J. W. Jukema, S. Middeldorp, F. R. Rosendaal, and O. M. Dekkers, “Heart rate variability and first cardiovascular event in populations without known cardiovascular disease: meta-analysis and dose-response meta-regression,” *Europace*, vol. 15, no. 5, pp. 742–749, 2013.
- [21] S. MacMahon, R. Peto, R. Collins, J. Godwin, J. Cutler, P. Sorlie, R. Abbott, J. Neaton, A. Dyer, and J. Stamler, “Blood pressure, stroke, and coronary heart disease: part 1, prolonged differences in blood pressure: prospective observational studies corrected for the regression dilution bias,” *The Lancet*, vol. 335, no. 8692, pp. 765–774, 1990.
- [22] P. K. Whelton, “Epidemiology of hypertension,” *Lancet (London, England)*, vol. 344, no. 8915, pp. 101–106, 1994.
- [23] N. H. Flebach, P. R. Hebert, M. J. Stampfer, G. A. COLDITZ, W. C. Willett, B. Rosner, F. E. Spelzer, and C. H. Hennekens, “A prospective study of high blood pressure and cardiovascular disease in women,” *American journal of epidemiology*, vol. 130, no. 4, pp. 646–654, 1989.
- [24] H. R. Black *et al.*, “The paradigm has shifted, to systolic blood pressure,” *Hypertension*, vol. 34, no. 3, pp. 386–7, 1999.
- [25] W. B. Kannel, T. Gordon, and M. J. Schwartz, “Systolic versus diastolic blood pressure and risk of coronary heart disease: the Framingham study,” *The American journal of cardiology*, vol. 27, no. 4, pp. 335–346, 1971.
- [26] W. B. Kannel, “Elevated systolic blood pressure as a cardiovascular risk factor,” 2000.
- [27] S. E. Kjeldsen, “Hypertension and cardiovascular risk: General aspects,” *Pharmacological research*, vol. 129, pp. 95–99, 2018.
- [28] “British Heart Foundation - Your Heart Rate.” [Online]. Available: <https://www.bhf.org.uk/informationsupport/how-a-healthy-heart-works/your-heart-rate>
- [29] J. Achten and A. E. Jeukendrup, “Heart rate monitoring,” *Sports medicine*, vol. 33, no. 7, pp. 517–538, 2003.
- [30] U. R. Acharya, K. P. Joseph, N. Kannathal, C. M. Lim, and J. S. Suri, “Heart rate variability: a review,” *Medical and biological engineering and computing*, vol. 44, no. 12, pp. 1031–1051, 2006.
- [31] A. J. Camm, M. Malik, J. T. Bigger, G. Breithardt, S. Cerutti, R. J. Cohen, P. Coumel, E. L. Fallen, H. L. Kennedy, R. Kleiger *et al.*, “Heart rate variability: standards of measurement, physiological interpretation and clinical use. Task Force of the European Society of Cardiology and the North American Society of Pacing and Electrophysiology,” 1996.
- [32] F. Shaffer and J. Ginsberg, “An overview of heart rate variability metrics and norms,” *Frontiers in public health*, vol. 5, p. 258, 2017.
- [33] F. Shaffer, R. McCraty, and C. L. Zerr, “A healthy heart is not a metronome: an integrative review of the heart’s anatomy and heart rate variability,” *Frontiers in psychology*, vol. 5, p. 1040, 2014.
- [34] M. Hadase, A. Azuma, K. Zen, S. Asada, T. Kawasaki, T. Kamitani, S. Kawasaki, H. Sugihara, and H. Matsubara, “Very low frequency power of heart rate variability is a powerful predictor of clinical prognosis in patients with congestive heart failure,” *Circulation Journal*, vol. 68, no. 4, pp. 343–347, 2004.

- [35] B. Pomeranz, R. Macaulay, M. A. Caudill, I. Kutz, D. Adam, D. Gordon, K. M. Kilborn, A. C. Barger, D. C. Shannon, and R. J. Cohen, "Assessment of autonomic function in humans by heart rate spectral analysis," *American Journal of Physiology-Heart and Circulatory Physiology*, vol. 248, no. 1, pp. H151–H153, 1985.
- [36] D. E. Becker, "Fundamentals of electrocardiography interpretation," *Anesthesia progress*, vol. 53, no. 2, pp. 53–64, 2006.
- [37] W. F. Ganong, *Review of medical physiology*. Mcgraw-hill, 1995.
- [38] J. Allen, "Photoplethysmography and its application in clinical physiological measurement," *Physiological measurement*, vol. 28, no. 3, p. R1, 2007.
- [39] M. Elgendi, "On the analysis of fingertip photoplethysmogram signals," *Current cardiology reviews*, vol. 8, no. 1, pp. 14–25, 2012.
- [40] T. Tamura, Y. Maeda, M. Sekine, and M. Yoshida, "Wearable photoplethysmographic sensors past and present," *Electronics*, vol. 3, no. 2, pp. 282–302, 2014.
- [41] J. Dyro, *Clinical engineering handbook*. Elsevier, 2004.
- [42] A. Leatham, *Auscultation of the Heart and Phonocardiography*. Churchill Livingstone, 1975.
- [43] S. Leng, R. San Tan, K. T. C. Chai, C. Wang, D. Ghista, and L. Zhong, "The electronic stethoscope," *Biomedical engineering online*, vol. 14, no. 1, p. 66, 2015.
- [44] A. K. Dwivedi, S. A. Imtiaz, and E. Rodriguez-Villegas, "Algorithms for Automatic Analysis and Classification of Heart Sounds—A Systematic Review," *IEEE Access*, vol. 7, pp. 8316–8345, 2018.
- [45] P. Sharma, S. A. Imtiaz, and E. Rodriguez-Villegas, "An algorithm for heart rate extraction from acoustic recordings at the neck," *IEEE Transactions on Biomedical Engineering*, vol. 66, no. 1, pp. 246–256, 2018.
- [46] D. Deuchar, "Ballistocardiography," *British heart journal*, vol. 29, no. 3, p. 285, 1967.
- [47] O. T. Inan, P.-F. Migeotte, K.-S. Park, M. Etemadi, K. Tavakolian, R. Casanella, J. Zanetti, J. Tank, I. Funtova, G. K. Prisk *et al.*, "Ballistocardiography and seismocardiography: A review of recent advances," *IEEE journal of biomedical and health informatics*, vol. 19, no. 4, pp. 1414–1427, 2014.
- [48] M. Nosrati and N. Tavassolian, "High-accuracy heart rate variability monitoring using Doppler radar based on Gaussian pulse train modeling and FTPR algorithm," *IEEE Transactions on Microwave Theory and Techniques*, vol. 66, no. 1, pp. 556–567, 2017.
- [49] F.-K. Wang, M.-C. Tang, S.-C. Su, and T.-S. Horng, "Wrist pulse rate monitor using self-injection-locked radar technology," *Biosensors*, vol. 6, no. 4, p. 54, 2016.
- [50] C. Li, V. M. Lubecke, O. Boric-Lubecke, and J. Lin, "A review on recent advances in Doppler radar sensors for noncontact healthcare monitoring," *IEEE Transactions on microwave theory and techniques*, vol. 61, no. 5, pp. 2046–2060, 2013.
- [51] S. W. Kim, S. B. Choi, Y.-J. An, B.-H. Kim, D. W. Kim, and J.-G. Yook, "Heart rate detection during sleep using a flexible RF resonator and injection-locked PLL sensor," *IEEE Transactions on Biomedical Engineering*, vol. 62, no. 11, pp. 2568–2575, 2015.
- [52] Y.-J. An, B.-H. Kim, G.-H. Yun, S.-W. Kim, S.-B. Hong, and J.-G. Yook, "Flexible non-constrained RF wrist pulse detection sensor based on array resonators," *IEEE transactions on biomedical circuits and systems*, vol. 10, no. 2, pp. 300–308, 2015.
- [53] R. M. Laukkanen and P. K. Virtanen, "Heart rate monitors: state of the art," *Journal of sports sciences*, vol. 16, no. sup1, pp. 3–7, 1998.

- [54] S. R. Pasadyn, M. Soudan, M. Gillinov, P. Houghtaling, D. Phelan, N. Gillinov, B. Bittel, and M. Y. Desai, "Accuracy of commercially available heart rate monitors in athletes: a prospective study," *Cardiovascular diagnosis and therapy*, vol. 9, no. 4, p. 379, 2019.
- [55] M. Etiwy, Z. Akhrass, L. Gillinov, A. Alashi, R. Wang, G. Blackburn, S. M. Gillinov, D. Phelan, A. M. Gillinov, P. L. Houghtaling *et al.*, "Accuracy of wearable heart rate monitors in cardiac rehabilitation," *Cardiovascular Diagnosis and Therapy*, 2019.
- [56] J. Hwang, J. Kim, K.-J. Choi, M. S. Cho, G.-B. Nam, and Y.-H. Kim, "Assessing accuracy of wrist-worn wearable devices in measurement of paroxysmal supraventricular tachycardia heart rate," *Korean circulation journal*, vol. 49, no. 5, pp. 437–445, 2019.
- [57] A. M. Müller, N. X. Wang, J. Yao, C. S. Tan, I. C. C. Low, N. Lim, J. Tan, A. Tan, and F. Müller-Riemenschneider, "Heart rate measures from wrist-worn activity trackers in a laboratory and free-living setting: Validation study," *JMIR mHealth and uHealth*, vol. 7, no. 10, p. e14120, 2019.
- [58] B. Sañudo, M. De Hoyo, A. Muñoz-López, J. Perry, and G. Abt, "Pilot Study Assessing the Influence of Skin Type on the Heart Rate Measurements Obtained by Photoplethysmography with the Apple Watch," *Journal of medical systems*, vol. 43, no. 7, p. 195, 2019.
- [59] B. W. Nelson and N. B. Allen, "Accuracy of Consumer Wearable Heart Rate Measurement During an Ecologically Valid 24-Hour Period: Intraindividual Validation Study," *JMIR mHealth and uHealth*, vol. 7, no. 3, p. e10828, 2019.
- [60] Y. Bai, P. Hibbing, C. Mantis, and G. J. Welk, "Comparative evaluation of heart rate-based monitors: Apple Watch vs Fitbit Charge HR," *Journal of sports sciences*, vol. 36, no. 15, pp. 1734–1741, 2018.
- [61] J. A. BUNN, J. W. Navalta, C. J. Fountaine, and J. D. REECE, "Current state of commercial wearable technology in physical activity monitoring 2015–2017," *International journal of exercise science*, vol. 11, no. 7, p. 503, 2018.
- [62] J. Xie, D. Wen, L. Liang, Y. Jia, L. Gao, and J. Lei, "Evaluating the validity of current mainstream wearable devices in fitness tracking under various physical activities: comparative study," *JMIR mHealth and uHealth*, vol. 6, no. 4, p. e94, 2018.
- [63] A. N. Koshy, J. K. Sajeev, N. Nerlekar, A. J. Brown, K. Rajakariar, M. Zureik, M. C. Wong, L. Roberts, M. Street, J. Cooke *et al.*, "Smart watches for heart rate assessment in atrial arrhythmias," *International journal of cardiology*, vol. 266, pp. 124–127, 2018.
- [64] J. Liang, D. Xian, X. Liu, J. Fu, X. Zhang, B. Tang, and J. Lei, "Usability study of mainstream wearable fitness devices: feature analysis and system usability scale evaluation," *JMIR mHealth and uHealth*, vol. 6, no. 11, p. e11066, 2018.
- [65] A. Henriksen, M. H. Mikalsen, A. Z. Woldaregay, M. Muzny, G. Hartvigsen, L. A. Hopstock, and S. Grimsgaard, "Using fitness trackers and smartwatches to measure physical activity in research: analysis of consumer wrist-worn wearables," *Journal of medical Internet research*, vol. 20, no. 3, p. e110, 2018.
- [66] D. Hernando, S. Roca, J. Sancho, Á. Alesanco, and R. Bailón, "Validation of the Apple watch for heart rate variability measurements during relax and mental stress in healthy subjects," *Sensors*, vol. 18, no. 8, p. 2619, 2018.
- [67] B. D. Boudreaux, E. P. Hebert, D. B. Hollander, B. M. Williams, C. L. Cormier, M. R. Naquin, W. W. Gillan, E. E. Gusew, and R. R. Kraemer, "Validity of Wearable Activity Monitors during Cycling and Resistance Exercise." *Medicine and science in sports and exercise*, vol. 50, no. 3, pp. 624–633, 2018.



- [68] A. Shcherbina, C. M. Mattsson, D. Waggott, H. Salisbury, J. W. Christle, T. Hastie, M. T. Wheeler, and E. A. Ashley, "Accuracy in wrist-worn, sensor-based measurements of heart rate and energy expenditure in a diverse cohort," *Journal of personalized medicine*, vol. 7, no. 2, p. 3, 2017.
- [69] S. Gillinov, M. Etiwy, R. Wang, G. Blackburn, D. Phelan, A. M. Gillinov, P. Houghtaling, H. Javadikasgari, and M. Y. Desai, "Variable Accuracy of Wearable Heart Rate Monitors during Aerobic Exercise." *Medicine and science in sports and exercise*, vol. 49, no. 8, pp. 1697–1703, 2017.
- [70] M. P. Wallen, S. R. Gomersall, S. E. Keating, U. Wisløff, and J. S. Coombes, "Accuracy of heart rate watches: implications for weight management," *PloS one*, vol. 11, no. 5, p. e0154420, 2016.
- [71] R. Wang, G. Blackburn, M. Desai, D. Phelan, L. Gillinov, P. Houghtaling, and M. Gillinov, "Accuracy of wrist-worn heart rate monitors," *Jama cardiology*, vol. 2, no. 1, pp. 104–106, 2017.
- [72] F. El-Amrawy and M. I. Nounou, "Are currently available wearable devices for activity tracking and heart rate monitoring accurate, precise, and medically beneficial?" *Healthcare informatics research*, vol. 21, no. 4, pp. 315–320, 2015.
- [73] "Apple Watch ECG App FDA Approval," 2018. [Online]. Available: [https://www.accessdata.fda.gov/cdrh\\_docs/pdf18/DEN180044.pdf](https://www.accessdata.fda.gov/cdrh_docs/pdf18/DEN180044.pdf)
- [74] S. Haghayegh, S. Khoshnevis, M. H. Smolensky, and K. R. Diller, "Accuracy of PurePulse photoplethysmography technology of Fitbit Charge 2 for assessment of heart rate during sleep," *Chronobiology international*, pp. 1–7, 2019.
- [75] E. A. Thomson, K. Nuss, A. Comstock, S. Reinwald, S. Blake, R. E. Pimentel, B. L. Tracy, and K. Li, "Heart rate measures from the Apple Watch, Fitbit Charge HR 2, and electrocardiogram across different exercise intensities," *Journal of sports sciences*, vol. 37, no. 12, pp. 1411–1419, 2019.
- [76] G. Nazari, J. C. MacDermid, K. E. Sinden, J. Richardson, and A. Tang, "Reliability of Zephyr Bioharness and Fitbit Charge Measures of Heart Rate and Activity at Rest, During the Modified Canadian Aerobic Fitness Test, and Recovery," *The Journal of Strength & Conditioning Research*, vol. 33, no. 2, pp. 559–571, 2019.
- [77] L. M. Feehan, J. Geldman, E. C. Sayre, C. Park, A. M. Ezzat, J. Y. Yoo, C. B. Hamilton, and L. C. Li, "Accuracy of Fitbit devices: systematic review and narrative syntheses of quantitative data," *JMIR mHealth and uHealth*, vol. 6, no. 8, p. e10527, 2018.
- [78] S. Benedetto, C. Caldato, E. Bazzan, D. C. Greenwood, V. Pensabene, and P. Actis, "Assessment of the Fitbit Charge 2 for monitoring heart rate," *PLoS One*, vol. 13, no. 2, p. e0192691, 2018.
- [79] L. Cadmus-Bertram, R. Gangnon, E. J. Wirkus, K. M. Thraen-Borowski, and J. Gorzelitz-Liebhauser, "The accuracy of heart rate monitoring by some wrist-worn activity trackers," *Annals of internal medicine*, vol. 166, no. 8, p. 610, 2017.
- [80] D. T. Weiler, S. O. Villajuan, L. Edkins, S. Cleary, and J. J. Saleem, "Wearable heart rate monitor technology accuracy in research: A comparative study between PPG and ECG technology," in *Proceedings of the Human Factors and Ergonomics Society Annual Meeting*, vol. 61, no. 1. SAGE Publications Sage CA: Los Angeles, CA, 2017, pp. 1292–1296.
- [81] K. Kaewkannate and S. Kim, "A comparison of wearable fitness devices," *BMC public health*, vol. 16, no. 1, p. 433, 2016.
- [82] S. E. Stahl, H.-S. An, D. M. Dinkel, J. M. Noble, and J.-M. Lee, "How accurate are the wrist-based heart rate monitors during walking and running activities? Are they accurate enough?" *BMJ open sport & exercise medicine*, vol. 2, no. 1, p. e000106, 2016.
- [83] E. Jo, K. Lewis, D. Directo, M. J. Kim, and B. A. Dolezal, "Validation of biofeedback wearables for photoplethysmographic heart rate tracking," *Journal of sports science & medicine*, vol. 15, no. 3, p. 540, 2016.

- [84] M. P. Støve, E. Haucke, M. L. Nymann, T. Sigurdsson, and B. T. Larsen, “Accuracy of the wearable activity tracker Garmin Forerunner 235 for the assessment of heart rate during rest and activity,” *Journal of sports sciences*, vol. 37, no. 8, pp. 895–901, 2019.
- [85] J. BUNN, E. WELLS, J. MANOR, and M. WEBSTER, “Evaluation of Earbud and Wristwatch Heart Rate Monitors during Aerobic and Resistance Training,” *International journal of exercise science*, vol. 12, no. 4, p. 374, 2019.
- [86] D. K. Spierer, Z. Rosen, L. L. Litman, and K. Fujii, “Validation of photoplethysmography as a method to detect heart rate during rest and exercise,” *Journal of medical engineering & technology*, vol. 39, no. 5, pp. 264–271, 2015.
- [87] J. Parak and I. Korhonen, “Evaluation of wearable consumer heart rate monitors based on photoplethysmography,” in *2014 36th Annual International Conference of the IEEE Engineering in Medicine and Biology Society*. IEEE, 2014, pp. 3670–3673.
- [88] J. Montes and J. W. Navalta, “Reliability of the Polar T31 Uncoded Heart Rate Monitor in Free Motion and Treadmill Activities,” *International journal of exercise science*, vol. 12, no. 4, p. 69, 2019.
- [89] I. T. Hettiarachchi, S. Hanoun, D. Nahavandi, and S. Nahavandi, “Validation of Polar OH1 optical heart rate sensor for moderate and high intensity physical activities,” *PloS one*, vol. 14, no. 5, p. e0217288, 2019.
- [90] R. T. Li, S. R. Kling, M. J. Salata, S. A. Cupp, J. Sheehan, and J. E. Voos, “Wearable performance devices in sports medicine,” *Sports health*, vol. 8, no. 1, pp. 74–78, 2016.
- [91] G. Nazari, P. Bobos, J. C. MacDermid, K. E. Sinden, J. Richardson, and A. Tang, “Psychometric properties of the Zephyr bioharness device: a systematic review,” *BMC Sports Science, Medicine and Rehabilitation*, vol. 10, no. 1, p. 6, 2018.
- [92] B. A. Dolezal, D. Boland, J. Carney, M. Abrazado, D. Smith, and C. Cooper, “Validation of heart rate derived from a physiological status monitor-embedded compression shirt against criterion ECG,” *Journal of occupational and environmental hygiene*, vol. 11, no. 12, pp. 833–839, 2014.
- [93] J. Montes, J. C. Young, R. TANDY, and J. W. Navalta, “Reliability and Validation of the Hexoskin Wearable Bio-Collection Device During Walking Conditions,” *International journal of exercise science*, vol. 11, no. 7, p. 806, 2018.
- [94] R. Delgado-Gonzalo, J. Parak, A. Tarniceriu, P. Renevey, M. Bertschi, and I. Korhonen, “Evaluation of accuracy and reliability of PulseOn optical heart rate monitoring device,” in *2015 37th Annual International Conference of the IEEE Engineering in Medicine and Biology Society (EMBC)*. IEEE, 2015, pp. 430–433.
- [95] J. Parak, A. Tarniceriu, P. Renevey, M. Bertschi, R. Delgado-Gonzalo, and I. Korhonen, “Evaluation of the beat-to-beat detection accuracy of PulseOn wearable optical heart rate monitor,” in *2015 37th Annual International Conference of the IEEE Engineering in Medicine and Biology Society (EMBC)*. IEEE, 2015, pp. 8099–8102.
- [96] S. Passler, N. Müller, and V. Senner, “In-Ear Pulse Rate Measurement: A Valid Alternative to Heart Rate Derived from Electrocardiography?” *Sensors*, vol. 19, no. 17, p. 3641, 2019.
- [97] E. Jortberg, I. Silva, V. Bhatkar, R. S. McGinnis, E. Sen-Gupta, B. Morey, J. A. Wright Jr, J. Pindado, and M. T. Bianchi, “A novel adhesive biosensor system for detecting respiration, cardiac, and limb movement signals during sleep: validation with polysomnography,” *Nature and science of sleep*, vol. 10, p. 397, 2018.
- [98] A. A. Akintola, V. van de Pol, D. Bimmel, A. C. Maan, and D. van Heemst, “Comparative analysis of the Equivital EQ02 lifemonitor with holter ambulatory ECG device for continuous measurement

- of ECG, heart rate, and heart rate variability: A validation study for precision and accuracy,” *Frontiers in physiology*, vol. 7, p. 391, 2016.
- [99] K. Georgiou, A. V. Larentzakis, N. N. Khamis, G. I. Alsuhaibani, Y. A. Alaska, and E. J. Giallafos, “Can wearable devices accurately measure heart rate variability? A systematic review,” *Folia medica*, vol. 60, no. 1, pp. 7–20, 2018.
  - [100] “Holter Monitor - Mayo Clinic.” [Online]. Available: <https://www.mayoclinic.org/tests-procedures/holter-monitor/about/pac-20385039>
  - [101] P. Muntner, D. Shimbo, R. M. Carey, J. B. Charleston, T. Gaillard, S. Misra, M. G. Myers, G. Ogedegbe, J. E. Schwartz, R. R. Townsend *et al.*, “Measurement of blood pressure in humans: a scientific statement from the American Heart Association,” *Hypertension*, vol. 73, no. 5, pp. e35–e66, 2019.
  - [102] L. A. Geddes, *Handbook of blood pressure measurement*. Springer Science & Business Media, 2013.
  - [103] J. A. Potkay, “Long term, implantable blood pressure monitoring systems,” *Biomedical microdevices*, vol. 10, no. 3, pp. 379–392, 2008.
  - [104] N. Korotkoff, “On methods of studying blood pressure,” *Izv. Venno-Med. Akad.*, vol. 11, p. 365, 1905.
  - [105] E. H. Goodman and A. A. Howell, “Further clinical studies in the auscultatory method of determining blood pressure. 1,” *The American Journal of the Medical Sciences (1827-1924)*, vol. 142, no. 3, p. 334, 1911.
  - [106] J. Allen, T. Gehrke, J. J. O’Sullivan, S. T. King, and A. Murray, “Characterization of the Korotkoff sounds using joint time–frequency analysis,” *Physiological measurement*, vol. 25, no. 1, p. 107, 2003.
  - [107] T. G. Pickering, J. E. Hall, L. J. Appel, B. E. Falkner, J. Graves, M. N. Hill, D. W. Jones, T. Kurtz, S. G. Sheps, and E. J. Roccella, “Recommendations for blood pressure measurement in humans and experimental animals: part 1: blood pressure measurement in humans: a statement for professionals from the Subcommittee of Professional and Public Education of the American Heart Association Council on High Blood Pressure Research,” *Hypertension*, vol. 45, no. 1, pp. 142–161, 2005.
  - [108] G. Ogedegbe and T. Pickering, “Principles and techniques of blood pressure measurement,” *Cardiology clinics*, vol. 28, no. 4, pp. 571–586, 2010.
  - [109] P. Padfield, S. Jyothinagaram, D. Watson, P. Donald, and I. McGinley, “Problems in the measurement of blood pressure,” *Journal of human hypertension*, vol. 4, pp. 3–7, 1990.
  - [110] G. Mauck, C. Smith, L. Geddes, and J. Bourland, “The meaning of the point of maximum oscillations in cuff pressure in the indirect measurement of blood pressure,” 1980.
  - [111] J. Liu, J.-O. Hahn, and R. Mukkamala, “Error mechanisms of the oscillometric fixed-ratio blood pressure measurement method,” *Annals of biomedical engineering*, vol. 41, no. 3, pp. 587–597, 2013.
  - [112] M. Forouzanfar, H. R. Dajani, V. Z. Groza, M. Bolic, S. Rajan, and I. Batkin, “Oscillometric blood pressure estimation: past, present, and future,” *IEEE reviews in biomedical engineering*, vol. 8, pp. 44–63, 2015.
  - [113] S. Lee, M. Bolic, V. Z. Groza, H. R. Dajani, and S. Rajan, “Confidence interval estimation for oscillometric blood pressure measurements using bootstrap approaches,” *IEEE Transactions on Instrumentation and Measurement*, vol. 60, no. 10, pp. 3405–3415, 2011.
  - [114] G. Drzewiecki and J. Bronzino, “Noninvasive arterial blood pressure and mechanics,” *The Biomedical Engineering Handbook*, vol. 1, pp. 1–16, 2000.
  - [115] G. Drzewiecki, R. Hood, and H. Apple, “Theory of the oscillometric maximum and the systolic and diastolic detection ratios,” *Annals of biomedical engineering*, vol. 22, no. 1, pp. 88–96, 1994.

- [116] P. D. Baker, J. A. Orr, D. R. Westenskow, and T. P. Egbert, "Method for determining blood pressure utilizing a neural network," Aug. 23 1994, uS Patent 5,339,818.
- [117] M. Forouzanfar, H. R. Dajani, V. Z. Groza, M. Bolic, and S. Rajan, "Feature-based neural network approach for oscillometric blood pressure estimation," *IEEE transactions on instrumentation and measurement*, vol. 60, no. 8, pp. 2786–2796, 2011.
- [118] S. Lee and J.-H. Chang, "Oscillometric blood pressure estimation based on deep learning," *IEEE Transactions on Industrial Informatics*, vol. 13, no. 2, pp. 461–472, 2016.
- [119] P. Palatini, D. Longo, G. Toffanin, O. Bertolo, V. Zaetta, and A. C. Pessina, "Wrist blood pressure overestimates blood pressure measured at the upper arm," *Blood pressure monitoring*, vol. 9, no. 2, pp. 77–81, 2004.
- [120] S. Forsberg, M. de Guzman, and S. Berling, "Validity of blood pressure measurement with cuff in the arm and forearm," *Acta Medica Scandinavica*, vol. 188, no. 1-6, pp. 389–396, 1970.
- [121] A. Elseed, E. Shinebourne, and M. Joseph, "Assessment of techniques for measurement of blood pressure in infants and children." *Archives of Disease in Childhood*, vol. 48, no. 12, p. 932, 1973.
- [122] K. Ameloot, P.-J. Palmers, and M. L. Malbrain, "The accuracy of noninvasive cardiac output and pressure measurements with finger cuff: a concise review," *Current opinion in critical care*, vol. 21, no. 3, pp. 232–239, 2015.
- [123] K. Wesseling, B. De Wit, J. Settels, and W. Klawer, "On the indirect registration of finger blood pressure after penaz," *Funktl Biol Med*, vol. 1, pp. 245–250, 1982.
- [124] M. Maxwell, P. Schroth, A. Waks, M. Karam, and L. Dornfeld, "Error in blood-pressure measurement due to incorrect cuff size in obese patients," *The Lancet*, vol. 320, no. 8288, pp. 33–36, 1982.
- [125] R. P. Smith, J. Argod, J.-L. Pépin, and P. A. Lévy, "Pulse transit time: an appraisal of potential clinical applications," *Thorax*, vol. 54, no. 5, pp. 452–457, 1999.
- [126] S. Ahmad, S. Chen, K. Soueidan, I. Batkin, M. Bolic, H. Dajani, and V. Groza, "Electrocardiogram-assisted blood pressure estimation," *IEEE Transactions on Biomedical Engineering*, vol. 59, no. 3, pp. 608–618, 2012.
- [127] C. Poon and Y. Zhang, "Cuff-less and noninvasive measurements of arterial blood pressure by pulse transit time," in *2005 IEEE engineering in medicine and biology 27th annual conference*. IEEE, 2006, pp. 5877–5880.
- [128] F. S. Cattivelli and H. Garudadri, "Noninvasive cuffless estimation of blood pressure from pulse arrival time and heart rate with adaptive calibration," in *2009 Sixth international workshop on wearable and implantable body sensor networks*. IEEE, 2009, pp. 114–119.
- [129] R. T. Netea, P. Smits, J. W. Lenders, and T. Thien, "Does it matter whether blood pressure measurements are taken with subjects sitting or supine?" *Journal of hypertension*, vol. 16, no. 3, pp. 263–268, 1998.
- [130] P. L. Mitchell, R. W. Parlin, and H. Blackburn, "Effect of vertical displacement of the arm on indirect blood-pressure measurement," *New England Journal of Medicine*, vol. 271, no. 2, pp. 72–74, 1964.
- [131] L. Smith, "New AHA recommendations for blood pressure measurement," 2005.
- [132] G. Parati, G. Pomidossi, R. Casadei, and G. Mancia, "Lack of alerting reactions to intermittent cuff inflations during noninvasive blood pressure monitoring." *Hypertension*, vol. 7, no. 4, pp. 597–601, 1985.
- [133] C. Moore, A. Dobson, M. Kinagi, and B. Dillon, "Comparison of blood pressure measured at the arm, ankle and calf," *Anaesthesia*, vol. 63, no. 12, pp. 1327–1331, 2008.

- [134] E. O'Brien, J. Petrie, W. Littler, M. de Swiet, P. L. Padfield, D. Altman, M. Bland, A. Coats, N. Atkins *et al.*, "The British Hypertension Society protocol for the evaluation of blood pressure measuring devices," *J hypertens*, vol. 11, no. Suppl 2, pp. S43–S62, 1993.
- [135] E. O'Brien, N. Atkins, G. Stergiou, N. Karpettas, G. Parati, R. Asmar, Y. Imai, J. Wang, T. Mengden, A. Shennan *et al.*, "European Society of Hypertension International Protocol revision 2010 for the validation of blood pressure measuring devices in adults," *Blood pressure monitoring*, vol. 15, no. 1, pp. 23–38, 2010.
- [136] A. for the Advancement of Medical Instrumentation *et al.*, "Non-invasive sphygmomanometers—part 2: clinical investigation of automated measurement type ANSI/AAMI," ISO 81060-2/ANSI-AAMI, 2nd ed. Arlington, VA: AAMI, Tech. Rep., 2013.
- [137] B. Beime, R. Krüger, G. Hammel, P. Bramlage, and C. Deutsch, "Validation of the Microlife BP A3 PC upper arm blood pressure monitor in patients with diabetes mellitus according to the ANSI/AAMI/ISO 81060-2: 2013 protocol," *Blood pressure monitoring*, vol. 23, no. 1, pp. 52–57, 2018.
- [138] P. Palatini, C. Fania, and F. Gasparotti, "Accuracy of the WatchBP office ABI device for office blood pressure measurement over a wide range of arm sizes," *Blood pressure monitoring*, vol. 23, no. 2, pp. 117–119, 2018.
- [139] J. F. Van Den Heuvel, A. T. Lely, A. Franx, and M. N. Bekker, "Validation of the iHealth Track and Omron HEM-9210T automated blood pressure devices for use in pregnancy," *Pregnancy hypertension*, vol. 15, pp. 37–41, 2019.
- [140] F. Grover-Páez, E. G. Cardona-Muñoz, D. Cardona-Müller, V. H. Guzmán-Saldívar, M. Rodríguez-De la Cerda, M. B. Jiménez-Cázares, S. E. Totsuka-Sutto, G. A. Alanis-Sánchez, and C. G. Ramos-Becerra, "Validation of the Omron HEM-7320-LA, upper arm blood pressure monitor with Intelli Wrap Technology Cuff HEM-FL1 for self-measurement and clinic use according to the European Society of Hypertension International Protocol revision 2010 in the Mexican population," *Blood pressure monitoring*, vol. 22, no. 6, p. 375, 2017.
- [141] M. Kuwabara, K. Harada, Y. Hishiki, and K. Kario, "Validation of a wrist-type home nocturnal blood pressure monitor in the sitting and supine position according to the ANSI/AAMI/ISO81060-2: 2013 guidelines: Omron HEM-9600T," *The Journal of Clinical Hypertension*, vol. 21, no. 4, pp. 463–469, 2019.
- [142] H. Takahashi, M. Yoshika, and T. Yokoi, "Validation of Omron RS8, RS6, and RS3 home blood pressure monitoring devices, in accordance with the European Society of Hypertension International Protocol revision 2010," *Vascular health and risk management*, vol. 9, p. 265, 2013.
- [143] A. Kollias, A. Ntineri, K. G. Kyriakoulis, E. Stambolliu, and G. S. Stergiou, "Validation of the iHealth ambulatory blood pressure monitor in adults according to the American National Standards Institute/Association for the Advancement of Medical Instrumentation/International Organization for Standardization standard," *Blood pressure monitoring*, vol. 23, no. 2, pp. 115–116, 2018.
- [144] J. Huang, Z. Li, G. Li, and Z. Liu, "Validation of the Andon KD-5965 upper-arm blood pressure monitor for home blood pressure monitoring according to the European Society of Hypertension International Protocol revision 2010," *Blood pressure monitoring*, vol. 20, no. 5, pp. 283–285, 2015.
- [145] Y.-Y. Kang, Q. Chen, C.-Y. Liu, Y. Li, and J.-G. Wang, "Validation of the AVITA BPM64 upper-arm blood pressure monitor for home blood pressure monitoring according to the European Society of Hypertension International Protocol revision 2010," *Blood pressure monitoring*, vol. 23, no. 1, pp. 45–48, 2018.
- [146] Y.-Y. Kang, W.-F. Zeng, L. Zhang, Y. Li, and J.-G. Wang, "Validation of the AVITA BPM15S wrist blood pressure monitor for home blood pressure monitoring according to the European Society

- of Hypertension International Protocol revision 2010,” *Blood pressure monitoring*, vol. 19, no. 3, pp. 183–186, 2014.
- [147] Y.-Y. Kang, Q. Chen, C.-Y. Liu, Y. Li, and J.-G. Wang, “Validation of the AVITA BPM17 wrist blood pressure monitor for home blood pressure monitoring according to the European Society of Hypertension International Protocol revision 2010,” *Blood pressure monitoring*, vol. 22, no. 4, pp. 230–233, 2017.
  - [148] Q. Chen, Y.-Y. Kang, Y. Li, and J.-G. Wang, “Validation of the BPUMP BF1112 upper-arm blood pressure monitor for home blood pressure monitoring according to the European Society of Hypertension International Protocol revision 2010,” *Blood pressure monitoring*, vol. 22, no. 2, pp. 105–108, 2017.
  - [149] Z.-Y. Liu, Q.-H. Zhang, X.-L. Ye, D.-P. Liu, K. Cheng, C.-H. Zhang, and Y. Wan, “Validation of the G. LAB MD2200 wrist blood pressure monitor according to the European Society of Hypertension, the British Hypertension Society, and the International Organization for Standardization Protocols,” *Blood pressure monitoring*, vol. 22, no. 2, pp. 101–104, 2017.
  - [150] Y. Jiao, Q. Guan, L. Wu, C. Wang, and L. Cao, “Validation of the G. LAB MD2231 digital automatic wrist blood pressure monitor according to multiple protocols,” *Blood pressure monitoring*, vol. 22, no. 4, pp. 226–229, 2017.
  - [151] C. Fania, L. Vezzù, I. Lazzaretto, and P. Palatini, “Validation of the Hingmed WBP-02A device for ambulatory blood pressure monitoring according to the European Society of Hypertension International Protocol revision 2010,” *Blood pressure monitoring*, vol. 24, no. 3, pp. 151–154, 2019.
  - [152] W. Zhang, L. Lei, Y. Li, and J.-G. Wang, “Validation of the HL868ED upper-arm blood pressure monitor for clinical use and self-measurement according to the European Society of Hypertension International Protocol revision 2010,” *Blood pressure monitoring*, 2019.
  - [153] H. Zhao, W. Qiao, R. Zhang, P. Cui, F. Hou, and W. Zhang, “Validation of the Pangao PG-800A36 automatic wrist blood pressure monitor according to the European Society of Hypertension and the British Hypertension Society protocols,” *Blood pressure monitoring*, vol. 23, no. 1, pp. 37–40, 2018.
  - [154] S. Bing, C. Zhang, L. Wang, L. Li, and Y. Wan, “Validation of the Pangao PG-800B11 blood pressure monitor according to the European Society of Hypertension and the British Hypertension Society protocols,” *Blood pressure monitoring*, vol. 19, no. 6, pp. 366–369, 2014.
  - [155] L. Chen, J. Li, J. Wen, C. Guo, J. Zhang, and Z. Yu, “Validation of the Pangao PG-800B26 upper arm blood pressure monitor in the general population according to the European Society of Hypertension and the British Hypertension Society protocols,” *Blood pressure monitoring*, vol. 23, no. 1, pp. 41–44, 2018.
  - [156] L. Zhang, Y.-Y. Kang, W.-F. Zeng, Y. Li, and J.-G. Wang, “Validation of the Rossmax CF175 upper-arm blood pressure monitor for home blood pressure monitoring according to the European Society of Hypertension International Protocol revision 2010,” *Blood pressure monitoring*, vol. 20, no. 2, pp. 104–107, 2015.
  - [157] L. Lei, Y. Chen, Q. Chen, Y. Li, and J.-G. Wang, “Validation of the SEJOY BP-1307 upper-arm blood pressure monitor for home blood pressure monitoring according to the European Society of Hypertension International Protocol revision 2010,” *Blood pressure monitoring*, vol. 22, no. 6, pp. 371–374, 2017.
  - [158] A. Kollias, E. Stambolliu, K. G. Kyriakoulis, S. S. Papadatos, and G. S. Stergiou, “Validation of the single-cuff oscillometric blood pressure monitor InBody BPBIO320 for public use according to the 2010 European Society of Hypertension International Protocol,” *Blood pressure monitoring*, vol. 24, no. 1, pp. 30–32, 2019.

- [159] B. S. Alpert, “Validation of the Welch Allyn Pro BP 2000, a professional-grade inflation-based automated sphygmomanometer with arrhythmia detection in a combined pediatric and adult population by ANSI/AAMI/ISO standard testing,” *Blood pressure monitoring*, vol. 23, no. 6, p. 315, 2018.
- [160] J.-F. Huang, W. Zhang, Y. Li, and J.-G. Wang, “Validation of the YuWell YE680B upper-arm blood pressure monitor in adults according to the ANSI/AAMI/ISO 81060-2: 2013 standard,” *Blood Pressure Monitoring*, vol. 24, no. 6, pp. 315–318, 2019.
- [161] Q. Chen, L. Lei, Y. Li, and J.-G. Wang, “Validation of the YuWell YE690A upper-arm blood pressure monitor, for clinic use and self-measurement, according to the European Society of Hypertension International Protocol revision 2010,” *Blood pressure monitoring*, vol. 22, no. 5, pp. 295–297, 2017.
- [162] K. Kario, K. Saito, K. Sato, H. Hamasaki, H. Suwa, A. Okura, and S. Hoshide, “Validation of the A&D BP UA-1200BLE device for home blood pressure measurement according to the ISO 81060-2: 2013 standard,” *Blood pressure monitoring*, vol. 23, no. 6, pp. 312–314, 2018.
- [163] M. Forouzanfar, S. Ahmad, I. Batkin, H. R. Dajani, V. Z. Groza, and M. Bolic, “Coefficient-free blood pressure estimation based on pulse transit time–cuff pressure dependence,” *IEEE Transactions on Biomedical Engineering*, vol. 60, no. 7, pp. 1814–1824, 2013.
- [164] J. Talts, R. Raamat, K. Jagomägi, and J. Kivastik, “An Influence of Multiple Affecting Factors on Characteristic Ratios of Oscillometric Blood Pressure Measurement,” in *15th Nordic-Baltic Conference on Biomedical Engineering and Medical Physics (NBC 2011)*, K. Dremstrup, S. Rees, and M. Ø. Jensen, Eds. Berlin, Heidelberg: Springer Berlin Heidelberg, 2011, pp. 73–76.

## 2 Wearable sensing of the pulse sounds at the wrist

### 2.1 Introduction

#### 2.1.1 The circulatory system

The circulatory system plays a vital role in healthy metabolism of tissue cells and organs in the human body. It acts as a transportation mechanism and is responsible for the exchange of nutrients, hormones and substances with the metabolic waste from the cells. This is carried out through a distribution network of blood, blood vessels and the heart. Simply put, the circulatory system is a network of tubes carrying fluid from the pumping source [1]. The circulatory system also plays an important role in regulating the body temperature, blood flow volume by communicating continuously between different regions of the body. This dynamic regulation as well as the supply mechanism is mainly performed by controlling the width of the blood vessels and the pumping force of the heart. A reduction in the blood vessel diameter, a state known as vasoconstriction, reduces the exposed surface area thereby reducing the rate of heat loss from the body [2]. The constriction of the blood vessels also reduces the blood flow to the peripheral regions of the body. A reverse phenomenon is observed for an increase in the blood vessel diameter, a state known as vasodilatation. The vasoconstriction and vasodilatation phases of blood flow in the arteries are primarily governed by the pumping action of the heart.

The human heart serves as a four-chambered pump and propels the blood through the circulatory system in periodic heart cycles. A heart cycle mainly consists of two phases: systole and diastole. Systole indicates the period of ventricular contraction to eject blood from the heart whereas diastole involves the refilling of blood by ventricular expansion to attain the relaxed position of the heart. In the systolic phase, the heart forces the blood to flow with high pressure throughout the arterial system. The blood flow in the arteries is preceded by a travelling pressure wave generated corresponding to periodic contraction and relaxation of the heart [2]. This association of the heart cycle with the pressure wave can be utilised to study the pulse phenomenon that provides a valuable indicator of the cardiac function at various locations of the body.



### 2.1.2 The pulse

Pulse reflects the state of health of an individual as it directly relates with the functioning of the heart and the arteries. In clinical medicine, pulse is treated as the fundamental sign of life and is studied as a physiological signal that propagates through the arterial system corresponding to systolic and diastolic phases of the cardiac cycle [3]. The contraction of heart in the systolic phase generates a pressure wave that exerts maximal pressure inside the arteries. The refilling of blood back into the heart during the diastolic phase restores the baseline pressure in the artery. These rhythmic pressure variations causes pulsations in the arterial system. The pulse in addition to the pressure wave also consist of flow wave which governs the actual flow of blood in the arteries [4]. Therefore, the propagation of pulse wave involves two stages: the contraction of heart causing the outward force (pressure wave) and the actual movement of blood in response to this force (flow wave). The following sections establish the significance of each wave in forming the pulse.

#### 2.1.2.1 Pressure wave

The human heart is divided into left and right parts. These parts are further divided into two sections each to form a total of four chambers. The upper chambers of the heart, known as the left and the right atrium, collects the blood from the circulatory system and forwards it to the lower chambers. The lower chambers, also known as the left and the right ventricle, ejects blood away from the heart by performing rhythmic contractions. Each chamber is also associated with “one-way” valve to regulate the blood flow in a particular direction and prevent the back flow of blood. The atrioventricular (AV) valves function as the gates between atria and ventricles whereas the semilunar (SL) valves interact with the aorta and pulmonary artery to complete the loop of blood flow. A complete cardiac cycle runs in a sequential cycle of ventricular systole and atrial systole; ventricular diastole and atrial diastole [5]. During the ventricular systole, a large amount of blood is dumped into the left and right atrium. Due to the closure of the AV valves, the accumulation of blood inside the atrium builds up a pressure to a certain level at which the pressure on atrium side becomes higher than the ventricle side. At this point, the cardiac cycle enters the phase of ventricular diastole where the differential pressure forces the AV valves to open and allow the blood flow into the ventricles. The rising levels of blood in the ventricles after the closure of the AV valves initiates the process of ventricular contraction to cause an abrupt rise in the pressure profile as shown in Fig. 2.1. This rise in the pressure level is also known as the period of isovolumic contraction, and is caused by an increment in the muscle tension [6]. When the pressure inside the ventricle becomes higher in comparison to the baseline pressure of aorta (around 80 mmHg), the SL (or aortic) valves are opened to allow a rapid ejection of blood through the aorta. The ejection of blood is preceded by the actual force generated by the ventricular contractions, also referred to as the pressure wave. The pressure wave propagates through the arterial

system and creates a differential pressure to allow the flow of blood from higher pressure in the heart to the lower pressure in the arteries. During the ventricular systole, the arterial walls sustain maximal pressure (around 120 mmHg) from the travelling pressure wave. These continuous cycles of rise and fall in ventricular pressure as shown in Fig. 2.1 produces volumetric cycles of blood flow causing constriction and dilation (or pulsation) of the arteries.

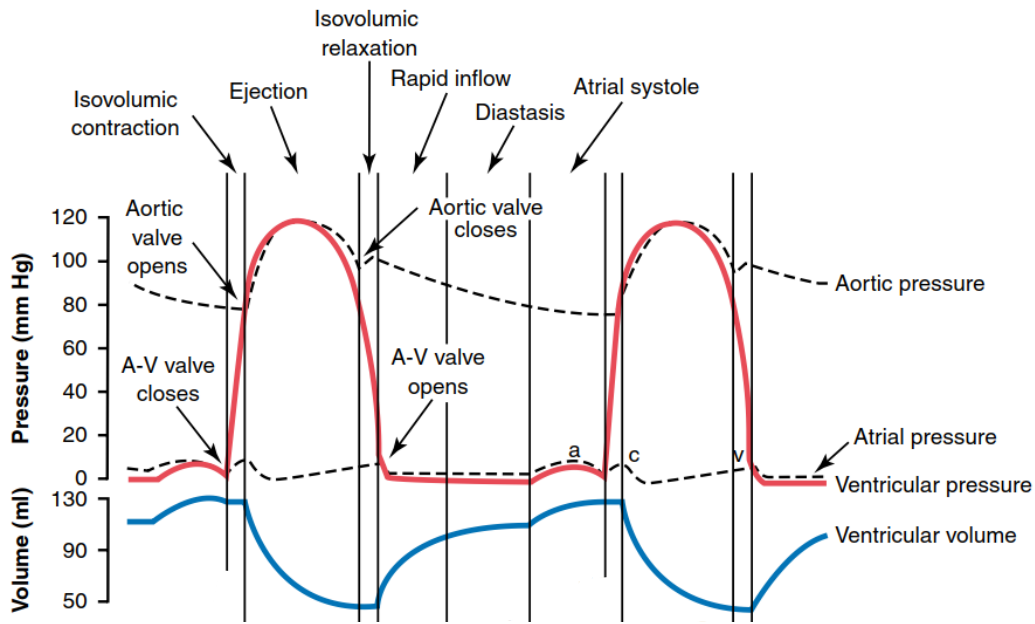


**Figure 2.1:** Cardiac cycle events with variation in atrial, ventricular and aortic pressure [6].

The pressure wave generated from the heart movements propagate as a forward travelling wave. Since an incoming wave is partly transmitted and partly reflected because of the material properties, the pressure wave also undergo a wave reflection phenomenon [4]. The reflected wave can be understood as an echo of the incoming pressure wave travelling from heart to the peripheral arteries. The narrowing of the arteries in the peripheral regions increases the arterial resistance causing the reflection of the pressure wave [2] back to the heart. Therefore, the pressure wave propagating through the circulatory system is a superposition of a forward and a backward travelling wave. A sudden rise in the pressure after dirotic (or diastolic) notch in Fig. 2.2 indicates the superposition of incoming and rebound pressure waves. An increased arterial stiffness or inflexibility can push the dirotic notch towards the peak with maximum arterial pressure (systolic peak) causing irregular blood flow in the heart. Since the reflective component of the pressure wave changes with the arterial parameters such as width and elasticity, the arteries in different regions of the body have different diagrammatic representations of the pressure waveform (sphygmograms). The strength of pressure wave also depends on the amount of blood ejected from the heart (stroke volume). A higher stroke volume leads to a higher

volume of blood flowing through the arteries, therefore, further increasing the maximum pressure applied on the arterial walls. A majority number of arteries in the body are wide and elastic allowing a smooth flow of blood [7]. In such cases, the systolic pressure in the arteries resemble with the systolic pressure in the aorta. However, the narrowing of the peripheral arteries such as brachial and radial artery can lead to significantly higher systolic pressures in comparison to the aortic pressure [2]. These enhanced pressure levels makes it easy to palpate the brachial and radial artery for pulse waveform analysis.

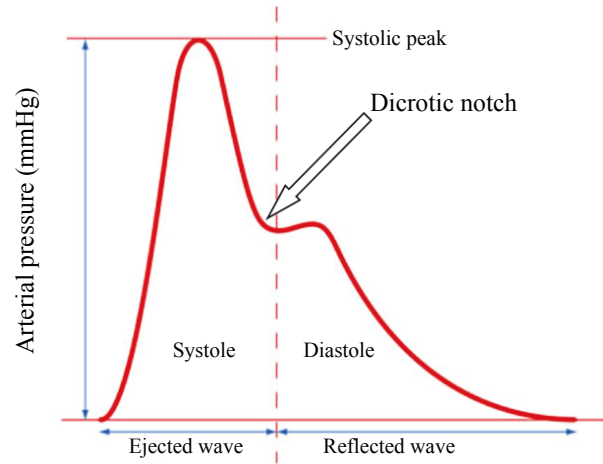


**Figure 2.2:** Normal arterial pressure waveform corresponding to systolic and diastolic phase of the cardiac cycle [8].

#### 2.1.2.2 Flow wave

Flow wave is the longitudinal movement of blood in response to the differential pressure created by the pressure wave throughout the arterial system in the body. The pressure and flow wave, therefore, indicate a periodic relationship of cause and effect in pulse formation. The strength and characteristics of the flow wave depends on the stroke volume, fluid properties and the momentum imparted by the ventricular contractions. The viscosity of the blood among other fluid properties plays a vital role in the formation of the flow wave. Since blood is a combination of red blood cells, white blood cells and plasma, any change in the percentage ratio of these components can affect the viscosity of the blood [9]. The blood with higher viscosity requires higher force to move through the blood vessels and vice-versa. These factors in combination with arterial stiffness and elasticity affects the movement of the flow wave. The strength of heart contractions determine the momentum imparted to the blood to flow through the blood vessels. This is evident in Fig. 2.1 where majority of the ventricular volume is emptied during the first third period of ejection cycle. The remaining blood volume is emptied in the last two thirds of the ejection period [6]. Therefore, the contraction force also plays an important role in the formation of the flow wave.

### 2.1.3 Arteries

Pulse in the human body can be sensed at several arterial locations including the temporal artery, carotid artery, brachial artery, radial artery, femoral artery, etc. The arterial system is mainly divided into central and peripheral subdivisions. The central subdivision encircles all the arteries present in the torso whereas the peripheral subdivision includes all the arteries in the upper and lower limbs. The arterial divisions are based on the muscular and elastic properties of the blood vessels. The arteries in the central part of the body are wider and more elastic to sustain high volumes of blood flow and larger pressure exerted from within the arterial walls. The elasticity of these arteries also help in propagating the pressure and flow wave to the peripheral regions of the body without much resistance. A typical example of artery in the central region include carotid artery which can be palpated easily by locating it lateral to the larynx. The peripheral arteries such as brachial and radial artery on the other hand have better muscular properties due to a greater proportion of smooth muscles in comparison to elastic fibres in the blood vessels [2]. The presence of these smooth muscles in the peripheral arteries allow them to demonstrate a higher functionality of vasoconstriction and vasodilatation as compared to arteries in the central region of the body [10]. This feature makes it easier to monitor the pulse at the peripheral locations such as brachial and radial artery.

The radial artery is a clinically important site to measure the human pulse. Its size, ease of access and proximity to the surface of the skin makes it a suitable location to study the pulse, also referred to as the radial pulse. It has also been found that the vascular properties of the radial artery are less affected by ageing, blood pressure and various movements as compared to other arteries, thus making it an ideal site for pulse assessment [13]. However, a number of factors such as arterial elasticity, arterial width,

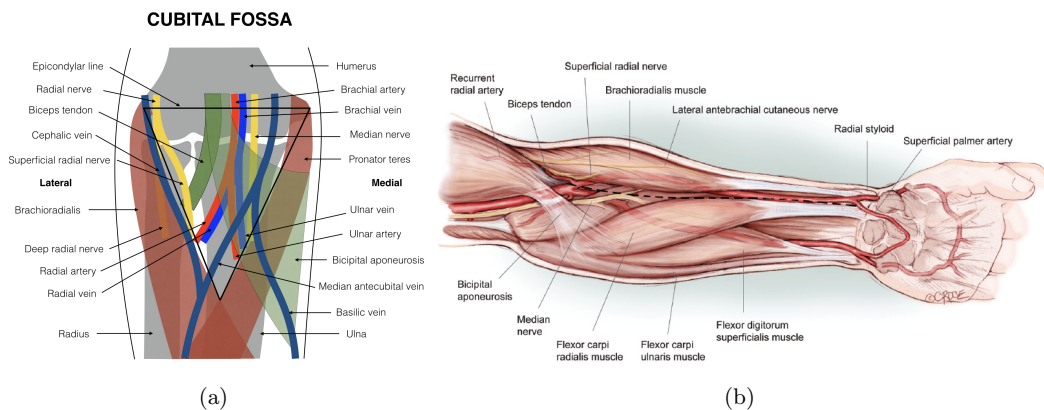


**Figure 2.3:** (a) Origin of the radial artery from bifurcation of the brachial artery at the cubital fossa of the forearm [11]. (b) Anatomy of the radial artery and the deep flexor muscles of the left forearm [12].

arterial tension, blood viscosity, blood volume, etc. affects the characteristics of the radial pulse [2]. Anatomically, the radial artery originate as a smaller terminal branch of the brachial artery and arises from its bifurcation at the cubital fossa of the forearm as shown in Fig. 2.3(a). In the proximal part of the forearm as shown in Fig. 2.3(b), the radial artery is overlapped anteriorly by the brachioradialis muscle which descends lateral throughout its length. Thereafter, the artery runs from the medial side of the radial shaft to its anterior, where it can be palpated between flexor carpi radialis and the anterior border of the radius. An examination of the pulse is most accessible at the lower end of the radius since the radial artery here is only covered by the skin, and superficial and deep fasciae [14]. The radial artery during its course in the forearm is supported by pronator teres in the proximal part, superficial radial nerve in the middle part and flexor carpi radialis in the distal part. The course of the radial artery extends further to divide into dorsal carpal and dorsal metacarpal branches to cater the blood flow to thumb and fingers in the hand [14], [15].

Traditionally, the pulse is studied at the radial artery in an approximate length of 3-5 cm on the wrist as shown in Fig. 2.4. The pulse here can be sensed at three distinct locations: distal, middle and proximal. The middle position can be located by palpating the pulse in front of the radial styloid process (protruded bone near the wrist crease). The palpation can be performed by sensing an outward force from within the radial artery when gently pressed by the fingers. The proximal and distal positions are generally 1-2 cm on either sides of the middle position, towards upper arm and fingers respectively.

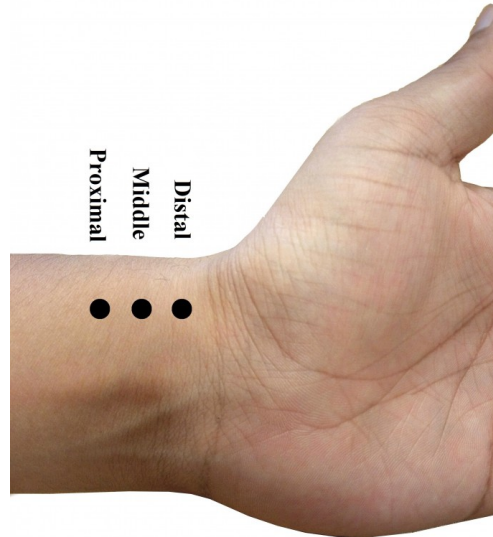


**Figure 2.4:** *Distal, middle and proximal locations on the radial artery to sense the pulse.*

## 2.2 Literature review of sensing the radial pulse

The arterial pulse has been a subject of great interest from the ancient times. Early physicians like Galen [16], Harvey [17], Marey [18], Mohamed [19], etc. recognised the clinical importance of pulse and paid great attention to its characteristics in normal health and disease [20]. Although the pulse is driven by the heart, it is transmitted by a channel of blood flow throughout the arterial system and suffers a continuous state of change. It is not only affected by the condition of the heart, but also by the functional state of the organs, nerves, muscles, skin, blood vessel walls, blood related parameters (volume, viscosity, pressure, velocity), etc. Since the bodily functions are regulated by the autonomic nervous system (ANS), the pulse also manifests the actions of ANS in its characteristics [21]. Therefore, the state of health of an individual can cumulatively effect the shape, amplitude and other characteristics of the pulse wave. A long-term continuous monitoring of the pulse can thus assist in diagnosis of certain health related parameters. However, for such an analysis over long periods of time, a monitoring system with very small and light sensors that can be easily worn on the body is required [22]. The power requirements also play an important role in governing the recording duration, processing complexity, and therefore, the battery size of the wearable system. A number of techniques have been proposed in the literature to record the pulse waveform from the wrist using different wearable sensing methods to extract features that can be used to monitor certain biomarkers of an individual.

### 2.2.1 Monitoring techniques and their applications

Physicians usually perform a routine checkup by examining the radial pulse to measure the cardiac activity of an individual before applying an advanced analysis. Such an examination is performed by sensing the rhythmic changes in the radial artery using contact and non-contact based methods. The contact-based methods typically include ECG and PPG, and are regarded as the gold standard approaches to monitor cardiac activity at the wrist. With the advancement in technology, some contactless methods based on resonators and radars have also been proposed recently. While a detailed review on contact and non-contact based systems to monitor cardiac activity at different locations of the body have been discussed in Section 1.2, the application of these techniques at the wrist along with the algorithmic methods are presented here.

Heart rate monitoring is one of the most common applications of studying the pulse at the wrist. The technological advancements have enabled researchers to record the electrical activity of the heart at the wrist. Zhang *et al.* [23] proposed a semi customised biopotential acquisition platform consisting of an evaluation board and a launchpad to record wrist-ECG signals from healthy people in a Lead I configuration. The proposed prototype used a serial peripheral interface (SPI) and a universal serial bus (USB) to

communicate with the graphical user interface (GUI) on the computer. The data was recorded by placing the signal electrode on the left wrist and the reference electrode on the right wrist. Therefore, in principle, the platform used both the wrists for data acquisition in a non-wearable fashion. The work focused on a continuous monitoring of the instantaneous heart rate (IHR) from wrist-ECG signals corrupted heavily by the motion artifacts. The proposed support vector machine (SVM) based framework was implemented on 22 thirty-minutes recordings to achieve a mean absolute error (MAE) of 1.4 bpm (beats per minute) and root mean square error (RMSE) of 6.5 bpm respectively. Zhang *et al.* introduced a new algorithm for the IHR determination in [24] and extended the implementation over the dataset consisting of a public database in addition to the two-wrist ECG signals. The proposed methodology projected the ECG signals to a high-dimensional phase space to differentiate the heartbeat features from the motion artifacts using the multiview dynamic time warping approach. The IHR comparisons for signals with SNR as low as -9 dB achieved an MAE of 2.5 bpm and RMSE of 7.0 bpm respectively. Salehizadeh *et al.* [25] also designed and developed a two-wrist acquisition system named, NohChon, to record a single channel ECG signal in Lead I configuration. The modules on both the wrists included 3-axis accelerometers and were connected through a wire threaded through a compression shirt to minimise the motion artifacts. The study implemented spectral filter algorithm for an accurate estimation of heart rate from ECG signals corrupted during intense physical activities. The method applied on a dataset of 17 minutes recordings from 4 subjects resulted in an MAE of 1.18 bpm and MAE percentage of 1.26% respectively<sup>1</sup>.

Zhang *et al.* extended the use of the hardware platform developed in [23] to the other studies [26], [27] and recorded ECG signals from non-standard positions. The electrodes in [26] were placed on the left arm and the signal-to-reference electrode distance was maximised to achieve a better SNR. The study used an SVM-based framework to find the duration of the QRS complex and detect any cardiac-related diseases. The work in [27] integrated the PPG sensor with ECG electrodes into a one-arm band to measure both the signals simultaneously at the left arm. The ECG and PPG-based heartbeats were extracted to find the pulse transmit time (PTT) and model it further to determine the systolic blood pressure (SBP).

While the above integration of ECG and PPG sensors was designed for the left arm, similar systems have been designed for the wrist as well. Thomas *et al.* [28] developed a wearable wristwatch based system to measure ECG and PPG simultaneously. The device named, BioWatch, consists of three ECG electrodes, two on the bottom and one on the top. The watch, when worn on the left hand, provides contact with the two electrodes on the bottom whereas a manual touch of the finger from the right arm completes the connection with the top electrode. The simultaneous measurement of ECG and PPG

---

<sup>1</sup>The real-time implementation of the algorithm can be watched on the following link: [https://www.youtube.com/watch?v=hEumm\\_OPwls](https://www.youtube.com/watch?v=hEumm_OPwls).

signals have been used to measure the PTT for blood pressure determination. The implementation of the proposed PTT model achieved an average RMSE between 7.83 and 9.37 mmHg (millimetres of mercury) for systolic, and 5.77 and 6.90 mmHg for diastolic blood pressure (DBP) respectively. The integration of a nine-axis MEMS inertial sensor in the device allowed an automatic detection of the sensor height to accurately locate the arm position. A similar device was also designed by Krachunov *et al.* [29] with two ECG electrodes, one on the bottom and one on the top. The electrodes were made from a flexible ink which can be painted on the casing to make it adaptable for different shapes and users. The design also focused on energy efficiency with front end consuming  $8 \mu\text{W}$  (microwatts) power at 1.8 V (volts) supply. ECG signals were recorded from 8 subjects for 12 five-minutes recordings. The heart rate comparisons resulted in an MAE of 4.56 bpm and standard deviation (SD) of 3.23 bpm respectively. Although both these devices can be easily worn on the wrist, the use of another hand to complete the connection for signal acquisition makes them unsuitable for long-term monitoring. Other wearable devices such as the Apple Watch (Apple Inc., California, United States), KardiaBand (AliveCor Inc., California, United States) and Salutron (Salutron Inc., California, United States) also, provide spot measurements of ECG at the wrist, but they are not suitable for long-term cardiac monitoring. KardiaBand from AliveCor, for example, required the placement of thumb on the band to record the ECG signal. Systems such as Zephyr Biomodule (Medtronic Inc., Maryland, United States) and Kenzen patch (Kenzen Inc., California, United States) record the ECG data continuously, however, they are worn on the chest and not on the wrist. While Zephyr is widely used in the sports context to measure several physiological and biomechanical measurements, Kenzen is currently field-testing its technology to monitor heart rate continuously.

To overcome the challenges faced by ECG sensing at the wrist, PPG-based devices have been widely used for continuous monitoring of cardiac activity. PPG records the optical activity of the radial artery by sensing beat-to-beat volumetric changes in the arterial blood flow. An extensive amount of commercial PPG-based wearable monitors, mainly smartwatches produced by Fitbit (Fitbit Inc., California, United States), Apple (Apple Inc., California, United States), TomTom (TomTom N.V., Amsterdam, Netherlands), Scosche (Scosche Industries Inc., California, United States), etc., allow for continuous heart rate measurement at the wrist. The accuracy and reliability of such devices have been validated in several studies during rest and exercise [30]–[33]. Stahl *et al.* [30] validated the Scosche Rhythm, Mio Alpha, Fitbit Charge HR, Basis Peak, Microsoft Band, and TomTom Runner Cardio wireless monitors by comparing their heart rate outputs with the ECG-based reference monitor. The experiment involving 50 subjects required 30 minutes of continuous walking and running at different speeds with the heart rate recorded every 1 minute. The comparisons with the reference ECG indicated that the wireless monitors provide accurate measurements of the heart rate during walking and



running activities. These results, however, are contradictory to the validation results obtained in [31], [32]. Cadmus *et al.* [31] performed an experiment with 4 wrist-worn devices, recording the heart rate at 1-minute intervals from 10 minutes of data recorded each at rest and 65% of maximum heart rate. The heart rate comparisons for 40 subjects delivered significantly broader limits of agreement (LOA) with the ECG reference for both the states, specially during the state of moderate exercise. The best LOA of [-5.1, 4.5] bpm at rest, and [-22.5, 26.0] bpm for the state of 65% of maximum heart rate were obtained for Fitbit Surge and Mio Fuse monitor respectively. Only 2 trackers (Basis Peak and Fitbit Charge) were studied in [32] for a 77-minute protocol over 24 subjects. Although the LOA for both the monitors exceeded 20 bpm, it was concluded that the Basis Peak satisfied the validation criteria whereas the Fitbit Charge failed to satisfy the criteria. Both the monitors demonstrated a substantial decrease in accuracy with the reference ECG heart rate exceeding 116 bpm.

Since the performance of the commercial PPG-based heart rate monitors significantly degrade with the intensity of the exercise, several research papers have worked on the removal of motion artefacts (MAs) using different algorithmic methods for an accurate heart rate estimation at the wrist. A review about different signal processing techniques to remove or attenuate MAs from the wrist-PPG signal is provided in [34]. Although these techniques adopt multiple processing stages, the heart rate estimation is performed using one of the several methods including adaptive filtering [35]–[38], Weiner filtering [39], Kalman filtering [40], independent component analysis [41], [42], frequency-domain ICA [43], empirical mode decomposition [44], [45] and machine-learning [46] approaches. Many of these methods transform the signal into time-frequency domain to identify the spectral peak corresponding to the heart rate among different peaks generated by MAs. However, the accuracy of such methods rely prominently on data from multiple sensors attached to the wrist. The publicly available IEEE Signal Processing Competition (SPC) database includes 2-channel PPG and 3-axis accelerometer recordings from 12 male subjects of 18-35 years age. The reference heart rate was recorded simultaneously from the chest-ECG while the subjects walked and ran at different speeds. Zhang *et al.* [47] proposed a general framework, termed as TROIKA, to estimate the HR from the PPG signals in the SPC database. The framework consisted of signal decomposition for denoising, sparse signal reconstruction for high-resolution spectrum estimation, and spectral peak tracking with verification to find the spectral peak corresponding to the heart rate. The algorithm obtained a Pearson correlation of 0.992 and MAE  $\pm$  SD of  $2.34 \pm 0.82$  bpm. This work was extended in [48] and a new framework, named JOSS (joint sparse spectrum reconstruction), was proposed. The framework calculated a joint spectrum of the PPG and acceleration signal and utilised a common sparsity constraint on spectral coefficients to remove spectral peaks of MAs from the PPG spectra. A better performance with MAE  $\pm$  SD of  $1.28 \pm 2.61$  bpm was obtained. Mashhadi *et al.* [35] also

used a high resolution spectrum estimation technique using iterative method with adaptive thresholding (IMAT) for peak selection. The PPG signals were cleaned by successive application of adaptive filters using the reference generated from the 3-axis acceleration data. The MAE of 1.25 bpm was obtained for the SPC database. The use of adaptive filtering to remove MAs from the PPG signals have also been utilised in other studies. Khan *et al.* [44] decomposed the corrupted PPG signals into intrinsic mode functions using the empirical mode decomposition method for signal denoising. In the second stage of the algorithm, a recursive least squares adaptive filter is used to deal with close proximity of MA and PPG peaks and spectral shadowing. The technique obtained better results than TROIKA and JOSS framework with MAE  $\pm$  SD of  $1.02 \pm 1.79$  bpm. While these studies generate a reference from the acceleration data to feed into the adaptive filters, several algorithms utilise the reference extracted from the PPG signal itself for the noise cancellation [36]–[38]. The algorithms described above rely on different filtering methods to clean the PPG signal and estimate the heart rate based on tracking the spectral peaks. Grisan *et al.* [46] proposed a supervised learning approach for the PPG signals in the SPC database. The training set included 282 features extracted from the labelled PPG segments. However, only the best 25 features having maximum variance were used with the random forest classifier to obtain MAE of  $6.4 \pm 0.28$  bpm.

Majority of the studies concerning the removal of MAs uses multiple signal channels by integrating the accelerometer and gyroscope sensors with the PPG sensing at the wrist [47], [49]–[53]. These additional signal channels, as discussed before, serve as a reference to separate MAs from the corrupted PPG signals. However, some research studies avoid the use of an accelerometer sensor to reduce the computational complexity of the algorithm. Yang *et al.* [54] used a dual-wavelength technique and observed the difference in the two PPG detection modules (blue and infra-red filter) to reduce the effect of MAs. The proposed device reported an error of less than 3 bpm for the heart rate estimation. Zhou *et al.* [55] did a similar study and used a differential channel with green and red light PPG channels. The heart rate monitoring system was assembled in a wristwatch and four types of motions were studied. It was concluded that the average artifact ratio corresponding to these motions using the proposed detection technique was reduced as compared to the other studies.

Other wearable systems have also been proposed in academic papers to measure PPG from the radial artery. The ease of integrating PPG sensing with other miniaturised sensors at the wrist have allowed researchers to develop wearable devices and address other clinical applications as well. Kos *et al.* [56] integrated a temperature sensor, tri-axis accelerometer and gyroscope with infra-red (IR) light-emitting diodes (LEDs) to monitor the body temperature, arm movement and the heart rate of the subject. Malhi *et al.* [57] designed and developed a similar device to determine any medical distress in elderly people by measuring the oxygen content in the blood. The design also included an

impact sensor and a panic button to detect falls and raise the alarm in an emergency. The PPG sensors have also been integrated with accelerometer and gyroscope for application in driver alertness system [58]. Such systems focus on measuring the physiological state of the driver by measuring the heart and respiratory rate, and the steering movement.

PPG sensing has also been used to detect cardiac disorders by monitoring cardiac parameters. Bonomi *et al.* [59] used the integration of PPG sensing and accelerometer sensor to detect atrial fibrillation and determine periods of corrupted signal. Tarniceriu *et al.* [60] recorded PPG signals to monitor heart rate variability (HRV) from elderly people who were suffering from sinus rhythm and atrial fibrillation, and underwent a recent surgery. Baek *et al.* [61] did a similar study and investigated the measurement of HRV in regions where inter-beat intervals (IBI) could not be found due to the presence of corrupted PPG signals. The analysis found that the errors in the HRV measurement were proportional to the missing IBI data.

The slowly varying baseline of the PPG waveform has been found to contain frequencies corresponding to the respiratory cycle [62]. Wang *et al.* [63] developed a constant power circuit to obtain stable PPG waveforms from the radial artery to monitor the heart rate and the respiratory rate simultaneously. The respiration frequency was also found by Chang *et al.* [64] where the wrist-PPG signals were recorded by mounting a green-light LED and a photodiode on a wrist band. Adib *et al.* [65] studied the effect of respiration rate on the correlation between the wrist and finger-PPG signals and found that the AC and DC components become highly correlated in fast breathing conditions.

A high correlation between the aortic and radial pressure wave, measured invasively, have been proven before [66]. The integration of PPG sensing with the applanation tonometer in [67], [68] has made it possible to predict the aortic pressure waveform by fitting different autoregressive models to the radial PPG waveform. Therefore, the aortic pressure can be accurately determined from the non-invasive radial pulse waveform.

Blood pressure determination using cuffless techniques has been made possible by modelling the pulse onset time between two different sites. The acquisition of PPG signal at the wrist has allowed monitoring the pulse transit time (PTT) by placing two different sensors on the forearm to determine the blood pressure [69], [70]. Rajala *et al.* [71], for example, estimated pulse arrival time (PAT) using wrist-PPG signal and arm-ECG signal to correlate it with blood pressure. A similar cuffless technique was presented by Priyanka *et al.* [72] to estimate blood pressure, but solely using the PPG signal. Four features from the PPG waveform were extracted to train an artificial neural network for blood pressure estimation. Song *et al.* proposed a cuff-based method to determine blood pressure from wrist-PPG signals analysed over a deflation cycle of the wrist cuff. The prototype included an array of PPG sensors with 4 IR-LEDs and a phototransistor.

While the devices discussed above have mainly been developed using off-the-shelf components, some studies have designed chip-based prototypes. Xiang *et al.* [73] developed

a low-power wavelet denoising chip for PPG detection and heart rate monitoring. The chip was designed and fabricated in  $0.18\ \mu\text{m}$  N-well CMOS technology. The power consumption of the chip was reported to be  $8.12\ \mu\text{W}$  at an operating voltage of 1 volt (V). Mechanical compatibility of the sensing device to multiple locations on the body requires the sensor to be deformable and attachable on the non-flat positions. Kim *et al.* [74] proposed such an attachable and flexible pulse sensor, integrated with micro-sized inorganic photodetectors and red LED to monitor vital parameters such as heart rate and blood flow. The pulse waveform using the small-factor sensor can also be recorded from finger, fingertip, nail, forearm and finger ring. The functionality of the sensor was validated by testing the change in the heart rate from relaxed to running position.

Apart from ECG and PPG-based methods, other contact methods include the development of flexible sensors using different material properties. Li *et al.* [75] proposed a flexible and wearable optical fiber strain sensor using side-polished fibre Bragg grating to produce an optomechanical response corresponding to the pulse waves. The sensor also detected the forward and backward bending of the wrist but showed large sensitivity towards motion artifacts. Zang *et al.* [76] designed a graphene-based sensor to record the radial pulse wave. They developed the sensor on a core of highly elastic polyurethane fiber wrapped in two helically-wound polyester fibers. The wrapped core was processed through multiple chemical procedures to enable a better conduction for the pulse monitoring. Such wearable sensors have also been proposed in other studies [77], [78]. While these sensors provide good wearability, they are highly sensitive to motion artifacts resulting in very low SNR.

The pulse at the radial artery can also be sensed using non-contact methods, however, they are still in their early development stages and are not available commercially. The studies in [79]–[81] used radio frequency (RF) array resonators to detect very weak pulse signals to generate a heartbeat pulse. An *et al.* [79], [80] utilised the reflection coefficient from a non-contact resonator to monitor the changes in the diameter of the radial artery. Kim *et al.* [81] proposed a sleep monitoring system by measuring the heart rate using three different types of RF sensors. The heart rates were detected at 0.2 to 1 mm of distance from the surface of the skin. The studies claimed that the proposed system can be implemented in wearable technology, however, the prototype and the power requirements (45 mA at 5 V supply) limited their usage for short-term cardiac monitoring. High sensitivity towards motion artifacts is another concern as a small artifact can easily interfere with the signal of interest. He *et al.* [82] proposed a method to detect the impedance pulse wave at the wrist using a self-balancing bridge, flexible electrode and a high-speed digital lock-in algorithm. The impedance variation corresponding to the heartbeat pulse was compensated by the self-balancing bridge and a corresponding pulse wave was extracted. On the other hand, Wang *et al.* [83] explored the radar technology in wearable devices to detect the heart and respiratory rates using two different radars.

The heart rate of a subject was calculated by modulating an oscillator using a patch antenna corresponding to the associated Doppler signal.

The detection of the pulse from the radial artery using microphones have also been explored by a limited number of works [84]–[90]. However, these studies focused on the pulse diagnosis and did not address the pulse auscultation from the wearable aspect. Mandal *et al.* [84], [85] developed a wearable, battery-free tag to monitor the heart sounds on the chest. The tag consisted of an integrated circuit, an antenna and up to four microphones to generate digital flags whenever the output from the microphones exceeded a programmable threshold. It was shown that two such tags when attached to the carotid and the radial artery simultaneously can provide time-delay between the onset of two pulses which can be utilised to determine the blood pressure. The study, however, discussed the wearability of only the chip and the antenna, and not the complete system. Chen *et al.* [86] palpated the radial artery using a specialised pulse wave measuring system which could apply varying amounts of pressure on the artery using a non-wearable setup. Chen *et al.* [87] analysed the variations in the pulse sounds recorded using a condenser microphone with three different weights applied on the radial artery using a spring pressure gauge. Khaire *et al.* [88] did a similar pulse diagnosis to investigate whether a subject has taken a meal or not. Nomura *et al.* [89] extracted the pulse waveform using an electret condenser microphone to explore the characteristic points of the pulse acceleration signal and relate its changes with cardiovascular diseases. Shi *et al.* [90] developed a wearable wrist sensor and a chest sensor to reproduce heart sounds at the wrist. The study modelled the sound attenuation and travel process of the pulse from the heart to different arterial locations using a neural network with two layers.

### 2.2.2 Summary

ECG is the gold standard approach for monitoring cardiac activity and obtaining cardiac parameters such as heart rate and its variability. While the current systems do not provide continuous measurements of ECG signal at the wrist, a better way of long-term cardiac monitoring is based on PPG sensing. However, the accuracy and reliability of PPG-based wearable devices are vulnerable to several factors, including motion artifacts, the brightness of the environment, or having a stable contact force between the sensor and the measurement site [91]. Also, PPG uses an infra-red light as an active input signal. This imposes constraints on the size of the device, and consequently the length of monitoring, as a result of the power demands of infrared LEDs. Academic papers have shown how cardiac activity could also be measured using non-contact techniques such as radars and resonators, but these systems are still in very early development stages. The cardiac activity could, in principle, also be measured by using piezoelectric probes [92], however, these sensors require a stable and continuous pressure through externally applied forces, and are highly sensitive to movements; all of this resulting in

a very low SNR [93].

While all these techniques provide useful information to extract the cardiac activity, they suffer from several issues, particularly with the constraints in terms of device size and shape, power budget for long-term continuous monitoring, reliability and accuracy concerns posed by wearable technologies. Acoustic sensing of chest sounds, using a stethoscope, is the most widely used technique to detect cardiac output and diagnose heart problems. As with the sounds on the chest, pulse sounds can also provide important clinical information to monitor the cardiac activity. The use of a microphone as a passive sensor in comparison to active sensing by PPG reduces the constraints on the power consumption of the system by significant magnitudes. Therefore, acoustic sensing of the pulse appear to be an attractive option for wearable applications. The cardiac rhythms within the radial artery can possibly be sensed using a microphone with small-factor, without requiring any additional power consuming input signal. Such an approach could potentially be used either as an alternative new physiological signal to extract cardiac information from a wearable device, or as an additional physiological channel to complement existing systems, without posing an overhead in terms of size.

## 2.3 Wearable sensing of the pulse sounds

With the rise in population and limited resources available in the hospitals, the health-care costs have been rising at a rapid pace over the last few years. The waiting time for a patient to see a physician have also become longer. The recent developments in health-care technology, however, has allowed advancing physiological monitoring from clinical settings to a patient's home. Such an advancement would not only reduce the burden on the hospitals allowing a reduction in the healthcare costs but also provide medical attention to a larger cohort of the population. The implementation of medical care in home settings, however, imposes a lot of constraints on the technological forefront. The development of biomedical devices should incorporate the user-friendliness and operational simplicity to be handled by patients and not trained clinicians. The device should be designed in a manner that it can be easily integrated into the user's lifestyle and does not require a significant change in their daily activities. These factors require a device to be smaller in size, operate over a long period, be safe and easy to use, and integrate comfortably with the desired body location. While these devices are not intended to replace the medical care provided by the hospitals, they can provide useful diagnostic information to aid the physicians and reduce the monitoring times.

The advancements in the electronics sector to produce electronic parts with smaller sizes has allowed the development of wearable devices for biomedical applications. These devices have the potential to revolutionise the healthcare services both in the hospital as well as home settings. The devices have been designed in a manner that they can be easily operated by the patients in the absence of the clinicians. A typical blueprint of such a

device includes a miniaturised non-invasive sensor that transmits the sensed physiological signal to a nearby base station. The size and shape of the device are designed to integrate comfortably into the patient's lifestyle without requiring any significant change. The base station carries enough processing capability to analyse the signal and extract meaningful parameters that can be of interest to the physician. The availability and wide usage of the smartphones have made it easier to reduce the cost of the wearable system by eliminating the need for a separate base station. Smartphones not only provide the wireless connectivity but they also carry multi-core processors to allow the signal analysis using sophisticated algorithms.

The design and development of wearable devices impose several constraints on the electrical and mechanical specifications of the system. The development of an acoustic wearable device to sense the pulse sounds at the wrist require the sensor to be light-weight and integrate easily with the contour of the patient's wrist. The strict limitations of size and shape along with the need for a long-term continuous cardiac monitoring impose strict regulations on the power-budget of the system. While there is an option to analyse the signal on the device itself, a limited power-budget require the signal processing algorithms to be of low-complexity and demand less computational cycles while still maintaining the accuracy and reliability of the sensing approach. These tradeoffs make it challenging to design the sensor using such an approach. The availability of a higher computational power on the smartphones can be used to receive the raw data wirelessly and process high-complexity algorithms on the platform. The design of the acoustic sensor, therefore, adopts the architecture shown in Fig. 2.5. In this architecture, the microphone senses the pulse sounds from the radial artery at a specific sampling frequency. The analogue front end contains the electronic circuitry to filter and amplify the information relevant to the pulse sounds. The raw information is bundled into data packets that can be transmitted wirelessly to a patient's smartphone. The received data is analysed using the computational resources available on the smartphone to extract meaningful parameters for the diagnostic purposes.

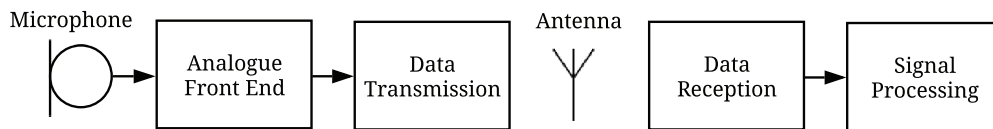


**Figure 2.5:** *Design approach for a wireless wearable device to sense pulse sounds at the wrist.*

The constraints imposed on the design of the acoustic wearable device requires a thorough understanding of different components to be used at different architectural stages. The small size of the overall device limits the size and shape of the battery. The operation of microphone and its related circuitry under specific voltage and current requirements

also restrict the choice of the battery. Since the data transmission consumes more power to transmit the data at a higher rate, the optimal choice of the hardware platform for wireless transmission is also required. The following sections discuss different types of acoustic sensors, batteries and data acquisition platforms to design and develop an acoustic wearable device to operate over longer durations and sense the pulse sounds effectively and reliably from the radial artery at the wrist.

### 2.3.1 Types of acoustic sensors

Alexander Graham Bell in the 1870s discovered that the acoustic pressure variations can be manifested as the time-varying electrical signals. He utilised such a variation to transmit speech on electrical wires [94]. While Bell became the inventor of the telephone, it was Edison who designed a carbon microphone that could record speech levels adequately to be sent over reasonable distances [95]. The microphone design, since then, has gone further developments in parallel to the manufacturing processes to refine the acoustic behaviour. The advancements in silicon micromachining and micro-electro-mechanical systems (MEMS) technology has allowed developing high-performance, miniaturised acoustic sensors with low cost and better reproducibility. The microphones based on several transduction principles such as the piezoelectric, the piezoresistive, the capacitive, etc. have been developed. For the design and development of a low-power, miniaturised wearable system to sense the pulse sounds at the wrist, it is important to understand the different types of acoustic sensors available in the market.

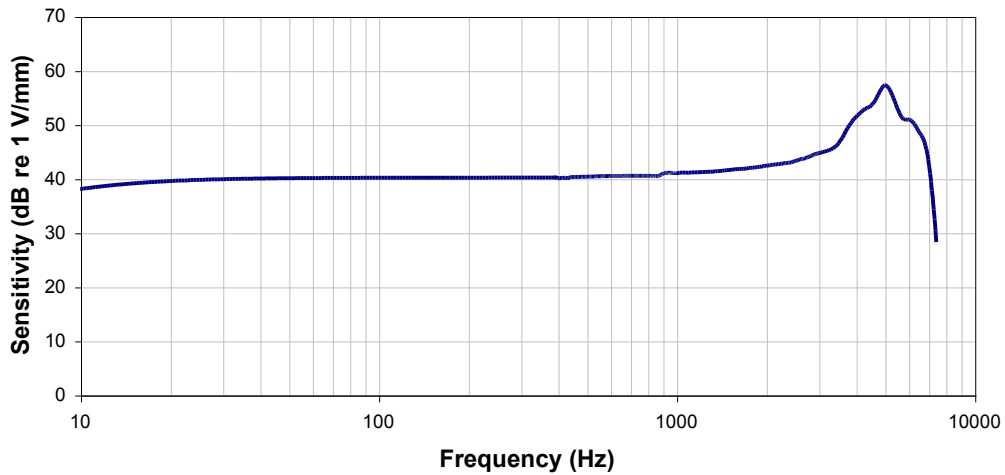


**Figure 2.6:** *Frequency response of a contact microphone when facing its rubber sensing pad to piston-like displacement of a structure [96].*



### 2.3.1.1 Contact microphone

Contact microphone, also known as the piezo microphone uses piezoelectric effect as the transduction principle to convert the sound waves into electrical energy. Piezoelectricity is a phenomenon observed in several materials which generates an electrical charge in response to an applied mechanical stress. The piezoelectric effect is reversible i.e., the piezo materials can also change mechanical dimensions in presence of an electric field. In case of a contact microphone, the sound waves apply stress on the diaphragm to create an electric charge on the plate which can be converted into an output voltage. These microphones are designed to sense vibrations through physical contact with the solid objects and are insensitive to the airborne sounds. Therefore, the diaphragm deformation only occurs because of the structure-borne sound. While a typical design of the contact microphone includes a diaphragm of piezo film affixed to a thin alloy metal disc with opposite charges, different mechanical structures have been proposed to improve the acoustic efficiency and sensitivity of the microphone [97]. The contact microphones operate by attaching the rubber sensing pad to a body part, for example, the neck or the chest and detects the sound propagating through a combination of the tissue, bone, muscle, and ligament. Although these microphones are highly sensitive to the mechanical vibrations, they are immune to any interference from the external noise. They are also immune to the moisture and can operate in conditions where the environmental stability is critical. Some of the applications in high noise environments include the electronic stethoscope and bone-conducted sound pickup in hospitals, impact sensing in factories, and waterproof microphones for divers. Typically, the sensitivity of the contact microphones as shown in Fig. 2.6 has a flat frequency response up to a few kHz and thereafter, a sharp rise in the sensitivity within the audible range is observed.

While the contact microphones provide certain advantages, their high sensitivity to mechanical vibrations makes them vulnerable to motion artifacts. A wearable sensor attached to the wrist can incorporate significant mechanical noise in the microphone with different hand gestures. These artifacts can interfere much strongly with the pulse sounds of weaker strength and can lead to a failure of the whole system. The larger diameter of such microphones and an absence of the flat frequency response in the audible range also imposes further constraints on the design of the wearable device.

### 2.3.1.2 Capacitor microphone

A capacitor is essentially formed when two charged metal plates are kept in close proximity. A capacitor microphone uses the capacitive phenomenon and consists of a moveable membrane and a fixed backplate with a thin air gap separating both the plates. When sound waves hit the moveable diaphragm, its back and forth motion change the relative distance between the membrane and the backplate. Therefore, the sound wave rhythm manifests as capacitive oscillations between both the plates. Any change in distance,  $d$ ,

between the two plates result in a corresponding change in the capacitance as follows:

$$C = \epsilon \frac{A}{d} \longrightarrow \Delta C = \epsilon \frac{A}{\Delta d} \quad (2.1)$$

where  $\epsilon$  is the permittivity of the air between the two plates and  $A$  is the overlapping area of the two plates. If the charge,  $Q$ , on the plates is kept constant, any change in capacitance produces a corresponding change in the voltage,  $V$ , as given by:

$$\Delta V = \frac{Q}{\Delta C} \quad (2.2)$$

Therefore, any change in the air gap caused by the force of the sound waves produces a proportional change in the voltage.

$$\Delta V \propto \Delta d \quad (2.3)$$

The overall sensitivity of a capacitor microphone is governed by its mechanical and electrical sensitivity [98]. The mechanical sensitivity,  $S_m$ , is defined as the ratio of change in deflection of the microphone diaphragm,  $\Delta w$ , corresponding to a change in the applied pressure on the diaphragm,  $\Delta P$ . The electrical sensitivity,  $S_e$ , on similar grounds, is defined as the ratio of change in the voltage following a change in the distance between the two plates.

$$S_m = \frac{\Delta w}{\Delta P}, \quad S_e = \frac{\Delta V}{\Delta d} \quad (2.4)$$

Since the charge on the plates remains constant and the change in voltage is proportional to the change in air gap thickness, the electrical sensitivity of the microphone is essentially equal to the electric field strength,  $E$ , between the two plates given by:

$$S_e = E = \frac{V_{bias}}{d_0} \quad (2.5)$$

where  $V_{bias}$  is the bias voltage and  $d_0$  is the initial air gap thickness. The electric field is generated by polarising one of the plates, mostly the backplate, with a built-in charge. The polarisation is practically achieved by affixing the backplate to a charged dielectric layer, also known as an electret. Due to the involvement of an electret in the design of a capacitor microphone, they are famously known as electret condenser microphone (ECM). The earlier ECMs required high bias voltages, in order of hundreds of volts, to polarise the plate and create sufficient electric field to sense small deflections in the microphone diaphragm. With the advent of thin electric films capable of permanent electric polarisation, the microphones without the need of power supply were made possible [99]. The electret layer, in principle, can be affixed either to the moveable microphone diaphragm or the perforated fixed backplate while maintaining a thin air gap between both the plates as shown in Fig. 2.7(a) to form a variable capacitor.

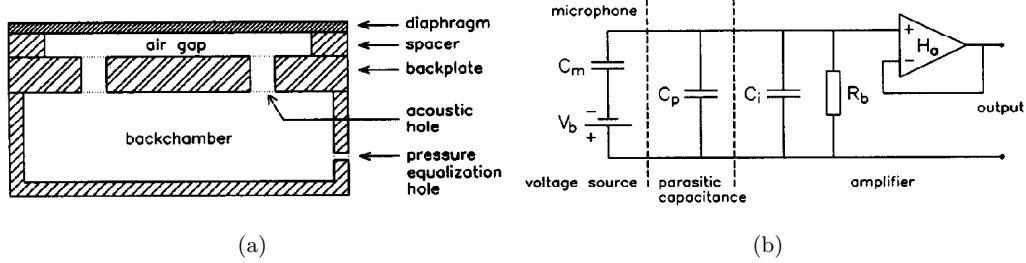


**Figure 2.7:** (a) Cross-sectional view of a condenser microphone with an air gap between the moveable diaphragm and the backplate [98]. (b) Condenser microphone connected to an external bias voltage source, parasitic capacitance and a preamplifier [98].

Unlike the contact microphone, the ECM senses the airborne sounds and reject the interference from mechanical vibrations. These microphones are low in cost and can operate without the need of a power supply. However, the electret material can lose charge over time causing a degradation in the sensitivity and resulting in poor performance of the microphone. The damping caused by the streaming of air in the thin air gap also results in a loss of sensitivity at higher frequencies [100].

The output capacitance of the condenser microphone is usually very small (in order of pF) because of the low charge deposited on the electret layer. The small capacitance of the microphone results in a high output impedance. Therefore, a buffer (or preamplifier) is required to convert the impedance from a higher to a lower value. This is necessary for an effective conversion of sound waves into an electrical signal without loading the microphone. Since the buffer is usually a source-follower, the capacitance of the microphone in combination with input resistance of the buffer forms a high-pass filter. Depending on the cut-off frequency of the high-pass filter, the buffer can possibly filter out the desired signal of interest. Another resistor,  $R_b$ , as shown in Fig. 2.7(b) is added to bias the circuit and improve the input impedance of the buffer. Since the cut-off frequency of the high-pass filter is inversely proportional to the resistance value,  $R_b$  in order of several M $\Omega$  is generally used. A typical frequency response of an ECM demonstrates high pass cut-off frequency of more than 100  $\Omega$  as shown in Fig. 2.8. While the ECMs provide certain advantages, their usable bandwidth imposes challenge on recording all the characteristics of the pulse sounds using the wearable sensor. The larger diameter and the height of the microphones also places certain constraints on the form factor of the wearable device.

### 2.3.1.3 MEMS microphone

The consumer demand for miniaturisation of portable devices such as smartphones, tape recorders, radio, tablets, and IoT devices required the microphones to be smaller in size, cost-effective while maintaining the low noise levels and high performance for a wide range of temperature and humidity conditions. With the advent of high precision

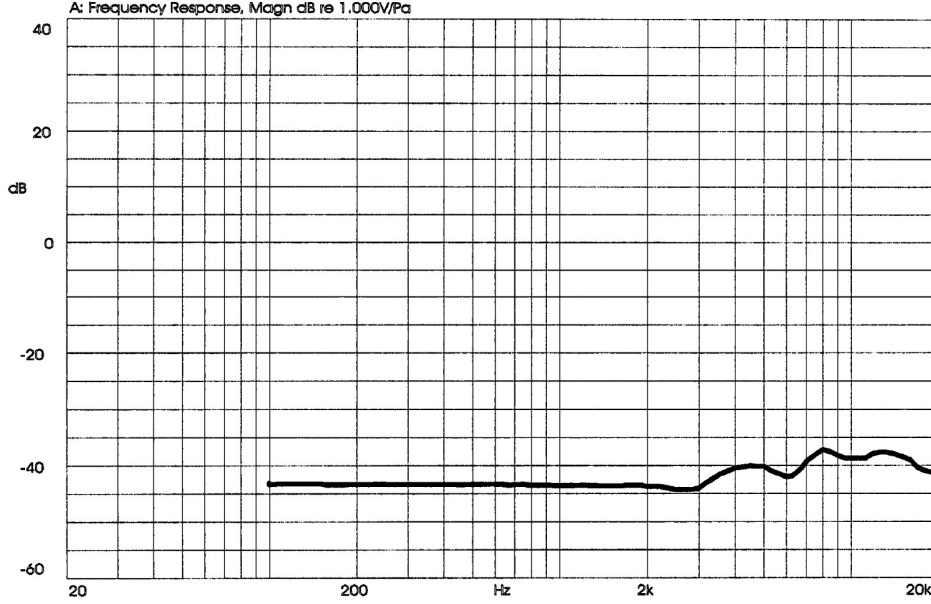


**Figure 2.8:** *Frequency response curve of an ECM (CMC-5044PF, CUI Inc.) with sensitivity at a baseline of -44 dB [101].*

silicon photolithography and etching process technologies, the MEMS structures with dimensions in order of microns were made possible. While the MEMS structures gained their initial popularity through automotive accelerometers for airbag deployment, they were later commercialised for acoustic applications [95]. Silicon micromachining has been used to fabricate MEMS microphones with different transduction principles including the piezoelectric, the piezoresistive and the capacitive phenomenon. The design and fabrication of MEMS microphones using the capacitive approach is most popular because of its advantages in terms of low cost, high sensitivity, high SNR and stable performance.

The capacitive MEMS technology offers excellent acoustic characteristics with very small form factors. This is achieved through a fabrication process which involves creating a moveable membrane and a fixed backplate over a cavity in the base silicon wafer. While the perforations in the fixed backplate allows air to flow easily through it, the moveable membrane flexes in response to the change in surrounding air pressure caused by the sound waves. These movements change the capacitance between the backplate and the membrane, which can be sensed by an application specific integrated circuit (ASIC) to convert the vibro-acoustic effects in an electrical signal. While the MEMS microphones are manufactured in different packages and output format depending on the particular application, the port location (or sound hole) are kept either on the top or the bottom as shown in Fig. 2.9(a). The top-port microphones have the sound hole in the lid and are used in applications where the traditional placement of the microphone is required. The bottom-port microphones receive the sound waves through a hole in the

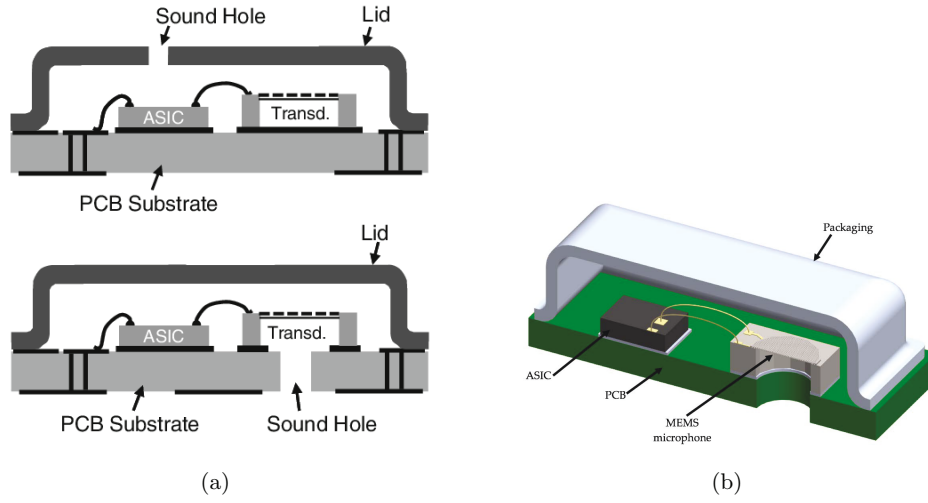


**Figure 2.9:** (a) MEMS microphone with transducer, ASIC and wire bonding. Top package has sound port on top (in lid) and bottom package has sound port on bottom (in PCB substrate) [103]. (b) Cross-sectional schematic view of a MEMS microphone with the sound port in the PCB substrate [104].

PCB substrate and are generally used in products with small-factors and components placed on opposite side of the acoustic port [102]. A 3-D model of a bottom-port MEMS microphone wire-bonded with the ASIC in a metal package is shown in Fig. 2.9(b).

Although the ECMs are still widely used in different applications, the MEMS microphones offer several advantages over them. They are as follows:

1. The silicon photolithography in the fabrication of the MEMS microphone provide excellent reproducibility as compared to ECM [95].
2. The integration of ASIC with the transducer in the MEMS package allows to read very small changes in the capacitance precisely. Since the ASIC realises complex circuits such as an analogue-to-digital converter (ADC), filter, buffer, etc. at the chip-level, its inclusion reduces the PCB area and cost of the overall system and provides better immunity from noise, power supply variation and electromagnetic interference.
3. The implementation of very low-noise electronic circuitry in the MEMS microphone generates a relatively lower output impedance as compared to ECM. This results in a better frequency response of the microphone as shown in Fig. 2.10.
4. MEMS microphones are surface mounted devices and can be easily integrated with other components on the PCB using an automatic pick and place process.
5. MEMS microphones are designed to provide very stable performance in extreme

conditions of humidity, mechanical shock and vibration, power supply noise, etc. These microphones can also operate over a wide temperature range [102].

6. While the polarisation of the electret layer in ECMs can demand high voltages, the silicon-based diaphragms in MEMS microphones operate at lower voltages. In fact, the majority of the MEMS microphones can operate at a voltage supply provided by a small battery.
7. Unlike ECM, the sensitivity of the MEMS microphone does not degrade with the reflow solder temperatures. The sensitivity curve also maintains a stable profile over time.
8. The grounded metal packaging of the MEMS microphone (Faraday cage) provide better electrical shielding and mechanical protection to the transducer from external shock and vibrations.

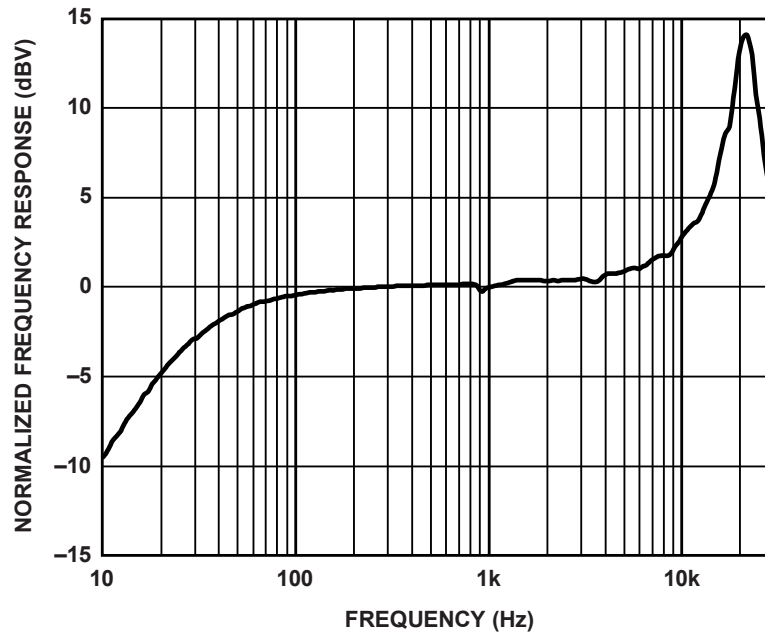


**Figure 2.10:** *Frequency response of a capacitive MEMS microphone (INMP411, Invensense Inc.) [105].*

#### 2.3.1.4 Summary

Following the detailed discussion on the types of acoustic sensors, it can be concluded that MEMS microphones offer certain advantages over contact microphone and ECM. For the design and development of the wearable device to sense the pulse sounds at the wrist, MEMS technology provides microphones with very small-factors resulting in

a smaller size of the device. The lower operating voltage allow the use of a small-sized battery, therefore, reducing the burden on the size of the overall system. A better and stable frequency response also ensure an accurate characterisation of the acoustic signal. Finally, a better performance in rejecting the interference from mechanical vibrations and external electrical noise further strengthens the choice of using the MEMS microphone in the design to sense the acoustic signal at the wrist. Therefore, the MEMS microphone has been used in the wearable device proposed for this work.

### 2.3.2 Power supply

The design approach for a wearable device as illustrated in Fig. 2.5 includes a miniaturised sensor which records the desired signal of interest from a body location and transmits the data to a nearby base station (such as a smartphone) to extract meaningful diagnostic parameters by employing sophisticated signal processing methods. While the biomedical monitoring devices are gaining huge attention in the market, factors such as reducing the size and weight of the device as well as operation over a long time are being continuously in demand from the consumers. One of the key considerations in the wearable design is the battery size which directly affects the size, weight and portability of the device. Efficient and reliable functioning of different components such as sensors, microcontrollers and other electronic components in the wearable design also depends on the power supply of the system. The current drawn by these components and the intended usage time plays a major role in governing the physical size of the battery. While a higher number of sensors are being integrated into a single device to monitor multiple physiological parameters, the power levels are falling short to sustain the higher power demand. This causes frustration among the users as a frequent recharge of batteries is often needed. Therefore, a wearable design should not only consider the physical size and capacity of the battery but it should also incorporate a maximum operation time of the device for widespread usage. Since the power is consumed at different nodes of the design, a proper choice of sensors, electronic components, wireless transmission, etc. plays a vital role in deciding the power draw and the operation time of the battery. Hence, the power requirements at every node of the design should be considered to maximise the operational lifetime of the wearable device.

There are different types of batteries available in the market for various applications. For smaller devices, the batteries mainly fall in one of the three categories: cylindrical cell, pouch cell and coin (or button) cell. While every type of battery cell may involve different chemical compositions, the chemistry of cylindrical cell is usually based on alkaline, nickel-metal-hydride or nickel-cadmium. Although these cells provide large power outputs, they are usually ideal for applications where size and space is not a constraint. The pouch cell batteries adopt lithium-polymer as the chemical composition and come in pouch shape with compact designs and smaller weights. They are widely used in mobile

devices where tight constraints on the height of the battery are placed. These batteries offer generous design flexibility as they can be manufactured in several form-factors and customised sizes. A major risk associated with the pouch cells is that they can overheat and puncture, if not handled carefully. Therefore, they can be dangerous to use and require great care during the operation. The pouch cell batteries are not user-replaceable and need a charging mechanism built into the device itself. This imposes additional constraints on the size of the device as more electronic circuitry for charging the battery is required. While the lithium-polymer batteries offer greatest design flexibility for wearable devices, the coin cell batteries are ideal for low power wearables as they are compact, user-replaceable and does not require any additional charging port in the design. The chemistry of these cells includes lithium, alkaline, silver oxide and zinc-air. Unlike pouch cells, the devices powered with coin cell batteries are safe to use and can be made waterproof. These batteries are relatively inexpensive, but require a holder to hold them in the device. A major drawback with the coin cell batteries is their low charge capacity restricting their use in applications where a low power draw is required.

Generally, the larger the size of the battery, the higher the power drive it can provide and vice-versa. For the wearable device to sense the pulse sounds at the wrist, it is important to consider this tradeoff between the size and the charge capacity of the battery to monitor the cardiac activity over a longer period of time. While the cylindrical cells provide higher power output, their larger size makes them unsuitable for the wearable design. Since the wearable device would be worn by the patient at the wrist, it might involve exposure to the moisture and require replacement of the battery. The safety issues and the charging circuit associated with the pouch cells does not make them feasible for the wearable design. Also, a customised pouch cell would require separate certification which might introduce higher costs in the design. Due to these reasons, the coin cell batteries prove to be the best choice for the power supply. The coin cells are available in many variants based on size, weight, charge capacity, supply voltage and supply current. The following sections discuss some important specifications of the coin-cell batteries to understand the design tradeoffs and achieve a longer operational lifetime by choosing the correct power supply in the wearable design.

### **2.3.2.1 Battery size**

The device size forms the most important factor in allowing the users to integrate such devices in their daily lives for vital sign monitoring. While a device typically consists of several electronic components including the sensors and signal conditioning and transmission circuitry, the invention of silicon fabrication technologies has allowed significant miniaturisation of these components. These electronic parts are readily available in surface-mount packages and consume very less PCB area in comparison to the battery size. Therefore, the size of the battery dominates the PCB area and will eventually



decide the form-factor of the wearable device. The coin-cell batteries are packaged in circular shape with different dimensions of diameter and height. The sizes of some commonly used non-rechargeable (primary) and rechargeable (secondary) coin-cell batteries in wearable designs are provided in Table 2.1. These batteries were primarily chosen as they cover a different spectrum of available sizes. Although the batteries with larger sizes are also available, they are not listed here as they would not be feasible for a device to be placed at the wrist. Only a few rechargeable Lithium batteries are listed here, mainly for comparison purposes, as similar size variants are available in lithium-manganese-dioxide chemistry with much higher energy densities. The rechargeable batteries with higher densities are generally bigger and not suitable for the wearable application here. The table also lists other parameters that are critical to the wireless design.

**Table 2.1:** *Specifications for commonly used non-rechargeable (primary) and rechargeable (secondary) batteries with varying physical sizes that can be used in different wearable applications [106], [107].*

Battery name	Chemical composition	Nominal voltage	Nominal capacity	Operating current (max)		Size		Weight
				Cont.	Pulse	Dia.	Height	
CR1220	LiMnO <sub>2</sub>	3.0 V	35 mAh	2 mA	5 mA	12.5 mm	2.0 mm	0.8 g
CR1620	LiMnO <sub>2</sub>	3.0 V	70 mAh	3 mA	8 mA	16.0 mm	2.0 mm	1.5 g
CR2032	LiMnO <sub>2</sub>	3.0 V	210 mAh	5 mA	20 mA	20.0 mm	3.2 mm	3.0 g
CR2430	LiMnO <sub>2</sub>	3.0 V	270 mAh	6 mA	21 mA	24.5 mm	3.0 mm	4.0 g
CR2477	LiMnO <sub>2</sub>	3.0 V	1000 mAh	3 mA	15 mA	24.5 mm	7.7 mm	8.3 g
LiR1620	LiCoO <sub>2</sub>	3.7 V	16 mAh	20 mA	32 mA	16.0 mm	2.0 mm	1.1 g
LiR2032	LiCoO <sub>2</sub>	3.7 V	40 mAh	40 mA	80 mA	20.0 mm	3.2 mm	2.7 g
LiR2450	LiCoO <sub>2</sub>	3.7 V	120 mAh	120 mA	240 mA	24.5 mm	5.0 mm	5.6 g

### 2.3.2.2 Supply voltage

Batteries, like other electronic components, are not ideal and carry small internal (leakage) resistance. Therefore, the full electric potential of the battery is not available to the connected load. A higher current draw from the battery will incur more loss across the internal resistance thereby causing a reduction in the supply voltage. Since all the other components in the electronic circuit function at a specific voltage, the supply voltage must meet such a requirement. Although electronic parts with different operating voltages can be used in the design, the use of boost-up or boost-down circuits to level up or level down the supply voltage levels can significantly increase the hardware overhead in the design. Such circuits also draw current for their operation, therefore, adding further constraints on the power budget of the system. Hence, it is advisable to use components with same operating voltages without trading off the quality of signal acquisition. Since a majority of the MEMS microphones and microcontrollers (with Bluetooth low-energy

functionality) available in the market operate in a voltage range of 1.5 - 3.6 V and 1.7 - 3.6 V respectively, the primary coin-cell battery proves to be an excellent choice for the power supply of the wearable design.

### 2.3.2.3 Supply current

The battery manufacturers provide two current specifications: maximum continuous current ( $I_{cont}$ ) and maximum pulse current ( $I_{pulse}$ ). While  $I_{cont}$  defines the maximum average current that can be drawn from the battery for continual usage,  $I_{pulse}$  is the maximum current that the battery can provide for very short bursts of time. It is intuitive to assume that a battery with a capacity of 210 mAH can supply a current of 210 mA for one hour of operation, or it can drive 1 mA of current for 210 hours. Due to the limitation of  $I_{cont}$ , this assumption is not true in practice. The battery capacity reduces rapidly with an increase in the discharge current. Therefore, the average current drawn from the battery for a particular application must be smaller than  $I_{cont}$  for the battery to function at its effective capacity.

Since most of the wearable devices incorporate wireless functionality, the transmission of data packets over the wireless channel requires a higher current draw over short periods. The choice of battery, therefore, must ensure that the maximum current demanded by the wearable device at any point of time does not exceed the  $I_{pulse}$  value. The variation of current in such applications can cause a significant ripple in the supply voltage because of variable drop across the internal resistance of the battery. Such voltage variations must not hinder the functionality of the electronic components and a constant supply voltage must be ensured by the battery. In cases where a single battery cannot cope up with such demands, multiple batteries can be connected to guarantee a regulated power supply. However, this would require few diodes to prevent any undesired charging of the battery and impose more constraints on the device size.

The current  $I_{pulse}$  defines the maximum pulse current and its value decreases exponentially with the pulse hold time [108]. The higher the pulse hold time, the lower the value of the maximum pulse current that is available to the circuit. Therefore, the battery choice should be compatible with the choice of the transceiver block to ensure the capability of the battery to provide maximum pulse current for the desired pulse hold time. In Table 2.1, we can observe that the secondary batteries offer higher values of  $I_{cont}$  and  $I_{pulse}$  than the primary batteries, but they often discharge too quickly limiting the operational lifetime of the battery. Hence, a tradeoff between the discharge current and the operational lifetime of the battery also exists.

### 2.3.2.4 Battery capacity and life

The capacity of the battery is another critical parameter to predict the operational lifetime for its usage. This is particularly important in applications where long term phys-

iological monitoring is desired as an intermediate power failure can miss signal events important for diagnosis. The nominal capacity of the battery is defined as the total ampere-hours available when the battery is discharged at a certain discharge current (also known as C-rate) from a fully charged state to its cut-off voltage. It is calculated by multiplying the discharge current (in Amps) with the discharge time (in hours). The nominal capacity does not remain constant and varies with respect to the discharge current. This varying capacity as a function of the discharge current is also known as the effective capacity of the battery. Since the current consumption of the device is generally higher than the maximum average current supplied by the battery, for at least short periods, the effective capacity is smaller than the nominal capacity of the battery.

The effective capacity of the battery plays an important role in determining the operational lifetime of the battery. The selection of a battery for the wearable design not only depends on its size and supply voltage, but it must also meet the average and maximum current requirements of the device so that the effective capacity of the battery does not deviate much from its nominal capacity. A close resemblance would allow the battery to function for a longer time as its lifetime varies inversely with the average current consumption of the device [108].

### **2.3.2.5 Battery choice**

The wearable device proposed in this thesis is designed to record pulse sounds from the adult population. A proper attachment of the device requires the battery to fit on one side of the wrist. Another requirement is that the entire battery can be contained in the middle part of the wrist as a placement on the curved contour can result in discomfort for the user. The wrist circumference in the adult population varies between 120 and 220 mm [109], [110]. Hence, a battery with a diameter of less than 25 mm can easily fit an individual with minimum wrist circumference. For end-users, it is also important that the weight of the overall device remains less than 10 g to allow a prolonged usage. While the surface mount components and PCB substrate add up to the weight, the battery contributes maximum to the overall weight of the device. A battery with less than 5 g of weight should be ideal for such a wearable design.

Since the battery life depends on the current consumption of the device, a battery with higher capacity provides a higher current drive and better operation time. Although the supply voltage and operating current depend on the electronic circuitry of the wearable design, the tradeoff between different battery parameters discussed above can be analysed to finalise the choice of the battery. As an illustration, the CR2032 and CR2430 coin-cell batteries in Table 2.1 seem to be better choices for the design of acoustic wearable device because of their low size and weight, and better nominal capacity. The secondary coin-cell batteries such as LiR2032 and LiR2450 can also be used in applications requiring higher operating currents. These batteries are cost-effective as they allow recharging for

a few hundreds of cycles. However, they are quite limited in their nominal capacity and would run out quickly.

### 2.3.3 Data acquisition hardware

Referring to Fig. 2.5, the data acquisition hardware is responsible to collect the physiological signal from the sensor node and apply signal conditioning for better data packaging and transmission to the nearby base station. The MEMS microphones provide different output formats from the perspective of electronic interfacing. The ASIC in the microphone package can contain the required circuitry to produce analogue or digital outputs. The digital (or pulse density modulated) microphones already incorporate an ADC into the package to accept an external clock and return the sampled data at the supplied clock frequency. While these microphones provide better noise immunity than their analogue counterparts, they are usually power-inefficient and consume power in the order of 500  $\mu\text{A}$  to 2 mA. Hence, they mostly find their applications in smartphones, cameras, laptops, etc. where a higher power budget is available. Since the power budget of the system directly affects the size of the battery, the analogue MEMS microphones prove to be a better choice. These microphones only consume power in the order of 15  $\mu\text{A}$  to 500  $\mu\text{A}$ . The availability of sophisticated microcontrollers with high power-efficiency, and integrated ADC and BLE blocks provide a high degree of freedom when using the analogue microphones in the wearable design.

The ASIC circuitry in the analogue microphones produces an AC (alternating current) signal superimposed on a DC (direct current) bias voltage corresponding to the sound waves. Since the vibrations produced by the pulse sounds are generally weak in strength, these AC ripples are smaller in amplitude. The microphone output can also contain frequencies in larger bandwidth as compared to the frequency content of the pulse sounds. Therefore, it is important to design an analogue front end which can filter out the undesired frequencies, and amplify the acoustic signal to match the amplitude range of the microphone output with the dynamic range of the ADC for maximum resolution. As an illustration, the circuit in Fig. 2.11(a) presents a simple analogue front end to filter and amplify the microphone output. Since the microphone output is usually biased at 0.7-0.8 V, the high pass filter formed by the capacitor  $C_1$  and resistor  $R_1$  completely blocks the DC signal. The high pass filter is followed by an inverting amplifier which amplifies the weak pulse sounds to match the ADC range. Since the microphone bandwidth is much larger than the desired frequency content (heart sounds  $< 150$  Hz), the analogue front end also incorporate a simple first-order passive RC low pass filter to restrict the signal bandwidth. The use of a low pass filter also avoids any anti-aliasing introduced due to the sampling at the ADC stage. The aliasing caused by the sampling reflects all the frequencies that are higher than the Nyquist frequency (i.e. half of the sampling frequency) back into the signal. This must be avoided for an accurate characterisation of the signal. The

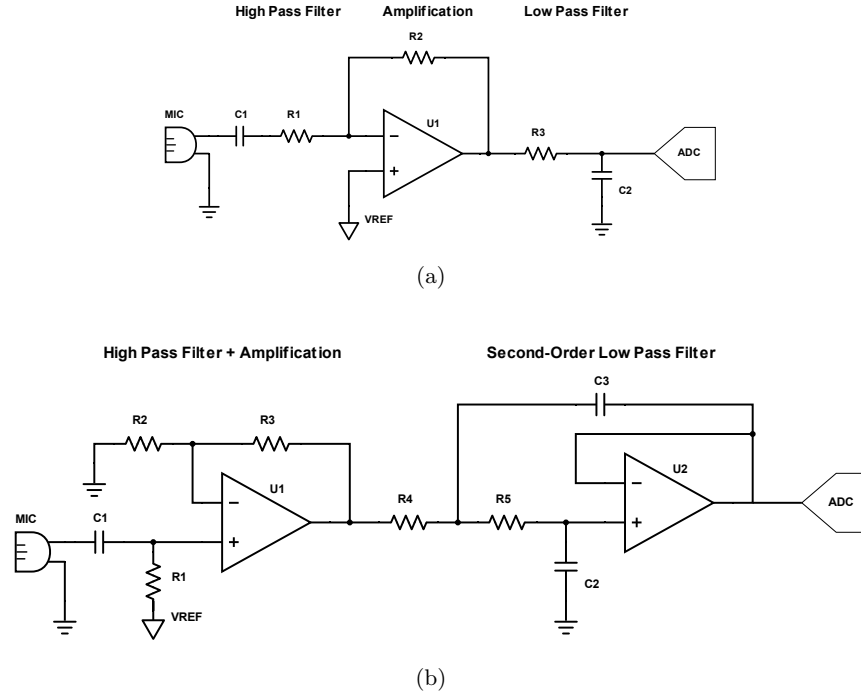


**Figure 2.11:** Analogue front end designs for data acquisition from the microphone. (a) The first design includes a high pass filter followed by an inverting amplifier and first-order passive RC low pass filter. (b) The second design includes a high pass filter followed by a non-inverting amplifier and a second-order active low pass filter.

second design of the analogue front end in Fig. 2.11(b) uses a non-inverting configuration for the amplification of the signal. A second-order active low pass filter is used instead of a simple RC filter to attenuate the higher frequencies with a steeper roll-off. This design also provides a relatively lower output impedance to the ADC allowing a better signal conversion, however, an extra operational amplifier might cause some hardware overhead. The values of the electronic components including the resistors and capacitors are chosen depending on the specifications of the wearable design.

In summary, the analogue front end in the wearable design conditions the acoustic signal for its effective conversion from the analogue to the digital domain at the ADC stage. Since it is crucial to avoid the anti-aliasing of the signal during conversion, a tradeoff between the filter order and the sampling frequency must be studied. For a simple first-order passive RC low pass filter, the frequency response after the cut-off frequency decreases at a slope of -20 dB/decade. This means that the gain corresponding to the higher frequencies attenuates at a slower rate. While the RC filter can be implemented in a very small PCB area, a higher ADC sampling frequency is required to avoid any aliasing caused by the frequencies beyond the cut-off frequency of the low pass filter. A higher sampling frequency would produce more data samples that need to be bundled

in data packets to be sent at the data transmission stage. An increased amount of data transmission would consume more power and reduce the battery lifetime. Instead, higher-order filters can be used in the wearable design at the cost of increased PCB area to realise a steeper roll-off in the frequency response of the filter. This would enable a reduction in the sampling frequency and the number of data packet transmissions. Therefore, the sampling frequency of the signal in combination with the filter order must be decided to understand the ADC requirements.

In relation to the PCB area, the advancements in the chip fabrication technologies have made it possible to integrate multiple signal channels with ADC and transceiver blocks in a single surface mount package. While standalone ADCs and transceivers are also available in the market, the integration of these blocks in SoCs (system-on-chip) reduces the overall size of the device. The SoCs typically implement the successive approximation register (SAR) or Sigma-Delta architecture of the ADCs. A successive approximation converter uses an iterative comparison of the signal levels with different proportions of the reference voltage to convert the signal into output bits. The sigma-delta converter, on the other hand, makes use of oversampling the signal and applying digital filters to achieve high conversion accuracy. Since the oversampling of data is undesirable, SAR ADCs are usually preferred over Sigma-Delta ADCs in wearable applications. In comparison to Sigma-Delta ADCs, the SAR ADCs also operate at a higher speed and require lower conversion current [111]. After the acquisition and conversion of the data in the digital domain, the data can be stored in SoC buffers to eventually bundle them in specific frame structures to be sent to the wireless transmitter.

## 2.4 Designing the wearable acoustic sensor

The last few sections discussed different constraints and tradeoffs involved in every stage of the wearable design presented in Fig. 2.5. Such an understanding can be utilised to design a wearable hardware platform for sensing the pulse sounds at the wrist. Since the wearable architecture involves sending the data to a nearby base station for signal processing, the hardware platform consists of the microphone sensor, an analogue front end, ADC and the transmitter block as shown in Fig. 2.12. The wearable device uses a single-channel, ultra-low noise, omnidirectional MEMS microphone sensor (INMP411, InvenSense Inc.) to sense the skin surface vibrations at the wrist. This microphone was chosen because of its low size of  $4.72 \times 3.76 \times 1.0$  mm, high SNR of 62 dBA, a uniform sensitivity of -46 dBV between 28 Hz and 20 kHz, and low power consumption of 210 uA at 3.3 V supply [105]. However, any microphone of similar size and specifications can be used to design the acoustic sensor. The chosen microphone has a DC offset of 0.8 V, however, all the proposed algorithms in the subsequent chapters of this thesis ensure the offset removal by following the normalisation procedure. The sensor node is followed by an analogue front end which blocks the DC bias of the microphone, amplifies the acoustic

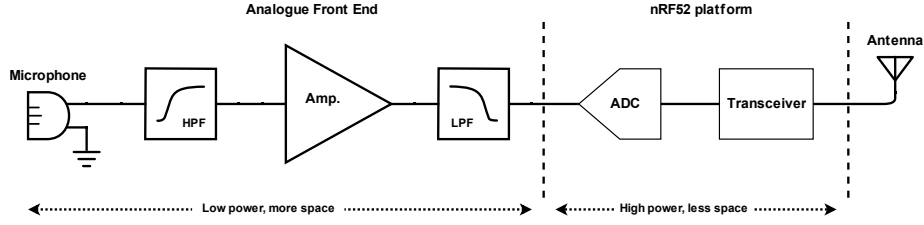


**Figure 2.12:** *Hardware design flow (consisting of the microphone, an analogue front end and nRF52 platform) for the acoustic wearable device to sense pulse sounds at the wrist.*

signal, and removes the undesirable frequency content from the signal to prevent anti-aliasing at the ADC stage. Since any electronic noise entering the microphone is amplified by the analogue front end, only electronic components with noise levels less than 10 dB or more in comparison to the noise floor of the microphone are chosen for the wearable design. The availability of multiple operational amplifiers in a single surface mount package is utilised in the design to implement an amplifier and second-order low pass filter without burdening the PCB area. The realisation of higher-order low pass filter allows the use of a low sampling frequency in the ADC block, therefore, reducing the overall power consumption of the device. The hardware platform uses the MCP6002 chip (Microchip Technology Inc.) to implement the analogue front end of the wearable design. It operates over a wide voltage range and consumes low supply current of 100  $\mu\text{A}$  per amplifier. The amplifier chip also provides a high power supply rejection ratio and common-mode rejection ratio. The conditioned analogue signal is subsequently connected to a 12-bit SAR ADC for its conversion to the digital domain. As discussed before, it is advisable to use a single microcontroller chip which incorporates both the ADC and the transceiver block in a single package to reduce the size constraints on the hardware. The wearable design uses the nRF52 series SoC platform for signal conversion and transmission. The data transmission is performed by utilising the Bluetooth low energy protocol available on the SoC platform and using a 2.4 GHz chip antenna (Johanson Technology Inc.).

While the analogue front end consumes more PCB space in comparison to the nRF52 SoC package, it consumes less overall power as demonstrated in Table 2.2. The PCB space can be further optimised by implementing the analogue front end in an ASIC, however, it will involve high fabrication costs and is not suitable for hardware prototyping. Since the sensor and the analogue front end operate at a duty cycle of 100%, a continuous current of less than 0.5 mA is demanded from the battery. Depending on the sampling frequency of the ADC and the clock of the wireless transmission, the battery has to supply a maximum current of approximately 6.5 mA at any instance. Based on these requirements, both the non-rechargeable (CR2032) and rechargeable (LiR2032) versions of the 2032 battery size are suitable as the power source of the proposed wearable device.

**Table 2.2:** *Current consumption of different components of the hardware platform.*

Block Name	Component Name	Peak Current
Sensor	Microphone	0.210 mA
Analogue front end	Voltage regulator	0.006 mA
	Amplifier	0.100 mA
	Filter	0.100 mA
	Reference voltage	0.027 mA
ADC	12-bit SAR ADC	0.700 mA
Wireless transmission	nRF52 transmitter	5.300 mA
Total	—	6.443 mA

From the design perspective, the selection of the surface mount components for every node of the wearable architecture allows them to be soldered on a PCB. Since the hardware contains a mixed-signal design, the analogue and digital blocks are layout in different regions of the PCB to minimise the noise interference. Also, middle layers of the 4-layer PCB are completely grounded to ensure proper grounding of the circuit. The hardware platform is implemented in two different PCBs that are connected through a thin and flexible insulated cable. The first PCB only contains the battery and is placed on the wrist side opposite to the radial artery. The microphone along with the analogue front end and the nRF52 platform are soldered on the second PCB. This PCB is attached to the radial artery to record the pulse sounds. The PCB is enclosed in a rectangular enclosure as shown in Fig. 2.13. The overall weight of the final wireless prototype is 8 g, although note that this can be further optimised by using more sophisticated manufacturing processes. In addition, its size ( $27 \times 20$  mm) and shape are designed so that it can be easily attached to the wrist using a 3M double-sided medical adhesive tape to keep the sensor affix to the measuring site, for long-term usage.

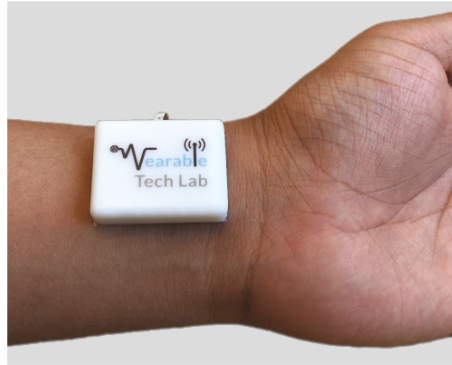


**Figure 2.13:** *Wearable device used to acquire acoustic signals. The device consists of a MEMS microphone sensor integrated with Bluetooth low energy transmission.*



## References

- [1] R. Berne and M. Levy, “Cardiovascular Physiology 4th Edn, Mosby,” *St. Louis*, 1981.
- [2] S. Walsh and E. King, *Pulse Diagnosis E-Book: A Clinical Guide*. Elsevier Health Sciences, 2007.
- [3] M. F. O’Rourke, “The arterial pulse in health and disease,” *American Heart Journal*, vol. 82, no. 5, pp. 687 – 702, 1971. [Online]. Available: <http://www.sciencedirect.com/science/article/pii/0002870371903401>
- [4] F. N. Van de Vosse and N. Stergiopoulos, “Pulse wave propagation in the arterial tree,” *Annual Review of Fluid Mechanics*, vol. 43, pp. 467–499, 2011.
- [5] B. B. Hamrell, *Cardiovascular Physiology*. Boca Raton: CRC Press, 2018.
- [6] A. C. Guyton and J. E. Hall, “Textbook of medical physiology 11th ed,” *Elsevier Saunders*, pp. 788–817, 2006.
- [7] J. Stettler, P. Niederer, and M. Anliker, “Nonlinear mathematical models of the arterial system: effects of bifurcations, wall viscoelasticity, stenoses, and counterpulsation on pressure and flow pulses,” *Handbook of Bioengineering eds. R. Skalak and S. Chien*, pp. 17–1, 1987.
- [8] Features of the Pulse Waveform. [Online]. Available: <http://www.uhsmed.com/bp-management/features-of-the-pulse-waveform.php>
- [9] G. Lowe, A. Lee, A. Rumley, J. Price, and F. Fowkes, “Blood viscosity and risk of cardiovascular events: the Edinburgh Artery Study,” *British journal of haematology*, vol. 96, no. 1, pp. 168–173, 1997.
- [10] S. R. Grabowski and G. J. Tortora, *Principles of anatomy and physiology*. Wiley, 2000.
- [11] Case courtesy of Dr Craig Hacking, rID: 70474. [Online]. Available: <https://radiopaedia.org/>
- [12] A. Blitz, R. M. Osterday, and R. F. Brodman, “Harvesting the radial artery,” *Annals of Cardiothoracic Surgery*, vol. 2, no. 4, 2013. [Online]. Available: <http://www.annalscts.com/article/view/2418>
- [13] C.-H. Chen, E. Nevo, B. Fetcs, P. H. Pak, F. C. Yin, W. L. Maughan, and D. A. Kass, “Estimation of central aortic pressure waveform by mathematical transformation of radial tonometry pressure: validation of generalized transfer function,” *Circulation*, vol. 95, no. 7, pp. 1827–1836, 1997.
- [14] S. Standring, *Gray’s anatomy e-book: the anatomical basis of clinical practice*. Elsevier Health Sciences, 2015.
- [15] K. L. Moore, A. F. Dalley, and A. M. Agur, *Clinically oriented anatomy*. Lippincott Williams & Wilkins, 2013.
- [16] R. J. Hankinson, *The Cambridge Companion to Galen*. Cambridge University Press, 2008.
- [17] W. Harvey *et al.*, “Exercitatio anatomica de motu cordis et sanguinis in animalibus,” *Frankfurt am Main*, vol. 1628, 1928.
- [18] E.-J. Marey, *Recherches sur le pouls au moyen d’un nouvel appareil enregistreur le sphygmographie...* E. Thunot et cie, 1860.
- [19] F. Mohamed, “The physiology and clinical use of the sphygmograph,” *Med Times Gazette*, vol. 1, p. 62, 1872.
- [20] K. H. Parker, “A brief history of arterial wave mechanics,” *Medical & biological engineering & computing*, vol. 47, no. 2, pp. 111–118, 2009.
- [21] C. T. Lee and L. Y. Wei, “Spectrum analysis of human pulse,” *IEEE Transactions on Biomedical Engineering*, no. 6, pp. 348–352, 1983.

- [22] S. C. Mukhopadhyay, "Wearable sensors for human activity monitoring: A review," *IEEE Sensors Journal*, vol. 15, no. 3, pp. 1321–1330, 2015.
- [23] Q. Zhang, D. Zhou, and X. Zeng, "A novel machine learning-enabled framework for instantaneous heart rate monitoring from motion-artifact-corrupted electrocardiogram signals," *Physiological measurement*, vol. 37, no. 11, p. 1945, 2016.
- [24] Q. Zhang, D. Zhou, and X. Zeng, "A novel framework for motion-tolerant instantaneous heart rate estimation by phase-domain multiview dynamic time warping," *IEEE Transactions on Biomedical Engineering*, vol. 64, no. 11, pp. 2562–2574, 2016.
- [25] S. M. Salehizadeh, Y. Noh, and K. H. Chon, "Heart rate monitoring during intense physical activities using a motion artifact corrupted signal reconstruction algorithm in wearable electrocardiogram sensor," in *2016 IEEE First International Conference on Connected Health: Applications, Systems and Engineering Technologies (CHASE)*. IEEE, 2016, pp. 157–162.
- [26] Q. Zhang, D. Zhou, and X. Zeng, "A novel single-arm-worn 24 h heart disease monitor empowered by machine intelligence," *Biomedical Signal Processing and Control*, vol. 42, pp. 129–133, 2018.
- [27] Q. Zhang, D. Zhou, and X. Zeng, "Highly wearable cuff-less blood pressure and heart rate monitoring with single-arm electrocardiogram and photoplethysmogram signals," *Biomedical engineering online*, vol. 16, no. 1, p. 23, 2017.
- [28] S. S. Thomas, V. Nathan, C. Zong, K. Soundarapandian, X. Shi, and R. Jafari, "Biowatch: A noninvasive wrist-based blood pressure monitor that incorporates training techniques for posture and subject variability," *IEEE journal of biomedical and health informatics*, vol. 20, no. 5, pp. 1291–1300, 2015.
- [29] S. Krachunov, C. Beach, A. J. Casson, J. Pope, X. Fafoutis, R. J. Piechocki, and I. Craddock, "Energy efficient heart rate sensing using a painted electrode ECG wearable," in *2017 Global Internet of Things Summit (GloTS)*. IEEE, 2017, pp. 1–6.
- [30] S. E. Stahl, H.-S. An, D. M. Dinkel, J. M. Noble, and J.-M. Lee, "How accurate are the wrist-based heart rate monitors during walking and running activities? Are they accurate enough?" *BMJ open sport & exercise medicine*, vol. 2, no. 1, p. e000106, 2016.
- [31] L. Cadmus-Bertram, R. Gangnon, E. J. Wirkus, K. M. Thraen-Borowski, and J. Gorzelitz-Liebhauser, "The accuracy of heart rate monitoring by some wrist-worn activity trackers," *Annals of internal medicine*, vol. 166, no. 8, pp. 610–612, 2017.
- [32] E. Jo, K. Lewis, D. Directo, M. J. Kim, and B. A. Dolezal, "Validation of biofeedback wearables for photoplethysmographic heart rate tracking," *Journal of sports science & medicine*, vol. 15, no. 3, p. 540, 2016.
- [33] R. Metz, "The struggle for accurate measurements on your wrist," 2015.
- [34] D. Biswas, N. Simues-Capela, C. Van Hoof, and N. Van Helleputte, "Heart Rate Estimation From Wrist-Worn Photoplethysmography: A Review," *IEEE Sensors Journal*, 2019.
- [35] M. B. Mashhadi, E. Asadi, M. Eskandari, S. Kiani, and F. Marvasti, "Heart rate tracking using wrist-type photoplethysmographic (PPG) signals during physical exercise with simultaneous accelerometry," *IEEE Signal Processing Letters*, vol. 23, no. 2, pp. 227–231, 2015.
- [36] M. R. Ram, K. V. Madhav, E. H. Krishna, N. R. Komalla, and K. A. Reddy, "A novel approach for motion artifact reduction in PPG signals based on AS-LMS adaptive filter," *IEEE Transactions on Instrumentation and Measurement*, vol. 61, no. 5, pp. 1445–1457, 2011.
- [37] H. Han and J. Kim, "Artifacts in wearable photoplethysmographs during daily life motions and their reduction with least mean square based active noise cancellation method," *Computers in biology and medicine*, vol. 42, no. 4, pp. 387–393, 2012.

- [38] K. Chan and Y. Zhang, "Adaptive reduction of motion artifact from photoplethysmographic recordings using a variable step-size LMS filter," in *SENSORS, 2002 IEEE*, vol. 2. IEEE, 2002, pp. 1343–1346.
- [39] A. Temko, "Accurate heart rate monitoring during physical exercises using PPG," *IEEE Transactions on Biomedical Engineering*, vol. 64, no. 9, pp. 2016–2024, 2017.
- [40] B. Lee, J. Han, H. J. Baek, J. H. Shin, K. S. Park, and W. J. Yi, "Improved elimination of motion artifacts from a photoplethysmographic signal using a Kalman smoother with simultaneous accelerometry," *Physiological measurement*, vol. 31, no. 12, p. 1585, 2010.
- [41] B. S. Kim and S. K. Yoo, "Motion artifact reduction in photoplethysmography using independent component analysis," *IEEE transactions on biomedical engineering*, vol. 53, no. 3, pp. 566–568, 2006.
- [42] J. Yao and S. Warren, "A short study to assess the potential of independent component analysis for motion artifact separation in wearable pulse oximeter signals," in *2005 IEEE Engineering in Medicine and Biology 27th Annual Conference*. IEEE, 2006, pp. 3585–3588.
- [43] R. Krishnan, B. Natarajan, and S. Warren, "Two-stage approach for detection and reduction of motion artifacts in photoplethysmographic data," *IEEE transactions on biomedical engineering*, vol. 57, no. 8, pp. 1867–1876, 2010.
- [44] E. Khan, F. Al Hossain, S. Z. Uddin, S. K. Alam, and M. K. Hasan, "A robust heart rate monitoring scheme using photoplethysmographic signals corrupted by intense motion artifacts," *IEEE Transactions on Biomedical engineering*, vol. 63, no. 3, pp. 550–562, 2015.
- [45] X. Sun, P. Yang, Y. Li, Z. Gao, and Y.-T. Zhang, "Robust heart beat detection from photoplethysmography interlaced with motion artifacts based on empirical mode decomposition," in *Proceedings of 2012 IEEE-EMBS International Conference on Biomedical and Health Informatics*. IEEE, 2012, pp. 775–778.
- [46] E. Grisan, G. Cantisani, G. Tarroni, S. K. Yoon, and M. Rossi, "A supervised learning approach for the robust detection of heart beat in plethysmographic data," in *2015 37th Annual International Conference of the IEEE Engineering in Medicine and Biology Society (EMBC)*. IEEE, 2015, pp. 5825–5828.
- [47] Z. Zhang, Z. Pi, and B. Liu, "Troika: A general framework for heart rate monitoring using wrist-type photoplethysmographic signals during intensive physical exercise," *IEEE Transactions on Biomedical Engineering*, vol. 62, no. 2, pp. 522–531, 2015.
- [48] Z. Zhang, "Photoplethysmography-based heart rate monitoring in physical activities via joint sparse spectrum reconstruction," *IEEE transactions on biomedical engineering*, vol. 62, no. 8, pp. 1902–1910, 2015.
- [49] M. T. Islam, I. Zabir, S. T. Ahamed, M. T. Yasar, C. Shahnaz, and S. A. Fattah, "A time-frequency domain approach of heart rate estimation from photoplethysmographic (PPG) signal," *Biomedical Signal Processing and Control*, vol. 36, pp. 146–154, 2017.
- [50] Y. Zhang, B. Liu, and Z. Zhang, "Combining ensemble empirical mode decomposition with spectrum subtraction technique for heart rate monitoring using wrist-type photoplethysmography," *Biomedical Signal Processing and Control*, vol. 21, pp. 119–125, 2015.
- [51] S. Chowdhury, R. Hyder, M. S. Hafiz, and M. A. Haque, "Real time robust heart rate estimation from wrist-type PPG signals using multiple reference adaptive noise cancellation," *IEEE journal of biomedical and health informatics*, 2016.
- [52] J. Xiong, L. Cai, F. Wang, and X. He, "Svm-based spectral analysis for heart rate from multi-channel WPPG sensor signals," *Sensors*, vol. 17, no. 3, p. 506, 2017.

- [53] D. Jarchi and A. J. Casson, "Towards photoplethysmography-based estimation of instantaneous heart rate during physical activity," *IEEE Transactions on Biomedical Engineering*, vol. 64, no. 9, pp. 2042–2053, 2017.
- [54] L. Yang, M. Liu, L. Dong, Y. Zhao, and X. Liu, "Motion-compensated non-contact detection of heart rate," *Optics Communications*, vol. 357, pp. 161–168, 2015.
- [55] C. Zhou, J. Feng, J. Hu, and X. Ye, "Study of artifact-resistive technology based on a novel dual photoplethysmography method for wearable pulse rate monitors," *Journal of medical systems*, vol. 40, no. 3, p. 56, 2016.
- [56] M. Kos and I. Kramberger, "A wearable device and system for movement and biometric data acquisition for sports applications," *IEEE Access*, vol. 5, pp. 6411–6420, 2017.
- [57] K. Malhi, S. C. Mukhopadhyay, J. Schnepfer, M. Haefke, and H. Ewald, "A zigbee-based wearable physiological parameters monitoring system," *IEEE sensors journal*, vol. 12, no. 3, pp. 423–430, 2012.
- [58] B.-G. Lee, B.-L. Lee, and W.-Y. Chung, "Smartwatch-based driver alertness monitoring with wearable motion and physiological sensor," in *2015 37th Annual International Conference of the IEEE Engineering in Medicine and Biology Society (EMBC)*. IEEE, 2015, pp. 6126–6129.
- [59] A. G. Bonomi, F. Schipper, L. M. Eerikäinen, J. Margarito, R. M. Aarts, S. Babaeizadeh, H. M. de Morree, and L. Dekker, "Atrial fibrillation detection using photo-plethysmography and acceleration data at the wrist," in *2016 Computing in Cardiology Conference (CinC)*. IEEE, 2016, pp. 277–280.
- [60] A. Tarniceriu, J. Harju, A. Vehkaoja, J. Parak, R. Delgado-Gonzalo, P. Renevey, A. Yli-Hankala, and I. Korhonen, "Detection of beat-to-beat intervals from wrist photoplethysmography in patients with sinus rhythm and atrial fibrillation after surgery," in *2018 IEEE EMBS International Conference on Biomedical & Health Informatics (BHI)*. IEEE, 2018, pp. 133–136.
- [61] H. J. Baek and J. Shin, "Effect of Missing Inter-Beat Interval Data on Heart Rate Variability Analysis Using Wrist-Worn Wearables," *Journal of medical systems*, vol. 41, no. 10, p. 147, 2017.
- [62] J. Allen, "Photoplethysmography and its application in clinical physiological measurement," *Physiological measurement*, vol. 28, no. 3, p. R1, 2007.
- [63] C. Wang, Z. Li, and X. Wei, "Monitoring heart and respiratory rates at radial artery based on ppg," *Optik-International Journal for Light and Electron Optics*, vol. 124, no. 19, pp. 3954–3956, 2013.
- [64] H.-H. Chang, C.-C. Hsu, C.-Y. Chen, W.-K. Lee, H.-T. Hsu, K.-K. Shyu, J.-R. Yeh, P.-J. Lin, and P.-L. Lee, "A method for respiration rate detection in wrist ppg signal using Holo-Hilbert spectrum," *IEEE Sensors Journal*, vol. 18, no. 18, pp. 7560–7569, 2018.
- [65] A. Keikhosravi and E. Zahedi, "Effect of deep breath on the correlation between the wrist and finger photoplethysmograms," in *2012 19th Iranian Conference of Biomedical Engineering (ICBME)*. IEEE, 2012, pp. 135–138.
- [66] A. Qasem, A. Avolio, and G. Frangakis, "A neural network for estimation of aortic pressure from the radial artery pressure pulse," in *2001 Conference Proceedings of the 23rd Annual International Conference of the IEEE Engineering in Medicine and Biology Society*, vol. 1. IEEE, 2001, pp. 237–239.
- [67] V. Sohani, E. Zahedi, M. M. Ali, K. B. Gan, and K. Chellappan, "A dynamic model between central aortic pressure and radial photoplethysmogram: Experimental proof of concept," in *2014 5th International Conference on Intelligent and Advanced Systems (ICIAS)*. IEEE, 2014, pp. 1–4.

- [68] E. Zahedi, V. Sohani, M. Ali, K. Chellappan, and G. K. Beng, "Experimental feasibility study of estimation of the normalized central blood pressure waveform from radial photoplethysmogram," *Journal of healthcare engineering*, vol. 6, no. 1, pp. 121–144, 2015.
- [69] S. Loukogeorgakis, R. Dawson, N. Phillips, C. N. Martyn, and S. E. Greenwald, "Validation of a device to measure arterial pulse wave velocity by a photoplethysmographic method," *Physiological measurement*, vol. 23, no. 3, p. 581, 2002.
- [70] A. Attarpour, A. Mahnam, A. Aminitabar, and H. Samani, "Cuff-less continuous measurement of blood pressure using wrist and fingertip photo-plethysmograms: Evaluation and feature analysis," *Biomedical Signal Processing and Control*, vol. 49, pp. 212–220, 2019.
- [71] S. Rajala, H. Lindholm, and T. Taipalus, "Comparison of photoplethysmogram measured from wrist and finger and the effect of measurement location on pulse arrival time," *Physiological measurement*, vol. 39, no. 7, p. 075010, 2018.
- [72] K. Priyanka, P. C.-P. Chao, T.-Y. Tu, Y.-H. Kao, M.-H. Yeh, R. Pandey, and F. P. Eka, "Estimating Blood Pressure via Artificial Neural Networks Based on Measured Photoplethysmography Waveforms," in *2018 IEEE SENSORS*. IEEE, 2018, pp. 1–4.
- [73] L. Xiang, Z. Xu, L. Peng, H. Xiaohui, and C. Hongda, "An 8.12  $\mu$ w wavelet denoising chip for PPG detection and portable heart rate monitoring in 0.18  $\mu$ m CMOS," *Journal of Semiconductors*, vol. 37, no. 5, p. 055006, 2016.
- [74] J. Kim, N. Kim, M. Kwon, and J. Lee, "Attachable Pulse Sensors Integrated with Inorganic Optoelectronic Devices for Monitoring Heart Rates at Various Body Locations," *ACS applied materials & interfaces*, vol. 9, no. 31, pp. 25 700–25 705, 2017.
- [75] C. Li, X. Peng, H. Zhang, C. Wang, S. Fan, and S. Cao, "Wearable side-polished fiber Bragg grating sensor for pulse wave and throat sound detection," in *SENSORS, 2017 IEEE*. IEEE, 2017, pp. 1–3.
- [76] S. Zang, Q. Wang, Q. Mi, J. Zhang, and X. Ren, "A facile, precise radial artery pulse sensor based on stretchable graphene-coated fiber," *Sensors and Actuators A: Physical*, vol. 267, pp. 532–537, 2017.
- [77] D. Jia, J. Chao, S. Li, H. Zhang, Y. Yan, T. Liu, and Y. Sun, "A fiber Bragg grating sensor for radial artery pulse waveform measurement," *IEEE Transactions on Biomedical Engineering*, vol. 65, no. 4, pp. 839–846, 2017.
- [78] S. Liu, S. Zhang, Y. Zhang, X. Geng, J. Zhang, and H. Zhang, "A novel flexible pressure sensor array for depth information of radial artery," *Sensors and Actuators A: Physical*, vol. 272, pp. 92–101, 2018.
- [79] Y.-J. An, G.-H. Yun, S. W. Kim, and J.-G. Yook, "Wrist pulse detection system based on changes in the near-field reflection coefficient of a resonator," *IEEE Microwave and Wireless Components Letters*, vol. 24, no. 10, pp. 719–721, 2014.
- [80] Y.-J. An, B.-H. Kim, G.-H. Yun, S.-W. Kim, S.-B. Hong, and J.-G. Yook, "Flexible non-constrained RF wrist pulse detection sensor based on array resonators," *IEEE transactions on biomedical circuits and systems*, vol. 10, no. 2, pp. 300–308, 2016.
- [81] S. W. Kim, S. B. Choi, Y.-J. An, B.-H. Kim, D. W. Kim, and J.-G. Yook, "Heart rate detection during sleep using a flexible RF resonator and injection-locked PLL sensor," *IEEE Transactions on Biomedical Engineering*, vol. 62, no. 11, pp. 2568–2575, 2015.
- [82] J. He, M. Wang, X. Li, G. Li, and L. Lin, "Pulse wave detection method based on the bio-impedance of the wrist," *Review of Scientific Instruments*, vol. 87, no. 5, p. 055001, 2016.

- [83] F.-K. Wang, M.-C. Tang, S.-C. Su, and T.-S. Horng, "Wrist Pulse Rate Monitor Using Self-Injection-Locked Radar Technology," *Biosensors*, vol. 6, no. 4, p. 54, 2016.
- [84] S. Mandal, L. Turicchia, and R. Sarpeshkar, "A battery-free tag for wireless monitoring of heart sounds," in *Wearable and Implantable Body Sensor Networks, 2009. BSN 2009. Sixth International Workshop on*. IEEE, 2009, pp. 201–206.
- [85] S. Mandal, L. Turicchia, and R. Sarpeshkar, "A low-power, battery-free tag for body sensor networks," *IEEE Pervasive Computing*, vol. 9, no. 1, pp. 71–77, 2009.
- [86] H.-C. Chen, S.-S. Kuo, S.-C. Sun, and C.-H. Chang, "A distinguishing arterial pulse waves approach by using image processing and feature extraction technique," *Journal of medical systems*, vol. 40, no. 10, p. 215, 2016.
- [87] Y.-Y. Chen and R.-S. Chang, "A Study of New Pulse Auscultation System," *Sensors*, vol. 15, no. 4, pp. 8712–8731, 2015.
- [88] N. N. Khaire and Y. V. Joshi, "Diagnosis of disease using wrist pulse signal for classification of pre-meal and post-meal samples," in *Industrial Instrumentation and Control (ICIC), 2015 International Conference on*. IEEE, 2015, pp. 866–869.
- [89] S. Nomura, Y. Hanasaka, M. Hasegawa-Ohira, T. Ishiguro, and H. Ogawa, "Identification of human pulse waveform by silicon microphone chip," in *Systems, Man, and Cybernetics (SMC), 2011 IEEE International Conference on*. IEEE, 2011, pp. 1145–1150.
- [90] W. Shi and J.-C. Chiao, "Neural network based real-time heart sound monitor using a wireless wearable wrist sensor," *Analog Integrated Circuits and Signal Processing*, vol. 94, no. 3, pp. 383–393, 2018.
- [91] T. Tamura, Y. Maeda, M. Sekine, and M. Yoshida, "Wearable photoplethysmographic sensors past and present," *Electronics*, vol. 3, no. 2, pp. 282–302, 2014.
- [92] V. Almeida, H. Pereira, T. Pereira, E. Figueiras, E. Borges, J. Cardoso, and C. Correia, "Piezoelectric probe for pressure waveform estimation in flexible tubes and its application to the cardiovascular system," *Sensors and Actuators A: Physical*, vol. 169, no. 1, pp. 217–226, 2011.
- [93] X. Wang, Z. Liu, and T. Zhang, "Flexible sensing electronics for wearable/attachable health monitoring," *Small*, vol. 13, no. 25, p. 1602790, 2017.
- [94] A. G. Bell, "Improvement in electric telegraphy," Jan. 30 1877, uS Patent 186,787.
- [95] G. W. Elko and K. P. Harney, "A history of consumer microphones: The electret condenser microphone meets micro-electro-mechanical-systems."
- [96] "Contact Microphone | Piezo Film Sensor | CM-01 B Series | TE Connectivity." [Online]. Available: <https://www.te.com/usa-en/product-CAT-PFS0013.html>
- [97] M. Toda, "Acoustic sensor using curved piezoelectric film," Aug. 30 2005, uS Patent 6,937,736.
- [98] P. Scheeper, A. Van der Donk, W. Olthuis, and P. Bergveld, "A review of silicon microphones," *Sensors and actuators A: Physical*, vol. 44, no. 1, pp. 1–11, 1994.
- [99] P. Chakraborty, M. Kapoor, and K. Pavate, "Electret Condenser Microphone," *IETE Journal of Research*, vol. 21, no. 7, pp. 383–385, 1975.
- [100] G. M. Sessler, "Silicon microphones," *Journal of the Audio Engineering Society*, vol. 44, no. 1/2, pp. 16–22, 1996.
- [101] "Electret Condenser Microphones | Microphones | CUI Inc." [Online]. Available: <https://www.cui.com/product/resource/cmc-5044pf-a.pdf>
- [102] K. Acoustics, "Sisonic design guide," *Application Note rev*, vol. 3, 2011.

- [103] G. Feiertag, M. Winter, and A. Leidl, “Flip chip packaging for MEMS microphones,” *Microsystem technologies*, vol. 16, no. 5, pp. 817–823, 2010.
- [104] N. Peña-García, L. Aguilera-Cortés, M. González-Palacios, J.-P. Raskin, and A. Herrera-May, “Design and modeling of a MEMS dual-backplate capacitive microphone with spring-supported diaphragm for mobile device applications,” *Sensors*, vol. 18, no. 10, p. 3545, 2018.
- [105] “INMP411 | TDK - Invensense.” [Online]. Available: <https://www.invensense.com/products/analog/inmp411/>
- [106] “Primary Lithium Manganese Dioxide Coin and Button Cell Batteries.” [Online]. Available: <http://powerstream.com/libutton.htm>
- [107] “Lithium Ion Battery - Voltaplex.” [Online]. Available: <https://voltaplex.com/lithium-ion-battery>
- [108] G. Chen and E. Rodriguez-Villegas, “System-level design trade-offs for truly wearable wireless medical devices,” in *2010 Annual International Conference of the IEEE Engineering in Medicine and Biology*. IEEE, 2010, pp. 1441–1444.
- [109] “The Average Wrist Size for a Man, Based on 1563 Answers.” [Online]. Available: <https://theslenderwrist.com/average-wrist-size-for-a-man/>
- [110] A. Öztürk, B. Çiçek, M. M. Mazıcıoğlu, G. Zararsız, and S. Kurtoğlu, “Wrist circumference and frame size percentiles in 6-17-year-old Turkish children and adolescents in Kayseri,” *Journal of clinical research in pediatric endocrinology*, vol. 9, no. 4, p. 329, 2017.
- [111] A. Siska and M. He, “Golden Gloves ADC Championship Match–SAR vs. Sigma-Delta ( $\Sigma$ ),” 2010.

## 3 Characterising the pulse sounds for continuous heart rate monitoring

*The work presented within this chapter is an edited version of research previously published in:*

*P. Sharma, S. A. Imtiaz and E. Rodriguez-Villegas, "Acoustic Sensing as a Novel Wearable Approach for Cardiac Monitoring at the Wrist," Scientific Reports, vol. 9, no. 1, pp. 1–13, 2019.*

### 3.1 Introduction

The sensing method proposed in this thesis works on the principle that the periodic blood flow in the radial artery causes rhythmic variations in the arterial diameter which produces corresponding vibrations at the skin surface. These vibrations introduce changes in the surrounding air pressure which can be transferred to the diaphragm of the MEMS microphone sensor embedded into the proposed wearable device. The conversion of pulse vibrations into the acoustic signal can provide vital information about the cardiac activity and can be used to monitor cardiac parameters such as heart rate on a continuous basis. Therefore, it is important to characterise the acoustic signal to establish its correlation with the cardiac activity. The following sections discuss the temporal and spectral characteristics of the acoustic signal to find the signal bandwidth and the optimal sensor site for better signal-to-noise ratio (SNR). The effect of internal and external noise on the signal characteristics have also been explored. Finally, a novel algorithm to monitor the heart rate based on acoustic sensing of the radial artery is presented.

### 3.2 Characteristics of pulse sounds

The acoustic signal is recorded by attaching the proposed wearable device to the radial artery using a double-sided medical adhesive tape. Since the characteristics of the pulse sounds have not been reported before in the literature, the device incorporates a wider bandwidth initially to avoid losing any information about the pulse sounds. The high-pass filter and the low-pass filter in Fig. 2.12 are designed to have cut-off frequencies of 6 Hz and 500 Hz respectively. A higher bandwidth is chosen to include the frequencies corresponding to the heart sounds. To avoid any aliasing in the signal, a sampling



frequency of 2100 Hz (around 4 times of the bandwidth) is adopted at the ADC stage to convert the data into digital domain with 12-bit resolution. The acoustic signal is bundled into several data packets and is wirelessly transmitted to a smartphone.

### 3.2.1 Temporal characteristics

To study the temporal characteristics of the acoustic signal, the PPG signals from the index finger are simultaneously recorded using a commercially available SOMNOscreen pulse oximeter [1]. As an illustration, the acoustic signal and the PPG signal recorded from a subject are plotted together in Fig. 3.1 by removing any time delay between the onset of pulse at wrist and finger to synchronise the corresponding peaks. It can be observed that the morphology of the PPG signal looks quite similar to the arterial pressure waveform in Fig. 2.2. The discussion on the arterial pressure waveform in Section 2.1.2.1 explained that the pressure wave propagating through the circulatory system is essentially a superposition of a forward and a backward travelling wave. While the systolic peak represents the maximum pressure exerted by the ejected wave on the arterial walls, the diastolic peak is formed by the superposition of incoming and reflected pressure waves. Therefore, the systolic and diastolic peak in the arterial pressure waveform formed the two essential components of the pressure (or pulse) wave. Since the strength of these components from within the radial artery are directly correlated with the amplitude of the skin surface vibrations, the pulse wave components are indirectly sensed by the microphone to produce corresponding peaks in the acoustic signal. The comparison of the acoustic signal with the PPG signal in Fig. 3.1 suggests that the first and second acoustic peak matches the systolic and diastolic component of the pulse wave

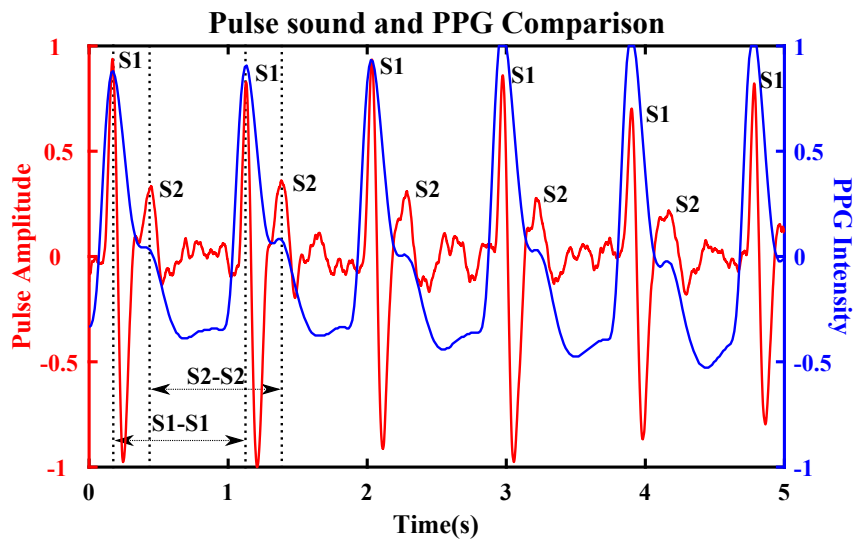


**Figure 3.1:** Temporal characteristics of the acoustic signal with respect to the PPG signal.

respectively. The higher pressure corresponding to the systolic peak in the pulse wave produces a peak of higher amplitude as compared to the diastolic peak. The presence of intermediate ripples in the acoustic signal are caused, amongst others, by noise of the measuring electronics, electromagnetic interference, and environmental noise.

The dominant peaks in the acoustic signal are termed as S1 and S2 sounds, for the reasons explained in the next section. The temporal correlation with the PPG signal indicates that the heartbeats can be continuously monitored by measuring the S1-S1 or S2-S2 inter-beat intervals as shown in Fig. 3.1. The amplitude of the S1 sounds for healthy subjects are always found to be greater than the S2 sounds. It can also be observed that the amplitude of the S1 and S2 sounds does not remain constant over the recording duration and are possibly modulated by the strength of the pressure wave. In other words, the amplitude of the acoustic signal for an individual varies with the blood pressure. However, the arterial elasticity, blood parameters, and the depth and surrounding anatomy of the radial artery also affects the characteristics of the acoustic signal. Since the temporal behaviour does not explain all the inherent features of the acoustic signal, it is important to find its spectral characteristics as well.

### 3.2.2 Spectral characteristics

The acoustic signals recorded from different subjects does not necessarily have the same polarity of signal oscillations. In Fig. 3.1, the S1 and S2 sounds transitioned from a positive lobe to a negative lobe around the zero-crossing of the signal. On the contrary, the acoustic signal in Fig. 3.2(I) transitions in an opposite direction from a negative lobe to a positive lobe. In order to characterise the spectral features of the acoustic signal, the PPG waveform is simultaneously plotted. As anticipated, a slight time delay between the onset of the pulse at the radial artery and the index finger can be observed. This time delay is a function of the pulse wave velocity and the arterial length, and is empirically found to be nearly constant over the length of the recording. The synchronisation of the acoustic and PPG pulse waveforms is achieved by overlapping the nearest systolic peaks by removing the time delay, as shown in Fig. 3.2(II).

As discussed before, the pulse wave originating from the heart- as a result of the opening and closing of the heart valves, propagate as a mechanical wave along the arterial branches of the circulatory system. Although negligible, the heart sounds also transmit an acoustic wave through the body [2]. Since these acoustic features are superimposed on the vessel vibrations caused by the mechanical constriction and dilation of the radial artery, a similar type of skin surface modulation is obtained. The PPG bandwidth of less than 10 Hz [3] suggests that the PPG signal only measures the pressure waveform and remain silent to the acoustic features of the pulse wave. The spectral analysis of the acoustic signal, on the other hand, demonstrates that the pulse sounds also contain the acoustic component of the pulse wave.

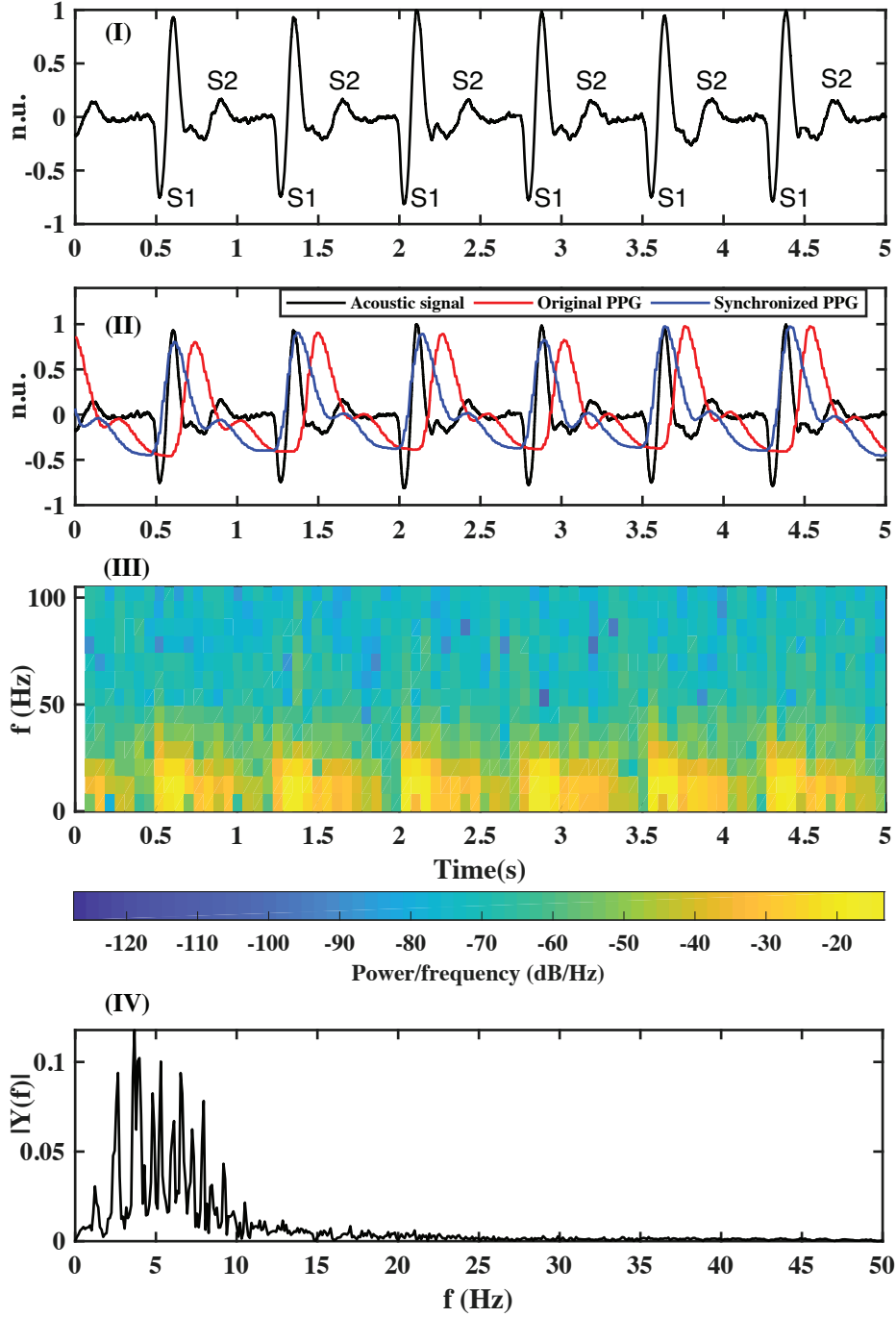


**Figure 3.2:** *Characterisation of the acoustic signal: (I) Pulse waveform recorded by placing the miniaturised device on the middle position of the radial artery at wrist. (II) Comparison of acoustic and PPG waveforms to synchronise both the signals by matching the nearest systolic peaks. PPG data was recorded using SOMNOscreen pulse oximeter [1]. (III) Joint time-frequency analysis of the acoustic signal obtained using STFT. The colour intensity of the grids demonstrates their relative power. (IV) Frequency response (FFT) of the acoustic signal.*

The frequency response of the acoustic signal, sampled at 2100 Hz, is obtained using the Fast-Fourier transform (FFT). It can be observed that the frequency content of the acoustic signal in Fig. 3.2(IV) mainly lies below 25 Hz and also consists of the audible frequencies. The spectral content of the acoustic signal is significantly smaller than the bandwidth of the heart sounds which usually lie between 20 and 150 Hz for a normal subject [4]. The reduction in the bandwidth is mainly attributed to the fact that the travel of the pulse wave from the source of the sounds (i.e. the heart) to the measurement site (i.e. the radial artery) causes an attenuation of the high frequency components. The attenuation results from a series of non-linear transformations as the pulse wave travels through multiple locations of the body [5].

A better spectral analysis in the joint time-frequency domain can be obtained by the short-time Fourier transform (STFT). The STFT analysis allows to understand the power distribution among different components of the signal by dividing the time-frequency space into several rectangular grids. Since the maximum time-frequency resolution of a rectangular grid is restricted by the Heisenberg's uncertainty principle, a suitable time and frequency width is chosen for a better time-frequency localisation of the signal. The STFT of the acoustic signal is obtained using a Blackman window of 256 samples and 50% overlap between consecutive frames. The resultant grids in Fig. 3.2(III) demonstrates the power distribution of the signal in the joint time-frequency space. The intensity of the power grids is represented by the colour bar where the yellow and blue colour denote the maximum and minimum power density respectively. The STFT analysis of the acoustic signal, therefore, suggests that the signal power is mainly concentrated in the S1 and S2 sounds, with S2 sounds carrying a relatively lower energy. While the dominant energies of the S1 and S2 sounds in STFT are mainly concentrated in the lower frequencies, a portion of the energy content also lie in the audible range as determined by the FFT analysis. Therefore, the spectral analysis reveals that the acoustic signal recorded from the radial artery also contain audible sounds. Since the heart sounds are primarily formed of the S1 and S2 sounds (also known as the fundamental heart sounds), the two dominant peaks of the acoustic signal are also termed as S1 and S2 sounds in this thesis.

The observation about the spectral characteristics of the pulse sounds are tested over a database of 20 adult subjects for generalisation purposes. As an illustration, four different morphology of the pulse sounds are plotted in Fig. 3.3. Since the heart rate and inter-beat intervals are inversely correlated, the number of S1 and S2 sounds in a 5-seconds window changes with the corresponding heart rate of the subject. The FFT and STFT analysis reveals similar observations about the signal bandwidth and contain frequencies in the audible range. Therefore, it can be concluded that the acoustic signal recorded from the radial artery at the wrist is essentially a combination of the acoustic features superimposed on the pulse wave component propagated from the heart. While the different pulse shapes and features in the subjects can be attributed to different ar-

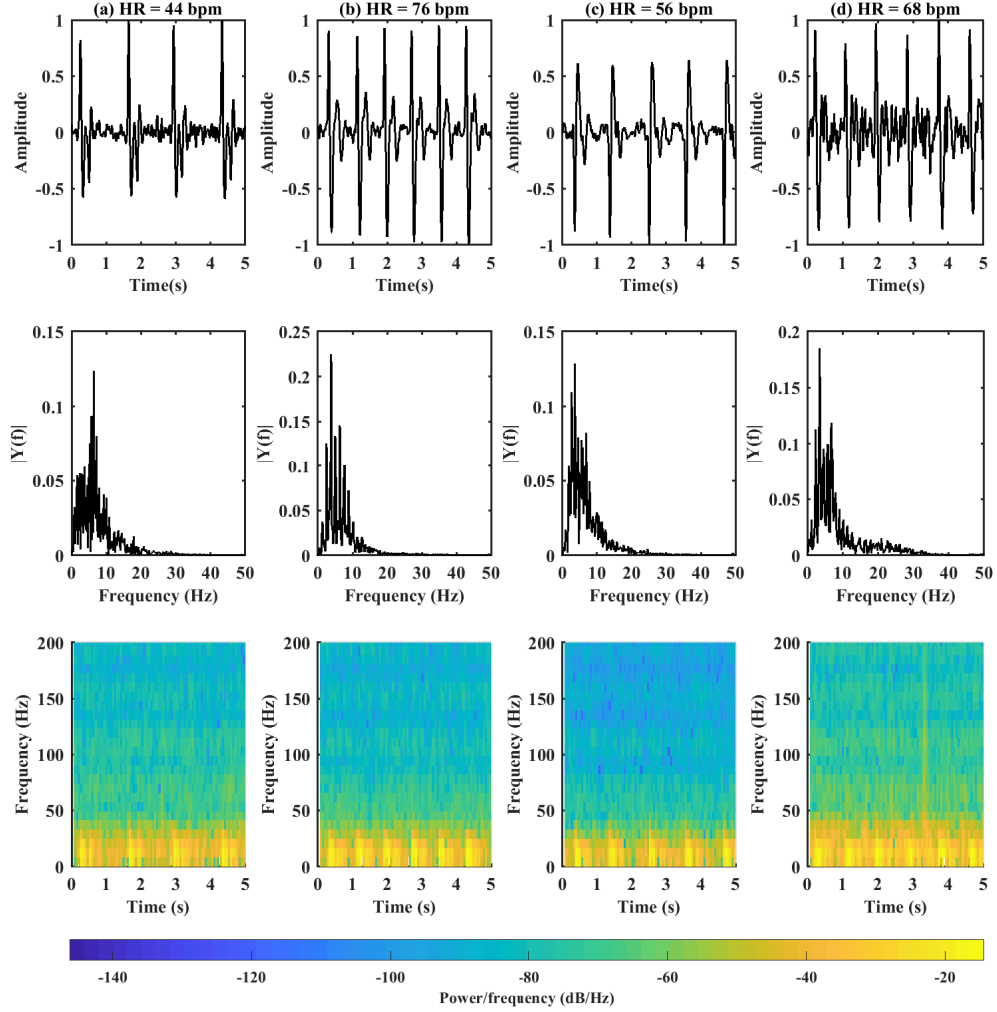


**Figure 3.3:** *Spectral characteristics of the acoustic signals with different morphology and recorded from different subjects.*

terial parameters and functioning of the cardiovascular system, the signal characteristics and its SNR are also dependent on the sensor location at the wrist.

### 3.3 Optimal sensor site

The pulse on the radial artery can be sensed at three locations: distal, middle and proximal. The middle position as shown in Fig. 2.4 can be easily located in front of the radial styloid process (protruded bone near the wrist crease). The proximal and distal positions are 1-2 cm on either sides of the middle position, towards the elbow and the wrist crease respectively. To determine the optimal auscultation site, a total of nine acoustic recordings, three from each location for every subject, are recorded from a total of 10

subjects to analyse the power spectrum at the different auscultation sites. Note that, although these recordings would be affected by the characteristics of the recording setup, in the experiment the environmental noise and motion artefacts are kept to a minimum. The power spectral density (PSD) of the acoustic signal is calculated by segmenting the signal into window frames of 1024 samples with a 50 % overlap and applying Fast Fourier Transform (FFT) to every frame. The FFT coefficients thus obtained are averaged to estimate the PSD of an acoustic recording in the range of 0 to 250 Hz. The PSDs of the three recordings for every location, and for every subject are averaged to compare the SNR on the different auscultation sites. For illustration, the PSD of the signal obtained by completely blocking the microphone port is also plotted in Fig. 3.4. The latter is an indication of the noise inherent to the sensing system itself in absence of any other sounds. A close correlation between the power spectrum of the signals at different locations can be observed. The anatomy of the radial artery suggests that the vessel depth at the middle position is relatively lower than in the other two sites [6]. Therefore, the operations of vasoconstriction and vasodilatation produces skin surface vibrations with higher amplitudes in the middle location due to a lower attenuation by the surrounding tissues and muscles. This, in turn, results in a higher SNR. The same reasoning can be followed to compare the PSDs of the distal and proximal positions. Due to the ease of locating the middle position, and the insignificant difference between the PSDs, all the experiments in this thesis records the acoustic signal with the microphone port placed on the middle position of the radial artery. While the middle position proves to be a better choice for the sensor attachment, the signal characteristics are also affected by the noisy artefacts both internal and external to the body.

### 3.4 Noise artefacts

The acoustic sensing of the heart sounds using a stethoscope is characterised in a controlled environment and involve human processing to identify the events of interest. Such constraints cannot be imposed on a wearable technology that is designed to integrate easily in a user's lifestyle. Therefore, the tolerance to noise artefacts is essential for a reliable operation of the device. Since the primary signal can be affected by different noise sources, the characteristics of the signal originating from such sources must be studied to remove them automatically without any human intervention. The removal of such artefacts ensures a better representation of the true signal. The microphone sensor in the proposed wearable device can pickup airborne sounds from internal or external locations of the body. While the noise originating from the internal location of the body is intrinsic to the region under observation, the external noise mainly arise from the surrounding environment. The following sections discuss the interference from these noise sources by recording the acoustic signal in the presence and absence of the noise. The comparison is established by calculating the PSD of the acoustic signal in both the scenarios. All

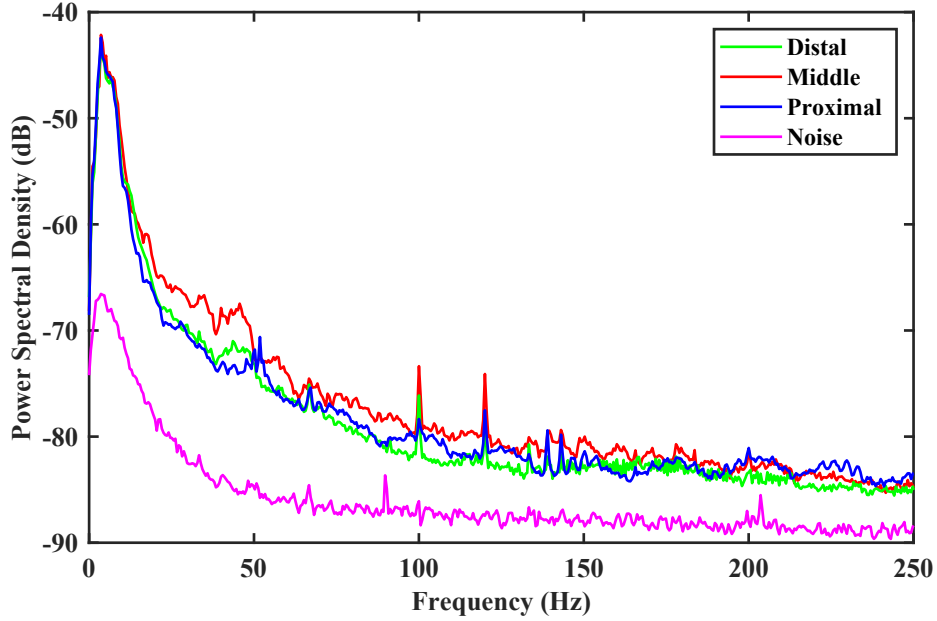


**Figure 3.4:** *PSDs of the acoustic signal obtained with the microphone placed on distal, middle and proximal site. For illustration, the PSD of the noise obtained from the signal recorded by completely blocking the microphone port is also plotted.*

the recordings are digitised at a sampling frequency of 2100 Hz and an ADC resolution of 12-bits.

### 3.4.1 Noise internal to the wrist

Over the chest, the heart sounds suffer a heavy interference from the lung sounds. However, the anatomy of the wrist does not suggest the presence of a different sound source in the distal, middle or proximal region of the radial artery. To characterise the noise source internal to the wrist, the sensor is placed on the opposite side of the wrist to avoid sensing an acoustic wave or pulse wave from the blood flow in the radial or ulnar artery. The PSD of the acoustic signals recorded from 5 subjects for 1 minute duration are averaged to plot the frequency response of the internal noise in Fig. 3.5. In the experiment, the noise from motion artefacts and the surrounding environment are kept at a minimum for an accurate noise characterisation.

To establish a comparison, the noise PSD for the acoustic signal recorded by sealing the bottom port of the microphone is also calculated. Since the microphone in such scenario does not sense any external pressure variations, the noise PSD indicates the noise intrinsic to the sensing system itself. This noise primarily generated by the electronic circuitry is a combination of the amplifier noise, ADC noise and the wireless transmission. To minimise the system noise, the proposed wearable device only included the electronic components with noise levels less than 10 dB or more in comparison to the noise floor

of the microphone. It can be observed that the frequency response of the internal noise in Fig. 3.5 resembles closely with the reference. The 50 Hz noise and its harmonics are possibly picked up from the environment. The close similarity between the PSDs indicate that the noise internal to the wrist is negligible. Therefore, the acoustic signals recorded from the radial artery only contain the physiological information about the pulse sounds in addition to the noise intrinsic to the sensing system.

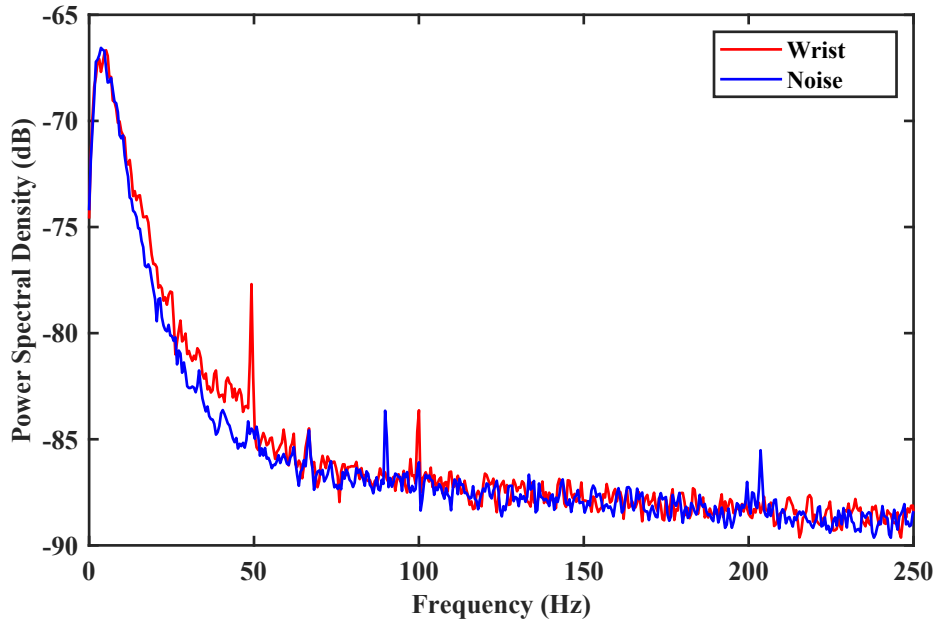


**Figure 3.5:** *PSD of the acoustic signal obtained with the microphone placed on the opposite side of the wrist. The noise PSD corresponds to the sealed microphone port.*

### 3.4.2 Noise due to the motion artefacts

A major challenge with the wearable technology is their tolerance to the motion artefacts. Myo-acoustic noise generated by the movement of the muscles can introduce significant amplitudes in the signal of interest and can possibly lead to a failure of the system. In case of the proposed wearable device, the acoustic signal can be reliably obtained when the wrist with attached sensor is relaxed on a table top without any interference from the hand movements. However, such movements cannot be restricted for a long-term monitoring of the subject and their interference must be addressed either in the sensing system itself or at the post-processing stage. The hand movements that can affect the characteristics of the acoustic signal at the wrist are shown in Fig. 3.6. These movements as described below are studied in isolation by recording the pulse sounds in presence of only one type of artefact at a time.

1. Finger movement - The fingers are moved in three ways: swinging in the left-right



direction, bending in the up-down direction, and moving in an arbitrary way while keeping the wrist, elbow and shoulder stationary.

2. Wrist movement - The wrist is rotated in either a clockwise or an anticlockwise direction while keeping the fingers, elbow and shoulder stationary.
3. Elbow Movement - The elbow is stretched and bent while keeping the fingers, wrist and shoulder stationary.
4. Shoulder movement - The shoulder joint is rotated in a circular manner while keeping the fingers, wrist and elbow stationary.
5. Arbitrary movement - The arbitrary motion involves all the hand movements listed above in a random way.

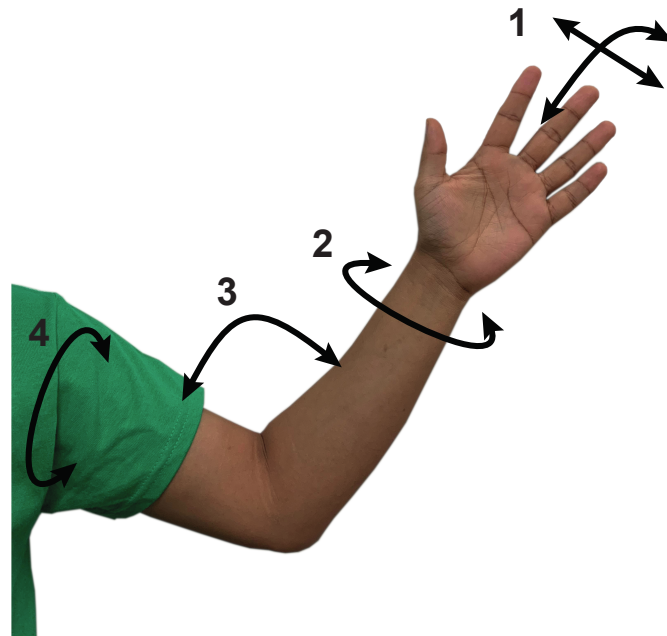


**Figure 3.6:** *Different types of hand movements that can introduce significant noise in the recording setup.*

To characterise the noise introduced due to the motion artefacts, seven recordings (three for fingers and one for every other movement), each of 1 minute duration, are recorded from 5 subjects. During the whole experiment, the acoustic sensor is placed on the middle position of the radial artery and records the acoustic signal in presence of one movement at a time. The subjects are asked to perform a specific type of movement (from the list above) for the complete recording while keeping the other parts of the hand

stationary. The frequency response for a particular movement is determined by averaging its PSDs across all the subjects.

The power spectrum corresponding to different types of finger movements is compared against the clean acoustic signal in Fig. 3.7. The representation of PSD over an absolute scale is made for a better comparison. It can be observed that the finger movements generate artefacts in the same spectrum and interferes heavily with the pulse sounds. This mainly happens because the finger movements create tension in the muscles surrounding the radial artery. The stretch and release of such muscular tension causes significant variation in the surrounding air pressure at the skin surface. These airborne vibrations are picked up by the microphone sensor to introduce large amplitudes in the acoustic signal. Since the bandwidth of these artefacts is similar to that of the pulse sounds, the hardware design cannot include a band-pass filter to reduce the effect of finger movements on the acoustic signal. Instead, these artefacts are dealt in the signal processing stage by identifying features to separate the artefacts from the signal of interest.

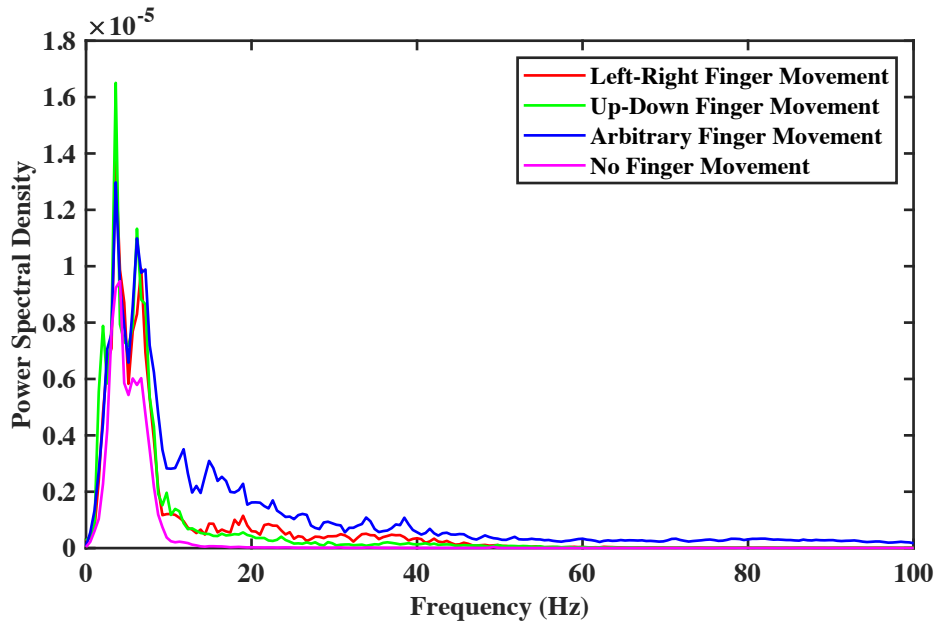


**Figure 3.7:** *Frequency response of artefacts introduced due to different finger movements.*

The artefacts generated by the wrist, elbow and shoulder movements are studied similarly. The frequency response plotted in Fig. 3.8 shows that the effect of elbow and shoulder movements on the pulse sounds is minimal. The reasoning behind such characteristics is that the bending of the elbow or the rotation of the shoulder does not affect the region of sensor attachment either internally or externally in a significant manner. This is not true for the wrist or the arbitrary motion which directly correlates with the muscle movement and therefore interferes heavily with the pulse sounds. The use of high-pass filtering with a low cut-off frequency in the signal processing can possibly attenuate the

effect of wrist movements. However, the inclusion of feature recognition to identify the corrupted sections of the acoustic signal is necessary to extract the cardiac parameters accurately.

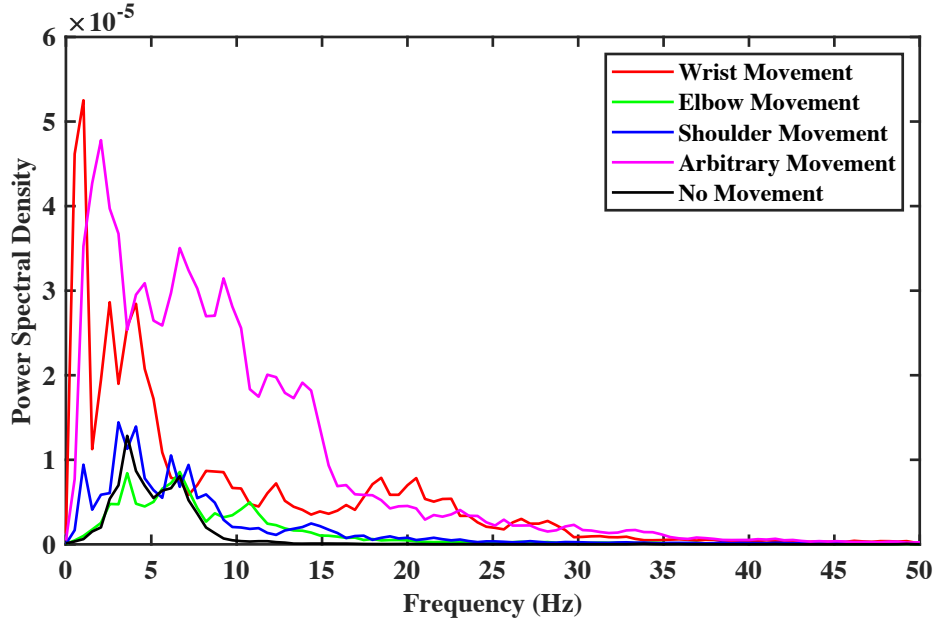


**Figure 3.8:** Frequency response of artefacts introduced due to wrist, elbow, shoulder and arbitrary movements.

### 3.4.3 Environmental noise

The surrounding environment is another source of noise in the recording setup. To characterise the environmental noise, the pulse sounds are recorded in the presence of vocal speech and background music. Following data acquisition protocol is adopted to study the effect of speech and music on the pulse recordings. The subjects are asked to minimise the motion artefacts during the whole experiment.

1. Record the pulse sounds for 1 minute duration with minimal environment noise. This is used as a reference signal.
2. Record the pulse sounds for 1 minute duration in the presence of *normal* vocal speech. During the recording, the subject read a piece of text towards the microphone at a distance of 10 cm from the wearable device.
3. Repeat the experiment in (2) at *loud* vocal speech reading the same piece of text.
4. Record the pulse sounds for 1 minute duration in the presence of loud music. The music is played at a distance of 10 cm from the wearable device.

The power spectrum determined for these recordings are plotted in Fig. 3.9. While the PSDs match closely within the bandwidth of the pulse sounds ( $< 25$  Hz), the speech and music signals also contain power in higher frequencies. As expected, the signal with loud speech carry higher PSD amplitudes than the signal with normal speech volume. The envelopes for the speech spectrum resemble in shape because the subject read the same piece of text. Since these amplitudes mainly lie in frequencies above 100 Hz, the interference from the environmental noise can be attenuated significantly by using a low pass filter in the post-processing of the signal.

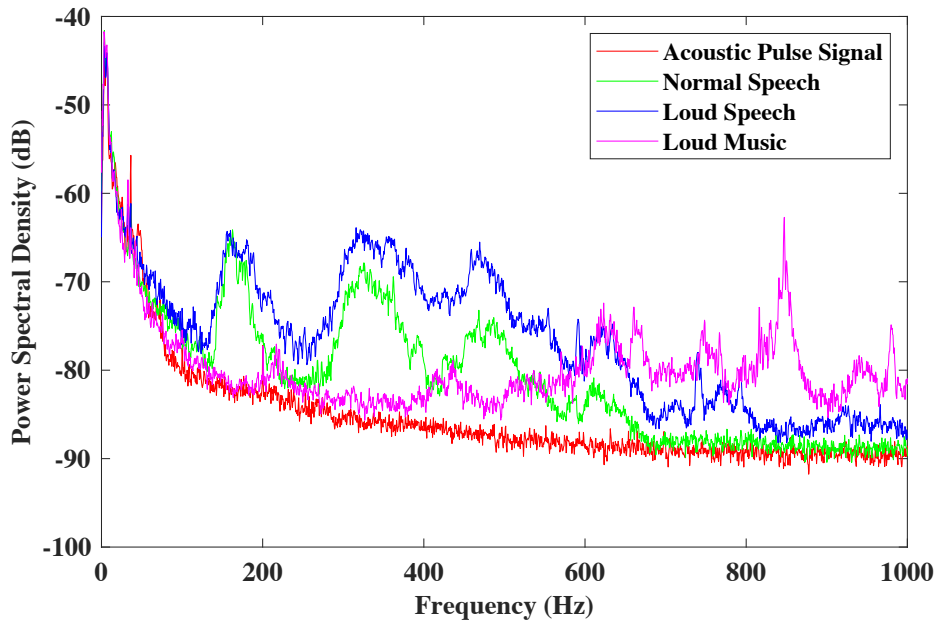


**Figure 3.9:** *PSDs of the acoustic signal recorded in the presence of vocal speech (normal and loud volume) and loud music.*

#### 3.4.4 Summary

Different noise sources that can interfere with the pulse sounds have been considered. The noise internal to the body is mainly introduced by the motion artefacts including the finger, wrist, elbow and shoulder movements. The finger and wrist movements significantly corrupts the acoustic signal and require post-processing of the signal to identify the corrupted regions. The interference from the elbow and shoulder movements, however, are found to be negligible. The environmental noise from the external sources mainly arises from the vocal speech and can be attenuated by simply adopting a low pass filter. Therefore, the inclusion of filtering and feature recognition blocks in the signal processing are essential in minimising the effect of the artefacts and using the pulse sounds as a novel physiological signal to extract biomarkers (such as heart rate) indicative of cardiac performance.

### 3.5 An algorithm to extract heart rate from pulse sounds

In addition to proving the feasibility of obtaining the cardiac signal from the wrist, this thesis also investigates the possibility of automatically extracting the most fundamental biomarker, namely heart rate, from the acoustic signal. Heart rate monitoring, among other vital signs, is an important application of recording the pulse at the wrist. While the techniques discussed in Section 2.2 provide useful physiological information to extract the heartbeat, they suffer from several issues, particularly with the constraints in terms of device size and shape, power budget for long-term monitoring, reliability and accuracy concerns posed by the wearable technology. The sensing of cardiac rhythms from the radial artery using a miniaturised, low power microphone sensor does not require an active input and can allow continuous heart rate monitoring over long periods. Since this is the first time such a signal has been sensed via means of wearable acoustic sensing, a novel algorithm to extract heart rate from the pulse sounds need to be developed. The following sections discuss different stages of the proposed algorithm and establishes a comparison with the PPG-based heart rate monitoring.

#### 3.5.1 Algorithmic blocks

An overview of the proposed algorithm to automatically determine the heart rate by extracting the S1 sounds from the acoustic pulse signal is shown in Fig. 3.10. The algorithm mainly consists of 3 stages: 1- The pre-processing blocks reduce contamination of the signal caused by noisy artefacts, in order to improve the SNR for further analysis; 2- The PSD of the signal is calculated in the following stage using STFT to extract the S1 sounds; 3- Finally, the peaks corresponding to these sounds are detected to provide a time index by constructing a squared energy envelope for HR determination. A pseudo-code for the proposed algorithm is also provided in Table 3.1. The following sections explain the details of the different blocks.

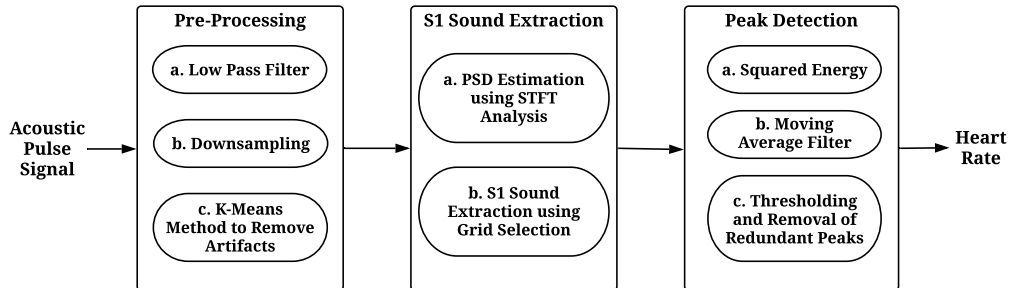


**Figure 3.10:** Block diagram of the proposed algorithm to determine HR from the acoustic signal by extracting S1 sounds using the STFT analysis.

### 3.5.2 Acoustic data pre-processing

The acoustic signal sensed at the wrist contains not just the signal of interest but also other signals that are picked up by the electronic system, such as motion artefacts and sounds from the surrounding environment. In order to achieve a better SNR by reducing the effects of the latter, the acoustic signal, denoted by time-series  $y$  is processed into rectangular windows of 5 seconds duration with 1 second of overlap between successive segments. The window length is chosen to include enough number of heart beats corresponding to an HR in a range of 40 to 200 beats per minute (bpm).

Most of the frequency content of the acoustic signal is contained below 25 Hz. Because of this, undesired higher frequency interference/noise is reduced by using a fifth-order Butterworth low-pass filter with a cut-off frequency of 25 Hz. The acoustic signal originally sampled at 2100 Hz ( $f_s$ ) possesses frequencies well below the corresponding Nyquist frequency after the filtering process. This redundant information is therefore removed by downsampling the signal by a factor of 10 reducing the sampling frequency to 210 Hz ( $f_d$ ), without introducing any aliasing in the signal.

Since the acoustic signals for the HR determination are continuously recorded in a single session of 30 minutes duration, the subjects could move their wrist/ fingers during the data acquisition. As discussed before, such movements introduce acoustic vibrations at the skin surface that are sensed by the microphone to introduce large amplitudes in the signal. The frequencies corresponding to these artefacts can lie within the bandwidth of the acoustic pulse signal and a simple band-pass filtering cannot eliminate their interference with the pulse sounds. However, the effect of such movements usually lies in smaller time frames. Because of this, K-means clustering method [7] with two classes,  $C1$  and  $C2$ , is used in the algorithm to identify the parts of the signal which are significantly corrupted by them. The method initially divides the signal blocks,  $y$ , of 5

**Table 3.1:** Pseudo-code algorithm for estimating HR from acoustic pulse signal. The symbol notations are referenced in the main text.

<p>1. Initial pre-processing of the signal.</p> <ul style="list-style-type: none"> <li>• Acoustic pulse signal: <math>y</math>, sampled at <math>f_s = 2100</math> Hz.</li> <li>• Low-pass filtering: <math>\text{LPF}(y)</math>, with <math>w_c = 25</math> Hz.</li> <li>• Downsampling operation: <math>\downarrow 10(y)</math>, <math>f_d = 210</math> Hz.</li> <li>• K-means method: Form two clusters by scoring the signal parts <math>y_n</math> using <math>\mathbf{S}_n = \{0,1\}</math> for <math>n \in [1,5]</math>.</li> </ul>	<p>2. S1 sound extraction from acoustic pulse signal.</p> <ul style="list-style-type: none"> <li>• Joint time-frequency analysis: <math>\mathbf{PSD} = \text{STFT}(y)</math>.</li> <li>• Maximum power, <math>\mathbf{P}_{\max} = \max(\mathbf{PSD})</math>.</li> <li>• Extract grids with <math>\mathbf{P} \geq \mathbf{P}_{\max} - \mathbf{P}_t</math>, where <math>\mathbf{P}_t \in [5,10]\text{dB}</math> such that <math>m \in [4,17]</math>.</li> <li>• Identify S1 regions: <math>(t_{sa}-0.15, t_{ea}+0.15)</math>, <math>a \in [1,m]</math>.</li> </ul>
<p>3. Peak detection from extracted S1 sounds.</p> <ul style="list-style-type: none"> <li>• Squared energy: <math>y^2</math>.</li> <li>• Averaging filter: <math>\int_1^{32} y^2</math>.</li> <li>• Artefact elimination using thresholds: <math>\mathbf{W}_z</math> and <math>\mathbf{A}_z</math>.</li> </ul>	<p>4. Find the continuous average HR.</p> <ul style="list-style-type: none"> <li>• Find the time indexes for maximum of energy peaks: <math>\mathbf{T}_m = \max(E_m)</math>.</li> <li>• Estimate the HR: <math>\mathbf{HR} = \frac{60}{(\sum_{m=1}^4 \Delta T_m)/4}</math></li> </ul>

seconds duration, into five equal parts, each of 1 second duration, and denoted by  $y_n$ ,  $n \in [1,5]$ . For every part, the maximum amplitude ( $A_{max}$ ) and the standard deviation ( $\sigma$ ) are determined to reflect the signal characteristics as  $x$  and  $y$ -coordinates respectively. These feature coordinates are fed to the K-means method to cluster the five signal parts into two different classes based on the similarity of the features. The method proceeds by choosing two cluster centroids,  $O1$  and  $O2$ , and groups the features into two classes by iteratively updating the centroid coordinates,  $(x_{O1}, y_{O1})$  and  $(x_{O2}, y_{O2})$ , to minimise the feature points-to-cluster-centroid distances. Once the iterative process converges, the horizontal change,  $\Delta x$ , between the centroids is determined, and the class  $C$  with a lower standard deviation is found. A change of less than 50% in  $\Delta x$  reflects a close correspondence between the maximum amplitudes of different signal parts, and indicates no significant corruption by the motion artefacts. Since the artefacts exhibit a higher standard deviation than the acoustic pulse signal, the class with a lower  $y$ -coordinate is chosen in cases where the change in  $\Delta x$  is more than 50%. Depending on the comparison between these parameters, in equation (3.1), the signal parts  $y_n$  are scored by assigning  $S_n$ ,  $n \in [1,5]$  a value of either 1 or 0. The signal parts with a score of 1 are ignored from the further processing.

$$\Delta x = \frac{|x_{O1} - x_{O2}|}{\min(x_{O1}, x_{O2})}$$

$$C = \begin{cases} C1, & \text{if } y_{O1} \leq y_{O2} \\ C2, & \text{if } y_{O1} > y_{O2} \end{cases}$$

$$S_n = \begin{cases} \begin{cases} 1 \ \forall \ n \in C2 \\ 0 \ \forall \ n \in C1 \end{cases} & \text{if } \Delta x \geq 0.5 \ \& \ C = C1 \\ \begin{cases} 1 \ \forall \ n \in C1 \\ 0 \ \forall \ n \in C2 \end{cases} & \text{if } \Delta x \geq 0.5 \ \& \ C = C2 \\ 0 & \text{if } \Delta x < 0.5 \end{cases} \quad (3.1)$$

Fig. 3.11 shows different pre-processing stages for a 5 seconds block of signal, a part of which is significantly corrupted by the motion artefacts. It can be seen how the pre-processing identifies the corrupted region and successfully ignores the first part of the signal from the further processing.

### 3.5.3 S1 sound extraction

An HR in a range of 40 to 200 bpm corresponds to a beat-to-beat interval of 1500 to 300 milliseconds respectively. The number of S1 sounds in a 5 seconds window therefore can vary from 4 to 17. The measured PSD of the acoustic pulse signal in Section 3.2.2 showed that the frequencies corresponding to the S1 sounds, in the joint time-frequency analysis, carried higher power than other parts of the signal. This property of the signal

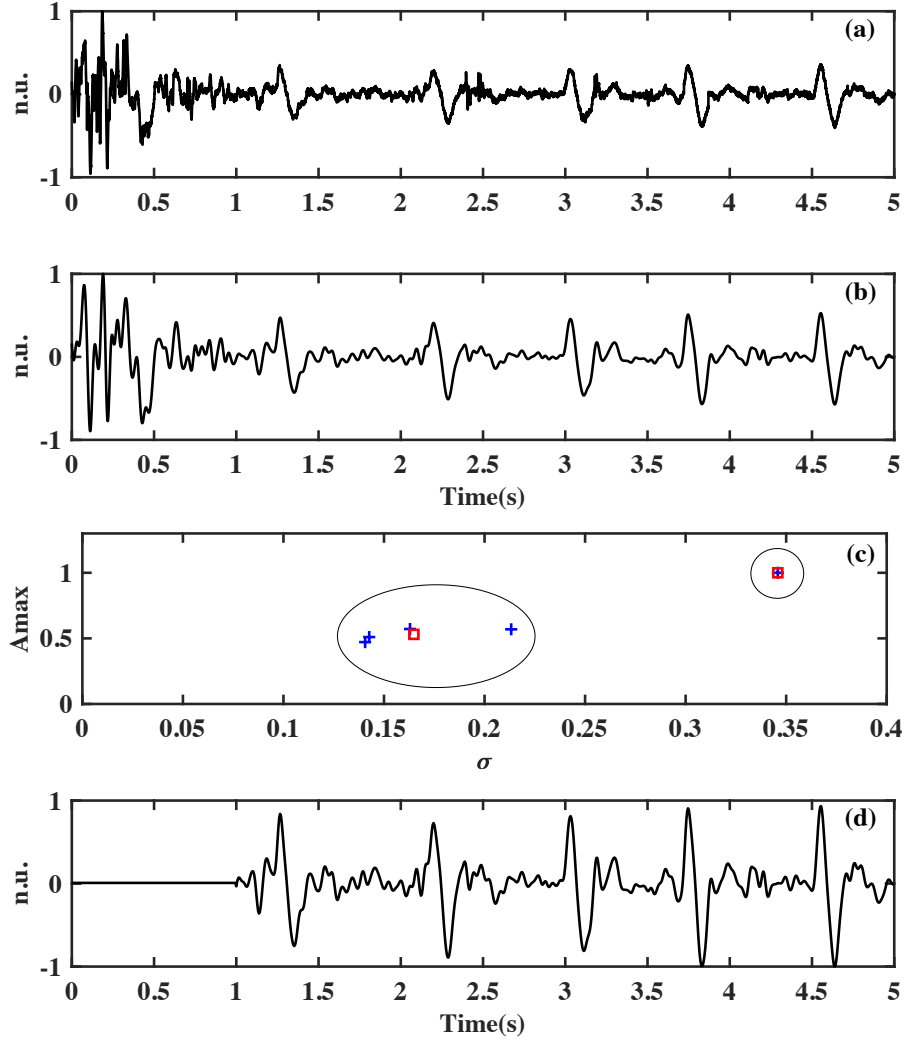


**Figure 3.11:** Pre-processing of the acoustic signal sensed by the system: (a) Original signal. (b) Low-pass filtered and downsampled signal to remove higher frequency components and redundant information respectively. (c) Clustering using the K-means method to identify signal segments corrupted with motion artefacts. Symbol + and  $\square$  represents the features and cluster centroids respectively. (d) Signal segment corrupted with motion artefact (due to wrist/ finger movement) removed from the downsampled signal.

is utilised to extract these sounds in the time-domain and process them further to find the HR. But it is also important to select a proper window length for calculating the PSD of the signal, as a better time resolution allows the extraction of the S1 waveform without interfering much with the nearby signal transitions.

The power spectrum of the acoustic signal with a downsampled frequency of 210 Hz is calculated in the algorithm using a Blackman window of 32 samples (approximately 150 milliseconds) with an overlap of 50% between successive frames. The chosen time



window, as shown in Fig. 3.12(b), provides the required time resolution to extract the S1 waveform by segmenting the time axis into a relatively higher number of grids. The colour intensity of these grids in the time-frequency space indicates their corresponding contribution to the overall power of the signal. The grid with the maximum power,  $P_{max}$  is found and all the grids with power not differing more than 5 dB with respect to  $P_{max}$  are also selected. It is understood that the beat-to-beat interval cannot be lower than 300 milliseconds [4] therefore, all the grids with a mutual separation within this time period supposedly belong to a single S1 sound, and hence they are all grouped together,

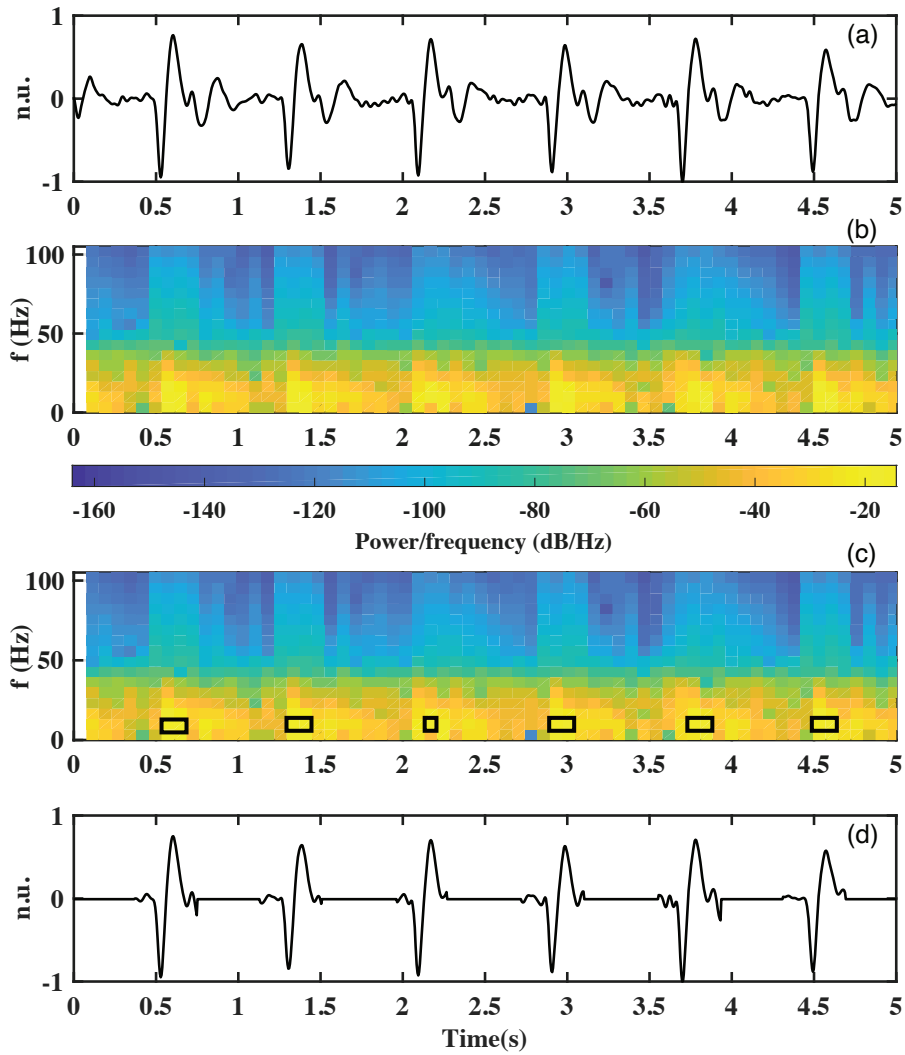


**Figure 3.12:** *S1 sounds extraction from a different pre-processed signal with no corrupted segment: (a) Acoustic signal after initial low-pass filtering, downsampling and K-means application. (b) PSD of the signal obtained using STFT to extract S1 sounds. (c) Rectangular windows representing the regions of interest. (d) S1 sounds extracted by adding a tolerance of 150 milliseconds on both sides of the rectangular windows.*

as shown by rectangular windows in Fig. 3.12(c). For  $m$  of such groupings, the starting and end time points,  $t_{sa}$  and  $t_{ea}$ , where  $a \in [1, m]$ , are noted. The threshold difference of 5 dB ( $P_t$ ) is increased in steps of 1 dB, up to a maximum of 10 dB, to limit these  $m$  number of groupings for a 5 seconds window between 4 and 17. A tolerance window of 150 milliseconds, observed empirically, is added to  $t_{sa}$  and  $t_{ea}$  to enlarge the region of interest in the time-domain, and ensure that the S1 waveform is completely extracted. Only the signal corresponding to the group timings of  $(t_{sa} - 0.15, t_{ea} + 0.15)$  seconds is retained, whereas the other parts of the signal are zeroed for the further processing as shown in Fig. 3.12(d).

### 3.5.4 Peak detection

#### 3.5.4.1 Constructing energy envelope of the extracted S1 sounds

Although a number of peak detection methods using the joint time-frequency analysis exist [8], [9], the power spectrum of the acoustic signal obtained using STFT provides an easy way to detect the S1 sounds as the peaks. However, it is important to determine a single time-index for every S1 sound in the signal, so that their mutual time differences can be utilised to calculate the HR. To obtain the peak-indexes, every sample of the signal is first squared so that the positive and the negative waveform of the S1 sounds can be transformed to only positive amplitudes above the baseline as shown in Fig. 3.13(a). The squaring process provides a nonlinear amplification of the signal by emphasising the higher frequencies corresponding to the S1 sounds, whilst attenuating the nearby transitions with lower energies.

A moving average filter is subsequently used to integrate the squared energy waveform. The width of the integration window is an important parameter to consider and should ideally be equal to the maximum time duration of the S1 sound in the signal. A window with a larger width can combine the energy of the S1 sound with the energy of nearby signal transitions, whereas a narrower window can produce multiple energy envelopes for the same sound [10]. For a signal with a sampling frequency of 210 samples/second, the filter averages the squared energy waveform over a window of 32 samples. The squared energy followed by an averaging process therefore produces an energy peak corresponding to the S1 sound, as shown in Fig. 3.13(b) which can be easily processed to find the corresponding time index.

#### 3.5.4.2 Artefact identification and elimination

In the pre-processing stage of the proposed algorithm, there are some instances when the artefacts introduced by the wrist or finger movements significantly corrupt some sections of the acoustic signal and are not detected by the K-means method. This usually happens when the maximum amplitude and standard deviation of the signal corrupted

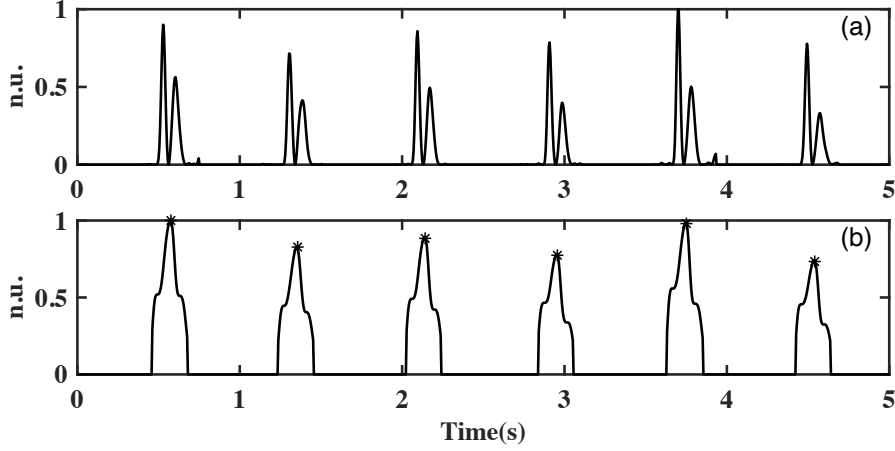


**Figure 3.13:** Peak detection in a clean signal: (a) Squared energy of the S1 sound waveform in Fig. 3.12(d). (b) Energy peaks obtained using the moving average filter. \* represent the time indexes corresponding to the S1 sounds.

with artefacts are close to the features of cleaner sections in a 5 seconds window. Since these artefacts may have significant power, in comparison to the S1 sounds, the STFT analysis allows such signal transitions to appear as well in the further analysis. The energy envelopes of such sections corrupted with artefacts can introduce misleading energy peaks, therefore, affecting the accurate determination of time indexes. To avoid the misclassification of an artefact as the S1 sound, features such as time width and amplitude of every energy peak, are determined in the algorithm. For the acoustic signal, the total number of 5 seconds blocks is defined as  $L$ , where  $y_z[n]$ ,  $z \in [1, L]$  represents each signal block. Assuming that the parameter  $l_z$  provides the total count of energy peaks in  $y_z[n]$ , the width and amplitude features of every energy peak  $E_m$  are denoted by  $w_m$  and  $a_m$ , respectively, where  $1 \leq m \leq l_z$ . The thresholds  $W_z$  and  $A_z$  to process the segment under consideration are determined using equation (3.2) and equation (3.3) respectively, by computing the average of the time widths and amplitudes of all the energy peaks present in the last three signal blocks. The initial value of these thresholds are determined by processing the first six data blocks (30 seconds of the signal) and analysing the corresponding features of the energy peaks.

$$W_z = \frac{\sum_{m=1}^{l_{z-1}} w_m + \sum_{m=1}^{l_{z-2}} w_m + \sum_{m=1}^{l_{z-3}} w_m}{l_{z-1} + l_{z-2} + l_{z-3}} \quad (3.2)$$

$$A_z = \frac{\sum_{m=1}^{l_{z-1}} a_m + \sum_{m=1}^{l_{z-2}} a_m + \sum_{m=1}^{l_{z-3}} a_m}{l_{z-1} + l_{z-2} + l_{z-3}} \quad (3.3)$$

Since the characteristics of the energy peaks corresponding to the S1 waveforms are continuously computed, the thresholds automatically adapt to the changing behaviour of the data, i.e. are not static in value. With the thresholds  $W_z$  and  $A_z$  calculated for

the segment under consideration, the following criteria filter out the energy peaks from the further processing:

1. The energy peaks  $E_m$  in Fig. 3.14(c) are clipped using an amplitude threshold equal to  $(0.25 \times A_z)$ . All the data points above this threshold are retained, while rest of the envelope is zeroed.
2. The thresholding procedure produces redundant peaks as shown in Fig. 3.14(d) which should be filtered out to avoid an incorrect determination of time indexes. The width  $W_z$  evaluated for the current segment is utilised in equation (3.4) to re-

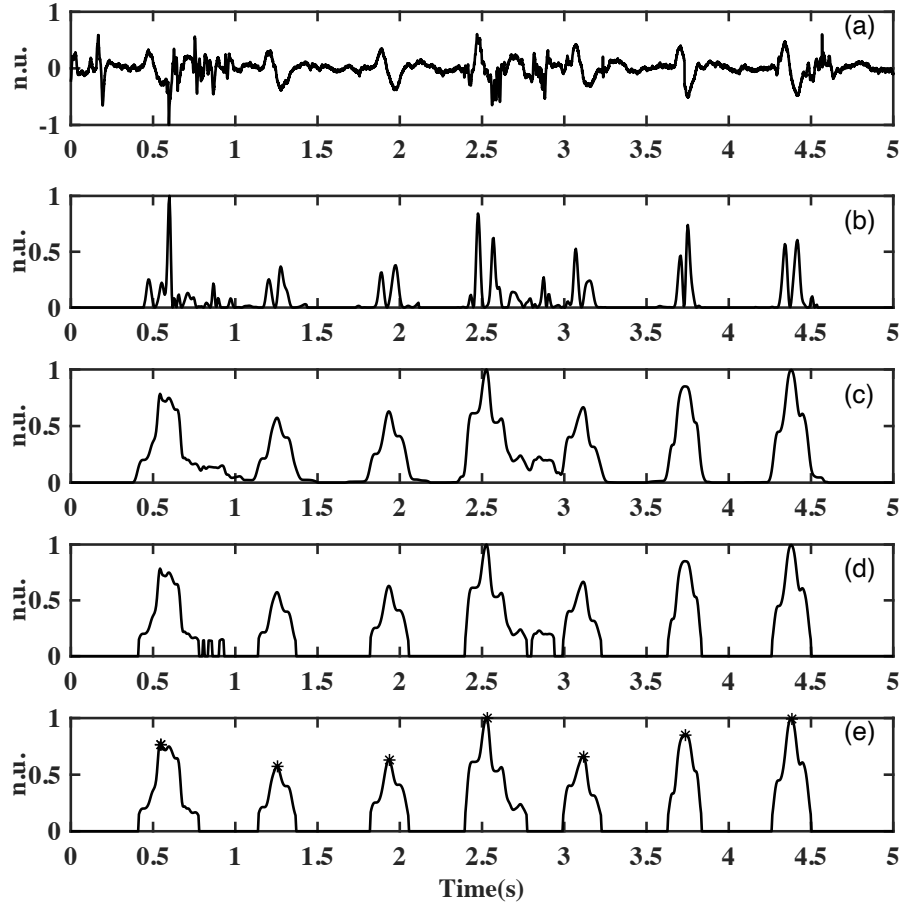


**Figure 3.14:** Peak detection in a corrupted signal: (a) Input acoustic signal corrupted with motion artefacts (introduced by wrist/ finger movements). (b) Squared energy of the signal obtained after PSD analysis. The redundant peaks due to the motion artefacts in systolic and diastolic phases of the cardiac cycle can be observed. (c) Energy envelope obtained using the moving average filter. (d) Thresholding of energy peaks to remove envelopes corresponding to the motion artefacts. (e) Time indexes of energy peaks corresponding to S1 sound waveforms in the signal. This shows how the algorithm successfully distinguishes between motion artefacts and S1 waveforms.

move the unnecessary peaks. The resultant energy peaks thus obtained correspond to the S1 sounds in the signal.

$$\begin{aligned} & \forall m \in [1, l_z] \\ E_m = & \begin{cases} \textit{Accept}, & \text{if } 0.75 \times W_z \leq w_m \leq 1.25 \times W_z \\ \textit{Reject}, & \text{otherwise} \end{cases} \end{aligned} \quad (3.4)$$

3. Finally, all the time indexes (also referred as HR indexes) corresponding to the maximum of the energy peaks, as indicated by \* in Fig. 3.14(e), are noted. These time locations and the number of energy peaks after the artefact removal procedure are defined as  $T_m$  (in seconds) and  $t_z$  respectively, where  $1 \leq m \leq t_z$ .

The time indexes obtained after processing the signal block under consideration can be utilised to determine the beat-to-beat interval,  $\Delta T$  in equation (3.5). The HR is calculated every  $(1/4)^{th}$  second by averaging the beat-to-beat time intervals corresponding to the last 4 heart beats and multiplying it by 60 as follows:

$$\begin{aligned} & \forall m \in [1, t_z - 1] \\ \Delta T_m = & T_{m+1} - T_m \\ \text{HR} = & \frac{60}{(\sum_{m=1}^4 \Delta T_m)/4} \end{aligned} \quad (3.5)$$

### 3.5.5 Subjects and experimental protocol

Acoustic signals to test the proposed algorithm are recorded from 12 healthy subjects aged 19-48 by placing the new miniature, battery-operated wearable device over the radial artery. The sensor attachment, over an area equal to the size of the sensor (27 x 20 millimetres), does not require any cleaning process. The data is recorded only through contact sensing without applying any external pressure on the device. The signals are sampled at a frequency of 2100 Hz and wirelessly transmitted to a nearby base station (a smartphone). The PPG signals from the index finger are simultaneously recorded using a commercially available SOMNOscreen pulse oximeter [1]. The SOMNOscreen monitor also provides an estimate of the HR every  $(1/4)^{th}$  second. The monitor uses a methodology to determine the HR for which the details are not publicly available. A total of 6 recordings, each of 5 minutes duration are recorded from every subject. All the recordings are collected in an uncontrolled environment, but the subjects are asked to sit and relax on a chair. Since the recordings are performed for a long duration, the subjects could move their wrist and fingers, as and when required. The synchronisation of the data from both the sensors, which is critical to evaluate the performance of the proposed system, is carried out by matching the nearest systolic peaks.

### 3.5.6 Results

In order to assess the performance of the proposed method, the algorithm results are compared with other state-of-the-art PPG-based devices, for a total of 12 subjects. The ground truth HR values (HR-PPG) are obtained using the FDA approved, and clinically used SOMNOscreen system [1]. The output from the processing of the acoustic pulse signal (APS) are regarded as the estimated HR values (HR-APS). As an illustration, the estimated and ground truth HR values corresponding to 6 recordings, each of 5 minutes duration for one of the subjects, are plotted simultaneously with upper and lower bounds of 5% respectively with respect to HR-PPG, in Fig. 3.15(a). The first computed performance metric, shown in Fig. 3.15(b), is the Bland-Altman plot [11]. This plot compares the difference between the estimated and ground truth HR values with respect to their corresponding mean. The circled data points in Fig. 3.15(b) indicate the HR differences at different HR averages and their diameter corresponds to the number of points coinciding on the same location. The bias  $\mu$  is calculated by averaging all the HR differences, whereas the limits of agreement (LOA) are obtained by computing  $(\mu \pm 2 \times \sigma)$  respectively, where  $\sigma$  is the standard deviation of the HR differences. While the bias for this comparison is found to be nearly zero, LOA indicated a variation of less than 1 bpm for more than 95% of the data points. As a second performance metric, the line of best fit between the estimated and ground truth HR values is also determined, to understand the degree of similarity using Pearson correlation. The  $R^2$  and root-mean-square-error (RMSE) values depict the corresponding measures of fitness of line to the data. A higher value of  $R^2$  and a lower value of RMSE represents a better fit. For the scatter plot in Fig. 3.15(c), the fitted line with equation:  $y = 0.9958x + 0.2512$  is obtained, where  $x$  indicates the ground truth HR value, and  $y$  indicates the associated estimate. The Pearson correlation is found to be 0.996 with corresponding  $R^2$  and RMSE values of 0.992 and 0.397 respectively.

A similar analysis is repeated for the complete dataset of 12 subjects, where a total of 6 recordings, each of 5 minutes duration are recorded from every subject. The Bland-Altman comparison and the line of best fit thus obtained are plotted in Fig. 3.16. A near zero bias and LOA of [-1.68,1.69] bpm suggests a narrow difference between the estimated and ground truth HR values over the whole database. The Pearson correlation is approximated to 0.998 with an equation for the line of best fit as:  $y = 1.0004x - 0.0266$ . The corresponding  $R^2$  and RMSE values are 0.997 and 0.861 respectively.

A further evaluation of the proposed method is obtained by computing the mean absolute error (MAE) and the mean absolute error percentage (MAEP) as defined in equation (3.6) and equation (3.7) respectively, where  $HR_{est}(i)$  is the estimated HR from the acoustic pulse signal and  $HR_{true}(i)$  is the ground truth HR from the SOMNOscreen monitor at the  $i^{th}$  index in a total of  $N$  values. MAE as an evaluation index provides an estimate of the deviation across the whole dataset whereas MAEP indicates the percentage of error

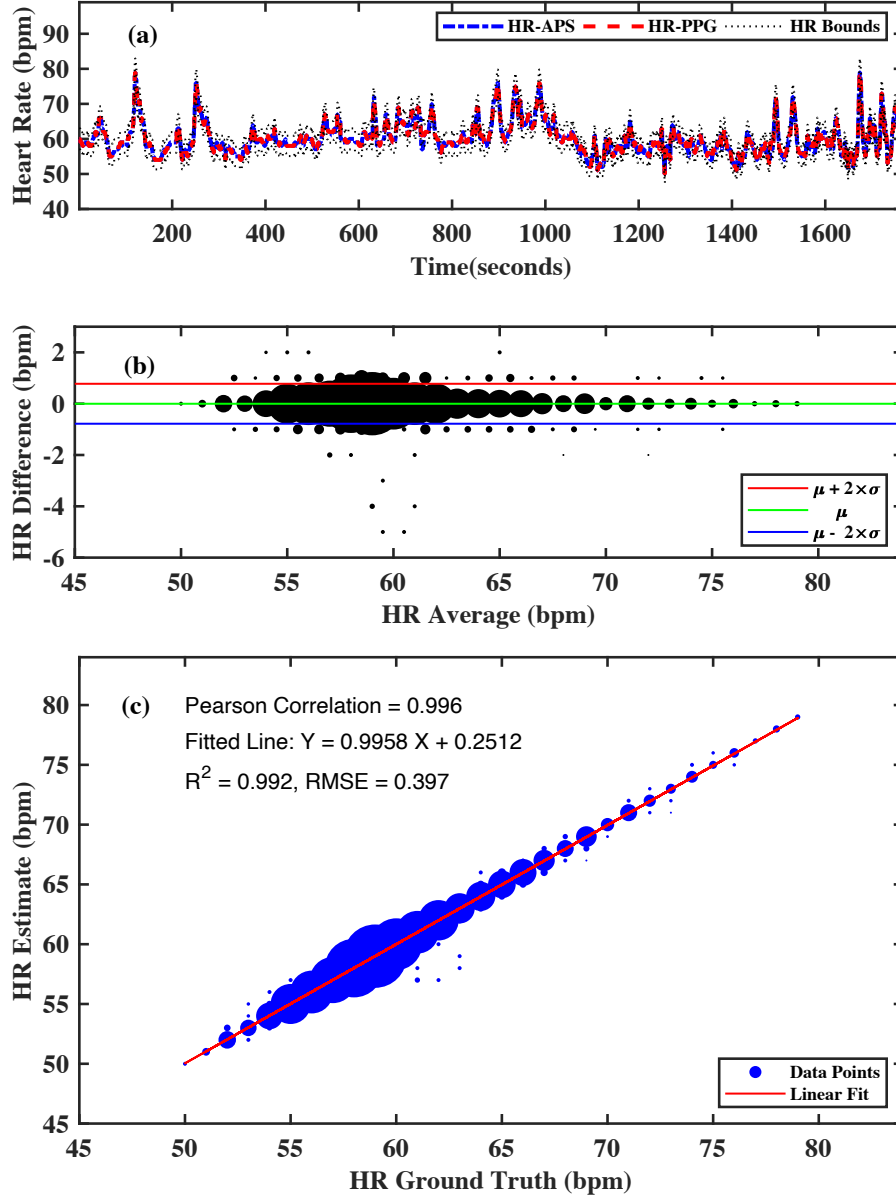


**Figure 3.15:** Results obtained for one of the subjects: (a) HR comparison between the estimated output (HR-APS) and reference output (HR-PPG) with upper and lower HR bounds of  $\pm 5\%$  respectively. (b) Bland-Altman analysis with more than 95% of HR differences lying within LOAs, defined by  $(\mu \pm 2 \times \sigma)$ . (c) Line of best fit between the estimated and ground truth HR values. The  $R^2$  and RMSE value, a measure of fitness of line to the data, were 0.992 and 0.397 respectively. The Pearson correlation was 0.996.

in the HR estimation. Along with these performance metrics, the standard deviation ( $\sigma$ ) and Pearson correlation (PC) are also determined to understand the degree of agreement between the corresponding HR outputs. The accuracy of the method is evaluated by cal-

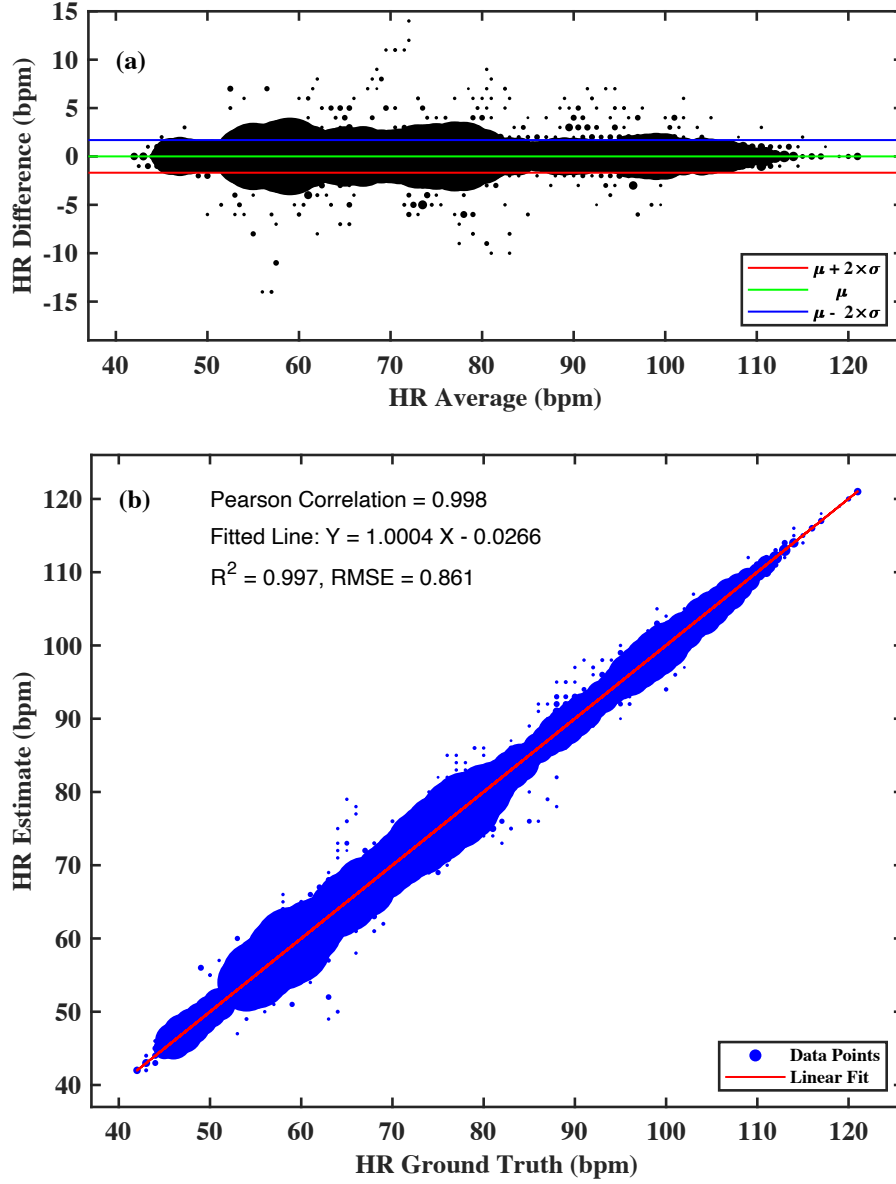


**Figure 3.16:** Results obtained for the complete dataset: (a) Bland-Altman analysis of the HR comparisons for all the subjects. (b) Line of best fit between the estimated and ground truth HR values for all the subjects. The  $R^2$  and RMSE value are 0.997 and 0.861 respectively. The Pearson correlation is 0.998.

culating the percentage of HR values obtained from the acoustic pulse signal and lying within  $\pm 5\%$  of the SOMNOscreen output.

$$\text{MAE} = \frac{1}{N} \sum_{i=1}^N |\text{HR}_{\text{est}}(i) - \text{HR}_{\text{true}}(i)| \quad (3.6)$$



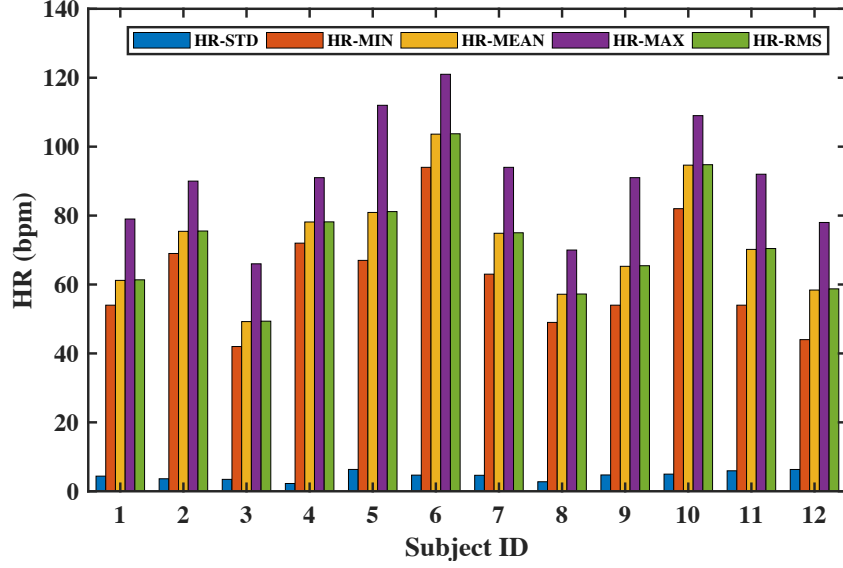


**Figure 3.17:** Variation of HR in individual subjects. *HR-STD*: standard deviation of the range; *HR-MIN*: minimum value of the range; *HR-MEAN*: mean value of the range; *HR-MAX*: maximum value of the range; *HR-RMS*: root-mean-square value of the range.

$$\text{MAEP} = \frac{1}{N} \sum_{i=1}^N \frac{|\text{HR}_{est}(i) - \text{HR}_{true}(i)|}{\text{HR}_{true}(i)} \times 100 \quad (3.7)$$

Table 3.2 lists the performance metrics of the proposed method for all of the 12 subjects. An overall accuracy of 98.78% with a mean absolute error and a standard deviation of 0.28 and 0.86 bpm respectively, are obtained. Fig. 3.17 plots the HR variations in individual subjects including the standard deviation (HR-STD), minimum (HR-MIN), mean (HR-MEAN), maximum (HR-MAX) and root-mean-square (HR-RMS) of the corresponding HR range. The HR in the complete dataset varies from 42 to 121 bpm.

**Table 3.2:** Performance metrics of the proposed method obtained by comparing the estimated and ground truth HR.

	P01	P02	P03	P04	P05	P06	P07	P08	P09	P10	P11	P12	Total
MAE (bpm)	0.10	0.34	0.19	0.24	0.36	0.14	0.18	0.15	0.40	0.34	0.38	0.61	0.28
MAEP (%)	0.17	0.44	0.42	0.31	0.44	0.13	0.24	0.26	0.62	0.36	0.53	1.03	0.39
$\mu$ (bpm)	-0.01	-0.18	0.03	0.03	-0.01	0.01	-0.01	-0.02	0.01	0.09	0.07	-0.06	0.01
$\sigma$ (bpm)	0.39	1.19	0.47	0.66	0.84	0.38	0.49	0.85	0.96	0.90	1.17	1.49	0.86
LOA (bpm)	[-0.78, 0.77]	[-2.48, 2.12]	[-0.88, 0.94]	[-1.26, 1.32]	[-1.65, 1.64]	[-0.73, 0.75]	[-0.98, 0.96]	[-1.68, 1.63]	[-1.87, 1.90]	[-1.67, 1.85]	[-2.23, 2.38]	[-2.97, 2.86]	[-1.68, 1.69]
PC	0.996	0.948	0.991	0.956	0.991	0.997	0.994	0.953	0.979	0.983	0.980	0.971	0.998
Acc (%)	99.91	96.92	99.74	99.01	98.75	99.87	97.29	98.41	97.73	99.19	98.14	94.05	98.78

To test the robustness of the algorithm, the proposed method is also tested using

acoustic signals recorded in a noisy environment. The signals of 5 minutes duration are collected from 5 subjects. During the experiment, the subjects are asked to read a page of text and loud music is played in background at the same time. The results in Table 3.3 indicate that the effect of environmental noise on the acoustic pulse recordings for the HR determination are insignificant.

Table 3.4 compares the results of the proposed method with other studies which analysed the accuracy and reliability of different state-of-the-art PPG-based wrist devices used in the commercial market by comparing them with the synchronous ECG signal. Although the testing of these devices involved different experimental conditions such as sitting in rest position, walking, and running at different speeds and slopes, Table 3.4 only includes the results corresponding to the data recorded at the rest position to provide an indicative comparison with the proposed method. Since there is neither a publicly available database nor a study that has published results on HR monitoring using an acoustic pulse signal, a direct comparison could not be established. Also, the devices in these studies were tested on different number of subjects, but the total data length were quite similar to this study. The table follows the same abbreviations for the comparison parameters as used in the literature. The mean error (ME) and standard deviation (SD) of the HR differences have the same definitions as  $\mu$  and  $\sigma$  respectively. These parameters obtain a value of 0.01 bpm and 0.86 bpm for the proposed method and are significantly lower than other devices. The MAE and MAEP in this work are found to be 0.28 bpm and 0.39%, and demonstrates better performance in comparison to the devices analysed by Stahl *et al.* [12] and Parak *et al.* [13]. A higher PC of 0.99 as compared to 0.96 for Basis Peak and 0.83 for Fitbit Charge HR, as studied by Jo *et al.* [14], also indicates a higher agreement between the estimated and ground truth HR for the proposed method. The standard error (SE) of the mean measures the deviation in the mean HR of all the subjects and attains a higher value of 4.55 bpm in this study. This is mainly because the SE is inversely proportional to the square root of the sample size [15]. Since the other

**Table 3.3:** *Performance metrics of the proposed method for acoustic signals recorded in a noisy environment.*

	P01	P02	P03	P04	P05
MAE (bpm)	0.26	0.20	0.36	0.63	0.09
MAEP (%)	0.41	0.28	0.47	0.89	0.14
$\mu$ (bpm)	-0.08	-0.07	-0.11	0.06	0.03
$\sigma$ (bpm)	0.69	0.48	0.89	1.99	0.35
LOA (bpm)	[-1.45,1.28]	[-1.02,0.88]	[-1.87,1.64]	[-3.83,3.96]	[-0.65,0.72]
PC	0.970	0.988	0.936	0.861	0.986
Acc (%)	99.29	98.12	98.81	95.00	99.05

**Table 3.4:** Performance comparison of the proposed method with results obtained from different PPG-based wrist devices used in the commercial market. The table only compares the results of the data collected at the rest position and provides an illustrative comparison because the experimental conditions varied between different works. <sup>+</sup> The data length is for all the subjects combined together. <sup>\*</sup> SD was calculated from the results of 95% equivalence testing given in this paper. <sup>†</sup> The results provided in the paper were obtained by averaging the data to 5 seconds epochs.

Literature	Wearable Device	Subjects	Data <sup>+</sup> Length	ME (bpm)	SD (bpm)	MAE (bpm)	MAEP (%)	PC	SE (bpm)
Stahl <i>et al.</i> [12]	Scosche Rhythm	50	5.0 hr	–	1.64 <sup>*</sup>	–	2.22	–	1.60
	Mio Alpha			–	1.52 <sup>*</sup>	–	2.72	–	1.50
	Fitbit Charge HR			–	1.45 <sup>*</sup>	–	7.73	–	1.40
	Basis Peak			–	1.58 <sup>*</sup>	–	3.15	–	1.50
	Microsoft Band			–	1.52 <sup>*</sup>	–	3.81	–	1.40
	TomTom Runner Cardio			–	2.06 <sup>*</sup>	–	2.54	–	2.00
Parak <i>et al.</i> [13]	Mio Alpha	21	4.2 hr	-0.20	–	3.92	5.37	–	–
	Scosche Rhythm			0.07	–	4.83	5.96	–	–
Jo <i>et al.</i> [14]	Basis Peak	24	6.0 hr	-0.20	–	–	–	0.96	6.04
	Fitbit Charge HR			-3.73	–	–	–	0.83	10.66
Cadmus <i>et al.</i> [16]	Basis Peak	40	6.7 hr	2.75	9.93	–	–	–	–
	Fitbit Charge			-0.65	4.92	–	–	–	–
	Fitbit Surge			-0.30	2.40	–	–	–	–
	Mio Fuse			1.05	4.42	–	–	–	–
Spierer <i>et al.</i> [17]	Omron HR500U	47	4.7 hr	2.22 <sup>†</sup>	–	–	–	–	3.67 <sup>†</sup>
	Mio Alpha			2.39 <sup>†</sup>	–	–	–	–	6.28 <sup>†</sup>
This Work	Proposed Acoustic Device	12	6.0 hr	0.01	0.86	0.28	0.39	0.99	4.55

studies were tested on a higher number of subjects, the inverse proportionality results in a lower estimate of the SE. The comparison over these parameters show that, considering PPG is a widely accepted technique, the proposed method utilising the acoustic sensing can provide accurate results for HR monitoring at wrist under equivalent conditions.

### 3.6 Discussion

The feasibility of acoustic sensing of the radial pulse using a wearable device has been investigated in this chapter. While ECG has always been used as the gold standard method to record cardiac signals from the chest, measuring it continuously with a wearable device presents lots of limitations, varying from reliability to usability. An alternative to ECG, which improves on the usability aspects, is to use PPG-based devices instead. This approach is very popular due to the fact that it allows monitoring with the sensor attached on the wrist. But methods based on wrist PPG are not limitations free either. The requirements of an active input signal limit either the size of the system and/or the battery lifetime. In addition the systems are very sensitive to motion and other artefacts. Hence, having an alternative lower power sensing approach would be desirable to either complement the PPG to increase the sensing accuracy, or replace it altogether, depending on the clinical target. The passive sensing mechanism of state-of-the-art acoustic sensors (MEMS microphones) imposes significantly less constraints in terms of power, hence

being more suitable from the size and maintenance perspective for a wearable device.

The characteristics of the pulse wave originating from the heart- as a result of the opening and closing of the heart valves, and propagating as a mechanical wave along the arterial branches have also been investigated, by comparing the acoustic and PPG pulse waveforms. Although negligible, the heart sounds also transmit an acoustic wave through the body. Since these acoustic features are superimposed on the vessel vibrations caused by the mechanical constriction and dilation of the radial artery, a similar type of skin surface modulation is obtained. While PPG only measures the pulse wave component, the acoustic-based sensing allowed the detection of both cardiophysiological characteristics of the radial pulse. The bandwidth of the acoustic pulse waveform, which contained energies in the audible range as compared to the bandwidth of less than 10 Hz for the PPG waveform proved this observation. Consequently, the proposed approach showed that it is possible to monitor both, the heart sounds as well as the pulse wave using just one wearable system.

The characterisation of the pulse sounds also allowed to determine the optimal auscultation site on the radial artery, since this is a factor to consider when comparing the ease of sensor attachment with respect to ECG- and PPG-based approaches. The PSD comparisons showed that the acoustic sensing allows for a relatively wide region of sensor placement with an insignificant difference between the SNR of the signals recorded from different locations over the radial artery.

Studying the characteristics of the noise artefacts both internal and external to the body made it possible to remove them automatically for a better representation of the acoustic signal. Among different types of hand movements, only the wrist and finger motions introduced large amplitudes in the signal making it difficult to extract meaningful cardiac information. The proposed algorithm incorporated their removal by identifying the signal regions corrupted with these artefacts using selected features. The effect of wrist and finger movements on the SNR of the acoustic signal can be minimised by adding additional signal channels using an accelerometer and/or gyroscope. These sensors can provide critical information about the motion artefacts and act as a reference input, for example, to an adaptive filter in extracting a cleaner signal. However, the usage of these sensors imposes extra burden on size and shape of the PCB, power budget and computational resources of the wearable system. Although these sensors were not included in the current prototype proposed in this thesis, they can possibly be added to the future prototypes of the wearable device by studying the trade-off between the accuracy of cardiac monitoring and the power budget of the system. Regarding the environmental noise that also interfered with the pulse sounds, simply using a low-pass filter attenuated their effect significantly.

Furthermore, by comparing the HR obtained from acoustic sensing with other state-of-the-art PPG based devices, it has been shown that the presence of fundamental heart

sounds in the acoustic pulse waveform improved the heartbeat detection, an important variable in continuous vital sign monitoring. Heartbeat detection based on extraction of S1 sounds using the new proposed method further reduced the error between the estimated and ground truth HR and achieved a high accuracy of 98.78% with a PC of 0.99 and narrower LOAs of [-1.68,1.69] bpm. These results prove that the proposed method could be used as an alternative, or to complement PPG for continuous monitoring of HR at wrist.

As a summary, with this work, it can be concluded that the acoustic signal sensed from the radial artery in the wrist can be used as a novel physiological signal to extract biomarkers indicative of cardiac performance. Furthermore, this signal provides advantages with respect to other conventionally used ones, which make it specially suitable for wearable devices. The concept and feasibility has been proven with the automatic extraction of HR.

## References

- [1] SOMNOmedics: Polysomnography SOMNOscreen plus. [Online]. Available: <http://somnomedics.eu/products/polysomnography-somnoscreentm-plus/>
- [2] C. Will, K. Shi, S. Schellenberger, T. Steigleder, F. Michler, J. Fuchs, R. Weigel, C. Ostgathe, and A. Koelpin, "Radar-Based Heart Sound Detection," *Scientific reports*, vol. 8, no. 1, p. 11551, 2018.
- [3] M. Elgendi, "On the analysis of fingertip photoplethysmogram signals," *Current cardiology reviews*, vol. 8, no. 1, pp. 14–25, 2012.
- [4] P. Sharma, S. A. Imtiaz, and E. Rodriguez-Villegas, "An Algorithm for Heart Rate Extraction from Acoustic Recordings at the Neck," *IEEE Transactions on Biomedical Engineering*, 2018.
- [5] W. Shi and J.-C. Chiao, "Neural network based real-time heart sound monitor using a wireless wearable wrist sensor," *Analog Integrated Circuits and Signal Processing*, vol. 94, no. 3, pp. 383–393, 2018.
- [6] J. U. Kim, Y. J. Lee, J. Lee, and J. Y. Kim, "Differences in the properties of the radial artery between Cun, Guan, Chi, and nearby segments using ultrasonographic imaging: a pilot study on arterial depth, diameter, and blood flow," *Evidence-Based Complementary and Alternative Medicine*, vol. 2015, 2015.
- [7] S. Lloyd, "Least squares quantization in PCM," *IEEE transactions on information theory*, vol. 28, no. 2, pp. 129–137, 1982.
- [8] B.-U. Kohler, C. Hennig, and R. Orglmeister, "The principles of software QRS detection," *IEEE Engineering in Medicine and biology Magazine*, vol. 21, no. 1, pp. 42–57, 2002.
- [9] O. Pahlm and L. Sörnmo, "Software QRS detection in ambulatory monitoring a review," *Medical and Biological Engineering and Computing*, vol. 22, no. 4, pp. 289–297, 1984.
- [10] J. Pan and W. J. Tompkins, "A real-time QRS detection algorithm," *IEEE Trans. Biomed. Eng.*, vol. 32, no. 3, pp. 230–236, 1985.
- [11] J. M. Bland and D. Altman, "Statistical methods for assessing agreement between two methods of clinical measurement," *The lancet*, vol. 327, no. 8476, pp. 307–310, 1986.
- [12] S. E. Stahl, H.-S. An, D. M. Dinkel, J. M. Noble, and J.-M. Lee, "How accurate are the wrist-based heart rate monitors during walking and running activities? Are they accurate enough?" *BMJ open sport & exercise medicine*, vol. 2, no. 1, p. 106, 2016.
- [13] J. Parak and I. Korhonen, "Evaluation of wearable consumer heart rate monitors based on photoplethysmography," in *Engineering in Medicine and Biology Society (EMBC), 2014 36th Annual International Conference of the IEEE*. IEEE, 2014, pp. 3670–3673.
- [14] E. Jo, K. Lewis, D. Directo, M. J. Kim, and B. A. Dolezal, "Validation of biofeedback wearables for photoplethysmographic heart rate tracking," *Journal of sports science & medicine*, vol. 15, no. 3, p. 540, 2016.
- [15] D. G. Altman and J. M. Bland, "Standard deviations and standard errors," *Bmj*, vol. 331, no. 7521, p. 903, 2005.
- [16] L. Cadmus-Bertram, R. Gangnon, E. J. Wirkus, K. M. Thraen-Borowski, and J. Gorzelitz-Liebhauser, "The accuracy of heart rate monitoring by some wrist-worn activity trackers," *Annals of internal medicine*, vol. 166, no. 8, pp. 610–612, 2017.
- [17] D. K. Spierer, Z. Rosen, L. L. Litman, and K. Fujii, "Validation of photoplethysmography as a method to detect heart rate during rest and exercise," *Journal of medical engineering & technology*, vol. 39, no. 5, pp. 264–271, 2015.

## 4 An algorithm to determine heart rate variability in short-term acoustic recordings

### 4.1 Introduction

Cardiac monitoring in healthcare applications provide critical information to study the normal functioning of the heart. The heartbeat rhythm is usually studied by calculating the heart rate of an individual using different techniques. While some of these techniques locate the biomedical events in the signal of interest, other methods utilise the spectral estimation of the time-varying frequencies in the cardiac signal. In the majority of applications, the average frequency estimation over several heartbeats is acceptable to reflect the variation in the heartbeat rhythm. However, studying the heart rate variability (HRV) by measuring the instantaneous changes in beat-to-beat cycles provide a reliable reflection of several physiological factors responsible for the modulation of the normal rhythm of the heart. Since heart rate is a non-stationary signal, tracking the instantaneous changes can allow studying the balance between sympathetic and parasympathetic branches of the autonomic nervous system (ANS) [1]. The analysis of the ANS using HRV, therefore, reflects the ability of the heart in detecting and responding to an unpredictable stimuli by regulating the cardiac activity. HRV analysis has been utilised in several studies to recognise and evaluate the driving stress [2], obstructive sleep apnea syndrome [3], chronic heart failure [4], diabetes mellitus [5], epileptic seizures [6], emotion recognition [7] and other disorders.

The initial step of the HRV analysis requires the computation of either the inter-beat interval (IBI) or the instantaneous heart rate (IHR) from the biomedical signal for subsequent determination of HRV parameters. The IBI (in seconds) and the IHR (in beats-per-minute) time-series are inversely proportional to each other and one can be derived from another by simply multiplying the reciprocal with a factor of 60. Although both the IBI and the IHR are exchangeable, the HRV is generally referred in terms of the IBI time-series. A typical approach for calculating the IBIs requires a precise localisation of the events of interest in the biomedical signal. Some of the examples of such events include the QRS complex in the ECG signal, systolic peak in the PPG waveform, and S1 and S2 sounds in the PCG signal. The signal processing techniques in Section 2.2.1

discussed different algorithms to determine heart rate from these signals. The heart rate algorithms mainly fall into 2 categories of spectral-based and peak-based methods. The spectral techniques transform a time-windowed signal into the frequency-domain to identify the fundamental frequency corresponding to the heart rate [8]–[11]. Since the signal spectrum contains other peaks including the peaks from the motion artifacts, the spectral estimation is carried out for a larger signal segment (few seconds to tens of seconds) to localise the heart rate frequency accurately [11], [12]. The determination of single frequency for such windowed signal segments provide only an average estimation of the heart rate and loses critical information about the beat-to-beat variation in the signal. The peak-based methods, on the other hand, identify the events of interest to extract the time-indices for IBI calculation. These events in the biomedical signal can be identified using several techniques, for example, by constructing the energy envelope to separate the desirable energy peaks from other signal transitions [13]–[15]; by identifying unique features corresponding to the events of interest and isolate them using learning-based approaches [16], [17]. The heart rate determined using the peak-based methods generally average the IBIs over a last few beats to filter out the instantaneous variations in the time-series output. While the algorithmic details implemented by the commercial devices are generally not available publicly, they measure heart rate over several beats, typically 4 to 8 heartbeats, and displays the output at different sampling frequencies [18], [19].

An accurate HRV analysis requires a beat-to-beat resolution [20]. Therefore, it is important to locate the characteristic points in the events of interest precisely, for example, the time location of R-peak in the QRS complex of the ECG waveform. Since the S1 sounds in the acoustic signal does not resemble with the QRS morphology, it would be ideal to preserve all its characteristic points to establish a comparison and find the best representation of the S1 sounds for the HRV analysis. The algorithm proposed in Section 3.5 utilised a peak-based method to extract S1 sounds from the acoustic signal. Although a strong correlation and statistical agreement for the average heart rate estimation between the acoustic signal and the PPG signal were obtained, the previous method poses some constraints on extracting an accurate IBI time-series. The method transformed the acoustic signal into joint time-frequency domain and identified the events of interest (S1 sounds) by only selecting the time grids with maximum power spectral density. Since the time-frequency resolution in STFT analysis is constrained by the Heisenberg’s uncertainty principle, there may be a few instances when the selected time grids does not contain the full S1 waveform. These instances can originate when the interference from noisy sources changes the power distribution among the signal components. Since the heart rate in the previous algorithm was obtained by averaging the last 4 IBIs, such a loss would not affect the average heart rate. However, it can possibly lead to a loss of few characteristic points for the HRV analysis. Another drawback of the previous algorithm



is that it only focused on detecting the zero-crossing of the S1 sounds as the characteristic point by constructing the energy envelope using the moving average filter. Since the adopted filtering is essentially a smoothing technique, a change in the shape of the S1 sound due to the noise interference can cause the maximum of the energy peak to deviate from the original location. This can potentially result in an inaccurate detection of the time-index corresponding to the zero-crossing. While a slight variation in the time localisation of the characteristic point does not affect the average heart rate, it can introduce significant variations in the HRV analysis. To overcome the issues faced by the previous method, a novel algorithm is proposed to extract the HRV from the short-term acoustic signals recorded at the wrist. Instead of zeroing the intermediate signal transitions as in STFT analysis, the proposed algorithm improves the localisation of the S1 sounds and preserves all the characteristic points by utilising the relative energies of the time-domain signal. The algorithm design also considers the computational complexity as an important constraint to allow the extraction of HRV parameters from larger data lengths. The following section discusses the existing methods for the HRV extraction from different biomedical signals. A subsequent discussion on different stages of the proposed algorithm is provided to establish a comparison of the HRV derived from the acoustic signal at the wrist with the PPG and ECG signals respectively.

## 4.2 Existing methods

The sympathetic and parasympathetic branches of the ANS modulate the heart rate at different frequencies [1]. The spectral analysis of the IBI time-series can therefore allow the separation of the rhythmic contributions from the sympathetic and parasympathetic activities. Such analysis can lead to an early intervention in taking preventive diagnostic measures. However, this requires an accurate extraction of the IBI time-series from the biomedical signal as little inaccuracies in the IBIs can introduce substantial variance into the frequency bands associated with the arrhythmia [21]. A gold standard approach to measure the IBI time-series is by detecting the QRS complex in the ECG signal. Several algorithms have been proposed in the literature to extract the R-peak from the ECG signal. However, a universal approach for the QRS detection has not been found due to the diversity of the QRS waveforms in different subjects, low SNR and the presence of

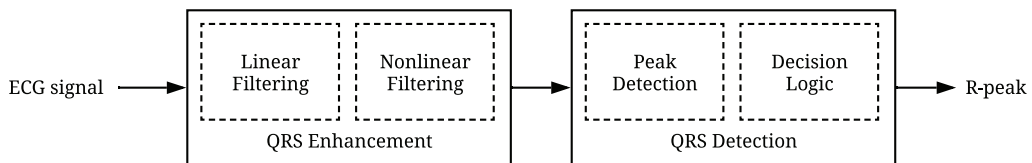


**Figure 4.1:** *Generic block diagram for R-peak extraction from the ECG signal.*

motion artifacts in ECG signals. Detailed reviews about the QRS detection methods for different applications are available in [22]–[26]. The R-peak detection typically involves 2 stages: QRS enhancement and QRS detection as shown in Fig. 4.1. The QRS enhancement stage, also known as the pre-processing block, enhances QRS complex with respect to other ECG signal transitions (such as P- or T- wave) by extracting different features using linear or non-linear filtering techniques. The QRS detection stage employs a relevant peak-detection method based on the pre-processing results followed by decision logic to identify the onset and offset of the QRS complex and extract the temporal location of the R-peak. The review in [22] discriminated the algorithms based on the QRS enhancement stage and focused on their operating principles. Elgendi *et al.* [26] also summarised such algorithms by evaluating their performance over the three assessment criteria: robustness to noise, parameter choice and numerical efficiency to find a suitable algorithm for implementation in battery-operated wearable ECG systems. Some of the commonly used R-peak extraction algorithms along with their operating principles and feature signals are briefly described in Table 4.1. Since the statistical parameters related to the HRV are traditionally obtained from the 24-hour ECG recordings, the numerical efficiency of the algorithm is highly desirable. In Table 4.1, not all the methods listed are suitable for the HRV analysis because of their varying computational complexities. The comparison of these methods in [26] showed that a simple and numerically efficient way of locating the R-peaks after the QRS enhancement stage is only possible with the thresholding technique. All the other QRS detection algorithms were found to have medium or high computational complexities.

**Table 4.1:** *R-peak extraction algorithms with different operating principles and feature signals.*

Technique	Operating Principle	Feature Signal
Derivative [27]–[30]	The high-pass filter implemented as a differentiator indicates the characteristic steep slope of the QRS complex. The QRS detection is accomplished by comparing the feature signal against a fixed or adaptive threshold followed by several decision rules.	Differentiated signal itself. A linear combination of different orders of derivatives being squared, averaged, modulus, etc.

**Table 4.1:** *R-peak extraction algorithms with different operating principles and feature signals.*

Technique	Operating Principle	Feature Signal
Digital Filters [31]–[34]	QRS complex consist of frequencies between 10 Hz and 25 Hz. The bandpass filtering removes baseline wandering, P- and T-wave, incoupling noise, etc. The non-linear operations using sophisticated digital filtering enhances the QRS complex and suppresses other parts of the ECG signal to make QRS detection easier using the adaptive thresholding.	The signal filtered using a combination of multiple digital filters with different bandwidths. The filtered signal is sometimes followed by first order derivative to extract the feature signal by computing the square and average of the differentiated output.
Wavelet transform/ Singularity detection [35]–[38]	The singularity in the ECG signal is detected using Mallat’s and Hwang’s approach [22]. The QRS detection is performed by matching the singularities with the local maxima in the wavelet transform of the signal. R-peaks are located where the relevant scales of the wavelet transform exceed a threshold and demonstrate a simultaneous modulus maxima.	Coefficients of the wavelet transform at different scales.
Filter banks [39]–[41]	QRS complex is characterised by simultaneously occurring frequency components in different subbands [22]. The ECG signal filtered through different subbands is followed by thresholding or decision logic for QRS detection.	A linear combination of different subband signals.
Neural networks [17], [42], [43]	Neural networks are used as adaptive nonlinear predictors to estimate the current signal value from its past samples. Since the non-QRS segments are present in a larger portion of the ECG signal, the neural networks converge when the prediction about non QRS samples is correct. Different statistics of the QRS complex produces a larger prediction error allowing its detection.	Prediction error obtained from the neural network with time-delayed ECG signal samples fed as an input.

**Table 4.1:** *R-peak extraction algorithms with different operating principles and feature signals.*

Technique	Operating Principle	Feature Signal
Adaptive filters [44]–[46]	Similar to neural networks, adaptive filters predict the current signal value as a weighted superposition of the signal values in the past. The weights adapt to the changing signal statistics by minimising the prediction error using algorithms such as least mean square method. The instantaneous prediction error becomes large when the QRS event is detected by an adaptive model.	The difference between the weight vectors at two different times. The difference of the short term energy of the residual error in adjacent windows.
Hilbert transform [47]–[49]	The instantaneous characteristics of the ECG signal obtained from the Hilbert transform is utilised to construct an energy envelope. The QRS complex produces higher energy peaks in comparison to other ECG transitions and are detected by using a threshold.	Energy envelope obtained from the real and imaginary part of the analytic signal computed using the Hilbert transform.
Empirical mode decomposition [50]–[53]	The EMD decomposes the ECG signal into several intrinsic mode functions. The first few IMFs filter out the noise components and preserve the information corresponding to the QRS complex. Rejecting the other IMFs improve the SNR for QRS detection using thresholding.	Intrinsic mode functions corresponding to the ECG signal.
Zero-crossing [54]	The running average of the zero-crossings in the modulus of the bandpass filtered ECG signal is higher during the non-QRS segments in comparison to the QRS complex. The average is compared against an adaptive threshold to detect the QRS complex.	Average count of the zero-crossings.

In addition to the gold standard approach of HRV measurement from the ECG signal, the HRV parameters can also be measured using pulse wave analysis. Commonly, the pulse waveform is recorded using the PPG-based wearable sensing. Since the signal acquisition using pulse oximetry is highly prone to motion artifacts, the heart cycle measurements with a beat-to-beat resolution becomes quite challenging. This is the main reason why the majority of studies mainly focus on estimating the average heart rate and not the instantaneous heart rate using the PPG signal. However, in principle, the HRV parameters can also be obtained from the PPG signal. The variability of the pulse cycles in the literature is usually known as the pulse rate variability (PRV). Unlike the R-peaks

in the ECG signal, the PPG signal does not have a fixed characteristic point and the accuracy of beat-to-beat interval depends not only on the choice of the characteristic point but also the algorithmic method to locate it [55]. For the HRV analysis, the PPG waveform is typically indexed temporally with one of the following characteristic points: systolic peak, point of maximum slope or first order derivative, diastolic minima or foot points denoting the onset of systole. Although majority of the studies concerning PPG processing focus on the average heart rate estimation (including motion artifacts), some of the research, as listed in Table 4.2, also test the feasibility of using different PPG characteristic points to extract the PRV and compare it with the ECG-derived HRV. Schäfer *et al.* [55] presented a detailed review of such studies and investigated the accuracy of PRV as an estimate of the HRV. Georgiou *et al.* [56] also investigated the accuracy of HRV and PRV in ECG and PPG signals respectively. The review focused on understanding whether wearable devices provide a reliable and accurate measurement of variability by studying sixteen ECG-based HRV technologies and two PPG-based PRV technologies. In majority of the studies, the temporal locations of the characteristic points are identified using traditional peak detection algorithms involving peak enhancement in the pre-processing stage. The pre-processing typically involves the use of band-pass filters and the first and second order derivatives [57]–[60]. The spectral techniques for extracting the IBIs have also been explored where the frequency corresponding to the average heart rate is used as the center point to find the instantaneous frequency using the Hilbert transform [61]. The conclusions drawn from Table 4.2 suggests that the PRV derived from the PPG signal recorded at different sensing locations demonstrate a high correlation with the ECG-based HRV and shows a good agreement mostly for the signals recorded at rest. The review in [56] also found a high correlation between PRV and HRV during rest, however, it decreased progressively with the intensity of the exercise. The difference in the agreement mainly arises because of the difference in the physiology of both the signals. While ECG records the electrical activity of the heart, PPG measures the volumetric change in the blood flow due to the propagation of the peripheral pulse wave. Therefore, a finite propagation time exists between the R-peak in the ECG signal and the onset of the pulse wave at a particular PPG site. This delay is usually known as the pulse transit time (PTT) and it correlates with the blood pressure, arterial stiffness and age of the subject [62]. Since the PTT depends on other parameters, its physiological variability can introduce a significant difference in the IBIs estimated from PPG and ECG signals respectively, despite the accurate determination of the characteristic points using the proposed algorithm. In such cases, a wide disagreement between the PRV and HRV can be observed.

While PPG provides a reliable way of recording the pulse waveform, the pulse wave analysis can also be performed using the blood pressure (BP) waveform and the impedance plethysmography. The beat-to-beat BP waveform is usually recorded using Finapres sys-

tem that employs photoplethysmographic finger cuff to assess BP continuously by using the vascular unloading principle [63]. Impedance plethysmography, on the contrary, uses multiple metallic electrodes to produce an electric signal in proportion to the instantaneous impedance of the tissue under the electrodes [64]. Therefore, the change in the average impedance corresponding to the periodic phases of the arterial blood flow can be detected by the metallic electrodes. Although advancements in the wearable technology have made the use of these systems obsolete, few studies listed in Table 4.2 utilised these systems to record the pulse waveform and extract the HRV. It can be observed that some studies indicate a strong agreement with the ECG-derived HRV whereas the other studies suggest the usage of pulse-based HRV only as an alternative to ECG. In conclusion, the pulse-to-pulse variability can be considered as a surrogate choice to HRV in cases where the data is recorded at rest.

**Table 4.2:** *HRV extraction from pulse waveforms recorded at different sensing locations. Studies are grouped according to the pulse sensing method.*

Ref.	Sensing Location	Characteristic Point	Algorithm	Remarks
<i>Photoplethysmography studies</i>				
[57]	Finger	First sample after 70% slope threshold	Peak detection using a threshold of 70% of maximum slope applied on first order derivative.	High correlation at rest between PPG- and ECG-based LF and HF bands.
[58]	Finger, wrist, arm, ear, ankle	Systolic and diastolic point	Peak detection based on first and second order derivative. IBIs compared against PSD peaks in 0.6-2.9 Hz for better accuracy.	Least mean square error for IBIs obtained at rest. Ideal wearable locations were arm and finger.
[59]	Wrist	Systolic peak, onset of pulse, dicrotic notch	Pre-processing (band-pass filtering, automatic gain control and smoothing filter) followed by beat-to-beat extraction using interpolation and delineation.	Average IBI difference around 12 ms showed strong HRV correlation between PPG and ECG.
[61]	Wrist	—	Average HR is determined as the center point for spectral masking of instantaneous frequency obtained from Hilbert transform.	IHR accuracy of 1.75 bpm obtained for PPG signals.

**Table 4.2:** *HRV extraction from pulse waveforms recorded at different sensing locations. Studies are grouped according to the pulse sensing method.*

Ref.	Sensing Location	Characteristic Point	Algorithm	Remarks
[65]	Earlobe	Rising edge of the pulse	Heartbeat pulses are detected using a comparator circuit in the analogue front end of the design.	Small differences between IBIs from PPG and ECG suggested that the wearable earlobe PPG may be suitable for HRV measurements.
[60]	Finger (Camera)	Systolic peak	Pre-processing including low-pass filtering, high-pass filtering, peak detection and removal of motion artifacts.	PPG-based PRV indices had small deviation in comparison to ECG-based HRV indices.
[66]	Finger	Minimum peak of averaged first order derivative	PPG denoising and detrending using the empirical mode decomposition method followed by selection of largest negative value of the first derivative of the down-slope phase.	PPG variability parameters are highly correlated with the HRV parameters and could be used as an alternative to HRV measurement.
[67]	Earlobe, finger	Diastolic peak (trough of the pulse)	—	PRV features from PPG and HRV features from ECG were found to be similar. The finger PRV and earlobe PRV can be used as surrogates for HRV.
[68]	Dorsal side of the wrist	—	Pulse frequency demodulation (PFDM) extracted the instantaneous heart rate frequency directly from the pulse wave.	PFDM of the pulse wave signal provided a reliable estimation of PRV and showed good agreement with HRV.

**Table 4.2:** *HRV extraction from pulse waveforms recorded at different sensing locations. Studies are grouped according to the pulse sensing method.*

Ref.	Sensing Location	Characteristic Point	Algorithm	Remarks
[69]	Earlobe	—	Analysis software using the first order derivative of PPG as the feature signal.	PRV and HRV parameters showed a good agreement but PRV should only be used for the screening purposes and not medical decisions.
<i>Blood pressure waveform studies</i>				
[70]	Finger (Finapres)	Pressure wave maxima	Peak detection using in-built Finapres software	Spectral HRV parameters were statistically different during standing and exercise, but not in supine and controlled breathing conditions.
[71]	Finger (Colin system)	Systolic peak	IBIs extracted using slope, peak and correlation detection.	BP waveform does not reflect HRV precisely but can be considered as an alternative to ECG with the slope detection method.
[63]	Finger (Finapres)	Peaks and troughs of BP waveform	Systolic peaks extracted using the in-built software were used to find the IBI time series.	High HRV reliability between the two methods, however, HF indexes were found to be less precise.
[72]	Finger (Finapres)	—	Heart instantaneous frequency algorithm to track HRV frequency around a PSD estimated fundamental frequency.	Statistically similar time-frequency HRV measurements between BP and ECG waveforms.
[73]	Finger (Finapres)	—	Peak detection using in-built Finapres software.	PRV does not reflect the HRV accurately, but it can be accepted as an alternative to ECG.
<i>Impedance plethysmography studies</i>				



**Table 4.2:** *HRV extraction from pulse waveforms recorded at different sensing locations. Studies are grouped according to the pulse sensing method.*

Ref.	Sensing Location	Characteristic Point	Algorithm	Remarks
[74]	Forearm	Onset of pulse	Diastolic point identified using product of digitised signals from first and second order derivative followed by weighted and frequency filter.	High sensitivity and accuracy indicated close agreement for variability analysis with two operators.
[64]	Radial artery (Wrist)	—	Heartbeats are identified using the the cross-correlation and template matching.	HRV analysis performed using root mean square of successive differences in the heart beat interval showed strong agreement with ECG.

Both ECG and PPG allow recording of the electrical and optical characteristics of the cardiac activity. However, the recent advances in the development of electromechanical sensors have made it possible to monitor the mechanical activity of the heart by using mechanocardiography techniques. These techniques capture the micro-motions of the site under test by measuring the recoil forces [75]. Seismocardiography (SCG) is one such method which measures accelerations caused by respiration and myocardial motions in the chest wall using miniaturized high-resolution and low-noise accelerometers [76]. While the SCG in relation to the cardiac activity has mainly been explored to monitor the heart rate, some studies have also extended its usage in extracting the HRV in an unobtrusive manner using the beat-to-beat resolution. Wahlström *et al.* [77] proposed a hidden Markov model approach to process the SCGs recorded using an accelerometer along the dorsoventral axis from 66 subjects. The algorithm described the heartbeat vibrations with a hidden Markov model and learned the related parameters using the Baum-Welch method. The most likely sequence of states was then found using the Viterbi algorithm to estimate the time point of each individual heartbeat. The algorithm achieved a mean absolute error of 5 ms for the IBI estimation in comparison to the ECG-based IBIs. Tadi *et al.* [78] used a tri-axial MEMS accelerometer to record SCGs in supine, left and right recumbent positions from 30 subjects. The heartbeat timings were identified using the Hilbert adaptive beat identification technique and a high correlation and agreement between the IBIs extracted from SCG and ECG were observed.

The accelerometer in the smartphone has also been utilised to record the SCGs. Landreani *et al.* [79] recorded the SCG signal from 9 subjects by positioning the 3-orthogonal axis accelerometer (available in the smartphone mobile device) on the subject's thorax in supine and standing postures. The characteristic points corresponding to the isovolumetric contraction in the SCG signal were identified using a fully automated algorithm based on amplitude thresholding and rectification. A strong correlation and narrow limits of agreement were obtained when compared to the RR interval series. The cardiac beats in the SCG signal were identified with 98% accuracy. The same dataset recorded during the supine posture was used in [80] to extract the beat-to-beat systolic complex from the SCG signal. The proposed algorithm utilised Newtonian equations of kinematics to calculate the linear power followed by its decomposition as a set of functions using the quadratic spline wavelet. Further, the continuous wavelet transform was applied to extract the peaks corresponding to the systolic complexes. A high sensitivity of 0.995, positive predictive value of 0.974 and narrow confidence interval of  $\pm 35$  ms were obtained when identifying a total of 2816 beats in comparison to the RR intervals. The integration of an accelerometer and a gyroscope in an inertial measurement unit (IMU) to utilise their functionality with higher degrees-of-freedom have also been used to record the SCG signal [77], [81]. Kaisti *et al.* [81] used such an embedded sensor array to measure the cardiogenic motions of the upper chest from 29 healthy subjects and 12 subjects with coronary artery disease. The beat-to-beat detection was performed using the wavelet enhancement and clustering techniques by utilising the features inherent to the signal envelope and the signal morphology. While a small average root mean square error of 5.6 ms between the mechanical- and ECG-based IBIs was obtained for the healthy patients, a 10-fold increment was observed for the heart disease patients.

Another approach to measure the body recoil forces is known as ballistocardiography (BCG). BCG, as one of the most promising unobtrusive techniques, has recently gained wide attention in the research community. A ballistocardiograph records the mechanical activity of the heart by measuring the body recoil forces resulting from the blood ejection in each cardiac cycle [82]. While the BCG technique has been known for a number of years, modern BCG systems integrated in beds, chairs, pillows, mattresses, scales etc. provide an unobtrusive and comfortable way of monitoring the cardiopulmonary activity for subjects requiring a prolonged monitoring [83]. The research concerning BCG signal mainly focuses on the coarse estimation of the heart rate because of the presence of multiple fiducial points. However, some of the algorithms detect individual heart beats from the BCG signal for advanced applications such as HRV analysis or sleep staging. Jiao *et al.* [84] utilised a hydraulic bed sensor consisting of a transducer and a pressure sensor to record the BCG signal from 40 subjects. The transducer was placed under the subject's torso to measure the heartbeat vibrations along with an interference from the respiratory activity. Although the individual heart beats in the BCG signal were identified

using a multiple instance dictionary learning approach, the results were only compared for an average heart rate computed over a one-minute window. The IBI comparison with the PPG signal resulted in 4.07% mean relative error over 40 subjects. BCG signals from bed-based systems have also been recorded by installing multiple strain gauges in a Wheatstone bridge configuration to the slatted frame of the bed [82], [83], [85]. The algorithms based on adaptive training were proposed in [83], [85] to estimate the beat-to-beat intervals from the BCG signals. The method employed an unsupervised learning approach to extract features from the first 30 s of the BCG data. Further, K-means clustering was used to identify the cluster of feature vectors. The results in both the studies showed a coverage of more than 95% with respect to the ECG signal. The algorithm in [82] also used an unsupervised learning approach to extract feature vector from the local maximum of the first derivative of the BCG signal. An overall detection rate of 83.9% was obtained for 7 subjects in four different lying positions. Brüser *et al.* [86] extended the previous work by acquiring the BCG signal from 33 subjects using a single electromechanical film sensor placed on the top of a mattress. Instead of employing a common peak-detection technique to estimate the IBIs, an approach based on pitch tracking to estimate the varying fundamental heart rate frequency by means of continuous local interval estimation was proposed. Unlike the previous algorithm, this method neither required a training phase nor any prior knowledge about the morphology of the heart beats in the analysed waveforms. However, the assumption that the consecutive heart beats in the BCG signal have similar morphology limits the use of the proposed algorithm in cases where an interference from the motion artifacts is present. The comparison with ECG-based IBIs yielded a mean error of 0.78%. The beat-to-beat intervals from the BCG signal have also been extracted using different types of template matching algorithms [87]–[89]. These methods are based on the reasoning that while the fiducial points in the BCG signal are sensitive to any external interference, the signal patterns repeat themselves with each heart beat. Wang *et al.* [87] based the BCG processing on this assumption and used a segmented dynamic time warping approach to estimate the beat-to-beat heart rate. The signals were recorded from 20 subjects using a modified electronic weighing scale. The IBI comparisons between JJ intervals (BCG) and RR intervals (ECG) produced an error of  $\pm 19$  ms for the 95% confidence interval. Krej *et al.* [90] installed a Fiber Bragg grating sensor in magnetic resonance imaging system to record the BCG signals from 8 subjects. The heartbeat positions were found using the local maximum of a detection function incorporating enhanced characteristics in comparison to the original signal. The detection function was determined by implementing a cascade of digital filters. A mean error of -0.62 bpm and the limits of agreement between -12.28 bpm and 11.04 bpm were obtained with respect to the IBIs estimated from the ECG signal. Optical-based BCG sensing using three IR-LEDs and one photodiode setup in a bed have also been performed for unobtrusive cardiac monitoring [91]. The optical

sensing works on the principle that any mechanical movements of the body deforms the air enclosures of the mattress, therefore, altering the path of the light. The photodiode detects such changes and produces a corresponding signal. An algorithm quite similar to [86] was implemented to achieve a relative error of 1.46% and 25.7% for the intervals estimation in the best and the worst channel respectively. Apart from bed- and mattress-based sensing systems, the BCG signals have also been collected by installing sensors on the chair top [92]. The ballistic force from 7 subjects was measured with a piezoelectric sensor fixed with an adhesive tape to the bottom side of the seat of a common office chair. The proposed algorithm utilised the continuous wavelet transform with splines to reduce the effect of noise and interference. It involved a learning stage to define the initial thresholds for the identification of BCG peaks using adaptive thresholding. In comparison to the ECG, a mean error of -0.03 bpm and 95% confidence intervals of  $\pm 2.7$  bpm were obtained.

An emerging approach for unobtrusive monitoring of the cardiac activity is based on radar sensing technology. Radar-based systems are designed to work without interfering with the daily activities of a user making the cardiac monitoring very user-friendly. These systems typically use Doppler radar to observe the phase shift in the transmitted microwave signal that is scattered back depending on the modulation caused by the subject's torso movements. The reflections from the body surface of the subject are dominated by cardiopulmonary activities in the radar measurements [93]. Different algorithms have been proposed in the literature to utilise the radar echo signal and extract the cardiac information at a beat-to-beat resolution. This is generally difficult even in a clean radar signal since it is not as sharp as the ECG or PPG signal [94]. The approach in [94] utilised a 2.4 GHz Doppler radar at a distance of 1.5 m and modelled the heart beat signal using a Gaussian pulse train. A combined autocorrelation and frequency-time phase regression technique was further used for high accuracy detection of the heart rate. The extracted IBIs showed an error of less than 2% in comparison to the PPG measurements and a high agreement was observed. The Doppler radar sensors have also been used in [95], [96] for the HRV analysis. While the IBIs in [95] were extracted using the time-frequency analysis utilising filter banks, the study in [96] used the approach of continuous wavelet transform and ensemble empirical mode decomposition to separate the cardiopulmonary activity. Both the studies showed a high level of agreement between the radar-extracted and the ECG-extracted HRV features. Bakhtiari *et al.* [97] recorded the cardiac information using a custom designed remote millimeter wave (mmW) I-Q sensor. The sensor allowed a remote and contactless measurement of the cardiac activity at relatively long standoff distances. The beat-to-beat heart rate was determined from only one subject using a parameter optimisation method based on the nonlinear Levenberg Marquardt algorithm. Although the reliability of the system was compared against a commercially available laser vibrometer, the study did not present the comparison of

HRV parameters.

As a summary, HRV monitoring techniques can be broadly divided into three groups. The first group includes ECG as the gold standard approach to extract HRV by sensing the electrical activity of the heart and continuously measuring the R-R peak intervals. The second group records the pulse wave using methods such as PPG, blood pressure waveform and impedance plethysmography to measure the HRV. These approaches typically use optical sensors at different locations of the body and measures volumetric changes in the blood flow. While both the first and the second groups are based on contact sensing, the third group records the mechanical movements of the heart using contactless techniques such as BCG, SCG and radar-based sensing. The Task Force of the European Society of Cardiology and the North American Society of Pacing and Electrophysiology [20] recommends HRV extraction from either the long-term 24-hour recordings or short-term 5-minute recordings. Although mechanocardiography techniques provide an unobtrusive manner of monitoring the cardiac activity, they constrain the subject to be present in clinical settings and are not feasible for long-term 24-hour HRV monitoring. The signals recorded using these techniques require advanced signal processing methods since the SNR is much lower than ECG and PPG signals [94]. A high sensitivity towards body movements put further limitations on the use of these techniques for HRV measurements [81]. It is because of these constraints that the long-term HRV is typically monitored using ECG and PPG-based sensing methods. Although the long-term HRV monitoring is usually recommended, the rise in battery-driven wearable systems (mainly PPG-based) have allowed researchers to extract HRV parameters from short-term physiological recordings. However, the limited processing capability of these systems imposes constraints on the algorithm design. Therefore, in principle, even when the processing capabilities of the processors have enormously increased, it is still desirable to develop simple algorithms with high numerical efficiency without trading off significantly on the detection results [26]. In combination to the low processing complexity, a feasible peak detection algorithm should also be robust to the noise sources and function properly without requiring any manual or patient-specific adjustment of the parameters. The subsequent sections discuss the data acquisition protocol followed in this study and proposes a low complexity algorithm to measure the short-term HRV by extracting S1-S1 inter-beat intervals from the acoustic signal recorded at the wrist.

### 4.3 Data acquisition protocol

The previous chapters proved the feasibility of recording the acoustic pulse signal from the radial artery using a miniaturised, battery-operated wearable data acquisition system. The pulse sounds were recorded using a MEMS microphone placed on the radial artery and the data was transmitted over a Bluetooth channel to a nearby base station. In addition to the average heart rate estimation from these acoustic signals, this thesis

also explores the possibility of extracting the HRV profile of a subject by acoustically recording the pulse from the radial artery at the wrist. For the HRV database, the acoustic data was digitised at a sampling frequency of 2100 Hz with 12-bits of ADC resolution. Since the HRV measurements are generally obtained using the gold standard approach of ECG with a recent emphasis on the PPG, the synchronous recordings of Lead I ECG signal from the chest and PPG signal from the index finger were also acquired using the state-of-the-art SOMNOscreen monitor [18]. The ECG and PPG signals were sampled at 256 Hz and 128 Hz respectively among different options available in the device. The SOMNOscreen monitor also provided the RR-intervals and heart rate profile as a reference by processing the ECG data using an inbuilt algorithm, the details of which are not available publicly. Since these references were only obtained from the ECG signal, the inter-beat intervals and the beat-to-beat heart rate corresponding to the PPG signal were extracted by simply locating the systolic peaks using the peak detection method in MATLAB software. A total of 12 healthy subjects with an age between 19 and 42 were asked to relax for 5 minutes on a chair with a comfortable back and arm support. It was also ensured that for normal functioning of the cardiac activity, the subjects did not exercise and consume any food or beverage in the last hour prior to the recording. Although the data was collected in an uncontrolled environment, the subjects were asked to remain silent and minimise the wrist movement to avoid the introduction of any external motion artifacts in the recording. A synchronous recording of the acoustic pulse signal, ECG and PPG signals were made for a total of 5 minutes duration for every subject. The subsequent section discusses the S1 extraction algorithm to derive the IBI time-series from the acoustic signal.

#### 4.4 S1 waveform extraction method

The algorithm proposed in this work is based on using the relative energy method to extract the short-term events of the S1 sound waveforms from the acoustic pulse signal by utilising the relative information between short- and long-term energies of the signal [13]. It is based on the principle that the power contained in the S1 waveform even in the presence of motion artifacts is significantly higher than the power in the baseline of the acoustic signal. Similar to the QRS enhancement stage in Fig. 4.1, the method computes a coefficient vector which, when multiplied with the original signal, amplifies the S1 event and attenuates the energy of the surrounding transitions. The calculation of the coefficient vector involves an optimal choice of short- and long-term window lengths to extract the waveform of interest from the signal. For every sample  $n$  of the acoustic signal  $y$ , the coefficient vector  $c(n)$  is defined as the ratio of the short- and long-term squared energies of the signal computed within two sliding windows,  $s_w$  and  $l_w$  respectively.

$$c(n) = \frac{\sum_{i=n-s_w}^{n+s_w} |y(i)|^2}{\sum_{j=n-l_w}^{n+l_w} |h(j) \times y(j)|^2} \quad (4.1)$$

The squared energy in Eq. 4.1 is calculated around the sample centred at  $n$  where the parameters  $s_w$  and  $l_w$  represent the half-lengths of the short and long sliding windows, respectively. For boundary points, only samples which can fit on either sides of the sliding windows are used. The parameter  $h$  denotes the Hamming window function with twice the length of  $l_w$ . The output signal  $y_{re}$  is determined by the element-wise multiplication (sample-by-sample basis) of the coefficient vector and the original acoustic signal for a total of  $N$  samples as follows:

$$y_{re}(n) = c(n) \times y(n), \quad \forall n \in [1, N] \quad (4.2)$$

The multiplication modulates the original signal based on the behaviour of the coefficient signal. Since the coefficient vector generates a higher weight for the waveforms containing higher energies, the modulation heightens the impulse-like events and attenuates the regions carrying lower energies. However, such a behaviour can only be obtained with an optimal choice of the sliding windows. As a rule, the length of the window  $s_w$  should ideally be equal to the maximum duration of the waveform of interest present in the signal. The duration of the longer window  $l_w$  should be chosen to reflect the long-term behaviour of the signal, however, care should be taken as a significantly longer length can make the variations in  $s_w$  insignificant.

As an illustration, the successive steps of the relative energy algorithm implemented on a 5-seconds block of the input acoustic pulse signal are plotted in Fig. 4.2. The goal of the algorithm is to extract all the S1 waveforms and attenuate the surrounding noisy transitions. This is achieved by using a short- and a long-term sliding window of time duration equal to 0.2 and 1 second, respectively. The normalised short-and long-term energies of the signal are plotted in Fig. 4.2(b). It can be observed that the short-term energy reflects the sudden changes in the signal whereas the long-term energy represents a slowly changing behaviour of the signal. The coefficient vector thus obtained amplifies the S1 regions of interest by attenuating the nearby transitions resulting in a cleaner output signal as shown in Fig. 4.2(d).

It is understood that the relative energy algorithm works efficiently in cases where the short-term events of the S1 waveforms in the acoustic signal are characterised by a local change in the amplitude. The STFT analysis in the previous chapter showed that the S1 waveforms contain higher power as compared to the nearby signal oscillations. Therefore, the proposed S1 waveform extraction method can robustly identify these regions of interest by discarding the baseline activity.

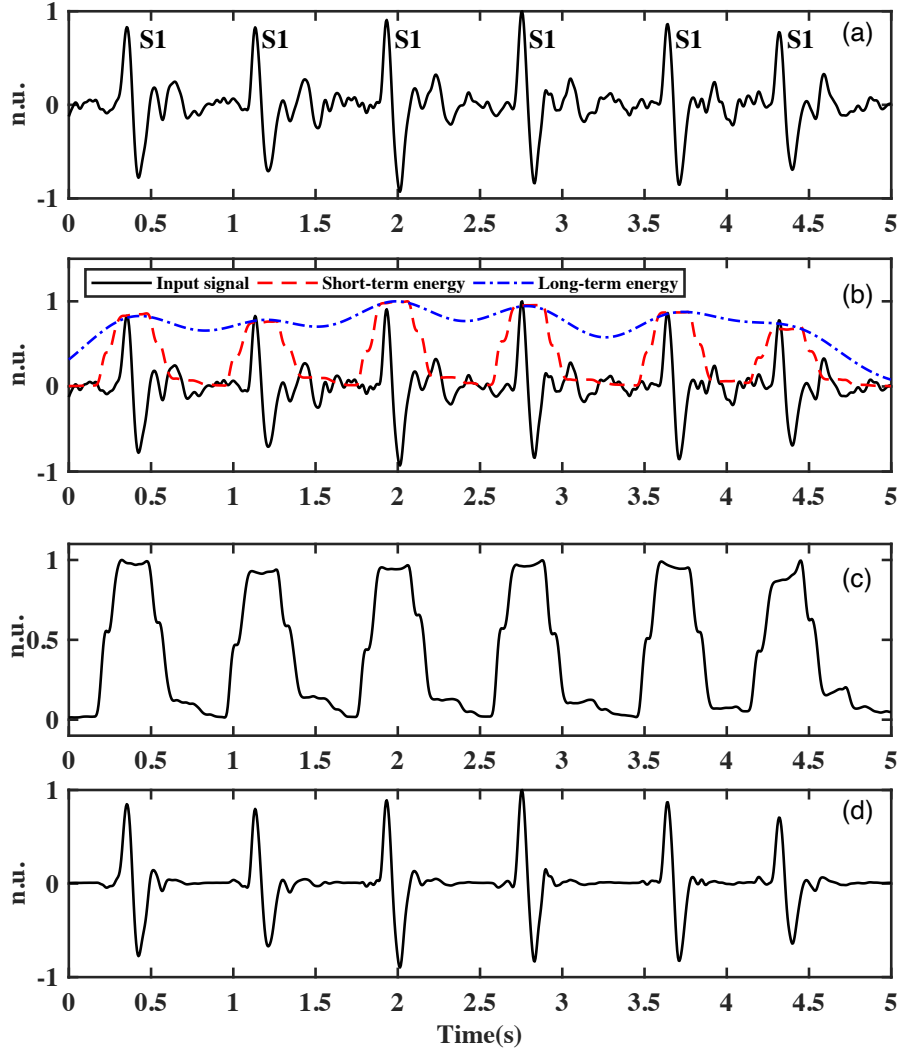


**Figure 4.2:** Relative energy algorithm implemented on the acoustic pulse signal. (a) Original input acoustic signal consisting of different S1 waveforms. (b) Normalised short- and long-term energies of the input signal depicting numerator and denominator in Eq. 4.1. (c) The coefficient signal,  $c(n)$ . (d) The output signal,  $y_{re}(n)$ .

## 4.5 Peak detection algorithm

The S1 waveform in the output signal demonstrates two different morphological variations for different subjects as shown in Fig. 4.3. This variation is characterised in terms of the waveform transitioning from a positive peak ( $APS_p$ ) to the zero crossing ( $APS_z$ ) to a negative peak ( $APS_n$ ) and vice-versa. For the same subject, it is empirically observed that these characteristics of the S1 waveform does not change over the length of the acoustic recording.

An accurate estimation of the HRV requires precise localisation of the S1 waveform in



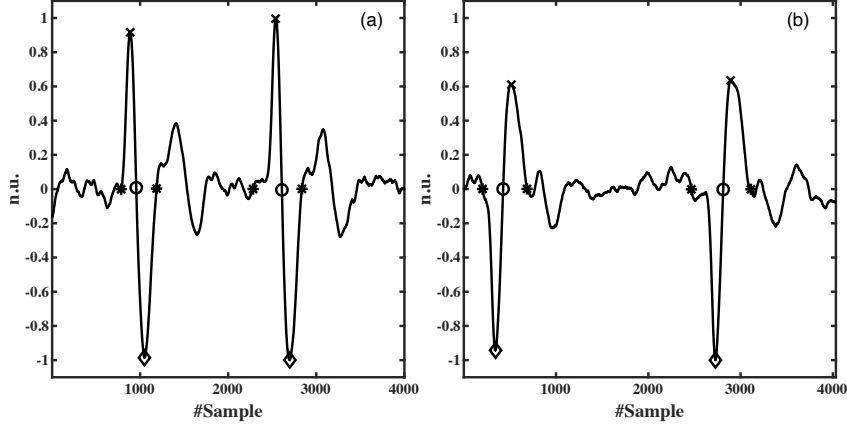


**Figure 4.3:** *Morphological variations in the pulse waveform. (a) Acoustic pulse transitioning from a positive peak to zero crossing to a negative peak. (b) Acoustic pulse transitioning from a negative peak to zero crossing to a positive peak. Symbol  $\times$ ,  $\circ$  and  $\diamond$  denotes the positive peak ( $APS_p$ ), zero crossing ( $APS_z$ ) and negative peak ( $APS_n$ ) respectively. Symbol  $*$  represents the nearest zero crossings on either sides of  $APS_z$ .*

the time-domain. Since the S1 waveform can be localised using 3 different characteristic points, it is important to identify all of them and compare their corresponding accuracies in the HRV analysis. This comparison will allow to understand the reliability of a particular characteristic point in representing the S1 waveform as a single time-index. The algorithm identifies these characteristic points by computing the squared energies of the positive ( $y_{re}^p[n]$ ) and the negative amplitudes ( $y_{re}^n[n]$ ) of the output signal  $y_{re}(n)$  as shown in Fig. 4.4(b). The squaring process in Eq. 4.3 amplifies the higher frequencies possessed by the S1 waveforms and further attenuates the nearby signal transitions. The maximum of the energy peaks are utilised to localise the time-index corresponding to the positive and the negative waveforms. Since the S1 waveform possesses a single zero-crossing between the two energy peaks, the time-instance of the zero crossing can be easily found by tracing back the original signal as shown in Fig. 4.4(c).

$$\begin{aligned} y_{sq}^p[n] &= (y_{re}^p[n])^2 \\ y_{sq}^n[n] &= (y_{re}^n[n])^2 \end{aligned} \quad (4.3)$$

Since the relative energy algorithm utilises a local change in the amplitude (or signal energy) to detect a short-term event, there can be instances when an input signal block is significantly corrupted by the artifacts with amplitudes higher than the S1 waveform. The squared energy of such an output signal can lead to an incorrect localisation of the characteristic points. To distinguish the artifacts from the S1 waveforms, the algorithm could incorporate the frequency-domain features computed using STFT as explained in the previous chapter. However, the computational complexity of  $\mathcal{O}(n \log n)$  for the STFT analysis will affect the run time of the algorithm and require more computational

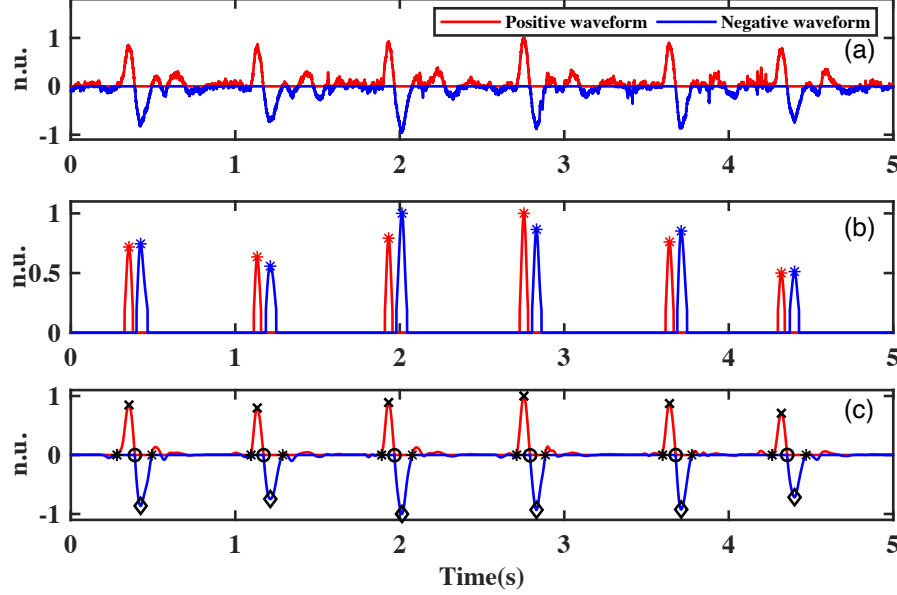


**Figure 4.4:** Localisation of characteristic points in the signal. (a) Clipped positive and negative waveforms of the original input signal. (b) Squared energy of the relative energy signal with its corresponding maximum. (c) Symbol  $\times$ ,  $\circ$  and  $\diamond$  denote the time-localisation of the positive peak ( $APSp$ ), the zero crossing ( $APSz$ ) and the negative peak ( $APSn$ ) respectively in the relative energy signal. Symbol  $*$  represents the nearest zero crossings on either sides of  $APSz$ .

resources. Therefore, a trade-off between an accurate S1 detection and the computational complexity of the algorithm does exist. Instead of processing the corrupted signal in the frequency-domain, this study only uses the time-domain features to remove the artifacts and constrain the complexity of the algorithm to  $\mathcal{O}(n)$ . Unlike ECG, the acoustic signal does not suffer from the baseline wandering. Since the baseline of the acoustic signal does not vary over the length of the recording, it is empirically observed that the following features for the S1 waveform remains nearly constant for a subject.

1. *Time width* - The time difference between the nearest zero-crossings indicated by ' $*$ ' on either sides of the zero-crossing denoted by symbol ' $\circ$ '.
2. *Amplitude* - Peak-to-peak amplitude of the S1 waveform calculated using the difference of the amplitudes at time locations denoted by symbol ' $\times$ ' and ' $\diamond$ ' respectively.

In cases where the acoustic signal is significantly corrupted with the artifacts, the morphology of the S1 waveforms can possibly get affected as shown in Fig. 4.5(a). This can not only lead to an improper detection of the characteristic points but can also include some erroneous peaks in the peak extraction process. Such peaks can be rejected by plotting the feature space using peak-to-peak amplitude ( $a$ ) and time width ( $w$ ) of all the detected peaks and calculating their corresponding standard deviations  $\sigma_a$  and  $\sigma_w$  respectively. The feature space for the clean signal in Fig. 4.4(c) and the corrupted signal

in Fig. 4.5(c) are plotted in Fig. 4.5(d) and Fig. 4.5(e) respectively. It can be observed that both the features  $a$  and  $w$  corresponding to the S1 waveforms in the clean signal yield a lower standard deviation, therefore, indicating a narrow variation as compared to the features of the corrupted signal. This property of the feature space can be utilised to reject the incorrect peaks present in the corrupted signal.

For an acoustic signal of 5 minutes duration, the standard deviation of the time width for a 5 second block is defined as  $\sigma_{wz}$ , where  $z \in [1, 60]$  represents each signal block. The time intervals between the successive peaks are also found by using the time differences between the zero-crossings (denoted by symbol ‘o’) of the current and the next adjacent S1 waveform. For a heart rate between 40 and 200 bpm, the inter-beat intervals must lie between 300 and 1500 milliseconds respectively. Therefore, in cases where multiple peaks are extracted within a mutual time distance of 300 milliseconds, only peak with the highest peak-to-peak amplitude  $a$  is selected and other redundant peaks are ignored for the further processing. Since a cleaner signal after the removal of redundant peaks have less disparity in the feature space, the initial value of threshold  $\sigma_0$  is determined by

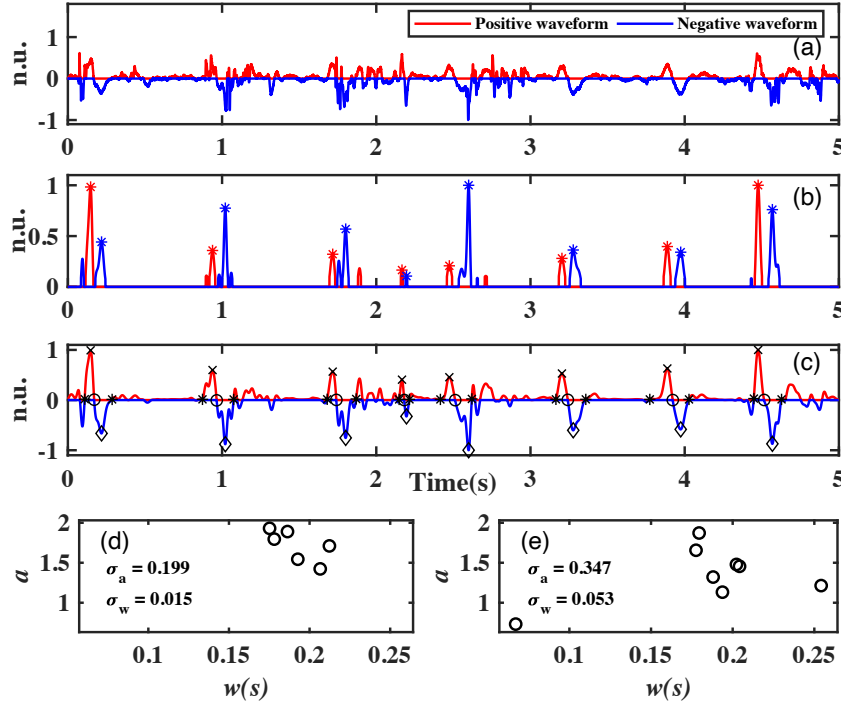


**Figure 4.5:** Localisation of the characteristic points in the acoustic signal corrupted with artifacts. (a) Clipped positive and negative waveforms of the original input signal. (b) Squared energy of the relative energy signal with its corresponding maximum. (c) Symbol  $x$ ,  $o$  and  $\diamond$  denoting the time-localisation of positive peak ( $APSp$ ), zero crossing ( $APSz$ ) and negative peak ( $APSn$ ) respectively on the relative energy signal. Symbol  $*$  represents the nearest zero crossings on either sides of  $APSz$ . (d) Time-domain features plotted for waveforms extracted in Fig. 4.4(c). (e) Time-domain features plotted for waveforms extracted in Fig. 4.5(c).

choosing the minimum value of  $\sigma_{wz}$  for the first three signal blocks. This is mainly done because the time width of the S1 waveform demonstrates less variation over the length of the acoustic recording. For every successive block, the relative change in standard deviation  $\Delta\sigma$  is found by comparing  $\sigma_0$  and  $\sigma_{wz}$  using the Eq. 4.4. A variation of less than 0.25 in  $\Delta\sigma$  classifies the signal block as clean and updates the threshold  $\sigma_0$  in Eq. 4.5 by averaging itself with the standard deviation of the current block. In cases where the variation of more than 0.25 in  $\Delta\sigma$  is observed, some of the peaks in the block are incorrectly extracted due to the presence of artifacts. Such peaks are identified and rejected as follows:

1. Firstly, the mean  $\mu_w$  of all the time widths in the signal block is determined.
2. Secondly, the standard deviation  $\sigma_{wz}$  is reevaluated by ignoring the peak with the largest distance of its time width  $w$  from  $\mu_w$ . As an illustration, the peak with feature coordinates (0.067,0.732) in Fig. 4.5(e) is rejected.
3. The new  $\sigma_{wz}$  is subsequently used to find the variation  $\Delta\sigma$ .
4. These steps are reiterated by rejecting the peaks with farthest time widths from  $\mu_w$  until the variation  $\Delta\sigma$  of less than 0.25 is observed.
5. The threshold  $\sigma_0$  is continuously updated in Eq. 4.5 by averaging itself with the new standard deviation  $\sigma_{wz}$  of the current block.

$$\Delta\sigma = \frac{|\sigma_{wz} - \sigma_0|}{\sigma_0} \quad (4.4)$$

$$\sigma_0 \leftarrow \frac{\sigma_0 + \sigma_{wz}}{2} \quad (4.5)$$

For the corrupted signal in Fig. 4.5(c), only the fourth peak is rejected as its removal produces a  $\Delta\sigma$  of value less than 0.25.

After the removal of erroneous peaks from the acoustic signal, the S1 waveforms can be easily localised using the time-indices of all the characteristic points to derive three different IBI and IHR profiles per subject. The number of S1 waveforms extracted in the  $z^{th}$  signal block of 5 seconds duration is  $N_z$ . The time-index of the positive characteristic point defined as  $t_m^p$ , for the beat number  $m \in [1, N_z - 1]$  can be utilised to calculate the IBI<sup>p</sup> and IHR<sup>p</sup> profile as follows:

$$\begin{aligned} \forall m \in [1, N_z - 1] \\ \text{IBI}_m^p &= t_{m+1}^p - t_m^p \\ \text{IHR}_m^p &= \frac{60}{\text{IBI}_m^p} \end{aligned} \quad (4.6)$$

The IBI and IHR determination in Eq. 4.6 are repeated corresponding to the time-indices of the zero crossing ( $t_m^z$ ) and the negative characteristic points ( $t_m^n$ ) respectively.

## 4.6 Results and discussion

### 4.6.1 Optimal choice of parameters

The performance of the proposed algorithm is dependent on the optimal choice of the short- and long-term sliding window lengths in the relative energy method to extract the S1 waveform. These optimal values are determined by evaluating the sensitivity ( $S_e$ ), positive predictive value (PPV) and detection error rate (DER), which are defined as follows:

$$S_e = \frac{TP}{TP + FN} \quad (4.7)$$

$$PPV = \frac{TP}{TP + FP} \quad (4.8)$$

$$DER = \frac{FP + FN}{TP + FP + FN} \quad (4.9)$$

where true positives (TP) denote the correctly detected S1 waveforms, false positives (FP) specify the number of events incorrectly classified as S1 waveforms, and false negatives (FN) refer to the count of S1 waveforms that remain undetected. Therefore,  $S_e$  essentially reflects the ability of the method to correctly extract the S1 waveforms from the acoustic signal whereas PPV signifies the probability of the classified S1 events being truly the S1 waveforms of interest. On the contrary, DER indicates the error in the accurate classification of the S1 waveforms.

The optimal choice of  $s_w$  and  $l_w$  is determined by studying the variation of these performance metrics, evaluated over the complete dataset for a combination of different window lengths. The short-term window length  $s_w$  is varied in the range of [0.1, 0.4] s in steps of 0.05 s whereas the long-term window length  $l_w$  is varied in the range of [1, 2.5] s and is incremented in steps of 0.25 s. The effect of  $s_w$  and  $l_w$  on the performance metrics of the proposed algorithm are illustrated by plotting the contours of  $S_e$ , PPV and DER in Fig. 4.6. It can be observed that the sensitivity in Fig. 4.6(a) remains almost constant with the variation in  $s_w$ , but decreases with an increase in  $l_w$ . On the other hand, PPV does not vary much with the choice of window lengths as shown by a narrow variation in the values of the colour bar in Fig. 4.6(b), and has a higher dependency on  $s_w$ . The minimum values on the DER contour plot in Fig. 4.6(c) indicates a dependency similar to the  $S_e$  plot. Although the analysis demonstrates that the performance of the algorithm is almost constant over a wide variation of  $s_w$  and  $l_w$  parameters, this study uses 200 ms and 1 s as the durations of the short and the long sliding windows respectively.

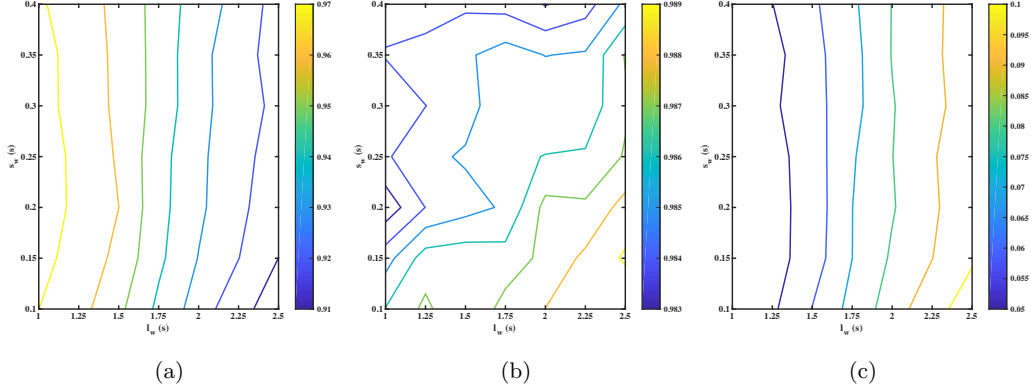


**Figure 4.6:** Effect of short- and long-term sliding windows on performance metrics of the proposed algorithm. (a) Contour plot for depicting variation in sensitivity ( $S_e$ ). (b) Contour plot for depicting variation in positive predictive value (PPV). (c) Contour plot for depicting variation in detection error rate (DER).

#### 4.6.2 Time-domain HRV analysis

To assess the performance of the proposed algorithm in determining the IHR and IBIs across 12 subjects, the following time-domain comparisons have been established:

1. *Correlation analysis:* In order to assess the measure of association between the estimated output and the gold standard, the Pearson correlation coefficient (PCC) is computed. The line of best fit for such an association is represented by  $y = m \times x + c$ , where  $y$  and  $x$  corresponds to the estimated output and the ground truth respectively, and  $m$  indicates the slope of the line of best fit. A slope of 1 indicates a strong positive relationship between both the outputs whereas the values nearer to -1 signify a strong negative correlation. The  $R^2$  and root-mean-square-error (RMSE) values indicate the measure of goodness of fit.
2. *Bland-Altman analysis:* In clinical applications, the Bland-Altman analysis provides a measure of statistical agreement between the estimated and the true output. This analysis is generally performed to assess the potential of the new method in replacing the existing one. The agreement is governed by comparing the difference with the mean of outputs derived from both the methods. The mean ( $\mu$ ) and the standard deviation ( $\sigma$ ) of differences between both the measures are utilised to define the limits of agreement (LOA) as  $(\mu \pm 2 \times \sigma)$ . For differences which follow a Gaussian distribution, 95% of the output differences should lie between the two LOAs [98]. A lower LOA suggests a higher degree of agreement between both the methods.
3. *MAE parameter:* The parameters  $\mu$  and  $\sigma$  in the Bland-Altman analysis provides the relative bias and an estimate of error between the two outputs. The mean

absolute error (MAE) as defined in Eq. 4.10 computes the average of absolute differences between the estimated and true outputs, and therefore indicates the overall error in the time-series analysis.

$$\text{MAE} = \frac{1}{N} \sum_{i=1}^N |\text{IHR}_{est}(i) - \text{IHR}_{true}(i)| \quad (4.10)$$

where  $\text{IHR}_{est}$  and  $\text{IHR}_{true}$  are the estimated and true instantaneous heart rates respectively, for a total of  $N$  heartbeats.

4. *Time-domain HRV measures:* To quantify the variation of IBI time-series in a subject, the selected time-domain HRV measures as defined in [20] are also found. The term NN interval is widely understood in the context of successive inter-beat intervals for a chosen characteristic point. Therefore, the NN interval in this study refers to the R-R interval in the ECG, systolic-systolic interval in the PPG and S1-S1 interval in the acoustic signal respectively. A total of five HRV parameters defined below are calculated to measure the time-domain variability.

- SDNN: the standard deviation of all NN intervals,
- MeanNN: the mean of all NN intervals,
- RMSSD: the root mean square of all the differences between adjacent NN intervals,
- SDSD: the standard deviation of all the differences between adjacent NN intervals, and
- pNN50: the percentage of the number of adjacent NN interval pairs differing by more than 50 ms (NN50) divided by the total number of NN intervals.

As discussed before, the morphology of the S1 waveform in the acoustic signal is mainly defined by three different characteristic points. It is empirically observed that the relative location of these points changes continuously in a subtle manner for different S1 waveforms in the signal. Table 4.3 lists some of the performance metrics for the IHR comparisons with respect to the synchronous ECG and PPG signals to understand the reliability of choosing a particular characteristic point in localising the S1 waveform and finding the heart rate accurately. The measures  $\mu$  and  $\sigma$  obtained from the Bland-Altman comparison plot along with the MAE and accuracy of IHR determination for a total of 12 subjects demonstrate a high degree of agreement between the estimated output and the ground truth values (ECG and PPG) for zero-crossing ( $\text{APS}_z$ ) as compared to the other characteristic points. The accuracy of the algorithm is determined by calculating the percentage of heart rate differences lying within a  $\pm 5\%$  variation with respect to the ground truth. Although the sensitivity  $S_e$  of extracting the S1 waveforms accurately are comparable, a higher PPV and a lower DER indicates zero-crossing as a better choice

to localise the S1 waveform. This can be justified using the fact that the presence of artifacts in the signal can introduce certain spikes which can alter the location of  $APS_p$  and  $APS_n$  by few milliseconds without affecting the position of the  $APS_z$  as shown in Fig. 4.5. Since even a small variation in the time-index of the characteristic points can introduce wide discrepancies in the heart rate, the results in Table 4.3 suggested the usage of zero-crossing as the characteristic point for the S1 waveform in determining the IHR profile of a subject.

**Table 4.3:** *Performance metrics of the IHR determination for different characteristic points of APS with respect to PPG and ECG signals for a total of 12 subjects.*

Characteristic APS points	MAE (bpm)		$\mu$ (bpm)		$\sigma$ (bpm)		Acc (%)		$S_e$	PPV	DER
	PPG	ECG	PPG	ECG	PPG	ECG	PPG	ECG			
$APS_p$	1.038	1.052	0.091	-0.019	2.409	2.731	96.28	95.55	0.976	0.965	0.057
$APS_z$	0.646	0.602	0.051	-0.061	1.069	1.353	98.96	98.50	0.971	0.989	0.039
$APS_n$	0.816	0.623	0.048	-0.058	1.601	1.626	97.35	98.79	0.980	0.975	0.043

The S1 waveform being localised with the time-index of the zero-crossing is used to establish the time-domain comparisons for IHR and IBI by comparing the estimated output of the proposed algorithm with the ground truth values of ECG and PPG signals respectively. Fig. 4.7 and Fig. 4.8 illustrates such a comparison for one of the subjects by plotting the IHR and IBI time-series, correlation using the line of best fit and Bland-Altman analysis for an acoustic signal of 5 minutes duration. The correlation and Bland-Altman comparison plot (abbreviated together as BACorr) for the complete dataset are also presented in Fig. 4.9 by combining the IHR and IBI time-series of all the 12 subjects. Since the heart rate has an inverse proportionality with the inter-beat intervals, it can be observed that their corresponding time-series variations and the BACorr comparisons are a mirror images of each other in the horizontal and vertical axes respectively, with amplitudes varying by a factor of 60.

The IHR and IBI time-series obtained from the proposed algorithm indicate a close overlap with the heart rate and RR-intervals of the ECG signal acquired using the SOMNOscreen monitor as shown in Fig. 4.7(b) and Fig. 4.8(b) respectively. It can be observed that the majority of these values lie within the upper and lower bounds of  $\pm 5\%$  variation. This observation is also evident in the correlation plot which depicts a narrow variation of the data points with respect to the line of best fit. The correlation analysis for the complete dataset in Fig. 4.9(c) and Fig. 4.9(d) with the values of PCC and slope of the fitted line close to 1 indicate a high degree of correlation and linear relationship between the estimated output and the ECG ground truth. The further assessment of the algorithm is performed using the Bland-Altman plot which compares the variation of HR differences ( $\Delta HR$ ) and IBI differences ( $\Delta IBI$ ) with the HR averages ( $\mu HR$ ) and IBI averages ( $\mu IBI$ ) respectively. The diameter of the circled data points in the BACorr plots increases corresponding to the number of points coinciding on the same



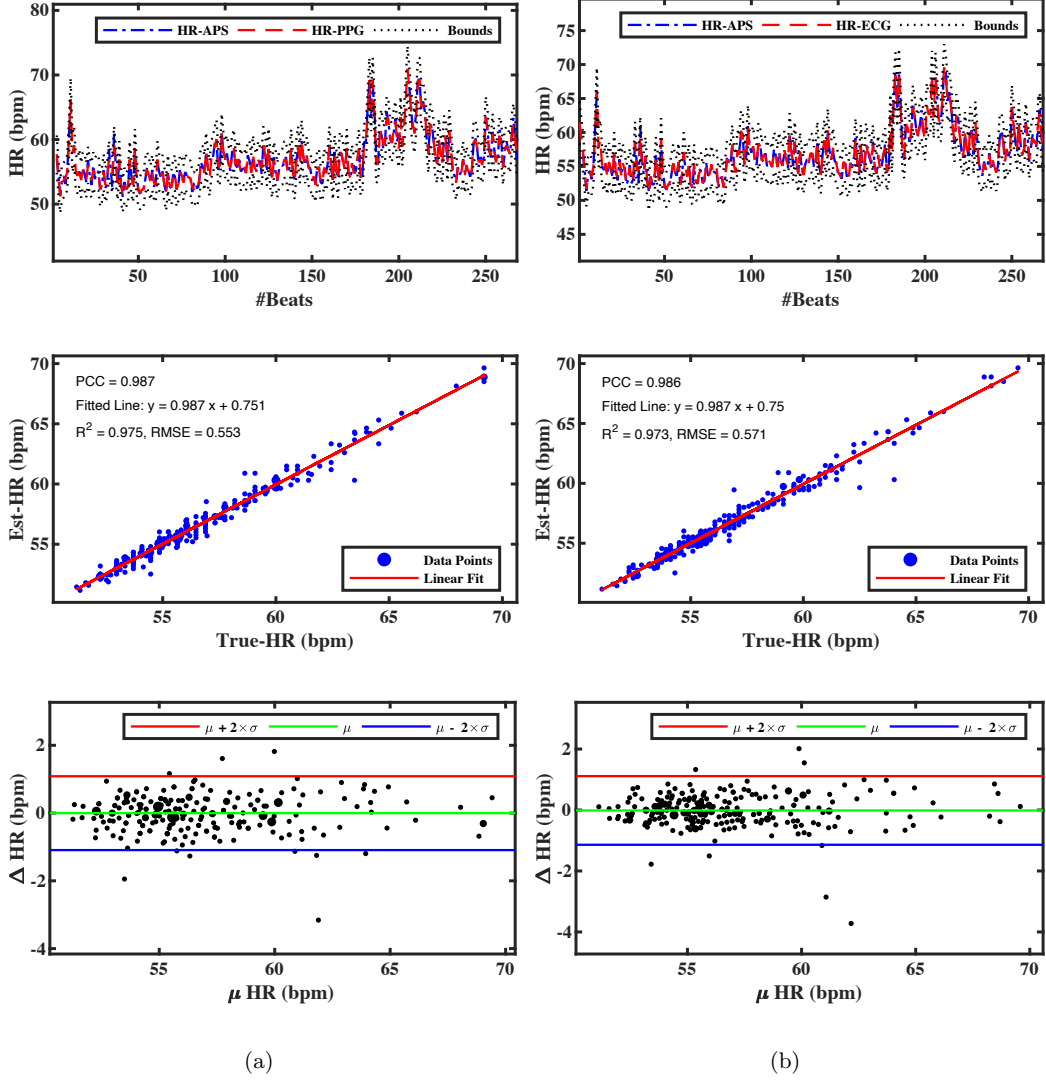


**Figure 4.7:** IHR comparisons for subject 8. (a) Full IHR time series, correlation analysis and Bland-Altman plot between APS- and PPG-derived HR. (b) Full IHR time series, correlation analysis and Bland-Altman plot between APS- and ECG-derived HR.

location. A near zero bias and LOAs of around 2.2 bpm and 0.02 seconds for the IHR and IBI comparisons in the complete dataset indicate a high degree of statistical agreement between the outputs obtained from the proposed algorithm and the ECG signal.

The results of the proposed algorithm are also compared with the heart rate and beat-to-beat intervals of the PPG signal recorded synchronously using the SOMNOscreen monitor in Fig. 4.7(a) and Fig. 4.8(a) respectively. It can be observed that a strong correlation between the IHR and IBI outputs in these plots exist, with PCC and slope of the fitted line obtaining values close to 1. The Bland-Altman plot also establishes a high degree of statistical agreement between the estimated and the PPG output with a near

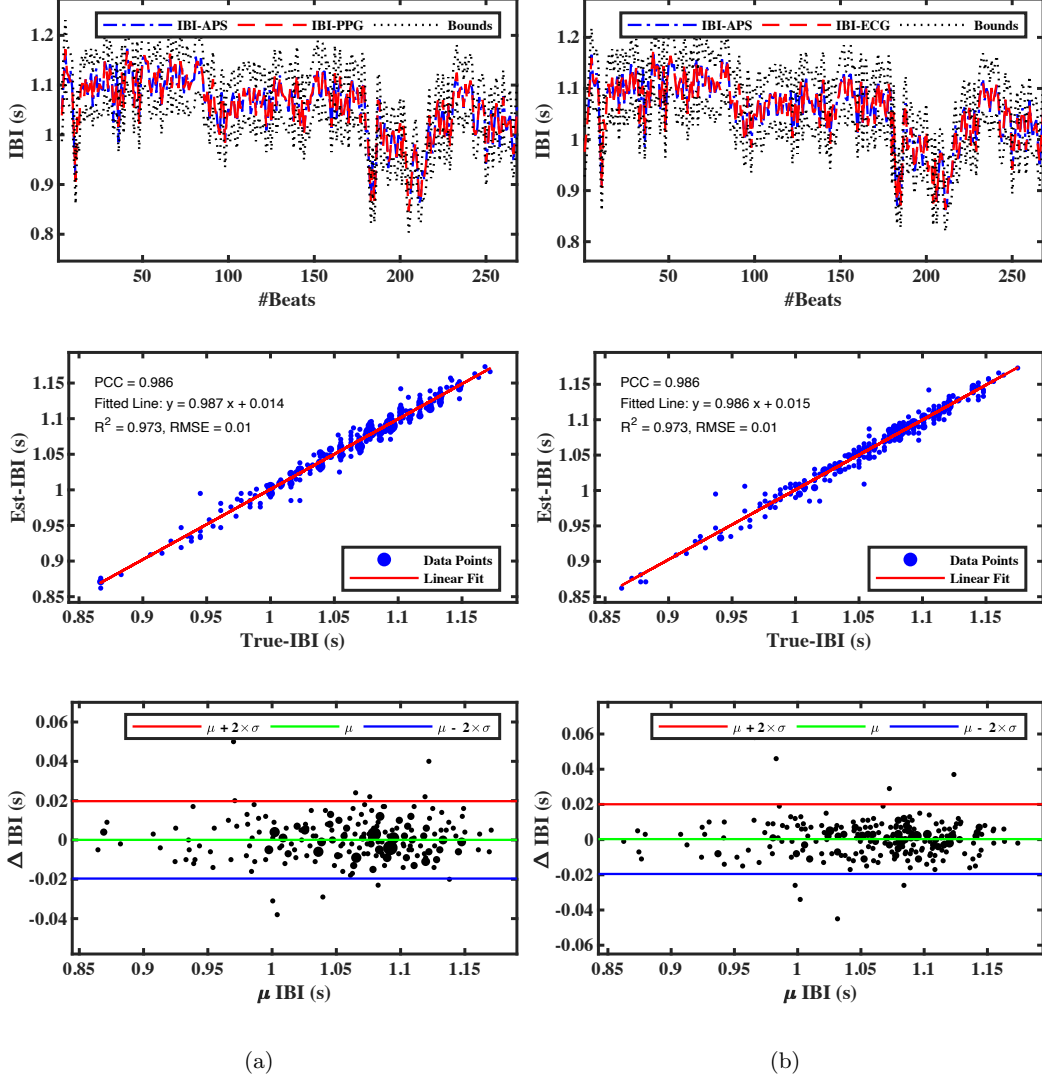


**Figure 4.8:** IBI comparisons for subject 8. (a) Full IBI time series, correlation analysis and Bland-Altman plot between APS- and PPG-derived IBI. (b) Full IBI time series, correlation analysis and Bland-Altman plot between APS- and ECG-derived IBI.

zero bias and LOAs of around 1.1 bpm and 0.02 seconds for IHR and IBI comparisons respectively. For the whole dataset, the BAcorr comparisons for the PPG signal are plotted in Fig. 4.9(a) and Fig. 4.9(b), where a near zero bias and LOAs of around 2.6 bpm and 0.03 seconds for the IHR and IBI comparisons are obtained respectively. A high degree of correlation and statistical agreement with more than 95% of the data points lying within the narrow LOAs suggests that the proposed algorithm is capable of extracting the instantaneous heart rate profile from the acoustic signal accurately. Although the performance metrics for the PPG and ECG comparisons are quite similar, few of the data points in the PPG analysis demonstrates wide variation. This is mainly

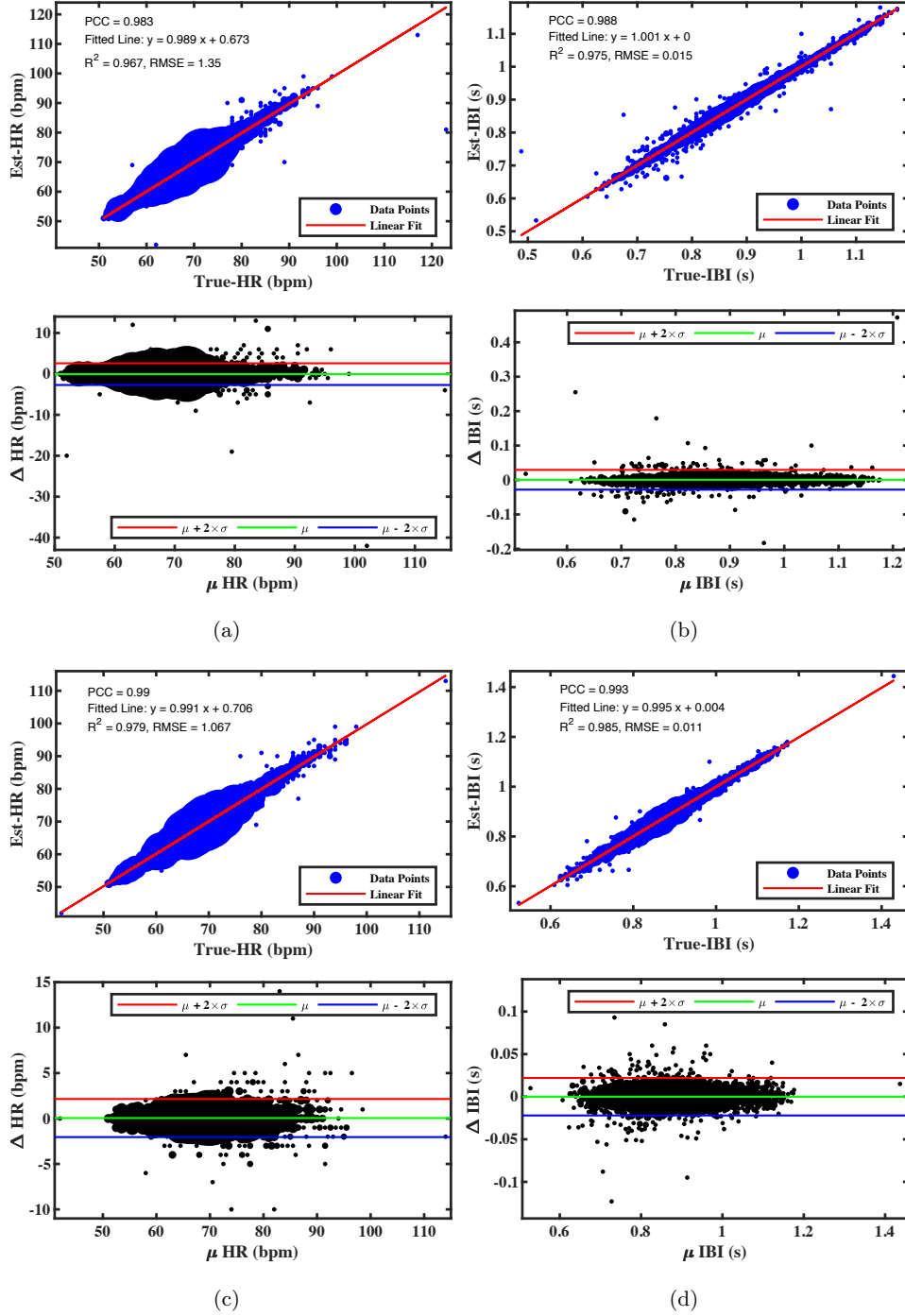


**Figure 4.9:** *IHR and IBI comparisons for the complete dataset. (a) Correlation analysis and Bland-Altman plot between APS- and PPG-derived HR. (b) Correlation analysis and Bland-Altman plot between APS- and PPG-derived IBI. (c) Correlation analysis and Bland-Altman plot between APS- and ECG-derived HR. (d) Correlation analysis and Bland-Altman plot between APS- and ECG-derived IBI.*

because of the high sensitivity of the PPG signal towards the motion artifacts which may introduce erroneous peaks and possibly lead to an incorrect systolic peak detection.

The NN intervals determined by localising the zero-crossing of the S1 waveform in the acoustic signal, R-peak in the ECG signal and systolic peak detection in the PPG signal can be utilised to measure the corresponding HRV. Table 4.4 lists the time-domain HRV parameters for every subject in the database to compare the variation of inter-beat intervals in APS, ECG and PPG signals respectively. SDNN is computed by taking the square root of the variance of the NN intervals. Since the variance reflects the total power of the spectral analysis, SDNN estimates the cycle lengths of the components responsible for the variability in the signal over the length of the recording [20]. The standard deviation of successive NN interval differences (SDSD) represents the short-term variability in the inter-beat intervals whereas MeanNN indicates the bias of this short-term variation [99]. The other metrics obtained from interval differences include RMSSD and pNN50 which estimates the high frequency variations in the instantaneous heart rate of the subject. For pNN50, the NN50 count in this study includes all the adjacent NN intervals for which the difference is more than 50 ms irrespective of whether the first or second interval is longer.

For all the time-domain HRV parameters in Table 4.4, a very close agreement between the APS and PPG measures can be observed with low values of the median of percentage differences. A relatively larger variation in the measures of APS and ECG comparisons are obtained. This difference is attributed to the fact that the APS and the PPG signals record the pulse wave at the wrist and finger respectively, whereas the ECG records the heart activity at the chest. Therefore, a finite propagation time exists between the onset of the R-peak and the onset of the pulse wave at a peripheral site. Although the HRV

**Table 4.4:** *Time-domain HRV parameters for IBI estimated from APS, PPG and ECG signals.*

Subject	SDNN (ms)			SDSD (ms)			MeanNN (ms)			RMSSD (ms)			pNN50 (%)		
	APS	PPG	ECG	APS	PPG	ECG	APS	PPG	ECG	APS	PPG	ECG	APS	PPG	ECG
1	58.02	57.72	59.09	29.11	28.52	38.15	835.51	835.45	834.89	29.06	28.52	38.09	5.73	5.44	6.88
2	45.46	45.73	44.84	40.61	41.69	38.92	873.67	873.72	872.66	40.54	41.62	38.86	20.59	21.19	20.89
3	77.81	77.86	74.87	72.76	73.59	68.69	922.18	922.23	921.74	72.64	73.47	68.57	34.28	36.79	31.45
4	44.34	44.65	43.88	42.71	43.59	42.50	900.49	900.52	900.08	42.64	43.52	42.44	25.00	25.31	26.87
5	49.16	48.84	48.06	50.71	49.99	49.08	864.11	864.14	863.79	50.64	49.91	49.01	31.58	30.99	34.50
6	58.00	57.12	56.28	43.13	40.82	39.98	850.48	850.53	850.08	43.07	40.76	39.92	22.92	20.92	21.20
7	44.24	44.47	44.16	31.94	32.00	31.64	948.16	948.22	947.59	31.89	31.95	31.59	11.55	11.22	12.04
8	60.88	60.85	60.87	46.68	45.42	47.04	1059.72	1059.67	1059.44	46.59	45.33	46.95	27.98	25.75	27.61
9	65.81	64.39	63.74	62.51	58.54	58.43	853.17	853.15	852.94	62.41	58.44	58.34	35.91	32.05	33.83
10	40.11	39.44	38.33	34.73	32.26	29.65	809.29	809.33	809.02	34.67	32.22	29.61	13.39	9.97	8.83
11	69.39	67.69	55.79	88.41	83.16	68.24	738.65	738.22	736.52	88.26	83.02	68.12	28.09	29.01	25.00
12	92.69	92.00	90.06	84.94	84.12	82.30	857.35	857.46	855.52	84.79	83.98	82.16	37.57	37.87	37.28
$m_1$	58.01	57.42	56.03	44.91	44.51	44.77	860.73	860.80	859.65	44.83	44.42	44.69	26.49	25.53	25.93
$m_2$	–	0.31	1.41	–	0.77	2.16	–	-0.04	0.43	–	0.77	2.15	–	0.31	0.33
$m_3$	–	0.58%	2.54%	–	1.72%	3.69%	–	-0.01%	0.05%	–	1.65%	3.68%	–	2.36%	1.05%
$p$	–	>0.05	>0.05	–	>0.05	>0.05	–	>0.05	>0.05	–	>0.05	>0.05	–	>0.05	>0.05

$m_1$ : median across all the subjects.  $m_2$ : median of the difference between APS and reference output.  $m_3$ : median of the percentage difference compared to APS output.  $p$ : probability value computed using the Wilcoxon rank sum test.

at the chest and the peripheral sites are generally in close agreement for the subjects at rest [66], they do possess minor differences depending on the pulse wave velocity and the pulse transit time through the arterial system. These parameters can vary significantly with the blood pressure, arterial stiffness and age of the subject [62]. Since the APS and PPG signals are recorded from the locations which are very close to each other in comparison to the ECG recording site, the variance between the synchronised APS and PPG data is significantly lower. As a result, the APS and ECG measures for the HRV comparisons are not expected to be identical, but they are indeed in close agreement.

The Wilcoxon rank sum test [100] is also used to estimate the  $p$ -value and test the null hypothesis that the HRV measures from the acoustic signal are not significantly different from the PPG- and ECG-based HRV measures. Thus, two  $p$ -values are generated for every HRV parameter in Table 4.4. For all the time-domain measures, the obtained  $p$ -values at the 5% significance level indicate that there is not enough evidence to reject the null hypothesis, and thus conclude that the HRV estimations using the proposed algorithm yields a high degree of statistical agreement with the HRV estimations obtained from PPG and ECG signals respectively.

#### 4.6.3 Frequency-domain HRV analysis

For the short-term recordings of 5 minutes duration, the frequency-domain HRV measures provide a better physiological interpretation as compared to the time-domain HRV analysis. The spectral analysis of the IBI tachogram provides vital information about the distribution of power in different frequency bands which are mainly divided into three components: very low frequency (VLF) for frequencies lower than 0.04 Hz, low frequency (LF) for frequencies between 0.04 and 0.15 Hz, and high frequency (HF) for frequencies between 0.15 and 0.4 Hz respectively. The total power (TP) in the bandwidth of 0.4 Hz is determined by adding the power from all the individual components. While the VLF component does not provide an interpretation during the spectral analysis of the short-term recordings, the power distribution and the central frequency of the LF and HF bands reflect the variations in the autonomic modulations of the heart activity [20].

The spectral analysis of the acoustic signal is performed by plotting the IBI tachogram with the difference of the time-indices of the adjacent peaks ( $N_i - N_{i-1}$ ) on the y-axis and the time occurrence of the second peak ( $N_i$ ) on the x-axis. This produces an irregularly sampled time-domain signal as shown in Fig. 4.10(a). In case of a continuous IBI tachogram, some of the IBI values can correspond to the corrupted regions of the signal leading to an inaccurate HRV analysis. The HRV spectra of such a tachogram can simply be obtained by calculating the power spectral density (PSD) of the corrupted sections of the data beforehand and removing these already known PSD contributions from the overall PSD of the IBI tachogram. However, identifying the PSDs of the artefacts in isolation is a challenging task and would require multiple features to separate

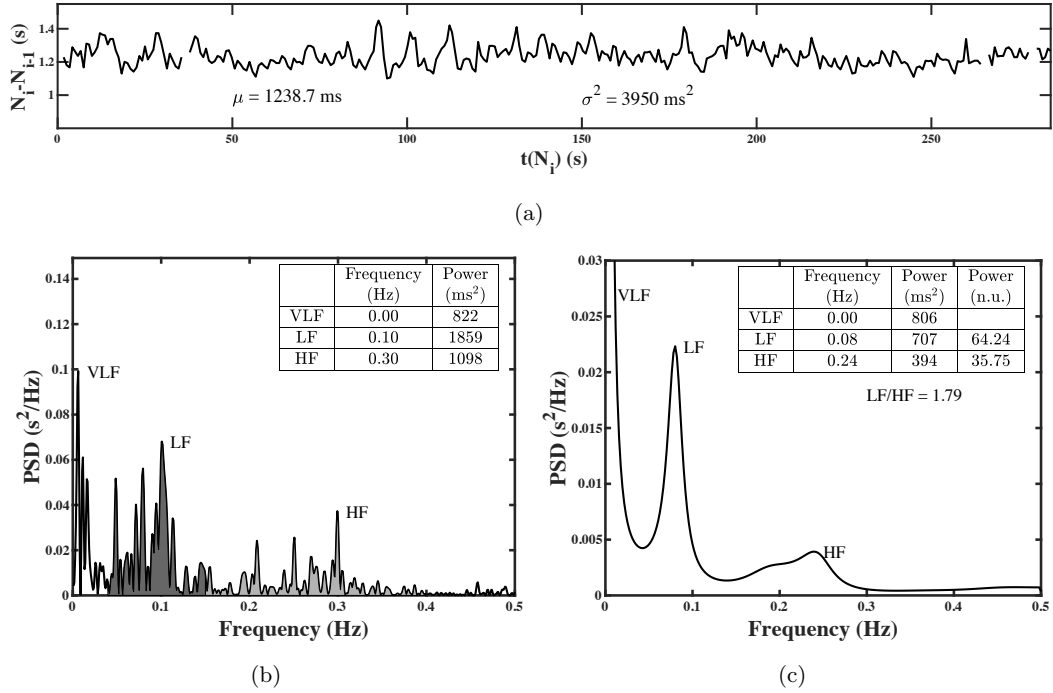


**Figure 4.10:** HRV spectra for acoustic signal recorded from subject 10. (a) NN interval tachogram with its corresponding mean and variance. (b) VLF, LF and HF central frequency and power in absolute value, calculated by a FFT based non-parametric algorithm. The LF component is indicated by dark shaded areas and the HF component by light shaded areas. (c) VLF, LF and HF central frequency, power in absolute value and power in normalised units (n.u.), calculated by parametric autoregressive modelling. In (a) and (b), the peak frequency and the power were calculated by integrating the PSD in the defined frequency bands.

the spectral content of the artefacts from the pulse sounds. Due to this reason, the IBIs which produce heart rate outside the range of 40 to 200 bpm due to an incorrect detection or missed detection of the S1 waveform are ignored leading to some missing data points in the tachogram. The HRV spectra can be obtained using the PSD analysis of the NN interval tachogram by employing either the non-parametric or the parametric methods. Although both the methods provide comparable results for the PSD analysis, one has certain advantages over the other [20]. While the non-parametric methods are simple to implement and faster to execute, the parametric methods provide smoother spectral components to easily distinguish between different frequency bands, therefore, allowing an easy post-processing of the HRV spectrum [101]. However, the complexity of the parametric methods can vary based on the requirement of a proper selection of the autoregressive model. In this study, the non-parametric method is used to estimate the absolute measure of the Lomb-Scargle PSD [102] by processing the signal that is unevenly sampled. On the contrary, the autoregressive PSD estimates using the parametric method are computed by employing the covariance method to produce smoother spectral

components. The spectral components are measured in absolute units of power ( $\text{ms}^2$ ) by integrating the PSD in the defined frequency bands. The normalised LF and HF components denoted by  $\overline{\text{LF}}$  and  $\overline{\text{HF}}$  respectively, and defined in Eq. 4.11 are also determined. The normalisation minimises the effect of total power variation on these components, and therefore reflect the balanced behaviour of sympathetic and parasympathetic branches of the autonomic nervous system [20]. The LF/HF ratio is also computed to indicate the sympathetic modulations.

$$\begin{aligned}\overline{\text{LF}} &= \frac{\text{LF}}{\text{TP} - \text{VLF}} \times 100 \\ \overline{\text{HF}} &= \frac{\text{HF}}{\text{TP} - \text{VLF}} \times 100\end{aligned}\tag{4.11}$$

As an illustration, Fig. 4.10(b) plots the non-parametric Lomb-Scargle PSD estimate of HRV and indicates the peak frequency and power of VLF, LF and HF components in absolute units respectively. The parametric PSD estimate is plotted in Fig. 4.10(c) where the LF and HF components in normalised units along with LF/HF ratio are also listed. It can be observed that the parametric HRV estimation produces smoother spectral components when compared to the non-parametric plot, but the central frequencies of the bands remain almost similar in both the estimates. Table 4.5 lists the frequency-domain HRV parameters for the acoustic signal in absolute ( $\text{ms}^2$ ) and normalised units (nu) computed using the FFT-based non-parametric estimation for every subject in the database.

**Table 4.5:** *Frequency-domain HRV parameters for IBI estimated from APS using FFT based non-parametric algorithm.*

Subject	TP	VLF	LF	$\overline{\text{LF}}$	HF	$\overline{\text{HF}}$	LF/HF	Correlation	
	( $\text{ms}^2$ )	( $\text{ms}^2$ )	( $\text{ms}^2$ )	(nu)	( $\text{ms}^2$ )	(nu)		LF	HF
1	9077.85	3653.10	4001.31	73.76	1423.44	26.23	2.81	1.00	0.96
2	3676.59	1313.97	893.24	37.80	1469.38	62.19	0.61	0.99	0.98
3	10957.99	985.53	5375.04	53.89	4597.41	46.10	1.16	1.00	0.99
4	2935.34	695.19	1389.44	62.02	850.70	37.97	1.63	1.00	0.99
5	4135.63	980.16	1505.36	47.70	1650.10	52.29	0.91	0.99	0.97
6	4643.18	1868.12	1238.60	44.63	1536.45	55.36	0.80	1.00	0.97
7	2261.99	1306.09	513.34	53.70	442.55	46.29	1.15	0.99	0.94
8	2815.81	1263.34	818.19	52.70	734.26	47.29	1.11	0.99	0.94
9	8384.40	2204.04	3370.89	54.54	2809.45	45.45	1.19	1.00	0.97
10	3778.55	821.61	1859.28	62.87	1097.65	37.12	1.69	0.99	0.93
11	9668.28	2160.00	2241.61	29.85	5266.66	70.14	0.42	0.99	0.98
12	14515.31	3803.90	5941.03	55.46	4770.37	44.53	1.24	0.99	0.99

$\overline{\text{LF}}$ : LF norm.  $\overline{\text{HF}}$ : HF norm. nu: normalised units.

The Pearson correlation values for the LF and HF components are also determined to compare the HRV obtained from the proposed algorithm with the reference HRV from the PPG signal. The results in Table 4.5 suggests a high correlation between both the HRV estimates for the LF and HF components. Therefore, similar to the time-domain HRV measures, the frequency-domain HRV measures also demonstrate a high similarity between the HRV derived from the acoustic signal and the PPG signal respectively.

## 4.7 Conclusion

In order to demonstrate the possibility of extracting the HRV from the acoustic signals recorded at the wrist, an algorithm based on the relative energies of the short- and the long-term signal content was proposed. The algorithm identified three different characteristic points to find the temporal location of the S1 waveforms on a beat-by-beat basis in the acoustic signal. The IHR and IBI profiles obtained from the proposed algorithm for 12 subjects were compared with the gold standard ECG and PPG signals respectively and a high degree of statistical agreement and correlation for the time-domain HRV was obtained. The comparison of the frequency-domain HRV measures obtained from the acoustic signal with the reference PPG signal also proved that the proposed algorithm can reliably detect the instantaneous changes in the IBI time-series.

Finally, the computational complexity of the proposed algorithm is determined by analysing the complexities of its individual blocks. Although the HRV in this study was derived from the short-term acoustic recordings, the algorithm incorporated low complexity in its design to be operated over 24-hour acoustic signals with limited computational resources. The computational complexity of calculating the coefficient vector and the output signal are found to be  $\mathcal{O}(n)$ , where  $n$  represents the size of the input acoustic signal. The algorithm was implemented in MATLAB version R2018a on a 64-bit Windows 7 operating system with an i7-6700, 3.40 GHz processor. The run time of the algorithm to derive the IHR and IBI time-series for a 5 minute acoustic signal varied between 2 and 3 seconds depending on the number of corrupted segments ignored for the further processing.



## References

- [1] U. R. Acharya, K. P. Joseph, N. Kannathal, C. M. Lim, and J. S. Suri, "Heart rate variability: a review," *Medical and biological engineering and computing*, vol. 44, no. 12, pp. 1031–1051, 2006.
- [2] J.-S. Wang, C.-W. Lin, and Y.-T. C. Yang, "A k-nearest-neighbor classifier with heart rate variability feature-based transformation algorithm for driving stress recognition," *Neurocomputing*, vol. 116, pp. 136–143, 2013.
- [3] T. Penzel, J. McNames, P. De Chazal, B. Raymond, A. Murray, and G. Moody, "Systematic comparison of different algorithms for apnoea detection based on electrocardiogram recordings," *Medical and Biological Engineering and Computing*, vol. 40, no. 4, pp. 402–407, 2002.
- [4] M. Galinier, A. Pathak, J. Fourcade, C. Androdias, D. Curnier, S. Varnous, S. Boveda, P. Massabuau, M. Fauvel, J. Senard *et al.*, "Depressed low frequency power of heart rate variability as an independent predictor of sudden death in chronic heart failure," *European heart journal*, vol. 21, no. 6, pp. 475–482, 2000.
- [5] I. O'Brien, J. O'hare, I. Lewin, and R. Corral, "The prevalence of autonomic neuropathy in insulin-dependent diabetes mellitus: a controlled study based on heart rate variability," *QJM: An International Journal of Medicine*, vol. 61, no. 1, pp. 957–967, 1986.
- [6] G. Giannakakis, M. Tsiknakis, and P. Vorgia, "Focal epileptic seizures anticipation based on patterns of heart rate variability parameters," *Computer Methods and Programs in Biomedicine*, 2019.
- [7] D. S. Quintana, A. J. Guastella, T. Outhred, I. B. Hickie, and A. H. Kemp, "Heart rate variability is associated with emotion recognition: direct evidence for a relationship between the autonomic nervous system and social cognition," *International Journal of Psychophysiology*, vol. 86, no. 2, pp. 168–172, 2012.
- [8] F. Foroozan, "MUSIC-Based Algorithm for On-Demand Heart Rate Estimation Using Photoplethysmographic (PPG) Signals on Wrist."
- [9] D. Zhao, Y. Sun, S. Wan, and F. Wang, "SFST: A robust framework for heart rate monitoring from photoplethysmography signals during physical activities," *Biomedical Signal Processing and Control*, vol. 33, pp. 316–324, 2017.
- [10] P.-H. Lai and I. Kim, "Lightweight wrist photoplethysmography for heavy exercise: motion robust heart rate monitoring algorithm," *Healthcare technology letters*, vol. 2, no. 1, pp. 6–11, 2015.
- [11] Z. Wei, C. Dechang, W. Xueyun, and L. Hongxing, "Heart rate estimation by iterative Fourier interpolation algorithm," *Electronics Letters*, vol. 50, no. 24, pp. 1799–1801, 2014.
- [12] A. Reiss, I. Indlekofer, P. Schmidt, and K. Van Laerhoven, "Deep PPG: Large-Scale Heart Rate Estimation with Convolutional Neural Networks," *Sensors*, vol. 19, no. 14, p. 3079, 2019.
- [13] S. Yazdani, S. Fallet, and J.-M. Vesin, "A Novel Short-term Event Extraction Algorithm for Biomedical Signals," *IEEE Transactions on Biomedical Engineering*, vol. 65, no. 4, pp. 754–762, 2018.
- [14] P. Sharma, S. A. Imtiaz, and E. Rodriguez-Villegas, "An algorithm for heart rate extraction from acoustic recordings at the neck," *IEEE Transactions on Biomedical Engineering*, vol. 66, no. 1, pp. 246–256, 2018.
- [15] F. Gritzali, G. Frangakis, and G. Papakonstantinou, "A comparison of the length and energy transformations for the QRS detection," in *Proc. 9th Annu. Conf. IEEE Engineering in Medicine and Biology Society*, 1987, pp. 549–550.
- [16] E. Grisan, G. Cantisani, G. Tarroni, S. K. Yoon, and M. Rossi, "A supervised learning approach for the robust detection of heart beat in plethysmographic data," in *2015 37th Annual International*

- Conference of the IEEE Engineering in Medicine and Biology Society (EMBC).* IEEE, 2015, pp. 5825–5828.
- [17] Y. H. Hu, W. J. Tompkins, J. L. Urrusti, and V. X. Afonso, “Applications of artificial neural networks for ECG signal detection and classification.” *Journal of electrocardiology*, vol. 26, pp. 66–73, 1993.
  - [18] SOMNOmedics: Polysomnography SOMNOscreen plus. [Online]. Available: <http://sommomedics.eu/products/polysomnography-somnoscreentm-plus/>
  - [19] “Onyx II 9550 | Nonin.” [Online]. Available: <https://www.nonin.com/products/9550/>
  - [20] A. J. Camm, M. Malik, J. T. Bigger, G. Breithardt, S. Cerutti, R. J. Cohen, P. Coumel, E. L. Fallen, H. L. Kennedy, R. Kleiger *et al.*, “Heart rate variability: standards of measurement, physiological interpretation and clinical use. Task Force of the European Society of Cardiology and the North American Society of Pacing and Electrophysiology,” 1996.
  - [21] G. G. Berntson and J. R. Stowell, “ECG artifacts and heart period variability: don’t miss a beat!” *Psychophysiology*, vol. 35, no. 1, pp. 127–132, 1998.
  - [22] B.-U. Kohler, C. Hennig, and R. Orglmeister, “The principles of software QRS detection,” *IEEE Engineering in Medicine and Biology Magazine*, vol. 21, no. 1, pp. 42–57, 2002.
  - [23] G. M. Friesen, T. C. Jannett, M. A. Jadallah, S. L. Yates, S. R. Quint, and H. T. Nagle, “A comparison of the noise sensitivity of nine QRS detection algorithms,” *IEEE Transactions on biomedical engineering*, vol. 37, no. 1, pp. 85–98, 1990.
  - [24] S. Jalaleddine and C. Hutchens, “Ambulatory ECG wave detection for automated analysis: a review.” *ISA transactions*, vol. 26, no. 4, pp. 33–43, 1987.
  - [25] O. Pahlm and L. Sörnmo, “Software QRS detection in ambulatory monitoring: a review,” *Medical and Biological Engineering and Computing*, vol. 22, no. 4, pp. 289–297, 1984.
  - [26] M. Elgendi, B. Eskofier, S. Dokos, and D. Abbott, “Revisiting QRS detection methodologies for portable, wearable, battery-operated, and wireless ECG systems,” *PloS one*, vol. 9, no. 1, p. e84018, 2014.
  - [27] J. Fraden and M. Neuman, “QRS wave detection,” *Medical and Biological Engineering and computing*, vol. 18, no. 2, pp. 125–132, 1980.
  - [28] M. L. Ahlstrom and W. J. Tompkins, “Automated high-speed analysis of Holter tapes with microcomputers,” *IEEE Transactions on Biomedical Engineering*, no. 10, pp. 651–657, 1983.
  - [29] P. Morizet-Mahoudeaux, C. Moreau, D. Moreau, and J. Quarante, “Simple microprocessor-based system for on-line ECG arrhythmia analysis,” *Medical and Biological Engineering and Computing*, vol. 19, no. 4, pp. 497–500, 1981.
  - [30] N. M. Arzeno, Z.-D. Deng, and C.-S. Poon, “Analysis of first-derivative based QRS detection algorithms,” *IEEE Transactions on Biomedical Engineering*, vol. 55, no. 2, pp. 478–484, 2008.
  - [31] P. S. Hamilton and W. J. Tompkins, “Quantitative investigation of QRS detection rules using the MIT/BIH arrhythmia database,” *IEEE transactions on biomedical engineering*, no. 12, pp. 1157–1165, 1986.
  - [32] J. Pan and W. J. Tompkins, “A real-time QRS detection algorithm,” *IEEE Trans. Biomed. Eng.*, vol. 32, no. 3, pp. 230–236, 1985.
  - [33] W. Engelse and C. Zeelenberg, “A single scan algorithm for QRS-detection and feature extraction,” *Computers in cardiology*, vol. 6, no. 1979, pp. 37–42, 1979.
  - [34] F. Zhang and Y. Lian, “Novel QRS detection by CWT for ECG sensor,” in *2007 IEEE Biomedical Circuits and Systems Conference*. IEEE, 2007, pp. 211–214.

- [35] H. Inoue, A. Miyazaki, S. Iwasaki, M. Shimazu, T. Katsura, and A. Teranishi, "Detection of QRS Complex in ECG Using a Wavelet Transform," in *ITC-CSCC: International Technical Conference on Circuits Systems, Computers and Communications*, 1997, pp. 361–364.
- [36] S. Kadambe, R. Murray, and G. F. Boudreaux-Bartels, "Wavelet transform-based QRS complex detector," *IEEE Transactions on biomedical Engineering*, vol. 46, no. 7, pp. 838–848, 1999.
- [37] C. Li, C. Zheng, and C. Tai, "Detection of ECG characteristic points using wavelet transforms," *IEEE Transactions on biomedical Engineering*, vol. 42, no. 1, pp. 21–28, 1995.
- [38] K. D. Rao, "DWT based detection of R-peaks and data compression of ECG signals," *IETE Journal of Research*, vol. 43, no. 5, pp. 345–349, 1997.
- [39] V. X. Afonso, W. J. Tompkins, T. Q. Nguyen, and S. Luo, "ECG beat detection using filter banks," *IEEE transactions on biomedical engineering*, vol. 46, no. 2, pp. 192–202, 1999.
- [40] F. Zhang, Y. Wei, and Y. Lian, "Frequency-response masking based filter bank for QRS detection in wearable biomedical devices," in *2009 IEEE International Symposium on Circuits and Systems*. IEEE, 2009, pp. 1473–1476.
- [41] M. I. Vai and L.-G. Zhou, "Beat-to-beat ECG ventricular late potentials variance detection by filter bank and wavelet transform as beat-sequence filter," *IEEE Transactions on Biomedical Engineering*, vol. 51, no. 8, pp. 1407–1413, 2004.
- [42] M. Strintzis, G. Stalidis, X. Magnisalis, and N. Maglaveras, "Use of neural networks for electrocardiogram (ECG) feature extraction recognition and classification," *Neural Netw. World*, vol. 3, no. 4, pp. 313–327, 1992.
- [43] Q. Xue, Y. H. Hu, and W. J. Tompkins, "Neural-network-based adaptive matched filtering for QRS detection," *IEEE Transactions on Biomedical Engineering*, vol. 39, no. 4, pp. 317–329, 1992.
- [44] P. Hamilton and W. Tompkins, "Adaptive matched filtering for QRS detection," in *Proceedings of the Annual International Conference of the IEEE Engineering in Medicine and Biology Society*. IEEE, 1988, pp. 147–148.
- [45] A. Kyrkos, E. Giakoumakis, and G. Carayannis, "Time recursive prediction techniques on QRS detection problem." 1987.
- [46] K.-P. Lin and W. H. Chang, "QRS feature extraction using linear prediction," *IEEE Transactions on Biomedical Engineering*, vol. 36, no. 10, pp. 1050–1055, 1989.
- [47] M.-E. Nygård and L. Sörnmo, "Delineation of the QRS complex using the envelope of the ECG," *Medical and Biological Engineering and Computing*, vol. 21, no. 5, pp. 538–547, 1983.
- [48] D. S. Benitez, P. Gaydecki, A. Zaidi, and A. Fitzpatrick, "A new QRS detection algorithm based on the Hilbert transform," in *Computers in Cardiology 2000. Vol. 27 (Cat. 00CH37163)*. IEEE, 2000, pp. 379–382.
- [49] U. D. Uluşar, R. Govindan, J. D. Wilson, C. L. Lowery, H. Preissl, and H. Eswaran, "Adaptive rule based fetal QRS complex detection using Hilbert transform," in *2009 Annual International Conference of the IEEE Engineering in Medicine and Biology Society*. IEEE, 2009, pp. 4666–4669.
- [50] S. Pal and M. Mitra, "Empirical mode decomposition based ECG enhancement and QRS detection," *Computers in biology and medicine*, vol. 42, no. 1, pp. 83–92, 2012.
- [51] J.-t. Tang, X.-l. Yang, J.-c. Xu, Y. Tang, Q. Zou, and X.-k. Zhang, "The algorithm of R peak detection in ECG based on empirical mode decomposition," in *2008 Fourth International Conference on Natural Computation*, vol. 5. IEEE, 2008, pp. 624–627.
- [52] M. A. Arafat and M. K. Hasan, "Automatic detection of ECG wave boundaries using empirical mode decomposition," in *2009 IEEE International Conference on Acoustics, Speech and Signal Processing*. IEEE, 2009, pp. 461–464.

- [53] Z.-E. H. Slimane and A. Naït-Ali, "QRS complex detection using Empirical Mode Decomposition," *Digital Signal Processing*, vol. 20, no. 4, pp. 1221–1228, 2010.
- [54] B. Kohler, C. Hennig, and R. Orglmeister, "QRS detection using zero crossing counts," *Applied genomics and proteomics*, vol. 2, no. 2, pp. 138–145, 2003.
- [55] A. Schäfer and J. Vagedes, "How accurate is pulse rate variability as an estimate of heart rate variability?: A review on studies comparing photoplethysmographic technology with an electrocardiogram," *International journal of cardiology*, vol. 166, no. 1, pp. 15–29, 2013.
- [56] K. Georgiou, A. V. Larentzakis, N. N. Khamis, G. I. Alsuhaibani, Y. A. Alaska, and E. J. Giallafos, "Can wearable devices accurately measure heart rate variability? A systematic review," *Folia medica*, vol. 60, no. 1, pp. 7–20, 2018.
- [57] N. D. Giardino, P. M. Lehrer, and R. Edelberg, "Comparison of finger plethysmograph to ECG in the measurement of heart rate variability," *Psychophysiology*, vol. 39, no. 2, pp. 246–253, 2002.
- [58] F. P. Akbulut, K. Lawless, A. Tanneeru, S. Rao, B. Lee, and V. Misra, "Estimation of Beat-to-Beat Interval from Wearable Photoplethysmography Sensor on Different Measurement Sites During Daily Activities," in *2018 IEEE SENSORS*. IEEE, 2018, pp. 1–4.
- [59] F. Foroozan, M. Mohan, and J. S. Wu, "Robust Beat-To-Beat Detection Algorithm for Pulse Rate Variability Analysis from Wrist Photoplethysmography Signals," in *2018 IEEE International Conference on Acoustics, Speech and Signal Processing (ICASSP)*. IEEE, 2018, pp. 2136–2140.
- [60] A. Bánhalmi, J. Borbás, M. Fidrich, V. Bilicki, Z. Gingl, and L. Rudas, "Analysis of a pulse rate variability measurement using a smartphone camera," *Journal of healthcare engineering*, vol. 2018, 2018.
- [61] D. Jarchi and A. J. Casson, "Towards photoplethysmography-based estimation of instantaneous heart rate during physical activity," *IEEE Transactions on Biomedical Engineering*, vol. 64, no. 9, pp. 2042–2053, 2017.
- [62] J. Allen, "Photoplethysmography and its application in clinical physiological measurement," *Physiological measurement*, vol. 28, no. 3, p. R1, 2007.
- [63] P. S. McKinley, P. A. Shapiro, E. Bagiella, M. M. Myers, R. E. De Meersman, I. Grant, and R. P. Sloan, "Deriving heart period variability from blood pressure waveforms," *Journal of Applied Physiology*, vol. 95, no. 4, pp. 1431–1438, 2003.
- [64] N. K. Kristiansen, J. Fleischer, M. Jensen, K. S. Andersen, and H. Nygaard, "Design and evaluation of a handheld impedance plethysmograph for measuring heart rate variability," *Medical and Biological Engineering and Computing*, vol. 43, no. 4, pp. 516–521, 2005.
- [65] B. Vescio, M. Salsone, A. Gambardella, and A. Quattrone, "Comparison between electrocardiographic and earlobe pulse photoplethysmographic detection for evaluating heart rate variability in healthy subjects in short-and long-term recordings," *Sensors*, vol. 18, no. 3, p. 844, 2018.
- [66] S. Lu, H. Zhao, K. Ju, K. Shin, M. Lee, K. Shelley, and K. H. Chon, "Can photoplethysmography variability serve as an alternative approach to obtain heart rate variability information?" *Journal of clinical monitoring and computing*, vol. 22, no. 1, pp. 23–29, 2008.
- [67] P. Shi, S. Hu, and Y. Zhu, "A preliminary attempt to understand compatibility of photoplethysmographic pulse rate variability with electrocardiographic heart rate variability," 2008.
- [68] J. Hayano, A. K. Barros, A. Kamiya, N. Ohte, and F. Yasuma, "Assessment of pulse rate variability by the method of pulse frequency demodulation," *Biomedical engineering online*, vol. 4, no. 1, p. 62, 2005.

- [69] R. Rauh, R. Limley, R.-D. Bauer, M. Radespiel-Troger, and M. Mueck-Weymann, "Comparison of heart rate variability and pulse rate variability detected with photoplethysmography," in *Saratov Fall Meeting 2003: Optical Technologies in Biophysics and Medicine V*, vol. 5474. International Society for Optics and Photonics, 2004, pp. 115–126.
- [70] S. Carrasco, R. Gonzalez, J. Jimenez, R. Roman, V. Medina, and J. Azpiroz, "Comparison of the heart rate variability parameters obtained from the electrocardiogram and the blood pressure wave," *Journal of medical engineering & technology*, vol. 22, no. 5, pp. 195–205, 1998.
- [71] A. Suhrbier, R. Heringer, T. Walther, H. Malberg, and N. Wessel, "Comparison of three methods for beat-to-beat-interval extraction from continuous blood pressure and electrocardiogram with respect to heart rate variability analysis/vergleich von drei methoden der schlag-zu-schlag-intervall-extraktion aus kontinuierlichen blutdruckverläufen und elektrokardiogrammen zur herzratenvariabilitätsanalyse," *Biomedizinische Technik*, vol. 51, no. 2, pp. 70–76, 2006.
- [72] F. Lucena, A. K. Barros, Y. Takeuchi, and N. Ohnishi, "Heart instantaneous frequency based estimation of HRV from blood pressure waveforms," *IEICE transactions on information and systems*, vol. 92, no. 3, pp. 529–537, 2009.
- [73] I. Constant, D. Laude, I. Murat, and J.-L. Elghozi, "Pulse rate variability is not a surrogate for heart rate variability," *Clinical Science*, vol. 97, no. 4, pp. 391–397, 1999.
- [74] E. F. Treo, M. C. Herrera, and M. E. Valentinuzzi, "Algorithm for identifying and separating beats from arterial pulse records," *Biomedical engineering online*, vol. 4, no. 1, p. 48, 2005.
- [75] O. T. Inan, P.-F. Migeotte, K.-S. Park, M. Etemadi, K. Tavakolian, R. Casanella, J. Zanetti, J. Tank, I. Funtova, G. K. Prisk *et al.*, "Ballistocardiography and seismocardiography: A review of recent advances," *IEEE journal of biomedical and health informatics*, vol. 19, no. 4, pp. 1414–1427, 2014.
- [76] J. M. Zanetti and D. M. Salerno, "Seismocardiography: a technique for recording precordial acceleration," in *[1991] Computer-Based Medical Systems@ m.Proceedings of the Fourth Annual IEEE Symposium*. IEEE, 1991, pp. 4–9.
- [77] J. Wahlström, I. Skog, P. Händel, F. Khosrow-Khavar, K. Tavakolian, P. K. Stein, and A. Nehorai, "A hidden markov model for seismocardiography," *IEEE Transactions on Biomedical Engineering*, vol. 64, no. 10, pp. 2361–2372, 2017.
- [78] M. J. Tadi, E. Lehtonen, T. Hurnanen, J. Koskinen, J. Eriksson, M. Pänkäälä, M. Teräs, and T. Koivisto, "A real-time approach for heart rate monitoring using a Hilbert transform in seismocardiograms," *Physiological measurement*, vol. 37, no. 11, p. 1885, 2016.
- [79] F. Landreani, A. Martín-Yebra, C. Casellato, C. Frigo, E. Pavan, P.-F. Migeotte, and E. G. Caiani, "Beat-to-beat heart rate detection by smartphone's accelerometers: Validation with ECG," in *2016 38th annual international conference of the IEEE engineering in medicine and biology society (EMBC)*. IEEE, 2016, pp. 525–528.
- [80] F. Landreani, E. Caiani, D. Golier, A. Hossein, J. Rabineau, P. Migeotte, and P. van de Borne, "Heartbeat Detection Using Three-Axial Seismocardiogram Acquired by Mobile Phone," in *2018 Computing in Cardiology Conference (CinC)*, vol. 45. IEEE, 2018, pp. 1–4.
- [81] M. Kaisti, M. J. Tadi, O. Lahdenoja, T. Hurnanen, A. Saraste, M. Pänkäälä, and T. Koivisto, "Stand-alone heartbeat detection in multidimensional mechanocardiograms," *IEEE Sensors Journal*, vol. 19, no. 1, pp. 234–242, 2018.
- [82] A. Albukhari, F. Lima, and U. Mescheder, "Bed-embedded heart and respiration rates detection by longitudinal ballistocardiography and pattern recognition," *Sensors*, vol. 19, no. 6, p. 1451, 2019.

- [83] C. Bruser, K. Stadlthanner, S. de Waele, and S. Leonhardt, "Adaptive beat-to-beat heart rate estimation in ballistocardiograms," *IEEE Transactions on Information Technology in Biomedicine*, vol. 15, no. 5, pp. 778–786, 2011.
- [84] C. Jiao, B.-Y. Su, P. Lyons, A. Zare, K. Ho, and M. Skubic, "Multiple instance dictionary learning for beat-to-beat heart rate monitoring from ballistocardiograms," *IEEE Transactions on Biomedical Engineering*, vol. 65, no. 11, pp. 2634–2648, 2018.
- [85] C. Brüser, K. Stadlthanner, A. Brauers, and S. Leonhardt, "Applying machine learning to detect individual heart beats in ballistocardiograms," in *2010 Annual International Conference of the IEEE Engineering in Medicine and Biology*. IEEE, 2010, pp. 1926–1929.
- [86] C. Brüser, S. Winter, and S. Leonhardt, "Robust inter-beat interval estimation in cardiac vibration signals," *Physiological measurement*, vol. 34, no. 2, p. 123, 2013.
- [87] C. Wang, X. Wang, X. Xiong, and R. Wang, "The Segmented Dynamic Time Warping Algorithm for Beat-to-Beat Heart Rate Estimation based on Ballistocardiogram Signals," *Journal of Fiber Bioengineering and Informatics*, vol. 6, no. 4, pp. 415–425, 2013.
- [88] J. Shin, B. Choi, Y. Lim, D. Jeong, and K. Park, "Automatic ballistocardiogram (BCG) beat detection using a template matching approach," in *2008 30th Annual International Conference of the IEEE Engineering in Medicine and Biology Society*. IEEE, 2008, pp. 1144–1146.
- [89] G. Cathelain, B. Rivet, S. Achard, J. Bergounioux, and F. Jouen, "Dynamic Time Warping for Heartbeat Detection in Ballistocardiography."
- [90] M. Krej, L. Dziuda, and F. W. Skibniewski, "A method of detecting heartbeat locations in the ballistocardiographic signal from the fiber-optic vital signs sensor," *IEEE journal of biomedical and health informatics*, vol. 19, no. 4, pp. 1443–1450, 2015.
- [91] A. Böhm, C. Brüser, and S. L. Leonhardt, "A novel bcg sensor array for unobtrusive cardiac monitoring," 2013.
- [92] C. Alvarado-Serrano, P. S. Luna-Lozano, and R. Pallàs-Areny, "An algorithm for beat-to-beat heart rate detection from the BCG based on the continuous spline wavelet transform," *Biomedical Signal Processing and Control*, vol. 27, pp. 96–102, 2016.
- [93] Ø. Aardal, Y. Paichard, S. Brovoll, T. Berger, T. S. Lande, and S.-E. Hamran, "Physical working principles of medical radar," *IEEE Transactions on Biomedical Engineering*, vol. 60, no. 4, pp. 1142–1149, 2012.
- [94] M. Nosrati and N. Tavassolian, "High-accuracy heart rate variability monitoring using Doppler radar based on Gaussian pulse train modeling and FTPR algorithm," *IEEE Transactions on Microwave Theory and Techniques*, vol. 66, no. 1, pp. 556–567, 2017.
- [95] V. L. Petrović, M. M. Janković, A. V. Lupšić, V. R. Mihajlović, and J. S. Popović-Božović, "High-Accuracy Real-Time Monitoring of Heart Rate Variability Using 24 GHz Continuous-Wave Doppler Radar," *IEEE Access*, vol. 7, pp. 74 721–74 733, 2019.
- [96] W. Hu, Z. Zhao, Y. Wang, H. Zhang, and F. Lin, "Noncontact accurate measurement of cardiopulmonary activity using a compact quadrature Doppler radar sensor," *IEEE Transactions on Biomedical Engineering*, vol. 61, no. 3, pp. 725–735, 2013.
- [97] S. Bakhtiari, S. Liao, T. Elmer, A. Raptis *et al.*, "A real-time heart rate analysis for a remote millimeter wave IQ sensor," *IEEE Transactions on Biomedical Engineering*, vol. 58, no. 6, pp. 1839–1845, 2011.
- [98] J. M. Bland and D. Altman, "Statistical methods for assessing agreement between two methods of clinical measurement," *The lancet*, vol. 327, no. 8476, pp. 307–310, 1986.

- [99] T. Kuusela, “Methodological Aspects of Heart Rate Variability Analysis,” in *Heart Rate Variability (HRV) Signal Analysis*. CRC Press, 2016, pp. 26–59.
- [100] J. D. Gibbons and S. Chakraborti, “Nonparametric statistical inference,” in *International encyclopedia of statistical science*. Springer, 2011, pp. 977–979.
- [101] A. Pichon, M. Roulaud, S. Antoine-Jonville, C. de Bisschop, and A. Denjean, “Spectral analysis of heart rate variability: interchangeability between autoregressive analysis and fast Fourier transform,” *Journal of electrocardiology*, vol. 39, no. 1, pp. 31–37, 2006.
- [102] N. R. Lomb, “Least-squares frequency analysis of unequally spaced data,” *Astrophysics and space science*, vol. 39, no. 2, pp. 447–462, 1976.

## 5 Blood pressure measurement by sensing Korotkoff sounds at the wrist

### 5.1 Introduction

The previous chapters showed how the heart rate and heart rate variability can be continuously monitored from the acoustic sensing of the pulse sounds at the wrist. Another important physiological marker associated with the diagnosis of cardiovascular diseases is the blood pressure. The gold standard approach of measuring the blood pressure utilises the auscultation of the Korotkoff sounds at the upper-arm by placing a stethoscope under the air cuff. However, the auscultation of Korotkoff sounds by a human observer requires intensive training and adequate hearing. Due to the human involvement, several sources of error can affect the blood pressure readings significantly [1]. Other blood pressure monitoring techniques as discussed in Section 1.3.1 also exist. Among these techniques, the oscillometric method addresses the drawbacks of the auscultation method by removing the human involvement and introducing the automation and user-friendliness in the blood pressure measurement. The method is based on sensing the pressure oscillations during the deflation of the air cuff, and establish a correlation of the oscillation envelope with the blood pressure. Unlike the auscultation method, there is no direct correlation between the oscillometric waveform envelope and the systolic blood pressure (SBP) and diastolic blood pressure (DBP) readings. The blood pressure is generally estimated using empirically-derived coefficients which might not be reliable for a diverse population in different measurement scenarios [2]. It would be ideal to combine the accuracy and reliability of the auscultation method with the automation and user-friendliness of the oscillometric technique. For the first time in the literature, the acoustic sensing of the pulse sounds at the wrist is studied during the inflation of the air cuff to correlate the appearance and disappearance of the Korotkoff sounds with the DBP and SBP respectively. While the acoustic signals are recorded automatically using the proposed wearable device, a separate pressure control system designed to inflate the cuff also operates automatically. Studying the Korotkoff sounds during the cuff inflation reduces the time period during which an external pressure is applied on the arterial branch. This makes it less uncomfortable for the subject requiring multiple readings throughout the day and also reduces the chances of any internal arterial damage.

In the following section, the hardware design and its components for the step-wise



inflation of the air cuff is discussed. A subsequent discussion on the temporal and spectral characteristics of the acoustic signal recorded during the cuff inflation is provided. This is followed by a detailed explanation of the different algorithmic stages for the DBP and SBP determination. Finally, the performance of the proposed DBP and SBP algorithms are assessed by establishing a comparison of the experimental blood pressure readings with the reference upper-arm and wrist blood pressure monitors respectively.

## 5.2 Hardware development for step-wise pressure inflation

The characterisation of the acoustic signal recorded at the wrist with varying pressure levels can be studied only when different pressure steps can be applied externally in a non-invasive and an automatic manner. This has been made possible by designing and developing a fully-automated pressure control system to generate varying levels of pressure by pumping air inside the air cuff. The hardware shown in Fig. 5.1 consists of the following off-the-shelf components with their associated functionalities.

1. *Air pump*: An air pump from Koge Micro Tech Co. Ltd was used to pump the air inside an inflatable air cuff. The pump operates at 6 V and provides a maximum flow of 1.9 litres/min up to a maximum pressure of 600 mmHg.
2. *Air valve*: A solenoid air valve from Koge Micro Tech Co. Ltd was used to control the passage of air in and out of the air cuff. The valve can sustain a maximum pressure of 350 mmHg and operates at 6 V with an exhaust speed of less than 6 seconds from 300 mmHg to 10mmHg in a 500 cc tank. The valve of normally closed state was chosen to reduce the power consumption while inflating the air cuff.
3. *Pressure sensor*: An amplified analogue gage pressure sensor from Honeywell International Inc. was used to sense the pressure variations inside the air cuff. The pressure sensor operates at 3.3 V and produces readings between 0 and 260 mmHg.
4. *Nordic nrf52 series microcontroller*: The nrf52 chip operating at 3.3 V acts as the central block of the system and controls the operation of the air pump and the air valve depending on the pressure readings fed by the pressure sensor. The chip, therefore, regulates the volume of the air inside the air cuff. The inbuilt ADC of the chip converts the analogue readings of the pressure sensor and stores them into an SD card at a sampling frequency of 100 Hz.
5. *Battery*: An alkaline battery of 9 V was used to supply the power to the pressure control system. Since the components operated at two different voltage levels, a voltage regulation at 3.3 V and 6 V was performed by using appropriate voltage regulators on the PCB.

6. *Inflatable air cuff*: Different sizes of the inflatable air cuffs from Welch Allyn Inc. were used depending on the arm circumferences of the subjects. The cuff sizes for the adults were chosen in compliance to the international protocols as follows:
- Small Adult: 20-26 cm
  - Adult: 25-34 cm
  - Large Adult: 32-43 cm
  - Thigh: 40-55 cm
7. *Tubing*: The installation of appropriate silicone tubing along with the connectors was done to ensure no leakage of air to sense the correct pressure inside the air cuff.

Based on the assumption that the DBP for a subject will not fall below 40 mmHg, the system is programmed to inflate the air cuff at a higher rate up to 40 mmHg pressure level. Thereafter, a step-wise inflation is performed at a rate of around 2-3 mmHg/s up to a maximum pressure of 20-30 mmHg higher than the entry SBP of the subject. Once the maximum pressure inside the air cuff is reached, the air valve is opened and the pressure is released. The design also incorporated a mechanism of releasing the air immediately at any time in case the subject feels uncomfortable with the pressure inflation.

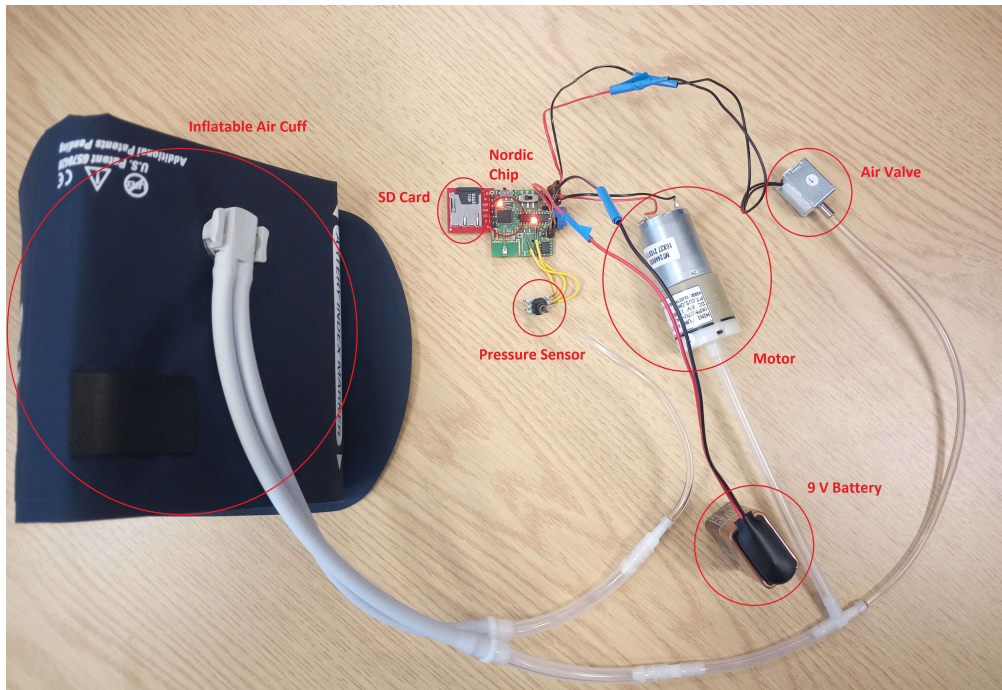


**Figure 5.1:** *Pressure control system to apply varying pressure levels on the site under test.*

### 5.3 Studying the variation of the acoustic signal with the inflating pressure levels

The traditional auscultation method measures the blood pressure of a subject by listening to the different phases of the Korotkoff sounds generated within the brachial artery at the upper arm using a stethoscope/ microphone. These phases of the Korotkoff sounds generated at different pressure levels tend to have energy contained within 600 Hz [3]–[6]. The spectral analysis of the acoustic signal in Section 3.2 demonstrated the presence of acoustic features superimposed on the pulse wave component propagated from the heart. These acoustic features in absence of any external pressure on the arterial branch have frequency content mainly below 25 Hz, a range in the lower human threshold of hearing. Although it is difficult for a physician to listen to these sounds at the wrist using a stethoscope, the presence of acoustic features in the pulse sounds reveal a possibility of recording the Korotkoff sounds from the radial artery using a microphone. To test such a hypothesis, the acoustic signal at the wrist is recorded continuously in synchronisation with varying pressure levels applied on the arterial branch. Since the wearable device to record the pulse sounds at the wrist was designed as a standalone system, the air cuff is placed on the upper arm to avoid the damage of device under the application of pressure on the PCB. The placement of air cuff on the upper arm also avoids the interference from cuff movements during inflation and allows a better characterisation of the acoustic signal at varying pressure levels. As an illustration, Fig. 5.2 plots the variation of the acoustic signal over an inflation period of approximately 45 seconds. For the first 10 seconds of the recording, the acoustic signal is recorded in the absence of an externally applied pressure. Thereafter, the pressure signal quickly jumps to a level around 40 mmHg and a gradual step wise inflation of the air cuff at a rate of 2-3 mmHg/s is subsequently performed. The pressure is incremented up to a level of 20-30 mmHg higher than the entry SBP of the subject. Since the pressure is incremented with short bursts of air flow inside the air cuff, small oscillations in the pressure signal can be observed. The post-processing of the pressure signal removes these oscillations and estimates a monotonic pressure profile from 40 mmHg to the maximum pressure. As soon as the maximum pressure level inside the air cuff is reached, the air is allowed to flow outside and a zero pressure level is reached within a span of few seconds as shown in Fig. 5.2(a).

The time-domain visualisation of the acoustic signal in Fig. 5.2(b) reveals a significant variation in the amplitude of the S1 and the S2 sounds with varying pressure levels. In the regions of zero external pressure, it can be observed that the S1 and S2 sounds possess similar amplitude and shape characteristics. However, the characteristics of these sounds tend to change significantly during the inflation period. The positive normalised amplitudes of the S1 sounds increases up to a maximum level and decreases with further increments in the pressure levels. On the contrary, the negative normalised amplitudes

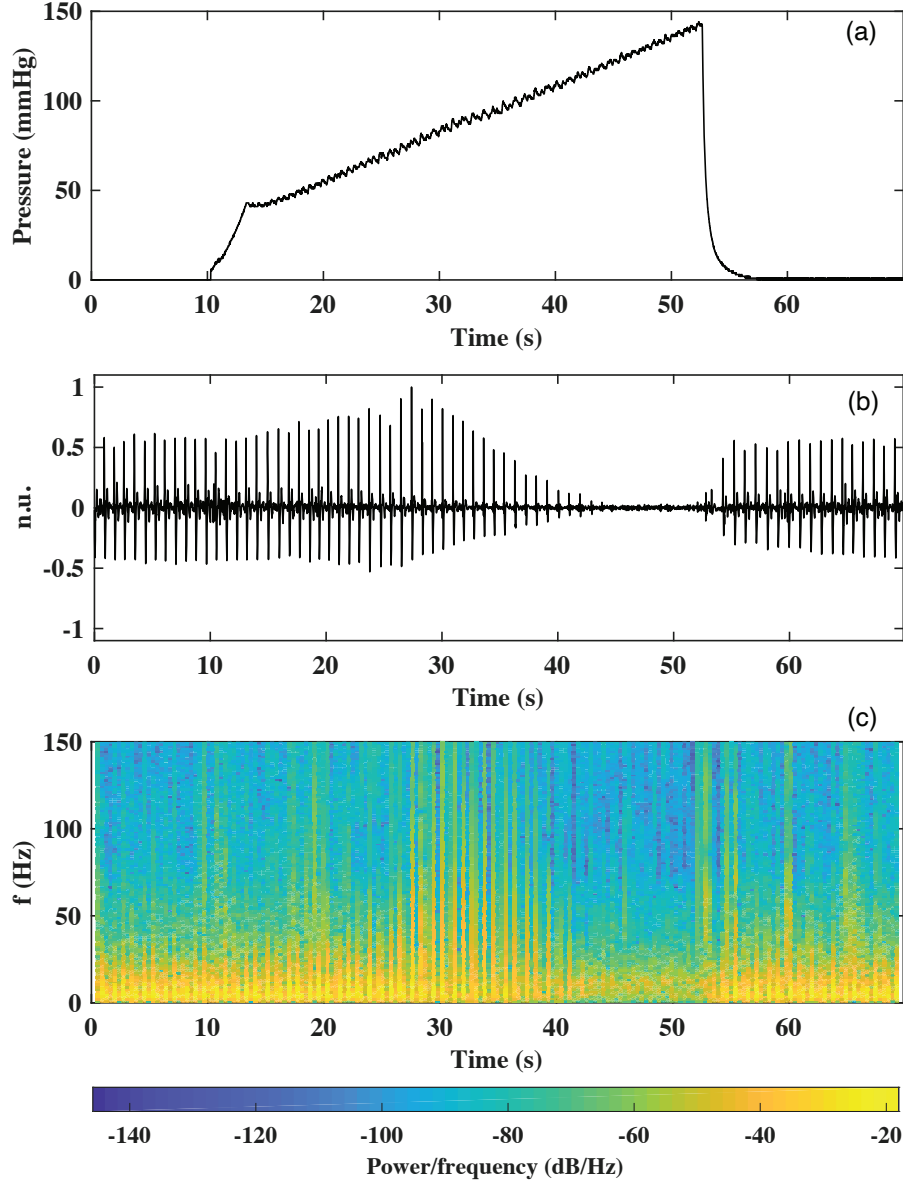


**Figure 5.2:** Variation in the acoustic signal with respect to the inflating pressure inside the air cuff. (a) Pressure applied on the arm increases between zero and a value above the systolic blood pressure. (b) Acoustic signal recorded from the radial artery in synchronisation with the pressure signal. n.u. denote the normalised units. (c) STFT analysis of the varying time-frequency characteristics of the acoustic signal.

of the S1 sounds only increase by a smaller magnitude and tend to decrease continuously with the rising levels of the pressure. While the S2 sounds seem to disappear earlier, the S1 sounds disappear only after the full occlusion of the brachial artery in the upper arm. It can also be observed that the pulse sounds appear as soon the pressure decreases below the SBP during the air release from the air cuff. This happens due to the rush

of blood flow inside the radial artery transferring vibrations to the skin surface that are picked up by the microphone.

The spectral characteristics of the acoustic signal plotted in Fig. 5.2(b) are obtained using a joint time-frequency domain STFT analysis similar to the one performed in Section 3.2. The STFT of the acoustic signal sampled at 2100 Hz is obtained using a Blackman window of 256 samples and 50% overlap between the consecutive frames. The resultant grids in Fig. 5.2(c) demonstrates the power distribution of the signal in the joint time-frequency space. The intensity of the power grids is represented by the colour bar where the yellow and the blue colour denote the maximum and the minimum power densities respectively. While the S1 sounds in the regions with zero pressure carry power mainly below 25 Hz, the spectral energy starts to spread across higher frequencies above a certain pressure level. The S1 sounds falling in the middle part of the pressure inflation profile carry significant power above 25 Hz as shown in Fig. 5.2(c). Therefore, the STFT analysis suggests that the acoustic signal produces S1 sounds in the audible range with varying levels of pressure applied on the arterial branch. Although the disappearance of the S1 sounds above the SBP causes a significant drop in the spectral energy, the motor noise transferred via the air flow also contributes some power in the STFT analysis. The motor noise, however, is minimised by using the wavelet denoising of the acoustic signal as discussed in later sections of this chapter.

The STFT analysis of the acoustic signal provided a broader view of the power distribution in the joint time-frequency space. A better spectral analysis of the acoustic signal can be obtained by finding the spectral content of the S1 sounds in isolation. The pressure profile in Fig. 5.3(a) is obtained after removing the small oscillations caused by the step wise inflation of the air cuff. The acoustic signal displayed in Fig. 5.3(b) behaves in an opposite manner to the acoustic signal plotted in Fig. 5.2(b). In this case, the negative normalised amplitudes of the S1 sounds increases up to a maximum level and decreases with further increments in the pressure levels, whereas the positive normalised amplitudes tend to decrease continuously with the rising levels of the pressure. Therefore, the amplitude envelopes of the acoustic signal can behave differently for different subjects. The zero-crossings of the S1 sounds falling within the pressure inflation region are found using the relative energy algorithm proposed in Section 4.5. A total of sixteen S1 sounds are extracted from the acoustic signal by taking a time-window of 0.15 seconds on either sides of the zero-crossings. The frequency response of these sounds, sampled at 2100 Hz, is obtained using the FFT and plotted in Fig. 5.3(c)-(r). It can be observed that the frequency content of the first few S1 sounds mainly fall below 25 Hz suggesting that the application of lower pressure levels does not affect the spectral characteristics of the acoustic signal significantly. However, further increments in the pressure levels tend to decrease the spectral content in the lower frequencies and start pushing the energy towards the higher frequencies as observed before in the STFT analysis. The spectral

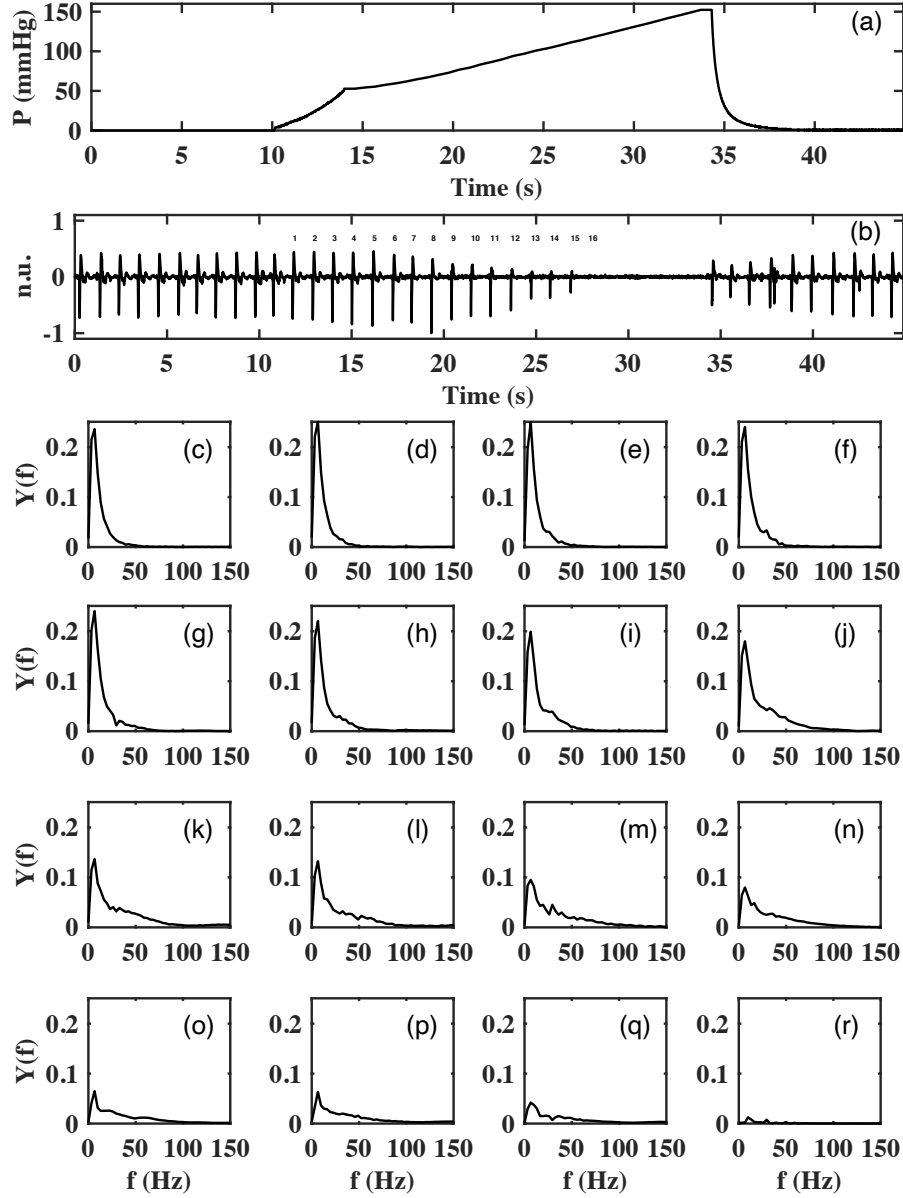


**Figure 5.3:** Frequency spectrum of the S1 sounds in the acoustic signal. (a) Pressure inside the air cuff increases between zero and a value above the systolic blood pressure. (b) Time-domain acoustic signal with numbered S1 sounds of interest. (c)-(r) FFT of the sixteen S1 sounds marked in the acoustic signal. The FFT coefficients are plotted in absolute units.

content of several S1 sounds in this case reaches around 100 Hz, therefore, introducing significant energy in the audible range. The spectral energy reduces to a minimum for the peaks detected after the SBP level as shown in Fig. 5.3(r). In conclusion, both the STFT and the FFT analysis suggests the presence of Korotkoff sounds with spectral energies in the audible range when the pressure on the upper arm is varied below the

DBP to above the SBP to cause a full occlusion of the artery.

## 5.4 Algorithm for determining the diastolic blood pressure

The blood pressure measurement using the auscultation method requires a trained clinician to listen to the appearance and disappearance of the Korotkoff sounds during the cuff deflation. While the appearance of the first Korotkoff sound correspond to the rush of blood flow as soon as the full occlusion of the arterial branch is removed, the Korotkoff sounds disappear only when the blood flow through the artery returns to the normal state. Since the blood flow is essentially preceded by a pressure wave, the Korotkoff sounds produces vessel vibrations which manifest themselves as S1 sounds in the acoustic pulse signal. Therefore, the algorithm for blood pressure determination in this study identifies the S1 peaks corresponding to the appearance and disappearance of the Korotkoff sounds, and correlate it with the blood pressure by matching the time-stamps with the pressure profile. The order of different phases of the Korotkoff sounds during the cuff inflation is exactly opposite to the one observed during the cuff deflation. While the appearance of the first Korotkoff sound during the cuff inflation corresponds to the DBP, the disappearance of the Korotkoff sound relates to the SBP (or full occlusion of the artery). Due to the importance of identifying all the S1 peaks (during the cuff inflation) for determining the SBP/ DBP accurately, it is desirable to minimise the noise by pre-processing the acoustic signal.

### 5.4.1 Pre-processing the acoustic signal

Studying the characteristics of the acoustic signal over the full occlusion of the artery required a precise localisation of the S1 peaks during the cuff inflation. The S1 peaks are identified using the relative energy algorithm proposed in Section 4.5. Since the relative energy algorithm works efficiently in cases where the short-term events of the S1 waveforms are characterised by a local change in the amplitude, it is important to minimise the noise in the baseline of the signal. Further constraints are imposed by the peaks lying in the high pressure regions where the peak-to-peak amplitudes of the S1 sounds become really low as shown in Fig. 5.2(b). The baseline noise in the signal is mainly introduced by the motor noise that is sensed by the microphone through the surrounding environment and the skin surface vibrations caused by the air flow.

The FFT of the S1 peaks in Fig. 5.3 demonstrated the spectral content of the isolated S1 sounds to lie below 150 Hz. Thus, a fifth-order Butterworth low pass filter with cut-off frequency of 150 Hz is used to remove the high frequency components from the acoustic signal. Since the acoustic signal is originally sampled at 2100 Hz ( $fs$ ), the filtered signal is downsampled by a factor of 6, reducing the sampling frequency down to 350 Hz ( $fd$ ). The downsampling, without introducing any aliasing in the signal, reduces the

number of computational cycles required for the further processing. While the low pass filtering removes the high frequency noise and interference from the signal, it is unable to eliminate the motor noise since its spectral energy falls below 100 Hz. The effect of motor noise is reduced by using the wavelet denoising with ‘db6’ as the orthogonal wavelet. The denoising is accomplished by using a fifth-level wavelet decomposition of the low pass filtered signal  $y$  followed by a soft thresholding of the detail coefficients using a universal threshold of  $\sqrt{2 \ln(\text{length}(y))}$ . A third-order median filtering is subsequently used to remove the impulsive spikes from the signal. As an illustration, the motor noise clearly visible in the baseline of the original signal in Fig. 5.4(a) makes it difficult for an accurate identification of the S1 sounds in later stages of the algorithm. The motor noise is significantly reduced in the pre-processed signal as shown in Fig. 5.4(b) and a better SNR is obtained.

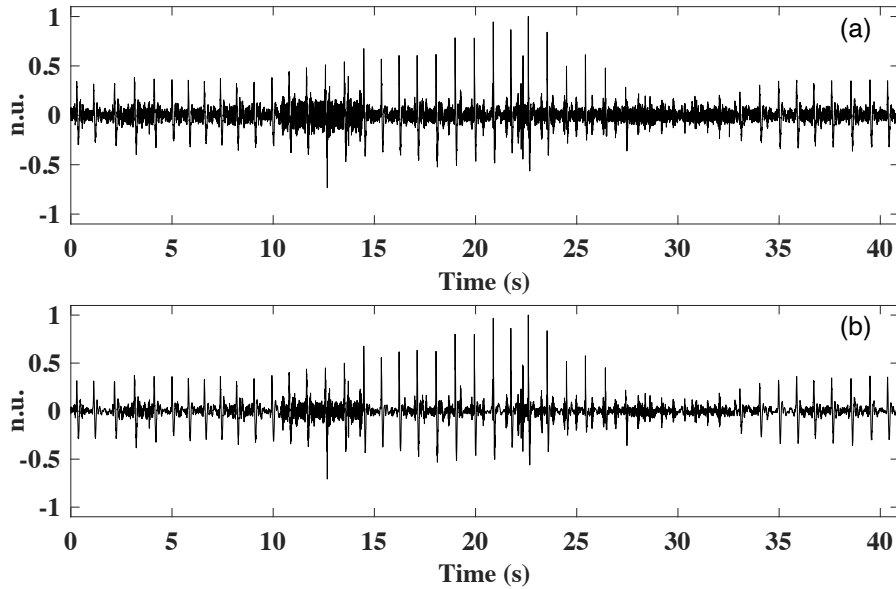


**Figure 5.4:** *Pre-processing the acoustic signal to reduce the noise content. (a) Original acoustic signal with significant interference from the motor noise. (b) Reduction of the external interference using low pass filtering, downsampling, wavelet denoising and median filtering.*

#### 5.4.2 Artifact removal and missed peaks detection

The hand movements during the blood pressure measurement can introduce artifacts in the signal that might not be removed by the pre-processing stage of the algorithm. These artifacts can interfere with the S1 peaks as shown by the blue circles in Fig. 5.5(a) and possibly lead to an inaccurate localisation of the S1 sounds. Therefore, the S1 sounds must be differentiated from the artifacts in the signal. The time-stamps of the S1 sounds in the pre-processed signal are marked as the negative characteristic points for the reasons



explained later. For an accurate determination of the blood pressure, it is also important to detect the missed S1 peaks marked by the magenta circles in Fig. 5.5(a). These peaks remain undetected because of significant variation in the amplitude envelope of the acoustic signal. This was not the case with the acoustic signal recorded in absence of any external pressure as both the positive and the negative amplitudes of the S1 sounds remained approximately constant throughout the recording. Since the acoustic signal in such scenario had a bandwidth of 25 Hz, the peak detection using the relative energy algorithm is repeated by low pass filtering the original signal with 25 Hz as the cut-off frequency. A relatively less amplitude variation in the acoustic signal filtered with 25 Hz as shown in Fig. 5.5(b) can be observed. For a better visualisation, the positive characteristic points of the detected S1 peaks are marked. The peaks detected in this signal are more reliable as erroneous peaks from the original signal are already removed. The missed S1 peaks in the original signal are also detected in the 25 Hz signal. The

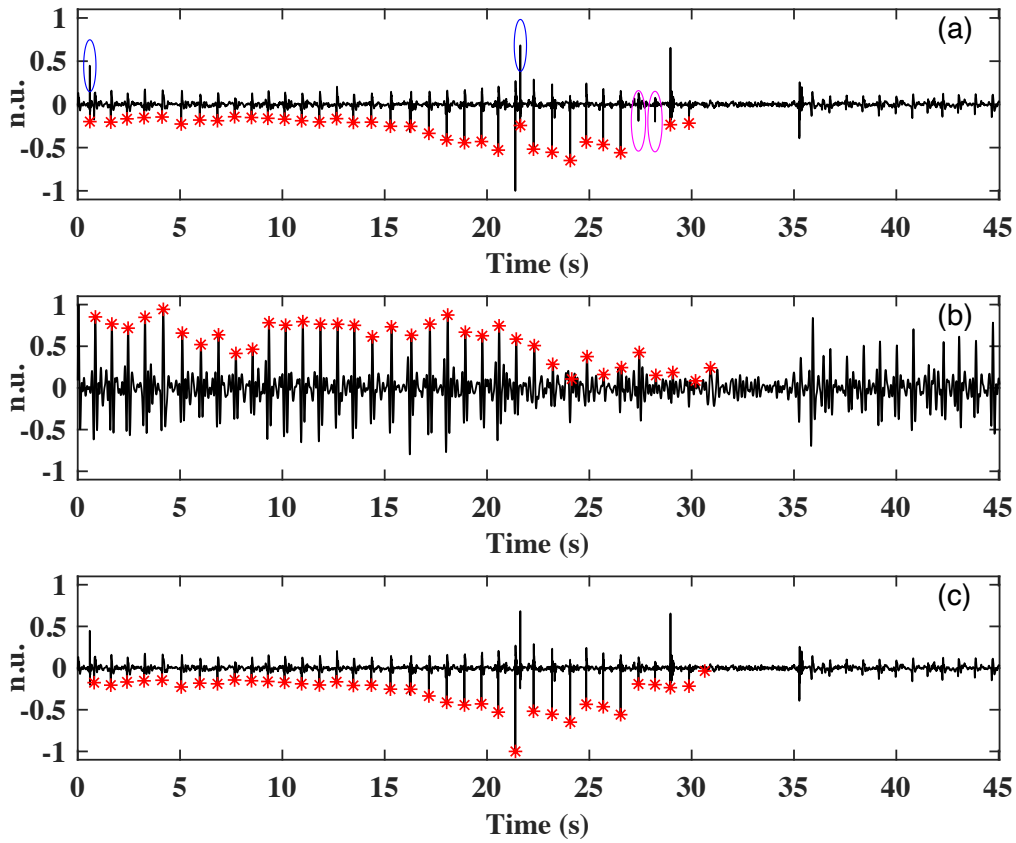


**Figure 5.5:** Identification of the erroneous peaks and missed S1 peaks in the acoustic signal. (a) S1 peaks detected by the relative energy algorithm. The peaks in the blue and magenta circles are the erroneous and missed peaks respectively. (b) S1 peaks detected by the relative energy algorithm in acoustic signal low-pass filtered with 25 Hz. (c) The peaks in (b) are utilised to remove the erroneous peaks and trace back the missed S1 peaks in the acoustic signal.

time-stamps of the S1 peaks in the 25 Hz signal are utilised to remove the erroneous peaks and trace back the missed S1 peaks in the pre-processed acoustic signal as shown in Fig. 5.5(c). Any extra peaks detected in the 25 Hz signal are also matched with the original signal as they are dealt in further stages of the algorithm. Since the heart rate in a range of 40 to 200 bpm is considered, it is ensured that the inter-beat intervals corresponding to the consecutive S1 peaks produce a heart rate within these limits. Otherwise, an analysis similar to the one in Section 3.5.4.2 is performed to remove the redundant peaks.

### 5.4.3 Feature signals to find the diastolic blood pressure

#### 5.4.3.1 Amplitude envelope

The relative energy algorithm provided a functionality of detecting the positive peaks, the zero-crossings and the negative peaks as three different characteristic points of S1 sounds in the acoustic signal. The amplitude envelopes of the acoustic signal are simply obtained by finding the positive and negative characteristic points of the S1 sounds shortlisted after identifying the artifacts. It can be observed that while the positive amplitudes of the acoustic signal in Fig. 5.6(b) only increase by a small margin before decreasing continuously with the rising levels of pressure, the negative amplitudes demonstrate a significantly larger variation in the envelope. This is evident in the upper and lower envelopes plotted in Fig. 5.6(d)-(e) respectively, where the amplitudes of all the S1 sounds before 40 mmHg have been zeroed as they are ignored for the further processing. The envelopes have been processed by adopting a fifth-order median filtering to obtain a smoother profile. Among these two envelopes, the envelope with larger amplitude variation is used as one of the feature signals to determine the experimental location of the DBP. Since the lower envelope in Fig. 5.6 is chosen as the feature signal, the negative characteristic points are marked in the original acoustic signal to represent this choice.

#### 5.4.3.2 Energy envelope

The spectral characteristics of the S1 sounds in the acoustic signal vary significantly in relation to the pressure applied on the arterial branch as demonstrated in Section 5.3. Such a variation can be utilised to find a correlation with the blood pressure. For  $N$  number of S1 sounds detected in the acoustic signal, the corresponding zero-crossings are found using the relative energy algorithm. These zero-crossings, denoted by  $z_n$  for  $n \in [1, N]$ , are used to extract all the S1 waveforms by choosing a rectangular window of 0.3 seconds duration centred at the characteristic point as follows:

$$\begin{aligned} \forall n \in [1, N] \\ S1_n = y [z_n - 0.15 : z_n + 0.15] \end{aligned} \tag{5.1}$$

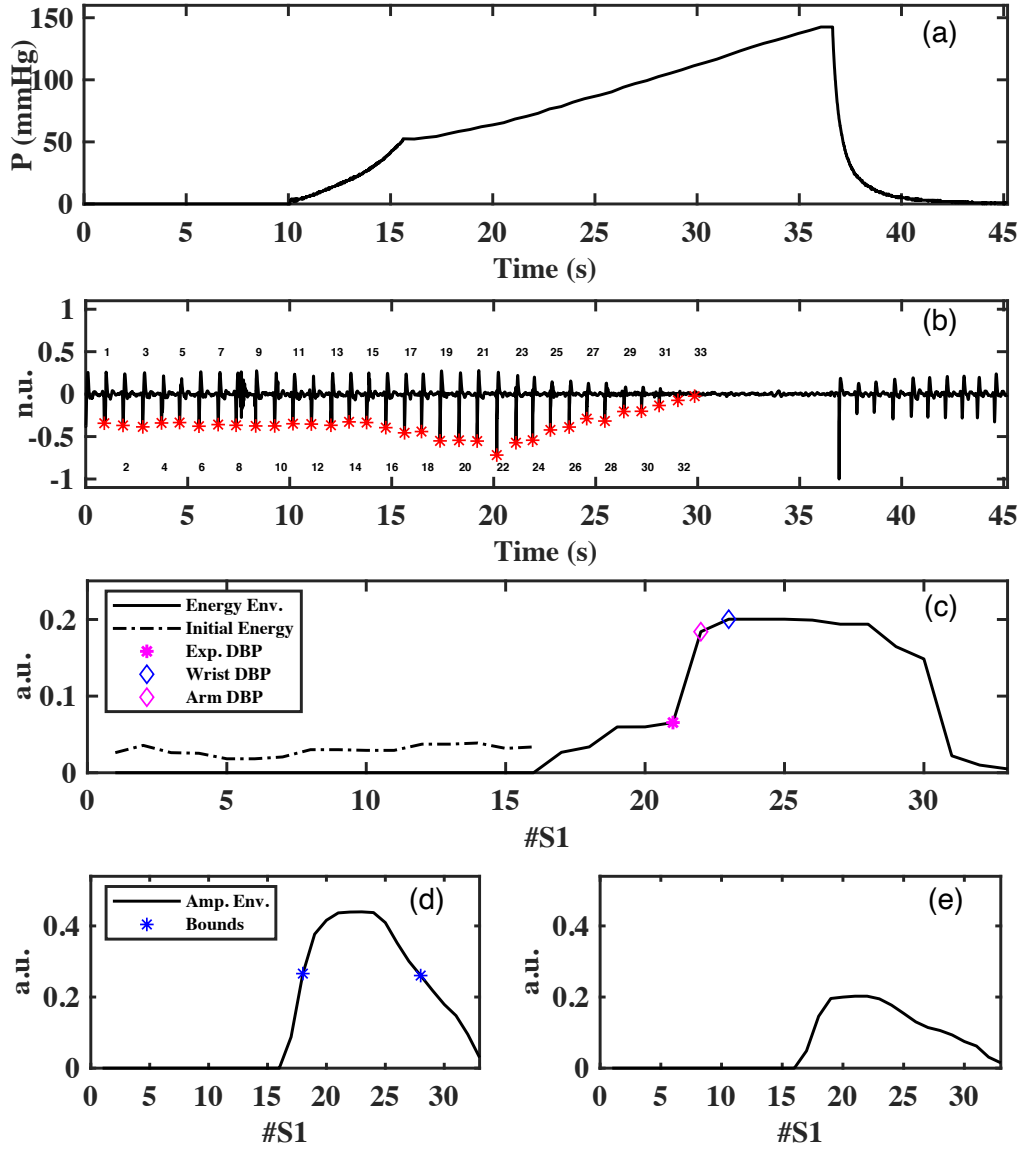


**Figure 5.6:** *Energy and amplitude envelopes of the Korotkoff sounds with peaks marked in the negative side of the acoustic signal. (a) Pressure applied on the arm increases between zero and a value above the SBP. (b) Pre-processed acoustic signal with all the S1 peaks identified. (c) Energy envelope of the Korotkoff sounds falling after the 40 mmHg pressure level. The experimentally determined Korotkoff sound location for DBP determination is also plotted along with the reference wrist and reference arm DBP location. An error of 5 and 1 mmHg was obtained with respect to the wrist and arm DBP references respectively. (d) Amplitude envelope of the negative amplitudes (lower envelope) of the S1 peaks falling after the 40 mmHg pressure level. The bounds used in the proposed algorithm are also plotted. (e) Amplitude envelope of the positive amplitudes (upper envelope) of the S1 peaks falling after the 40 mmHg pressure level.*

The frequency spectrum of these isolated S1 waveforms are obtained using the FFT as shown in Fig. 5.3. Depending on the frequency band, the absolute spectral energy corresponding to a S1 waveform can be obtained by summing up all the FFT coefficients falling within the defined frequency range. While the absolute energy envelope can be used as a feature signal to establish a correlation with the blood pressure, the normalised energy proves to be a better choice for determining the experimental location of the DBP. The normalisation is performed by dividing the spectral energy of the S1 sound with its peak-to-peak amplitude. This way the effect of amplitude modulation on the energy envelope is minimised allowing the algorithm to be more robust for the DBP determination. Since the DBP of an adult subject is assumed to be greater than 40 mmHg, all the S1 sounds lying before reaching this pressure level are ignored for the further processing and the corresponding energies are zeroed. As an illustration, the normalised energy envelope of 33 S1 sounds in a spectral band of 50-110 Hz is plotted in Fig. 5.6(c), where the energy of first 16 S1 sounds are zeroed. The envelope has been processed by adopting a fifth-order median filtering to obtain a smoother profile. The energy profile reveals that while the acoustic signal maintains a baseline energy for the first few S1 sounds as shown by the dashed line in Fig. 5.6(c), the energy jumps up with further increments in the pressure levels to reach a maximum value. Any further occlusion of the arterial branch causes the energy of the S1 sounds to decrease significantly.

#### 5.4.3.3 Diastolic band analysis of the S1 sounds

To use the normalised energy envelope as one of the feature signals, it is important to identify a suitable spectral band that correlates with the experimental location of the DBP [7]. Since the bandwidth of the acoustic signal is around 150 Hz, a wide-band analysis of the S1 sounds is performed using five different frequency bands as follows: 10-30 Hz, 30-50 Hz, 50-80 Hz, 80-110 Hz and 110-150 Hz. A total of 35 acoustic signals are randomly selected from the database recorded for this study. The normalised energy envelopes corresponding to these signals are computed in all the spectral bands. The correlation of the spectral bands with the reference DBP (obtained from the commercial monitor) can be established by observing the behaviour of the energy envelopes in its immediate surrounding. Therefore, only seven S1 sounds centred at the reference DBP are chosen for the wide-band analysis. As an illustration, the energy amplitudes in different spectral bands centred at the reference DBP (21<sup>st</sup> S1 sound in the acoustic signal) for a subject are plotted in Fig. 5.7. Similar plots from all the 35 acoustic signals are obtained for the wide-band analysis. The normalised energy amplitudes of these seven S1 sounds are examined to identify the spectral bands that demonstrate a significant increase in the energy when transitioning from before to after the reference DBP. In Fig. 5.7, it can be observed that while the normalised energy in the spectral bands of 30-50 Hz and 50-80 Hz remains almost constant before the reference DBP, the

energy increments to higher amplitudes for S1 sounds lying after the reference DBP. This observation supports the hypothesis that the generation of Korotkoff sounds after a certain pressure level produces a sudden jump in the energy as compared to the baseline energy of the S1 sounds. However, this behaviour is not apparent in all the spectral bands.

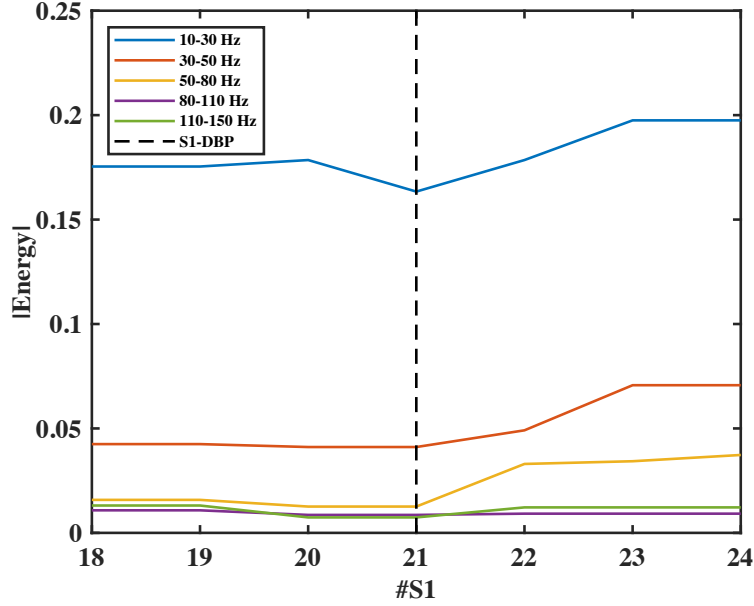


**Figure 5.7:** Wide-band analysis of the normalised energy envelope in different frequency bands for the DBP determination. Normalised energy of seven S1 sounds centred at the reference DBP are plotted.

The energy increments ( $R_n$ ) in a specific spectral band are calculated as the ratio of consecutive energy amplitudes ( $E_n$ ) as follows:

$$\forall n \in [1, 6] \text{ in } [f1, f2] \text{ Hz} \quad R_n\{f1, f2\} = \frac{E_{n+1}}{E_n} \quad (5.2)$$

Among every plot corresponding to the 33 acoustic signals, the frequency bands are rank ordered to find the most suitable band for establishing a correlation with the reference DBP. For every spectral band, the S1 location corresponding to the maximum energy ratio is determined and the bands are rank ordered depending on the closeness of the S1 location with the reference DBP. In cases where multiple bands produces maximum energy ratio corresponding to the same S1 location, the band with a higher value of energy ratio is placed at the higher preference. Since the introduction of the first Korotkoff sound in the acoustic signal is characterised by a higher energy amplitude than the previous S1 sound, only ratios greater than 1 are included in this analysis. The first three ranks awarded to different frequency bands with respect to reference arm and wrist DBP are

listed in Table 5.1. The feature band is determined by considering the sum of only the first and second ranks. Based on the rank ordering, it can be observed that for both the arm and the wrist references, the spectral bands of 50-80 Hz and 80-110 Hz arise as the best choices. Therefore, the spectral band of 50-110 Hz in combination demonstrates the highest amplitude increase in the energy envelope when transitioning from before to after the reference DBP. Hence, the algorithm uses the normalised energy envelope computed in the spectral band of 50-110 Hz as another feature signal to find the experimental location of the DBP.

**Table 5.1:** *Rank ordering the frequency bands as the best spectral feature band for determining the DBP. The bands are compared for a total of 35 files and ranked according to the closeness of the maximum energy ratio with the DBP location obtained from the commercial arm and wrist monitor.*

Reference	Frequency Band	Rank Order			Total
		First	Second	Third	
<b>Arm</b>	10-30 Hz	1	1	1	2
	30-50 Hz	3	7	6	10
	50-80 Hz	12	12	10	24
	80-110 Hz	12	11	8	23
	110-150 Hz	7	4	10	11
<b>Wrist</b>	10-30 Hz	0	2	3	2
	30-50 Hz	4	5	7	9
	50-80 Hz	10	14	8	24
	80-110 Hz	11	12	7	23
	110-150 Hz	10	2	10	12

#### 5.4.4 Utilising the feature signals to identify the S1 sound corresponding to the diastolic blood pressure

The feature signals extracted from the acoustic signal provide substantial information to find the DBP experimentally. The goal is to find the temporal location of a suitable S1 sound which when correlated with the pressure signal provides an accurate DBP. Since this is the first time in the literature that an acoustic signal recorded at the wrist has been used to determine the blood pressure, the algorithm design is mainly based on empirical observations. In the traditional auscultation method, a laminar flow of blood is achieved when the cuff is deflated to a level just below the DBP [8], [9]. The acoustic signal in this study is recorded during the cuff inflation, therefore, any disturbance to the laminar blood flow is caused only after the DBP. While no consensus on the origin of Korotkoff sounds has been reached in the literature, the cuff inflation beyond the

DBP affects the fully expanded state of the artery causing changes in the amplitude and frequency of the vessel wall vibrations [10]. An obstruction to the normal blood flow causes the pressure wave to exhibit higher force on the arterial walls. These changes in the vessel wall vibrations during the cuff inflation are sensed by the microphone producing different amplitude and energy characteristics of S1 sounds in the acoustic signal. An empirical observation of the acoustic signal in Fig. 5.6 already suggested an increment in the amplitude envelope when transitioning from before to after the reference DBP. A similar conclusion is made for the acoustic signal in Fig. 5.8 where the upper envelope is chosen as the feature signal for DBP determination. The positive characteristic points are marked in the original acoustic signal to represent this choice.

Instead of processing all the S1 sounds in the acoustic signal for DBP determination, the amplitude envelope selected as the feature signal is utilised in the following manner to shortlist only a few S1 sounds:

1. Firstly, the maximum value ( $A_{max}$ ) of the amplitude envelope  $A_n$  for  $n \in [1, N]$  is determined.
2. All the S1 sounds satisfying the following condition are accepted.

$$\begin{aligned} & \forall n \in [1, N] \\ S1_n = & \begin{cases} Accepted, & \text{if } A_n \geq 0.5 \times A_{max} \\ Rejected, & otherwise \end{cases} \end{aligned} \quad (5.3)$$

3. Only S1 sounds selected above that lie within  $\pm 5$  beats of the  $A_{max}$  location are included for the further analysis.

Using the above criteria, the shortlisted S1 sounds corresponding to the lower envelope in Fig. 5.6(d) are bounded by the blue asterisks. All the S1 sounds at and between these bounds (18 to 28) are included for the DBP determination. A different set of S1 bounds (27 to 38) are obtained for the upper envelope in Fig. 5.8(d).

The wide-band analysis of the S1 sounds suggested a sharp increment in the normalised energy (50-110 Hz) around the reference DBP. While the shortlisting of the S1 sounds in the amplitude envelope already narrowed the search region, the normalised energies corresponding to these sounds are further utilised to search for the experimental location of the DBP. For the S1 bounds defined by  $b_1$  and  $b_2$  in the amplitude envelope, the energy ratios are computed as follows:

$$\begin{aligned} & \forall n \in [b_1, b_2 - 1] \text{ in } [50, 110] \text{ Hz} \\ R_n\{50, 110\} = & \frac{E_{n+1}}{E_n} \end{aligned} \quad (5.4)$$

For the energy envelopes in Fig. 5.6(c) and Fig. 5.8(c), the energy ratios are determined

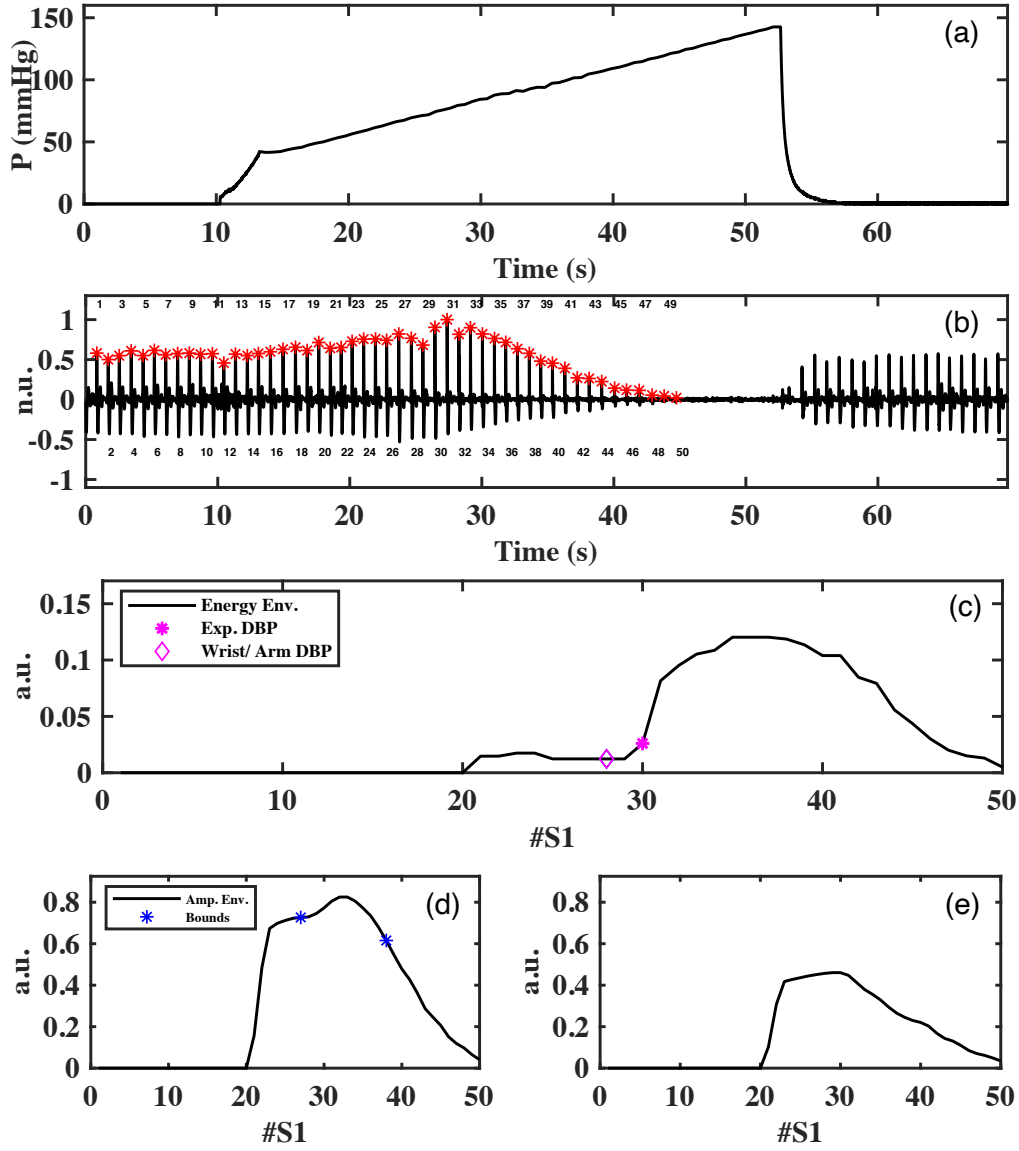


**Figure 5.8:** Energy and amplitude envelopes of the Korotkoff sounds with peaks marked in the positive side of the acoustic signal. (a) Pressure applied on the arm increases between zero and a value above the SBP. (b) Pre-processed acoustic signal with all the S1 peaks identified. (c) Energy envelope of the Korotkoff sounds falling after the 40 mmHg pressure level. The experimentally determined Korotkoff sound location for DBP determination is also plotted along with the reference wrist and reference arm DBP location. An error of 3 mmHg was obtained with respect to the wrist and arm reference DBP. (d) Amplitude envelope of the positive amplitudes (upper envelope) of the S1 peaks falling after the 40 mmHg pressure level. The bounds used in the proposed algorithm are also plotted. (e) Amplitude envelope of the negative amplitudes (lower envelope) of the S1 peaks falling after the 40 mmHg pressure level.



for S1 sounds numbered between [18,27] and [27,37] respectively. Among all these energy ratios, only the top three values ( $R_{m1}$ ,  $R_{m2}$  and  $R_{m3}$ ) with  $R_{m1}$  being the highest ratio, are considered for the further processing. The amplitude value pairs ( $[A_{m1}^1, A_{m1}^2]$ ,  $[A_{m2}^1, A_{m2}^2]$  and  $[A_{m3}^1, A_{m3}^2]$ ) and the S1 location pairs ( $[l_{m1}^1, l_{m1}^2]$ ,  $[l_{m2}^1, l_{m2}^2]$  and  $[l_{m3}^1, l_{m3}^2]$ ) corresponding to these ratios are also noted. A single ratio  $R_m$  corresponding to the maximum starting amplitude is chosen as follows:

$$A_m = \max\{A_{m1}^1, A_{m2}^1, A_{m3}^1\}$$

$$R_m = \begin{cases} R_{m1}, & \text{if } A_m = A_{m1}^1 \\ R_{m2}, & \text{if } A_m = A_{m2}^1 \\ R_{m3}, & \text{if } A_m = A_{m3}^1 \end{cases} \quad (5.5)$$

Depending on the chosen ratio, a single S1 sound location ( $l_m$ ) corresponding to the experimental location of the DBP is found as follows:

$$l_m = \begin{cases} \begin{cases} l_{m1}^1, & \text{if } A_{m1}^1 \geq A_{m1}^2 \\ l_{m1}^2, & \text{if } A_{m1}^1 < A_{m1}^2 \end{cases} & \text{if } R_m = R_{m1} \\ \begin{cases} l_{m2}^1, & \text{if } A_{m2}^1 \geq A_{m2}^2 \\ l_{m2}^2, & \text{if } A_{m2}^1 < A_{m2}^2 \end{cases} & \text{if } R_m = R_{m2} \\ \begin{cases} l_{m3}^1, & \text{if } A_{m3}^1 \geq A_{m3}^2 \\ l_{m3}^2, & \text{if } A_{m3}^1 < A_{m3}^2 \end{cases} & \text{if } R_m = R_{m3} \end{cases} \quad (5.6)$$

These comparisons are based on the reasoning that the S1 sound corresponding to the DBP is characterised with an increase in the amplitude and energy, therefore, the energy ratio corresponding to the maximum amplitude is chosen. The time-stamp of the chosen S1 sound is extracted from the acoustic signal and the corresponding pressure value from the synchronous pressure signal is found. This value of pressure is assumed to be the experimental DBP of the subject. As an illustration, the S1 numbered 21 in Fig. 5.6(b) correlates to an experimental DBP of 67 mmHg and produces an error of 5 mmHg and 1 mmHg with respect to the wrist and arm DBP references respectively. The same analysis for the acoustic signal in Fig. 5.8 produces an error of 3 mmHg with respect to the wrist and arm reference DBP. The 30<sup>th</sup> S1 sound is chosen as the experimental location of the DBP.

## 5.5 Algorithm for determining the systolic blood pressure

The appearance of the first Korotkoff sound (Phase 1) in the traditional auscultation method during the cuff deflation is characterised by a tapping sound. The pressure level corresponding to the first Korotkoff sound is termed as the SBP. A precise measurement of

the SBP requires a trained physician to deflate the air cuff gradually and read the pressure levels on a mercury sphygmomanometer at the appearance of the first Korotkoff sound. Since an automatic or manual cuff deflation only requires the release of air, the external noise introduced in the stethoscope is minimum allowing an accurate measurement of the SBP. This is not the case when measuring the SBP during the cuff inflation. The cuff inflation in this study is carried out using a DC motor which introduces significant noise into the sensing system either through the surrounding environment or through the air flow irrespective of the pressure levels. On the contrary, the temporal characteristics of the acoustic signal indicated a significant drop in the amplitudes of the S1 sounds with the rising pressure levels. These factors in combination makes it difficult for the relative energy algorithm to detect all the S1 sounds near the SBP. Unlike the S1 sounds lying near the DBP, the S1 sounds around SBP suffer from a significant drop in the SNR and their amplitudes are comparable to the noise levels near the full occlusion of the arterial branch. Although the wavelet denoising in the pre-processing of the acoustic signal reduces the motor noise significantly, there is a need of additional feature signals to find an accurate SBP. The following section discusses different feature signals used to find the S1 location corresponding to the SBP from the pre-processed acoustic signal.

### **5.5.1 Feature signals to find the systolic blood pressure**

#### **5.5.1.1 Amplitude envelope**

The upper and lower amplitude envelopes are found using the positive and negative characteristics points of the S1 sounds respectively. Among these two envelopes, the envelope with a larger amplitude variation is used as the feature signal to determine the experimental location of the SBP. The original envelopes are filtered using a fifth-order median filter to obtain a smoother profile. For the acoustic signal in Fig. 5.9(b), the lower envelope is chosen as the feature signal as represented by the markings on the negative characteristic points. On the contrary, the upper envelope for the acoustic signal in Fig. 5.12(b) is chosen as the feature signal and is represented by the markings on the positive characteristic points. The original and filtered envelopes for these signals are plotted in Fig. 5.9(d) and Fig. 5.12(d) respectively. Since the location of the S1 sound corresponding to the experimental DBP is already known, only S1 sounds lying after the DBP are processed further. It can be observed that the filtered amplitude of the S1 sounds decreases continuously with the rising levels of pressure and reaches a constant minimum for the erroneous peaks detected in the noisy region above the SBP.

#### **5.5.1.2 Systolic band analysis of the S1 sounds**

The spectral characteristics of the acoustic signal in Fig. 5.3 demonstrated a significant reduction in the magnitude of the FFT coefficients over a bandwidth of 150 Hz for S1

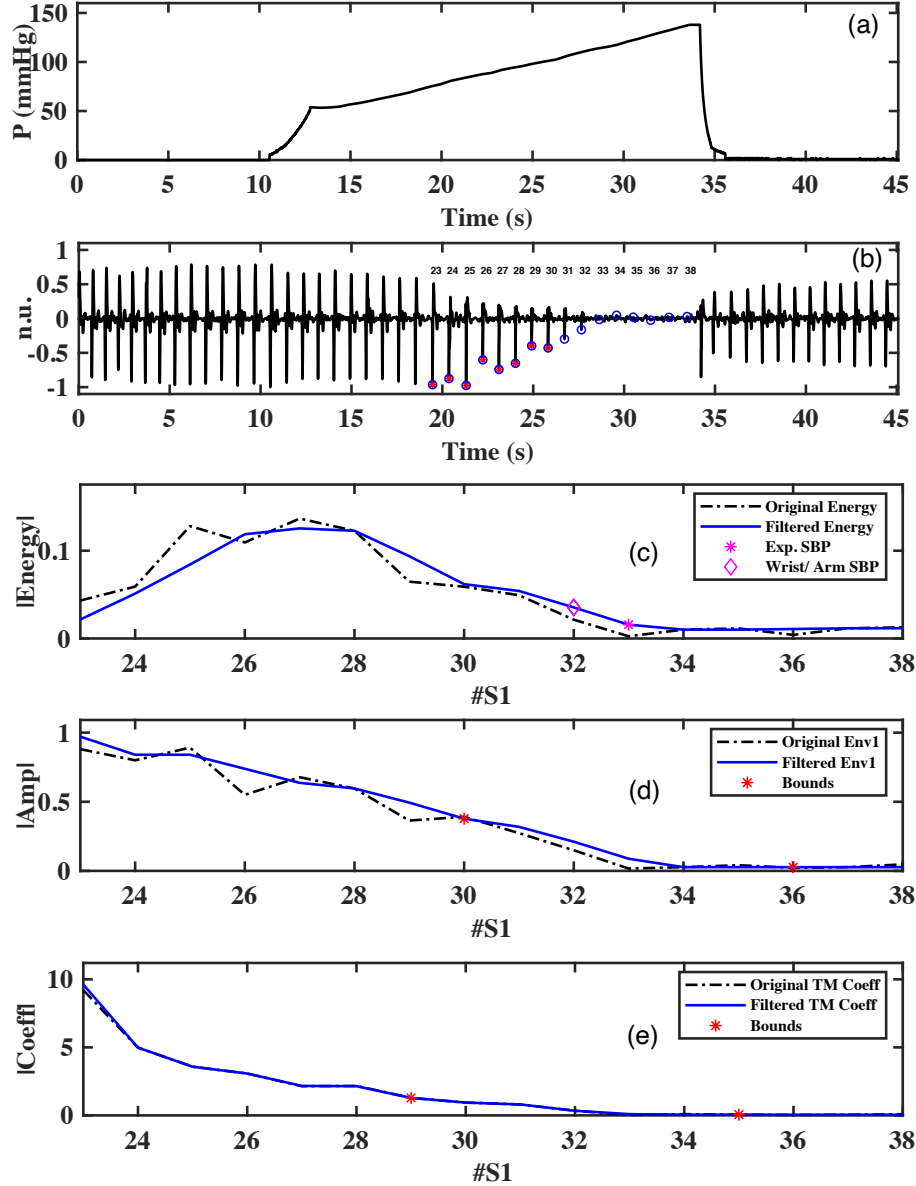


**Figure 5.9:** Energy and amplitude envelopes of the Korotkoff sounds with peaks marked in the negative side of the acoustic signal. (a) Pressure applied on the arm increases between zero and a value above the SBP. (b) Pre-processed acoustic signal with all the S1 peaks identified. (c) Energy envelope of the Korotkoff sounds falling after the 40 mmHg pressure level. The experimentally determined Korotkoff sound location for SBP determination is also plotted along with the reference wrist and reference arm SBP location. An error of 2 and 4 mmHg was obtained with respect to the wrist and arm SBP references respectively. (d) Amplitude envelope of the negative amplitudes (lower envelope) of the S1 peaks falling after the 40 mmHg pressure level. The bounds used in the proposed algorithm are also plotted. (e) Template matching coefficients envelope of the S1 peaks falling after the 40 mmHg pressure level. The bounds used in the proposed algorithm are also plotted.

sounds near the SBP. These coefficients after the full occlusion of the arterial branch acquired much lower values due to the absence of S1 sounds as shown in Fig. 5.3(r). The energy envelope, therefore, can be used as another feature signal to correlate the disappearance of the S1 sounds with the reference SBP. However, a suitable spectral band is required to extract the spectral energy from the FFT of the isolated S1 sounds. Similar to the diastolic wide-band analysis, five different frequency bands as follows: 10-30 Hz, 30-50 Hz, 50-80 Hz, 80-110 Hz and 110-150 Hz are chosen to compare the spectral energies in a total of 35 acoustic signals selected randomly from the database. The energy envelopes corresponding to these signals are computed in all the spectral bands and are normalised with the peak-to-peak amplitudes of the S1 sounds. Since the correlation of the spectral bands with the reference SBP can be established by observing the behaviour of the energy envelopes in its immediate surrounding, only seven S1 sounds centred at the reference SBP are chosen for the wide-band analysis. As an illustration, the energy amplitudes centred at the reference SBP (28<sup>th</sup> S1 sound in the acoustic signal) are plotted for different spectral bands in Fig. 5.10. Similar plots from all the 35 acoustic signals are obtained for the wide-band analysis. The normalised energy amplitudes of these seven S1 sounds are examined to identify the spectral bands that demonstrate a significant energy reduction at the reference SBP and attain a minimum energy level after the reference SBP. Such a behaviour in Fig. 5.10 is only observed for 30-50 Hz and 50-80 Hz frequency bands.

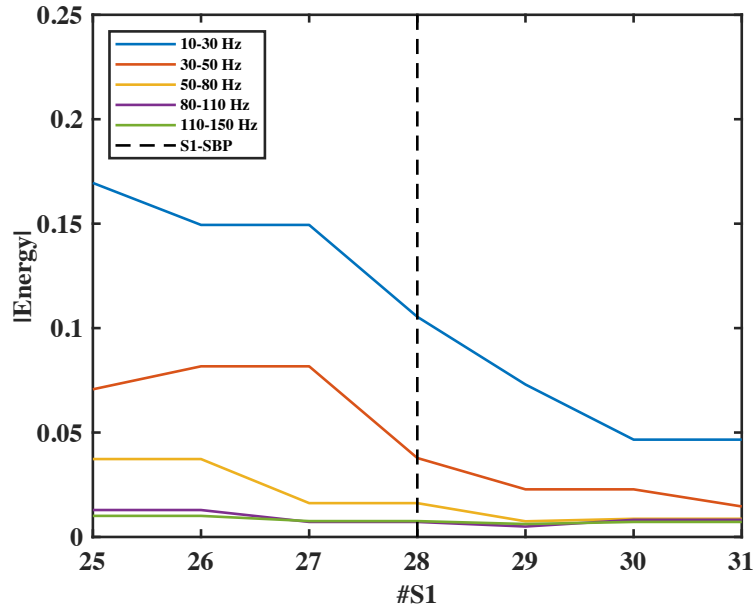


**Figure 5.10:** Wide-band analysis of the normalised energy envelope in different frequency bands for the SBP determination. Normalised energy of seven S1 sounds centred at the reference SBP are plotted.

The energy decrements in a specific spectral band are calculated as the ratio of con-

secutive energies given by Eq. 5.2. The spectral analysis of the acoustic signal showed that the appearance of the last S1 sound at the SBP yields a slightly higher energy than the noisy region lying above the SBP. The peaks in the noisy region as shown in Fig. 5.9(b) are intentionally extrapolated using the heart rate information to extract the energy envelope over the full pressure range. The extrapolation is explained with further details in the next section. Since the normalised energies corresponding to the peaks detected in the noisy region are quite similar, an energy ratio of around 1 is usually obtained after the disappearance of the last S1 sound. However, the energies before the SBP demonstrate a continuous reduction producing the ratios significantly lower than 1. This observation about the energy ratios is utilised to find the most suitable band for establishing a correlation with the reference SBP. For every spectral band, the last S1 location corresponding to an energy ratio of less than 0.9 (meaning significant reduction in the normalised energy) before transitioning to a nearly constant energy ratio of around 1 is noted. The bands are rank ordered depending on the closeness of the detected S1 location with the reference SBP. The first three ranks awarded to different frequency bands with respect to the reference arm and wrist SBP are listed in Table 5.2. The feature band is determined by considering the sum of only the first and the second ranks. Based on the rank ordering, it can be observed that for both the arm and the wrist references, the spectral bands of 50-80 Hz and 80-110 Hz arise as the best choices. Therefore, the normalised energy of the S1 sounds in the spectral band of 50-110 Hz reduces from a higher value to a constant value when transitioning from before to after the reference

**Table 5.2:** Rank ordering the frequency bands as the best spectral feature band for determining the SBP. The bands are compared for a total of 35 files and ranked according to the closeness of the maximum energy ratio with the SBP location obtained from the commercial arm and wrist monitor.

Reference	Frequency Band	Rank Order			Total
		First	Second	Third	
<b>Arm</b>	10-30 Hz	1	3	2	4
	30-50 Hz	2	2	8	4
	50-80 Hz	8	17	7	25
	80-110 Hz	17	6	6	23
	110-150 Hz	7	7	12	14
<b>Wrist</b>	10-30 Hz	2	3	2	5
	30-50 Hz	2	2	8	4
	50-80 Hz	7	17	6	24
	80-110 Hz	18	6	6	24
	110-150 Hz	6	7	13	13

SBP. Hence, the algorithm uses the normalised energy envelope computed in the spectral band of 50-110 Hz as another feature signal to find the experimental location of the SBP.

### 5.5.1.3 Template matching coefficient envelope

The motor noise transferred during the cuff inflation introduces significant baseline noise in the acoustic signal. While the S1 sounds around the DBP carry higher amplitudes and energies, they suffer a significant loss of SNR when reaching the pressure levels near the SBP. Some of these peaks around the SBP might get hidden in the baseline noise and remain undetected by the relative energy algorithm. The loss of peaks when correlated with the pressure signal can introduce significant error in determining the experimental SBP. Therefore, all the S1 sounds occurring before the full occlusion of the arterial branch must be determined. Since the relative energy algorithm works efficiently in cases where the S1 sounds are characterised by a local change in the amplitude, the method fails to detect the peaks near the SBP because of very low amplitudes. A new approach utilising the morphology of the S1 sounds, instead of the amplitude, is proposed to detect the peaks near the SBP.

In Section 4.5, the morphological variations of the S1 sounds were discussed and it was established that the shape characteristics of the S1 waveforms for a subject does not change over the length of the recording. However, the morphology of the S1 sounds during the cuff inflation vary continuously as shown in Fig. 5.11. It can be observed that while the S1 sounds maintain an approximately constant shape before the cuff inflation, the morphology of these waveforms change significantly around the DBP. Further changes

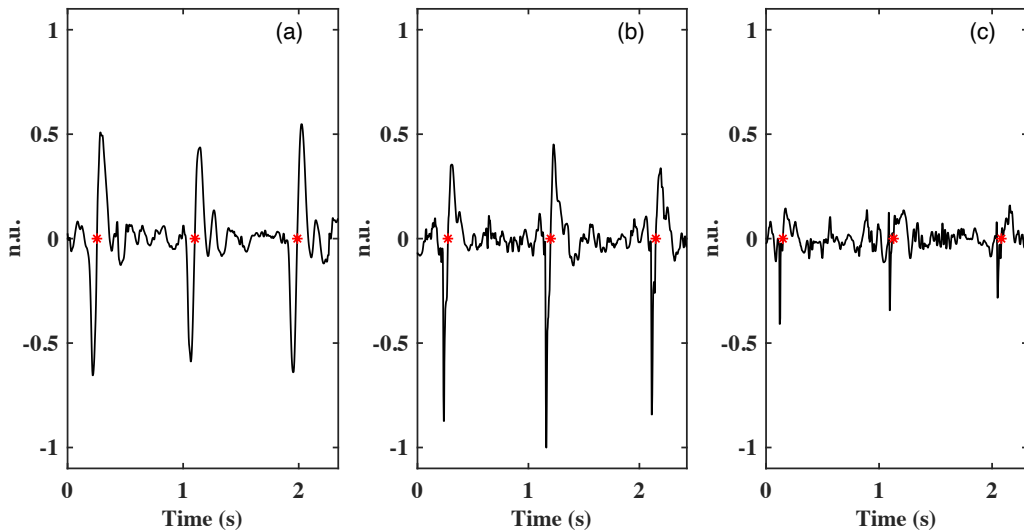


**Figure 5.11:** *S1 waveforms in the acoustic signal recorded from a subject (a) before cuff inflation, (b) around the DBP, (c) before reaching the SBP. The zero crossings of these peaks are also marked.*

to these waveforms occur before reaching the SBP. It is these changes that also reflect in the frequency domain to introduce energies in the higher frequencies. The template matching algorithm is used to detect the peaks near the SBP by utilising the shape of the S1 sounds. The template matching algorithm uses an already available waveform, also known as a template, to search and find the location of other similar waveforms in the signal [11]–[13]. The algorithm slides the template over the signal in specific windows to compare the cross-correlation between the template and the windowed segment of the signal. The cross-correlation measures the similarity between a time-series  $x$  and the shifted (lagged) copies of another time-series  $y$  as a function of the lag [14]. The polarity of the cross-correlation coefficients define a correlation to be positive or negative.

The relative energy algorithm performs quite well in detecting the S1 sounds around the DBP. Therefore, the S1 sound detected corresponding to the experimental location of the DBP is used as the initial template in the template matching algorithm. For the zero-crossing  $z_d$  of such S1 sound in the acoustic signal  $y$ , the initial template  $T_0$  is defined as follows:

$$T_0 = y [z_d - 0.1 : z_d + 0.1] \quad (5.7)$$

A narrower window is chosen to ensure that no noisy transitions around the S1 sound are included in the template. Since the morphology of the S1 sounds changes continuously during the cuff inflation, the same template cannot be used to find the correlation with the subsequent peaks. Hence, an adaptive template matching involving a continuous adaptation of the template is used for a reliable peak detection. Another input required for the cross-correlation is a suitable windowed segment containing the peak of interest. It is empirically observed that the inter-beat intervals does not change significantly during the short acoustic recordings of less than one minute for the blood pressure determination. Therefore, the inter-beat intervals corresponding to the detected S1 sounds from the relative energy algorithm are utilised to find the windowed segments. The peaks of interest in the acoustic signal using the template matching algorithm are found as follows:

1. The initial inter-beat interval  $IBI_0$  is calculated by taking the mean of the last three beats lying just before the DBP.

$$IBI_0 = \frac{\sum_{n=0}^2 (z_{d-n} - z_{d-n-1})}{3} \quad (5.8)$$

2. A windowed segment  $W_1$  is extracted from the original signal using the initial IBI. A relaxed tolerance is kept for an irregular heartbeat detection.

$$W_0 = y [z_d + 0.9 \times IBI_0 - 0.1 : z_d + 1.1 \times IBI_0 + 0.1] \quad (5.9)$$

3. The cross-correlation coefficient between the initial template  $T_0$  and the windowed segment  $W_0$  is found. The lag corresponding to the maximum correlation coefficient

is noted to find the best overlap between the template and the windowed segment. The zero-crossing of the peak detected from this overlap is identified to determine the next template.

4. The following template and the windowed segment are used in the next iteration.

$$\begin{aligned} T_1 &= y [z_{d+1} - 0.1 : z_{d+1} + 0.1] \\ \text{IBI}_1 &= 0.75 \times \text{IBI}_0 + 0.25 \times (z_{d+1} - z_d) \\ W_1 &= y [z_{d+1} + 0.9 \times \text{IBI}_1 - 0.1 : z_{d+1} + 1.1 \times \text{IBI}_1 + 0.1] \end{aligned} \quad (5.10)$$

The zero-crossing corresponding to the best overlap between the template  $T_1$  and the windowed segment  $W_1$  is found and the next template is determined.

5. The steps in (3) and (4) are reiterated until all the peaks falling between the DBP and the maximum pressure level are reached. The maximum pressure is generally 20-30 mmHg higher than the entry SBP of the subject. However, the templates are only changed when the maximum correlation coefficient obtained from the current overlap exceeds half the value obtained in the previous overlap. This ensures that the unreliable S1 sounds hidden in the baseline noise of the acoustic signal are not chosen as the templates for peak detection.
6. For every iteration, the maximum correlation coefficient  $C_n$  is stored and used as another feature signal to find the experimental location of the SBP.

For the acoustic signals in Fig. 5.9(b) and Fig. 5.12(b), the peaks detected using the relative energy algorithm and the template matching algorithm are marked by ‘\*’ and ‘o’ respectively. While the relative energy algorithm is able to detect majority of the peaks possessing higher SNR, it fails to detect the S1 sounds with lower amplitudes. On the contrary, the template matching algorithm successfully identifies all the S1 sounds during the cuff inflation. The peaks extrapolated using the IBIs in the noisy region provide a critical information about the energy in the baseline of the acoustic signal.

### 5.5.2 Utilising the feature signals to identify the S1 sound corresponding to the systolic blood pressure

In addition to the amplitude and the energy envelope, the SBP algorithm also uses the correlation coefficient envelope as a feature signal. These envelopes are computed for all the peaks detected using the template matching algorithm and lying after the DBP (including the noisy region). The goal of the SBP algorithm is to find the temporal location of a suitable S1 sound which when correlated with the pressure signal provides an accurate SBP. The feature signals for two different types of acoustic signals are plotted in Fig. 5.9(c)-(e) and Fig. 5.12(c)-(e) respectively. Both the original and the filtered envelopes are plotted, however, only the filtered envelopes are used for the further processing.



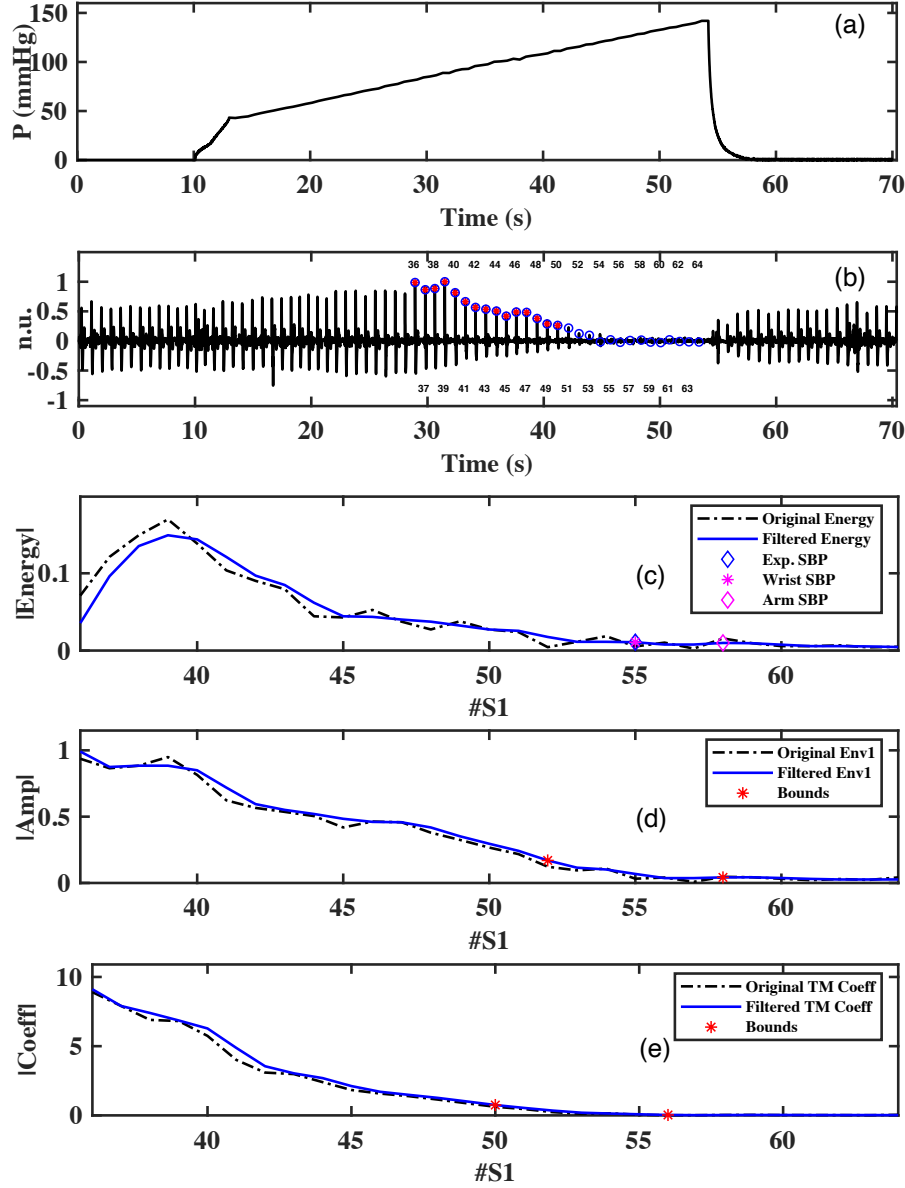


**Figure 5.12:** *Energy and amplitude envelopes of the Korotkoff sounds with peaks marked in the positive side of the acoustic signal. (a) Pressure applied on the arm increases between zero and a value above the systolic blood pressure. (b) Pre-processed acoustic signal with all the S1 peaks identified. (c) Energy envelope of the Korotkoff sounds falling after the 40 mmHg pressure level. The experimentally determined Korotkoff sound location for SBP determination is also plotted along with the reference wrist and reference arm SBP location. An error of 0 and 6 mmHg was obtained with respect to the wrist and arm SBP references respectively. (d) Amplitude envelope of the positive amplitudes (upper envelope) of the S1 peaks falling after the 40 mmHg pressure level. The bounds used in the proposed algorithm are also plotted. (e) Template matching coefficients envelope of the S1 peaks falling after the 40 mmHg pressure level. The bounds used in the proposed algorithm are also plotted.*

During the cuff inflation, the SBP is characterised as the disappearance of the pulse or the S1 sound. The S1 sounds disappear due to the complete blockage of the blood flow when an external pressure applied on the arterial branch exceeds the maximum arterial pressure. Therefore, if the noise inherent to the system and the surrounding environment is zero, then the amplitude and the energy of the S1 sounds transition from a finite value to a zero value when moving from before the SBP to after the SBP. Due to the presence of motor noise and noise inherent to the wearable device, the acoustic signal has a finite amplitude and energy even after the full occlusion of the artery. It can be observed that all the feature signals in Fig. 5.9 and Fig. 5.12 obtain a minimum value corresponding to the peaks detected in the noisy region. Similar to the DBP algorithm, firstly a narrow region of interest among  $N$  number of detected peaks, is searched using the amplitude ( $A_n$ ) and the correlation coefficient ( $CC_n$ ) envelope. These features for the peaks in the noisy region (i.e. above the SBP) take similar values and produces a ratio quite close to 1. However, the amplitude and the correlation coefficient for the last S1 sound near the SBP are large enough than the noisy peaks such that a ratio significantly less than 1 is obtained. The minimum amplitude  $A_{min}$  and the minimum correlation coefficient  $CC_{min}$  are calculated as follows:

$$\begin{aligned} A_{min} &= \text{mean}\{A_N, A_{N-1}, A_{N-2}\} \\ CC_{min} &= \text{mean}\{CC_N, CC_{N-1}, CC_{N-2}\} \end{aligned} \quad (5.11)$$

For both the feature signals, the last peak that has an amplitude greater than  $1.1 \times A_{min}$  and  $1.1 \times CC_{min}$  respectively, and has a ratio less than 0.9 is chosen as the centre point of the envelope bounds. All the peaks that lie within  $\pm 3$  beats of both the centre points are included for the further analysis of determining the SBP. For example, the bounds for the amplitude and the correlation coefficient envelopes in Fig. 5.9 are between [30,36] and [29,35] respectively. These bounds for the acoustic signal in Fig. 5.12 are between [52,58] and [50,56] respectively.

The bounds calculated using the amplitude and correlation coefficient envelopes narrowed the region to search for the S1 sound location corresponding to the SBP. For the acoustic signals in Fig. 5.9 and Fig. 5.12 respectively, only peaks that are numbered between [30,35] and [52,56] are processed further. Among the shortlisted peaks, the last peak that has an energy ratio less than 0.9 is chosen as the S1 sound corresponding to the SBP. The time-stamp of the chosen S1 sound is extracted from the acoustic signal and the corresponding pressure value from the synchronous pressure signal is found. This value of pressure is assumed to be the experimental SBP of the subject. As an illustration, the S1 numbered 32 in Fig. 5.9(b) correlates to an experimental SBP of 114 mmHg and produces an error of 2 mmHg and 4 mmHg with respect to the wrist and arm SBP references respectively. The same analysis for the acoustic signal in Fig. 5.12 produces an error of 0 mmHg and 6 mmHg with respect to the wrist and arm SBP references

respectively. The 55<sup>th</sup> S1 sound is chosen as the experimental location of the SBP.

## 5.6 Experimental procedure

To assess the performance of the proposed algorithm over a diverse cohort, a total of 40 subjects were recruited at Imperial College London. The study was approved by the local ethics committee of Imperial College London and all research was performed in accordance with the relevant guidelines and regulations. The informed consent was obtained from all the subjects before starting the data acquisition for the blood pressure measurement. The subjects were also asked to provide details regarding their age, gender, weight, height, BMI, any pre-existing diseases, arm and wrist circumferences, entry SBP and DBP at arm and wrist respectively. The subjects characteristics in this experiment are provided in Table 5.3.

**Table 5.3:** *Statistical information about the participants in the data acquisition.*

Parameters	Mean $\pm$ SD	Range
Men:Women	34:6	
Age (years)	23.27 $\pm$ 4.04	20 - 41
Weight (Kg)	71.48 $\pm$ 9.83	52 - 92
Height (cm)	176.08 $\pm$ 7.90	159 - 193
BMI	23.04 $\pm$ 2.73	16.6 - 29.3
Arm circumference (cm)	28.32 $\pm$ 2.95	22.0 - 33.5
Wrist circumference (cm)	16.18 $\pm$ 1.11	14.0 - 18.5
Entry wrist SBP (mmHg)	114.90 $\pm$ 10.57	98 - 137
Entry wrist DBP (mmHg)	74.37 $\pm$ 8.82	56 - 107
Entry arm SBP (mmHg)	115.30 $\pm$ 12.36	85 - 148
Entry arm DBP (mmHg)	70.25 $\pm$ 6.35	59 - 86
Entry heart rate (bpm)	64.63 $\pm$ 11.12	44 - 103

Data is expressed as mean  $\pm$  SD (standard deviation) and range (except the gender ratio). Entry SBP/ DBP denote the first readings obtained from the commercial monitors.

The reference blood pressure measurements were recorded using a wrist-based and an arm-based automated oscillometric blood pressure monitor. While the reference SBP/ DBP at the upper arm were recorded using the Omron M7 Intelli IT (HEM-7322T-E) monitor (Omron Healthcare Co., Ltd., Kyoto, Japan), the reference SBP/ DBP at the wrist were measured using the Omron RS6 monitor (Omron Healthcare Co., Ltd., Kyoto, Japan). The Omron M7 monitor uses an intelligent cuff wrap technology by providing

360° accuracy from any position around the upper arm [15], [16]. The monitor also detects any body movement and indicates if the cuff is wrapped too loose or too tight. The monitor has been validated clinically for healthy, diabetic and pregnant subjects and the company claims an accuracy of  $\pm 3$  bpm with respect to the gold standard mercury sphygmomanometer approach. The accuracy of the monitor has also been validated in the literature [17] where it passed the validation criteria for both the BHS and the AAMI protocols and was recommended for professional and home-use. The Omron RS6 monitor, on the contrary, uses an inbuilt positioning sensor to locate the wrist at the level of the heart while measuring the blood pressure [18]. The automatic detection of the wrist position removes any error arising from the hydrostatic pressure developed due to a vertical difference between the wrist and the heart levels. The monitor has been validated clinically and the company claims an accuracy of  $\pm 3$  bpm with respect to the gold standard mercury sphygmomanometer approach. The accuracy of the monitor has also been validated in the literature [19] where it passed the validation criteria for the ESH-IP 2010 protocol and was found to be suitable for home-use.

The following experimental protocol was followed during the data acquisition for all the subjects:

1. Before the actual appointment, the subjects were asked to avoid drinking any beverage or eating anything in the last 2 hours. The subjects on any medication related to the blood pressure were also asked to avoid the intake of such medication in the last 24 hours prior to the study.
2. The subjects at the start of the appointment were asked to sit on a chair with the feet flat on the floor (i.e. no crossed legs) and back straight with a support. This body state was maintained throughout the experimental procedure.
3. After recording the participant information, the subjects were asked to relax and be silent for 5 minutes duration before taking the first blood pressure measurement.
4. The first reference reading from the left wrist using Omron RS6 monitor was recorded by bending the elbow and raising the wrist at the level of the heart. The inbuilt position sensor only allows the measurement when the wrist lies at the level of the heart. Since the monitor works on the inflationary oscillometric principle, the rising pressure levels can cause wrist movements possibly leading to the wrong reference readings. This is avoided by providing a support to the subject's forearm using a small pillow. Further, the subjects were also asked to open the fist and avoid bending the wrist or clenching the fist during the recording.
5. After 1 minute of the relaxation period, the reference reading from the upper arm of the left hand was recorded using the Omron M7 monitor by placing the cuff at

the level of the heart with the lower end of the cuff 2-3 cm above the antecubital fossa.

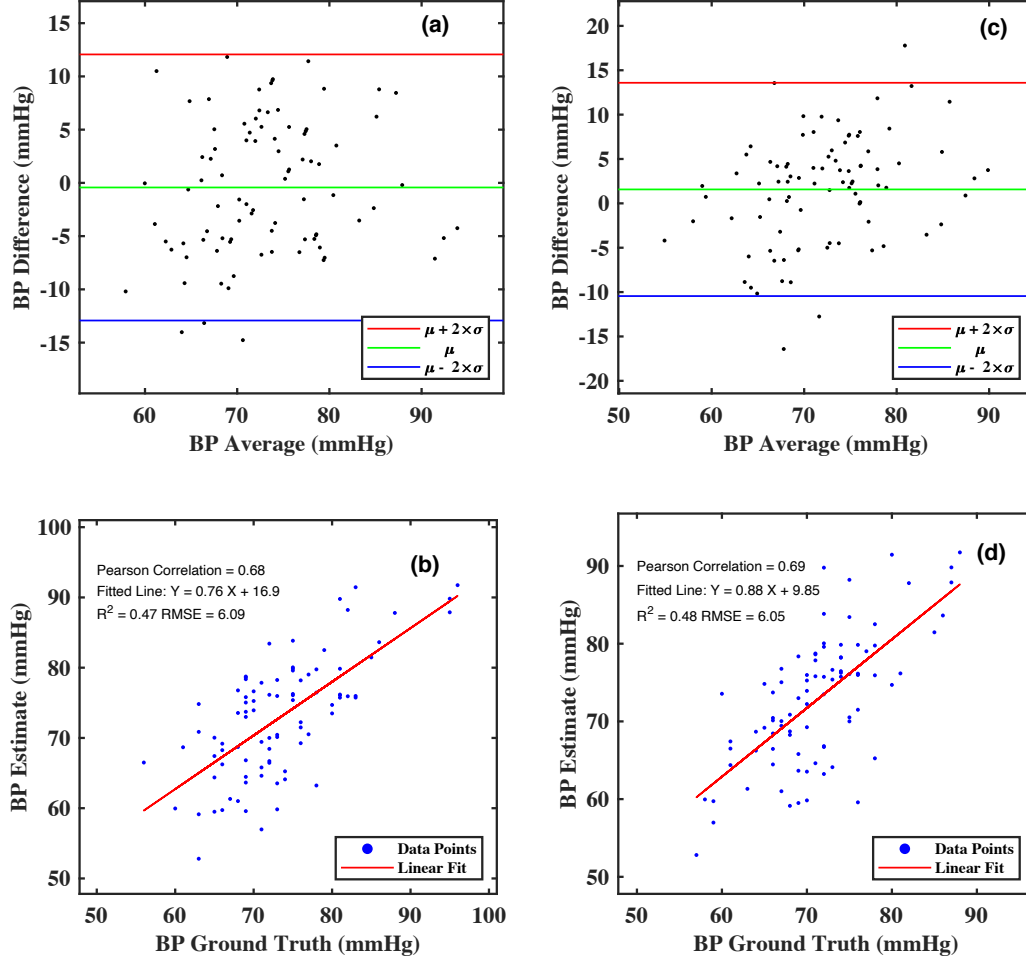
6. After 1 minute of the relaxation period, the acoustic signal from the radial artery of the left wrist was recorded in synchronisation with the pressure signal applied on the left arm. The wrist was positioned at the level of the heart during the measurement. The sampling frequencies of the acoustic signal and the pressure signal were 2100 Hz and 100 Hz respectively. Depending on the arm circumference of the subject, a suitable cuff size as discussed in Section 5.2 was wrapped around the upper arm.
7. Two more sets of blood pressure measurements (wrist/ arm reference readings + acoustic/ pressure experimental recordings) were performed for a total of 40 subjects. A relaxation period of 3 minutes was kept between two consecutive sets of the readings.
8. The reference measurements were repeated if a difference of more than 10 mmHg was observed between either the SBP or the DBP from the wrist and arm readings.

A total of 104 acoustic recordings along with the reference wrist/ arm blood pressure readings from 40 subjects were included in the database because some subjects felt uncomfortable after the first or second set of blood pressure measurement.

## 5.7 Results and discussion

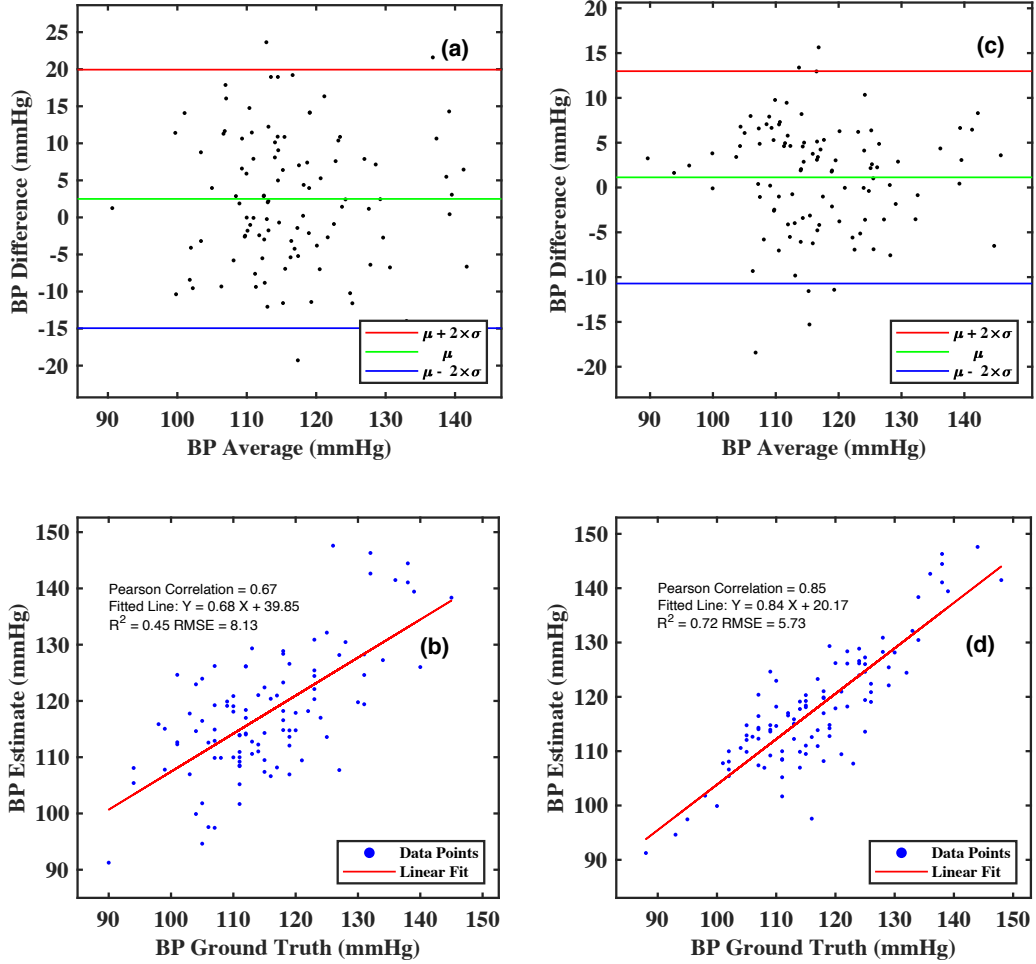
The performance of the proposed algorithm to determine the DBP and the SBP from the acoustic recordings is assessed using the Bland-Altman and the correlation analysis. The experimental DBP and SBP are compared separately with the reference readings from the wrist and arm blood pressure monitors. Therefore, a total of four different plots for the DBP and the SBP comparisons are individually presented in Fig. 5.13 and Fig. 5.14 respectively. While the Bland-Altman analysis indicate the extent of statistical agreement between the experimental and the reference outputs, the correlation analysis provides the degree of similarity between them. The details about these analysis methods have been discussed in earlier chapters of this thesis.

Table 5.4 lists the performance parameters obtained from the Bland-Altman analysis of 104 acoustic recordings from 40 subjects. A standard deviation of around 6 bpm is obtained for the DBP estimation using the proposed algorithm with respect to both the reference monitors. The SBP algorithm also achieves a standard deviation of approximately 6 bpm in comparison to the arm monitor. However, the SBP error with respect to the wrist monitor is significantly higher and a standard deviation of around 9 bpm is obtained. The percentage of samples with absolute differences less than 5 mmHg, 10 mmHg and 15 mmHg are also listed in Table 5.5. It can be observed that both the



**Figure 5.13:** Results obtained for the DBP determination from the acoustic signal. (a) Bland-Altman analysis for the DBP comparisons with the wrist DBP reference. (b) Correlation analysis for the DBP comparisons with the wrist DBP reference. (c) Bland-Altman analysis for the DBP comparisons with the arm DBP reference. (d) Correlation analysis for the DBP comparisons with the arm DBP reference.

DBP and the SBP algorithms demonstrate a higher statistical agreement with the arm monitor than the wrist monitor. A possible reasoning behind such an observation is that the commercial wrist-based blood pressure monitors have been found to overestimate the upper arm blood pressure [20]. While the discrepancy of the hydrostatic pressure developed due to the wrist position in relation to the heart is minimised using the inbuilt position sensor, the error in these monitors mainly arises because of insufficient occlusion of the forearm arteries [21]. This was not the case with the experiment in this study since an external pressure of 20-30 mmHg higher than the entry SBP was applied on the



**Figure 5.14:** Results obtained for the SBP determination from the acoustic signal. (a) Bland-Altman analysis for the SBP comparisons with the wrist SBP reference. (b) Correlation analysis for the SBP comparisons with the wrist SBP reference. (c) Bland-Altman analysis for the SBP comparisons with the arm SBP reference. (d) Correlation analysis for the SBP comparisons with the arm SBP reference.

brachial artery to ensure a full occlusion.

From the algorithmic point of view, a few sources of error exist. The pressure inside the air cuff is incremented in a staircase manner by controlling the operation of the motor and the valve. Since the staircase pressure is approximated by a linear pressure profile using the average values of the adjacent levels, a small pressure error can manifest when matching the time-stamp of the S1 sound with the pressure signal. The interference from the motor noise in a spectral band similar to the acoustic signal also affects the performance of the algorithm. Although the piezoelectric air pumps operating at high

**Table 5.4:** *Comparison results from the Bland-Altman analysis.*

Reference	SBP			DBP		
	$\mu$	$\sigma$	LOA	$\mu$	$\sigma$	LOA
Arm	1.13	6.04	[-10.71, 12.98]	1.57	6.13	[-10.45, 13.59]
Wrist	2.50	8.90	[-14.95, 19.94]	-0.43	6.37	[-12.92, 12.06]

frequencies (e.g. 25 KHz) are available in the market [22]–[25], their specifications about the air flow and the back pressure limit their usage in the blood pressure monitoring system. The piezoelectric pump designed and developed by Omron Healthcare Co., Ltd., is an exception [26], however, the pump is not available for commercial purchase. It would be ideal to integrate a piezoelectric pump with suitable specifications in the blood pressure monitoring system as the motor noise can simply be filtered using a low-pass filter with a cut-off frequency of 150 Hz. Another source of error is possibly because of the hydrostatic pressure. While the wrist is positioned at the level of the heart during the data acquisition, the absence of an inbuilt position sensor in the hardware designed for this study can possibly introduce errors due to the hydrostatic pressure. Since the acoustic signal is recorded from the wrist and the pressure is applied on the upper arm, the pulse arrival time (PAT) between the onset of pulse at the upper arm and the wrist can also introduce small differences in synchronising the signals. However, the PAT was experimentally calculated by placing the wearable device on the brachial artery and a PPG sensor on the index finger to record the pulse simultaneously from both the locations. The PAT was found to vary in the range of 100-200 ms producing an insignificant pressure error between 0.4 to 0.8 mmHg for an inflation rate of 4 mmHg/s. Apart from these error sources, the performance of the pressure sensor in generating a proportional output voltage corresponding to the differential input pressure can also introduce significant error in the blood pressure estimation. Although the accuracy of the pressure sensor in the proposed system was validated by comparing the programmed maximum pressure level with the obtained maximum cuff pressure, the future work will incorporate the frequent calibration of the pressure sensor to eliminate any variation in the sensitivity of the sensor.

**Table 5.5:** *Percentage SBP/ DBP samples below the absolute differences of 5mmHg, 10 mmHg and 15 mmHg respectively.*

Reference	SBP			DBP		
	Absolute difference (%)			Absolute difference (%)		
	$\leq 5$ mmHg	$\leq 10$ mmHg	$\leq 15$ mmHg	$\leq 5$ mmHg	$\leq 10$ mmHg	$\leq 15$ mmHg
Arm	66	93	99	70	92	98
Wrist	46	77	91	60	94	100



## 5.8 Conclusion

The gold standard approach of measuring the blood pressure requires a trained clinician to listen to the Korotkoff sounds at the brachial artery. In this chapter, the duplication of the auscultation method has been studied on the wrist to investigate the feasibility of recording the Korotkoff sounds from the radial artery. A total of 104 acoustic recordings from 40 subjects were recorded in synchronisation with the pressure signal applied on the arterial branch in a non-invasive manner. The temporal and spectral characteristics of the acoustic signal demonstrated the presence of Korotkoff sounds during the cuff inflation. These sounds had a bandwidth of less than 150 Hz, however, only the feature signal obtained from the spectral band of 50-110 Hz was used to correlate with the experimental DBP and SBP. The proposed algorithms achieved a low standard deviation of around 6 bpm with respect to the reference blood pressure monitors. Although all the recommendations of the BHS protocol [27] were not followed during the data acquisition as it demands a recruitment of 85 subjects with blood pressure falling in different ranges, an interpolation guarantees a grade of A/A for the DBP determination and a grade of A/C for the SBP determination using the proposed algorithms with respect to the arm and the wrist monitors respectively. Since a mean error of less than 5 mmHg and a standard deviation of error less than 8 mmHg are obtained, the proposed algorithm achieves a pass grade following a similar interpolation for the ANSI/AAMI/ISO protocol [28].

In conclusion, this study showed for the first time, that the acoustic signal recorded from the radial artery at the wrist can be used as a novel physiological signal to measure the blood pressure of a subject. Since the acoustic signal is already recorded from a wearable device, further improvements in the hardware design for cuff inflation using a piezoelectric pump can allow the complete system to be integrated in a watch-like wearable system. However, an availability of a suitable piezoelectric pump in the market is a must for such a design to become a reality.

## References

- [1] G. Ogedegbe and T. Pickering, "Principles and techniques of blood pressure measurement," *Cardiology clinics*, vol. 28, no. 4, pp. 571–586, 2010.
- [2] J. Talts, R. Raamat, K. Jagomägi, and J. Kivastik, "An Influence of Multiple Affecting Factors on Characteristic Ratios of Oscillometric Blood Pressure Measurement," in *15th Nordic-Baltic Conference on Biomedical Engineering and Medical Physics (NBC 2011)*, K. Dremstrup, S. Rees, and M. Ø. Jensen, Eds. Berlin, Heidelberg: Springer Berlin Heidelberg, 2011, pp. 73–76.
- [3] T. Rauterkus, J. F. Feltz, and J. W. Fickes, "Frequency analysis of Korotkov blood pressure sounds using the Fourier transform," SYSTEMS RESEARCH LABS INC DAYTON OH, Tech. Rep., 1966.
- [4] A. H. Maurer and A. Noordergraaf, "Korotkoff sound filtering for automated three-phase measurement of blood pressure," *American heart journal*, vol. 91, no. 5, pp. 584–591, 1976.
- [5] J. Allen and A. Murray, "Time-frequency analysis of Korotkoff sounds," 1997.
- [6] J. Allen, T. Gehrke, J. J. O'Sullivan, S. T. King, and A. Murray, "Characterization of the Korotkoff sounds using joint time–frequency analysis," *Physiological measurement*, vol. 25, no. 1, p. 107, 2003.
- [7] D. P. Golden, R. A. Wolthuis, G. W. Hoffler, and R. J. Gowen, "Development of a Korotkov Sound Processor for Automatic Identification of Auscultatory Events-Part I: Specification of Preprocessing Bandpass Filters," *IEEE Transactions on Biomedical Engineering*, no. 2, pp. 114–118, 1974.
- [8] S. Rodbard and A. S. Robbins, "The components of the Korotkoff sounds," *American heart journal*, vol. 74, no. 2, pp. 278–282, 1967.
- [9] M. Levy, A. Pappano, and R. Berne, "Cardiovascular physiology: Mosby Elsevier," 2007.
- [10] C. F. Babbs, "The origin of Korotkoff sounds and the accuracy of auscultatory blood pressure measurements," *Journal of the American Society of Hypertension*, vol. 9, no. 12, pp. 935–950, 2015.
- [11] P. Van Dam, S. Mouton, and P. Oosterhoff, "Template matching method for monitoring of ECG morphology changes," Aug. 9 2011, uS Patent 7,996,070.
- [12] T.-W. Shen, W. Tompkins, and Y. Hu, "One-lead ECG for identity verification," in *Proceedings of the Second Joint 24th Annual Conference and the Annual Fall Meeting of the Biomedical Engineering Society*[*Engineering in Medicine and Biology*, vol. 1. IEEE, 2002, pp. 62–63.
- [13] Q. Li and G. D. Clifford, "Dynamic time warping and machine learning for signal quality assessment of pulsatile signals," *Physiological measurement*, vol. 33, no. 9, p. 1491, 2012.
- [14] M. M. Daniel and A. C. Singer, *Computer explorations in signals and systems using MATLAB*. Upper Saddle River, NJ: Prentice Hall, 2002.
- [15] "Omron M7 Intelli IT." [Online]. Available: <https://www.omron-healthcare.co.uk/blood-pressure-monitors/M7.Intelli.IT.html>
- [16] "Automatic Upper Arm Blood Pressure Monitor M7 Intelli IT (HEM-7322T-E) Instruction Manual." [Online]. Available: [https://www.ajmedical.se/media/wysiwyg/ajm/pdf/Manual\\_Omron\\_M7\\_Intelli\\_IT\\_eng.pdf](https://www.ajmedical.se/media/wysiwyg/ajm/pdf/Manual_Omron_M7_Intelli_IT_eng.pdf)
- [17] A. Coleman, S. Steel, P. Freeman, A. de Greeff, and A. Shennan, "Validation of the Omron M7 (HEM-780-E) oscillometric blood pressure monitoring device according to the British Hypertension Society protocol," *Blood pressure monitoring*, vol. 13, no. 1, pp. 49–54, 2008.
- [18] "Omron RS6 Blood Pressure Monitor." [Online]. Available: <https://medaval.ie/docs/manuals/Omron-RS6-Manual.pdf>
- [19] H. Takahashi, M. Yoshika, and T. Yokoi, "Validation of Omron RS8, RS6, and RS3 home blood pressure monitoring devices, in accordance with the European Society of Hypertension International Protocol revision 2010," *Vascular health and risk management*, vol. 9, p. 265, 2013.

- [20] P. Palatini, D. Longo, G. Toffanin, O. Bertolo, V. Zaetta, and A. C. Pessina, “Wrist blood pressure overestimates blood pressure measured at the upper arm,” *Blood pressure monitoring*, vol. 9, no. 2, pp. 77–81, 2004.
- [21] M. Kikuya, K. Chonan, Y. Imai, E. Goto, M. Ishii *et al.*, “Accuracy and reliability of wrist-cuff devices for self-measurement of blood pressure,” *Journal of hypertension*, vol. 20, no. 4, pp. 629–638, 2002.
- [22] “mp6 piezoelectric diaphragm micropump.” [Online]. Available: <https://www.servoflo.com/micropumps/mp6>
- [23] “Piezoelectric Micro Air Compressor.” [Online]. Available: [https://www.koge.com/file\\_data/20170825-092219.pdf](https://www.koge.com/file_data/20170825-092219.pdf)
- [24] “Microblower MZB1001T02 — Microblower (air pump) — Micro mechatronics — Murata Manufacturing Co., Ltd.” [Online]. Available: [https://www.murata.com/en-eu/products/mechatronics/fluid/microblower\\_mzb1001t02](https://www.murata.com/en-eu/products/mechatronics/fluid/microblower_mzb1001t02)
- [25] “Micro Piezoelectric Hydraulic Pump-PSD35.” [Online]. Available: <http://www.vito-fluid.com/en/Product/info/5>
- [26] Y. Sano, T. Ogura, T. Kobayashi, Y. Yamashita, Y. Doi, and W. Tsunoda, “Piezoelectric pump and blood-pressure information measurement device provided therewith,” Sep. 6 2016, US Patent 9,433,359.
- [27] E. O'Brien, J. Petrie, W. Littler, M. de Swiet, P. L. Padfield, D. Altman, M. Bland, A. Coats, N. Atkins *et al.*, “The British Hypertension Society protocol for the evaluation of blood pressure measuring devices,” *J hypertension*, vol. 11, no. Suppl 2, pp. S43–S62, 1993.
- [28] A. for the Advancement of Medical Instrumentation *et al.*, “Non-invasive sphygmomanometers—part 2: clinical investigation of automated measurement type ANSI/AAMI,” ISO 81060-2/ANSI-AAMI, 2nd ed. Arlington, VA: AAMI, Tech. Rep., 2013.

## 6 Conclusions

### 6.1 Contributions

This thesis has presented the novel concept of using acoustic sensing over the radial artery to extract cardiac parameters for continuous vital sign monitoring. To test the validity of this principle, a miniaturised, battery-operated wireless device consisting of a MEMS microphone has been designed. The system has a small form-factor and low weight so that it could be easily attached to the wrist, comfortable to wear, non-intrusive, and provide automatic and accurate representation of the instantaneous cardiac activity. The wearable device allowed to record the heart sounds together with the pulse wave, an attribute not possible with existing wrist-based sensing methods.

Chapter 1 introduced the impact of cardiovascular diseases on the global population and healthcare costs. It was found that the regular monitoring of three important physiological signals including the heart rate (HR), the heart rate variability (HRV) and the blood pressure (BP) can allow an early detection, prevention and diagnosis of increased cardiovascular risks. Based on these findings, the definitions, importance and common techniques of monitoring these physiological markers were reviewed. This was followed by a comparison of commercially available monitors that have been validated in the literature and were based on different measurement principles. For the HR/HRV monitoring, it was concluded that there is a strict need of alternative sensing mechanisms that can simultaneously provide the user-friendliness of the photoplethysmography (PPG)-based monitors, the accuracy of the electrocardiography (ECG)-based monitors, and a longer operational lifetime. For the BP monitoring, similar conclusions were drawn in proposing the integration of the automatic features of the oscillometry-based monitors with the accuracy of the auscultation method by automatically listening to the Korotkoff sounds at the wrist using the proposed wearable device.

Chapter 2 provided a brief review about the origin and components of the pulse formation in the circulatory system. Among the different arterial pulse locations, the radial artery was found to be an ideal site for pulse assessment. A comprehensive literature review of different techniques and applications to monitor the radial pulse was presented. The discussion on existing technologies having one or more disadvantages pointed the acoustic sensing of the radial pulse as an attractive option for wearable applications. Since the design and development of a wearable device imposes tight constraints on the electrical and mechanical specifications of the system, different types of acoustic sen-

sors, batteries, data acquisition hardware have been reviewed. Finally, the electronic components and their specifications used in designing the wearable acoustic device were presented.

Chapter 3 studied the temporal and spectral characteristics of the acoustic signal recorded from the radial artery. The power spectral analysis revealed that the signal power is mainly concentrated in the S1 and S2 sounds, with S2 sounds carrying a relatively lower energy. The optimal sensing location on the wrist to record a signal with higher signal-to-noise ratio was found by comparing the power spectrum of signals recorded from the distal, middle and proximal locations of the radial artery. The noise sources were also characterised to incorporate their removal either in the sensing system itself or the signal processing software. Finally, a novel algorithm based on the power spectral density of the S1 sounds was proposed to determine the average HR from the acoustic signals. A comparison with the PPG-based reference HR and commercial monitors demonstrated the potential of the new sensing modality to be used as an alternative, or to complement existing methods, for continuous monitoring of HR at the wrist.

Chapter 4 provided a comprehensive literature review of the algorithms to extract the HRV from different types of signals and sensing locations. The importance of characteristic points to represent a waveform of interest in the biomedical signal and determine the HRV accurately was established. An algorithm based on short- and long-term energies of the acoustic signal was proposed to identify the time-indices of three different characteristic points corresponding to the S1 events. The time-domain and frequency-domain HRV parameters showed a strong correlation and high statistical agreement with the parameters derived from PPG and ECG signals respectively. The results proved the reliability and high accuracy of extracting the HRV parameters from the acoustic signal recorded at the wrist.

Chapter 5 proposed to extend the novel concept of acoustic sensing at the wrist by studying its relationship with the BP. An automatic pressure control system was designed for the step-wise inflation of the air cuff to apply varying levels of external pressure on the arterial branch. The temporal and spectral characteristics of the acoustic signal recorded under the influence of external pressure were utilised to identify the relevant features for the systolic blood pressure (SBP) and diastolic blood pressure (DBP) estimation. The wide-band analysis of the acoustic signals revealed the presence of maximum spectral content of the Korotkoff sounds in the frequency band of 50-110 Hz. While the DBP algorithm utilised the amplitude and energy envelopes as the corresponding feature signals, the SBP algorithm also included the template matching coefficient envelope to find an association with the disappearance of the Korotkoff sounds. The experimental BP readings were compared with the reference arm- and wrist-based monitors and a low mean error and standard deviation of error were obtained. The results proved that the acoustic signal recorded from the radial artery can also be used as a novel physiological

signal to measure the BP of a subject.

## 6.2 Further Work

The work presented in this thesis has some advantages and disadvantages over the gold standard approaches of monitoring the cardiovascular parameters. ECG monitoring in the clinical settings provide a detailed cardiac information to help diagnose and monitor conditions affecting the heart. Acoustic sensing at the wrist is obviously no substitute for the ECG, however, the proposed wearable technology can be used for home assessment of the cardiac activity by integrating it easily within the daily lifestyle. In relation to PPG-based sensing, the proposed method is clearly superior in terms of the low power consumption, low cost and high resilience to the external artefacts. Unlike PPG-based devices, the attachment of the acoustic sensor to the wrist using a double-sided medical adhesive tape also ensures a proper contact and durability for signal acquisition. However, the installation of the tape can be uncomfortable for some subjects. It is worth noting that although the proposed sensing mechanism has been tested experimentally, this thesis presented just the proof of concept. To be used as part of a medical device, full clinical validation would require testing on a larger cohort wearing a device based on this principle in an ambulatory setting. This would allow not only to investigate a wider range of cardiac signals, but also to test with real life artifacts.

Additionally, the signal processing algorithms proposed in this thesis were implemented on a software with floating point data representation. Such an implementation does not provide the optimal characteristics of speed and power consumption when run on a portable device. The future work would require the conversion of floating point data to the fixed point data while maintaining a similar accuracy for the cardiovascular monitoring at the wrist.

From the hardware point of view, the wearable prototype used in the current study used a Bluetooth channel to transmit the acoustic data. The next iteration of the wearable design would require testing the Bluetooth transmission in different scenarios and across different operating systems of the receiver. For the BP estimation, separate hardware systems were used to record the acoustic signal and the pressure signal. In the future, the availability of the suitable piezoelectric motors in the market could be utilised to design an integrated watch-like wearable system for the BP monitoring. Therefore, a single wearable device could be used to regularly monitor the HR, the HRV and the BP for an early detection of the increased cardiovascular risk.

# Appendices

## A Permission for the third party copyrighted works used in this thesis

Table A.1 lists the summary of the permissions taken for the third party copyrighted works used in this thesis. Following the summary, all the permission documents are also attached in the order of figure numbers as follows:

1. Fig 1.5: Page 231-232
2. Fig 1.6: Page 233-234
3. Fig 2.1: Page 235
4. Fig 2.3(b): Page 236-237
5. Fig 2.6: Page 238-239
6. Fig 2.7: Page 240
7. Fig 2.8: Page 241
8. Fig 2.9(a): Page 242
9. Fig 2.10: Page 243-244



**Table A.1:** *Summary of the permissions taken for the third party copyrighted works used in this thesis.*

Page no.	Type of work	Figure no.	Source of work	Copyright holder and contact	Permission requested on	Permis- sion? Yes/ No?	Permission note
50	Figure	Fig. 1.5	Long term, implantable blood pressure monitoring systems, Biomedical Microdevices, 2008	© Springer Nature, Journalpermissions@springernature.com	30-12-2019	Yes	Online permission from Marketplace
52	Figure	Fig. 1.6	Error Mechanisms of the Oscillometric Fixed-Ratio Blood Pressure Measurement Method, Annals of biomedical engineering, 2013	© Springer Nature, Journalpermissions@springernature.com	30-12-2019	Yes	Online permission from Marketplace
78	Figure	Fig. 2.1	Textbook of medical physiology 11th ed, Elsevier Saunders, 2006	© Saunders, <a href="https://www.elsevier.com/support">https://www.elsevier.com/support</a>	30-09-2019	Not yet	Requested permission through website contact page
79	Figure	Fig. 2.2	Universal Health Solutions website	© The Cardio Group, <a href="http://www.uhsmmed.com/index.php">http://www.uhsmmed.com/index.php</a>	30-09-2019	Yes	Out of copyright
80	Figure	Fig. 2.3(a)	Radiopaedia website	© 2005-2020 Radiopaedia.org, <a href="https://radiopaedia.org/">https://radiopaedia.org/</a>	30-09-2019	Yes	Licensed with a Creative Commons Attribution Noncommercial Share Alike 3.0 Unported licence
80	Figure	Fig. 2.3(b)	Harvesting the radial artery, Annals of cardiothoracic surgery, 2013	© AME Publishing Company	28-09-2019	Yes	Online permission from Copyright Clearance Center
92	Figure	Fig. 2.6	TE Connectivity CM-01 B Series microphone frequency response	© TE Connectivity, Brand@te.com	30-09-2019	Not yet	Requested permission through email

**Table A.1:** *Summary of the permissions taken for the third party copyrighted works used in this thesis.*

Page no.	Type of work	Figure no.	Source of work	Copyright holder and contact	Permission requested on	Permis- sion? Yes/ No?	Permission note
95	Figure	Fig. 2.7	A review of silicon microphones, Sensors and actuators A: Physical, 1994	© Elsevier, <a href="https://www.elsevier.com/support">https://www.elsevier.com/support</a>	30-09-2019	Yes	Online permission from Copyright Clearance Center
96	Figure	Fig. 2.8	CUI Devices CMC-5044 microphone frequency response	© CUI Devices, sales3@cuiddevices.com	30-09-2019	Yes	Written permission through email
97	Figure	Fig. 2.9(a)	Flip chip packaging for MEMS microphones, Microsystem technologies, 2010	© Springer Nature, Journalpermissions@springernature.com	30-09-2019	Yes	Online permission from Copyright Clearance Center
97	Figure	Fig. 2.9(b)	Design and modeling of a MEMS dual-backplate capacitive microphone with spring-supported diaphragm for mobile device applications, Sensors, 2018	© MDPI AG, <a href="https://www.mdpi.com/about/contact">https://www.mdpi.com/about/contact</a>	30-09-2019	Yes	Licensed with a Creative Commons Attribution 4.0 licence
98	Figure	Fig. 2.10	Invensense INMP411 microphone frequency response	© TDK Corporation, sales.eu@invensense.com	22-12-2019	Not yet	Requested permission through email



Marketplace™

## Order Confirmation

Thank you, your order has been placed. An email confirmation has been sent to you. Your order license details and printable licenses will be available within 24 hours. Please access Manage Account for final order details.

This is not an invoice. Please go to manage account to access your order history and invoices.

### CUSTOMER INFORMATION

Payment by invoice: You can cancel your order until the invoice is generated by contacting customer service.

#### Billing Address

Mr. Piyush Sharma  
Flat 24, Nansen Village  
21 Woodside Avenue  
London  
United Kingdom  
+44 2075946297  
sp.sharmapiyush@gmail.com

#### Customer Location

Mr. Piyush Sharma  
Flat 24, Nansen Village  
21 Woodside Avenue  
London  
United Kingdom

#### PO Number (optional)

N/A

#### Payment options

Invoice

### PENDING ORDER CONFIRMATION

Total Due: 0.00 GBP

Confirmation Number: Pending

Order Date: 30-Dec-2019

#### 1. Biomedical microdevices

0.00 GBP

Order license ID  
ISSN  
Type of Use  
Publisher  
Portion

Pending  
1572-8781  
Republish in a thesis/dissertation  
KLUWER ACADEMIC PUBLISHERS (BOSTON)  
Chapter/article

#### LICENSED CONTENT

Publication Title	Biomedical microdevices	Rightsholder	Springer
Date	01/01/1998	Publication Type	e-Journal

30/12/2019	<a href="https://marketplace.copyright.com/rs-ui-web/mp/checkout/confirmation-details/c3308629-aa88-4944-91fa-d8473eee953b">https://marketplace.copyright.com/rs-ui-web/mp/checkout/confirmation-details/c3308629-aa88-4944-91fa-d8473eee953b</a>		
Language	English	URL	<a href="http://www.springerlink.com/openurl.asp?genre=journal&amp;issn=1387-2176">http://www.springerlink.com/openurl.asp?genre=journal&amp;issn=1387-2176</a>
Country	United States of America		

## REQUEST DETAILS

Portion Type	Chapter/article	Rights Requested	Main product and any product related to main product
Page range(s)	381		
Total number of pages	1	Distribution	Worldwide
Format (select all that apply)	Electronic	Translation	Original language of publication
Who will republish the content?	Academic institution	Copies for the disabled?	Yes
Duration of Use	Life of current edition	Minor editing privileges?	No
Lifetime Unit Quantity	Up to 499	Incidental promotional use?	No
		Currency	GBP

## NEW WORK DETAILS

Title	Acoustic Sensing as a Novel Wearable Approach for Cardiovascular Monitoring at the Wrist	Institution name	Imperial College London
		Expected presentation date	2020-01-01
Instructor name	Prof. Esther Rodriguez-Villegas		

## ADDITIONAL DETAILS

Order reference number	N/A	The requesting person / organization to appear on the license	Piyush Sharma
------------------------	-----	---	---------------

## REUSE CONTENT DETAILS

Title, description or numeric reference of the portion(s)	Long term, implantable blood pressure monitoring systems	Title of the article/chapter the portion is from	Long term, implantable blood pressure monitoring systems
Editor of portion(s)	Springer US	Author of portion(s)	Joseph A. Potkay
Volume of serial or monograph	N/A	Issue, if republishing an article from a serial	N/A
Page or page range of portion	381	Publication date of portion	2007-12-20

## PUBLISHER TERMS AND CONDITIONS

A maximum of 10% of the content may be licensed for republication. The user is responsible for identifying and seeking separate licenses for any third party materials that are identified anywhere in the work. Without a separate license, such third party materials may not be reused.

**If you are placing a request on behalf of/for a corporate organization, please use RightsLink. For further information visit**

<http://www.nature.com/reprints/permission-requests.html> and  
<https://www.springer.com/gp/rights-permissions/obtaining-permissions/882>



Marketplace™

## Order Confirmation

Thank you, your order has been placed. An email confirmation has been sent to you. Your order license details and printable licenses will be available within 24 hours. Please access Manage Account for final order details.

This is not an invoice. Please go to manage account to access your order history and invoices.

### CUSTOMER INFORMATION

Payment by invoice: You can cancel your order until the invoice is generated by contacting customer service.

#### Billing Address

Mr. Piyush Sharma  
Flat 24, Nansen Village  
21 Woodside Avenue  
London  
United Kingdom  
+44 2075946297  
sp.sharmapiyush@gmail.com

#### Customer Location

Mr. Piyush Sharma  
Flat 24, Nansen Village  
21 Woodside Avenue  
London  
United Kingdom

#### PO Number (optional)

N/A

#### Payment options

Invoice

### PENDING ORDER CONFIRMATION

Total Due: 0.00 GBP

Confirmation Number: Pending

Order Date: 30-Dec-2019

#### 1. Annals of biomedical engineering

0.00 GBP

Order license ID  
ISSN  
Type of Use  
Publisher  
Portion

Pending  
0090-6964  
Republish in a thesis/dissertation  
SPRINGER NEW YORK LLC  
Image/photo/Illustration

#### LICENSED CONTENT

Publication Title	Annals of biomedical engineering	Country	United States of America
		Rightsholder	Springer

30/12/2019

<https://marketplace.copyright.com/rs-ui-web/mp/checkout/confirmation-details/a7555171-83a0-430e-85cd-5dcb008ed03b>

Author/Editor	BIOMEDICAL ENGINEERING SOCIETY.	Publication Type	Journal
Date	01/01/1972		
Language	English		

## REQUEST DETAILS

Portion Type	Image/photo/illustration	Distribution	Worldwide
Number of images / photos / illustrations	1	Translation	Original language of publication
Format (select all that apply)	Print, Electronic	Copies for the disabled?	Yes
Who will republish the content?	Academic institution	Minor editing privileges?	No
Duration of Use	Life of current edition	Incidental promotional use?	No
Lifetime Unit Quantity	Up to 499	Currency	GBP
Rights Requested	Main product and any product related to main product		

## NEW WORK DETAILS

Title	Acoustic Sensing as a Novel Wearable Approach for Cardiovascular Monitoring at the Wrist	Institution name	Imperial College London
		Expected presentation date	2020-01-01
Instructor name	Prof. Esther Rodriguez- Villegas		

## ADDITIONAL DETAILS

Order reference number	N/A	The requesting person / organization to appear on the license	Piyush Sharma
---------------------------	-----	---	---------------

## REUSE CONTENT DETAILS

Title, description or numeric reference of the portion(s)	Error Mechanisms of the Oscillometric Fixed-Ratio Blood Pressure Measurement Method	Title of the article/chapter the portion is from	Error Mechanisms of the Oscillometric Fixed-Ratio Blood Pressure Measurement Method
Editor of portion(s)	JIANKUN LIU	Author of portion(s)	BIOMEDICAL ENGINEERING SOCIETY.
Volume of serial or monograph	N/A	Issue, if republishing an article from a serial	N/A
Page or page range of portion	588	Publication date of portion	1972-01-01

## PUBLISHER TERMS AND CONDITIONS

A maximum of 10% of the content may be licensed for republication. The user is responsible for identifying and seeking separate licenses for any third party materials that are identified anywhere in the work. Without a separate license, such third party materials may not be reused.

If you are placing a request on behalf of/for a corporate organization, please use RightsLink. For further information visit

<https://marketplace.copyright.com/rs-ui-web/mp/checkout/confirmation-details/a7555171-83a0-430e-85cd-5dcb008ed03b>

2/3

30 September 2019

Dear Official,

I am completing my PhD thesis at Imperial College London entitled 'Acoustic sensing as a novel approach for cardiovascular monitoring at the wrist'.

I seek your permission to reprint, in my thesis a figure from the book: "Textbook of Medical Physiology – Volume 9" by authors Arthur C. Guyton, John E. Hall. The extract to be reproduced is the plot of the events of the cardiac cycle for left ventricular function (Figure 9-5) from Page 107 of the book.

I would like to include the extract in my thesis which will be added to Spiral, Imperial's institutional repository <http://spiral.imperial.ac.uk/> and made available to the public under a Creative Commons Attribution-Non Commercial-No Derivatives 4.0 International Licence (CC BY-NC-ND).

If you are happy to grant me all the permissions requested, please return a signed copy of this letter. If you wish to grant only some of the permissions requested, please list these and then sign.

Yours sincerely,

Piyush Sharma  
PhD Student  
Imperial College London

**Permission granted for the use requested above:**

I confirm that I am the copyright holder of the extract above and hereby give permission to include it in your thesis which will be made available, via the internet, for non-commercial purposes under the terms of the user licence.

**[please edit the text above if you wish to grant more specific permission]**

Signed:

Name:

Organisation:

Job title:



**Note:** Copyright.com supplies permissions but not the copyrighted content itself.

1  
PAYMENT

2  
REVIEW

3  
CONFIRMATION

### Step 3: Order Confirmation

**Thank you for your order!** A confirmation for your order will be sent to your account email address. If you have questions about your order, you can call us 24 hrs/day, M-F at +1.855.239.3415 Toll Free, or write to us at [info@copyright.com](mailto:info@copyright.com). This is not an invoice.

**Confirmation Number: 11854978**  
**Order Date: 09/28/2019**

If you paid by credit card, your order will be finalized and your card will be charged within 24 hours. If you choose to be invoiced, you can change or cancel your order until the invoice is generated.

#### Payment Information

Piyush Sharma  
sp.sharmapiyush@gmail.com  
+44 2075946297  
Payment Method: n/a

#### Order Details

##### Annals of cardiothoracic surgery

**Order detail ID:** 72020217  
**Order License Id:** 4677830524801  
**ISSN:** 2225-319X  
**Publication Type:** Journal  
**Volume:**  
**Issue:**  
**Start page:**  
**Publisher:** AME Publishing Company

**Permission Status:** **Granted**

**Permission type:** Republish or display content  
**Type of use:** Thesis/Dissertation

**Requestor type:** Publisher, not-for-profit

**Format:** Print, Electronic

**Portion:** image/photo

**Number of images/photos requested:** 1

**The requesting person/organization:** Piyush Sharma

**Title or numeric reference of the portion(s):** Figure 1 Anatomic landmarks and skin incision. The skin incision follows a curvilinear course over the medial edge of the brachioradialis muscle. The proximal extent of the incision starts just below the inverted "V" formed by the biceps tendon and the bicipital aponeurosis, which lies about a centimeter below the elbow crease. The distal extent of the incision ends approximately 1 cm proximal to the wrist crease, in between the



tendon of the flexor carpi radialis and the radial styloid. There are six structures of paramount importance to the surgeon: the brachioradialis muscle, the flexor carpi radialis muscle, the recurrent radial artery, the superficial palmar artery, the superficial radial nerve and the lateral antebrachial cutaneous nerve

**Title of the article or chapter the portion is from**

Harvesting the radial artery

**Editor of portion(s)**

N/A

**Author of portion(s)**

Arie Blitz, Robert M. Osterday, Richard F. Brodman

**Volume of serial or monograph**

2

**Page range of portion**

534

**Publication date of portion**

Jul 16, 2013

**Rights for**

Main product

**Duration of use**

Life of current edition

**Creation of copies for the disabled**

no

**With minor editing privileges**

no

**For distribution to**

Worldwide

**In the following language(s)**

Original language of publication

**With incidental promotional use**

no

**Lifetime unit quantity of new product**

Up to 499

**Title**

A novel approach for cardiovascular monitoring

**Institution name**

Imperial College London

**Expected presentation date**

Jan 2020

**Note:** This item will be invoiced or charged separately through CCC's **RightsLink** service. [More info](https://www.copyright.com/printCoiConfirmPurchase.do?operation=defaultOperation&confirmNum=11854978&showTCCitation=TRUE)  
<https://www.copyright.com/printCoiConfirmPurchase.do?operation=defaultOperation&confirmNum=11854978&showTCCitation=TRUE>

**\$ 0.00**

2/6

05/01/2020

Gmail - Request to reproduce a figure from TE microphone's datasheet



Piyush Sharma <sp.sharmapiyush@gmail.com>

---

## Request to reproduce a figure from TE microphone's datasheet

1 message

---

**Piyush Sharma** <sp.sharmapiyush@gmail.com>  
To: Brand@te.com

Mon, Sep 30, 2019 at 10:19 PM

Hello Sir/ Mam,

I am a PhD student at Imperial College London and I used one of the TE microphones in my project. Since I am completing my PhD thesis soon, I wanted to include the plot of the frequency response of the CONTACT MICROPHONE CM-01B from its datasheet in my thesis. I kindly request you to grant me permission to use the plot in my thesis by signing the attached request form as soon as possible.

Thanks!

Best Regards,

Piyush Sharma  
Electrical & Electronic Engineering Department  
Imperial College London

---

 **Request form.docx**  
20K

30 September 2019

Dear Official,

I am completing my PhD thesis at Imperial College London entitled 'Acoustic sensing as a novel approach for cardiovascular monitoring at the wrist'.

I seek your permission to reprint, in my thesis an extract from: TE contact microphone CM-01B datasheet. The extract to be reproduced is the plot of the typical frequency response on Page-2 of the datasheet.

I would like to include the extract in my thesis which will be added to Spiral, Imperial's institutional repository <http://spiral.imperial.ac.uk/> and made available to the public under a Creative Commons Attribution-Non Commercial-No Derivatives 4.0 International Licence (CC BY-NC-ND).

If you are happy to grant me all the permissions requested, please return a signed copy of this letter. If you wish to grant only some of the permissions requested, please list these and then sign.

Yours sincerely,

Piyush Sharma  
PhD Student  
Imperial College London

**Permission granted for the use requested above:**

I confirm that I am the copyright holder of the extract above and hereby give permission to include it in your thesis which will be made available, via the internet, for non-commercial purposes under the terms of the user licence.

**[please edit the text above if you wish to grant more specific permission]**

Signed:

Name:

Organisation:

Job title:

# ELSEVIER LICENSE TERMS AND CONDITIONS

Sep 30, 2019

This Agreement between Piyush Sharma ("You") and Elsevier ("Elsevier") consists of your license details and the terms and conditions provided by Elsevier and Copyright Clearance Center.

License Number	4678880801399
License date	Sep 30, 2019
Licensed Content Publisher	Elsevier
Licensed Content Publication	Sensors and Actuators A: Physical
Licensed Content Title	A review of silicon microphones
Licensed Content Author	P.R. Scheeper,A.G.H. van der Donk,W. Olthuis,P. Bergveld
Licensed Content Date	Jul 1, 1994
Licensed Content Volume	44
Licensed Content Issue	1
Licensed Content Pages	11
Start Page	1
End Page	11
Type of Use	reuse in a thesis/dissertation
Intended publisher of new work	other
Portion	figures/tables/illustrations
Number of figures/tables/illustrations	1
Format	both print and electronic
Are you the author of this Elsevier article?	No
Will you be translating?	No
Original figure numbers	Fig. 3. (a) Schematic cross-sectional view of a condenser microphone. (b) The condenser microphone, connected to an external d.c. bias voltage source, loaded by a parasitic capacitance $C_p$ , a bias resistor $R_b$ and a preamplifier with an input capacitance $C_i$
Title of your thesis/dissertation	A novel approach for cardiovascular monitoring
Publisher of new work	Imperial College London
Expected completion date	Jan 2020
Estimated size (number of pages)	1
Requestor Location	Piyush Sharma Flat 24, Nansen Village 21 Woodside Avenue  London, other United Kingdom Attn:
Publisher Tax ID	GB 494 6272 12
Total	0.00 GBP

30 September 2019

Dear Official,

I am completing my PhD thesis at Imperial College London entitled 'Acoustic sensing as a novel approach for cardiovascular monitoring at the wrist'.

I seek your permission to reprint, in my thesis an extract from the CMC-5044PF-A datasheet. The extract to be reproduced is the plot of the typical frequency response on Page-2 of the datasheet.

I would like to include the extract in my thesis which will be added to Spiral, Imperial's institutional repository <http://spiral.imperial.ac.uk/> and made available to the public under a Creative Commons Attribution-Non Commercial-No Derivatives 4.0 International Licence (CC BY-NC-ND).

If you are happy to grant me all the permissions requested, please return a signed copy of this letter. If you wish to grant only some of the permissions requested, please list these and then sign.

Yours sincerely,

Piyush Sharma  
PhD Student  
Imperial College London

**Permission granted for the use requested above:**

I confirm that CUI Devices is the copyright holder of the extract above and hereby gives permission to include it in your thesis which will be made available, via the internet, for non-commercial purposes under the terms of the user licence.

Signed:

Name: Adam Hamill (approved by JSchnabel)

Organisation: CUI Devices

Job title: Account Manager

## SPRINGER NATURE LICENSE TERMS AND CONDITIONS

Sep 30, 2019

This Agreement between Piyush Sharma ("You") and Springer Nature ("Springer Nature") consists of your license details and the terms and conditions provided by Springer Nature and Copyright Clearance Center.

License Number	4678931072297
License date	Sep 30, 2019
Licensed Content Publisher	Springer Nature
Licensed Content Publication	Microsystem Technologies
Licensed Content Title	Flip chip packaging for MEMS microphones
Licensed Content Author	Gregor Feiertag, Matthias Winter, Anton Leidl
Licensed Content Date	Jan 1, 2010
Licensed Content Volume	16
Licensed Content Issue	5
Type of Use	Thesis/Dissertation
Requestor type	academic/university or research institute
Format	print and electronic
Portion	figures/tables/illustrations
Number of figures/tables/illustrations	1
Will you be translating?	no
Circulation/distribution	1 - 29
Author of this Springer Nature content	no
Title	A novel approach for cardiovascular monitoring
Institution name	Imperial College London
Expected presentation date	Jan 2020
Portions	Fig. 1 MEMS Microphone package with chip and wire bonding; Top sound port in lid, Bottom Sound port in PCB substrate
Requestor Location	Piyush Sharma Flat 24, Nansen Village 21 Woodside Avenue  London, other United Kingdom Attn:
Total	0.00 GBP
Terms and Conditions	

### Springer Nature Customer Service Centre GmbH Terms and Conditions

This agreement sets out the terms and conditions of the licence (the **License**) between you and **Springer Nature Customer Service Centre GmbH** (the **Licensor**). By clicking 'accept' and completing the transaction for the material (**Licensed Material**), you also confirm your acceptance of these terms and conditions.

#### 1. Grant of License

05/01/2020

Mail - Sharma, Piyush - Outlook

### Request to reproduce a figure from Invensense microphone's datasheet

Sharma, Piyush <piyush.sharma14@imperial.ac.uk>

Sun 22/12/2019 00:43

To: sales.eu@invensense.com <sales.eu@invensense.com>; techsupport\_Europe@invensense.com <techsupport\_Europe@invensense.com>

■ 1 attachments (20 KB)

Figure 3.11 permission.docx;

Hello Sir/ Mam,

I am a PhD student at Imperial College London and I used one of the Invensense microphones in my project. Since I am completing my PhD thesis soon, I wanted to include the plot of the frequency response of the INMP411 microphone from its datasheet in my thesis. I kindly request you to grant me permission to use the plot in my thesis by signing the attached request form as soon as possible.

Thanks!

Best Regards,

Piyush Sharma  
PhD Student  
Circuits & Systems Research Group  
Department of Electrical & Electronic Engineering  
Imperial College London, South Kensington, London SW7 2AZ  
Tel: +44 (0) 20 759 46297

30 September 2019

Dear Official,

I am completing my PhD thesis at Imperial College London entitled 'Acoustic sensing as a novel approach for cardiovascular monitoring at the wrist'.

I seek your permission to reprint, in my thesis an extract from the INMP411 datasheet. The extract to be reproduced is the plot of the typical frequency response on Page-7 of the datasheet.

I would like to include the extract in my thesis which will be added to Spiral, Imperial's institutional repository <http://spiral.imperial.ac.uk/> and made available to the public under a Creative Commons Attribution-Non Commercial-No Derivatives 4.0 International Licence (CC BY-NC-ND).

If you are happy to grant me all the permissions requested, please return a signed copy of this letter. If you wish to grant only some of the permissions requested, please list these and then sign.

Yours sincerely,

Piyush Sharma  
PhD Student  
Imperial College London

**Permission granted for the use requested above:**

I confirm that I am the copyright holder of the extract above and hereby give permission to include it in your thesis which will be made available, via the internet, for non-commercial purposes under the terms of the user licence.

**[please edit the text above if you wish to grant more specific permission]**

Signed:

Name:

Organisation:

Job title: